

Control Strategies Leveraging Topology Benefits in Modular Multilevel Converters

Regelungsstrategien unter Ausnutzung topologischer Vorteile in Modularen Multilevel-Umrichtern

Vom Fachbereich Elektrotechnik und Informationstechnik der
Rheinland-Pfälzischen Technischen Universität Kaiserslautern-Landau
zur Verleihung des akademischen Grades
Doktor der Ingenieurwissenschaften (Dr.-Ing.)
genehmigte Dissertation

von
Pedro Leal dos Santos
geboren in Lissabon

D 386

Tag der mündlichen Prüfung:	10.10.2025
Dekan des Fachbereichs:	Prof. Dr.-Ing. Daniel Görges
Vorsitzender der Prüfungskommission:	Prof. Dr.-Ing. Daniel Görges
1. Berichterstatter:	Prof. Dr.-Ing. Steven Liu
2. Berichterstatter:	Prof. Dr.-Ing. Stefan Götz

Acknowledgment

This thesis presents the results of my work at the Institute of Control Systems in the Department of Electrical and Computer Engineering at the University of Kaiserslautern-Landau.

First and foremost, I would like to express my sincere gratitude to my supervisor, Prof. Dr.-Ing. Steven Liu, for his invaluable support, guidance, and supervision throughout my research. His insightful scientific discussions and constant encouragement greatly enriched my work and shaped my journey at the Institute of Control Systems.

Furthermore, I would like to thank Prof. Dr.-Ing. Stefan Götz for his interest in my research and for joining the thesis committee as a reviewer. My thanks also go to Prof. Dr.-Ing. Daniel Görge for joining the thesis committee as a chairman.

My time at the Institute of Control Systems has been both intellectually enriching and personally rewarding. I am grateful to all my colleagues for fostering an open, collaborative, and supportive environment. I am also sincerely thankful to my "working buddies" Dr.-Ing. Joe Ismail and M.Sc. Marco Guerreiro for all major research cooperations. Additionally, my appreciation goes to my colleagues M.Sc. Abd Alati Ahmed, M.Sc. Sebastian Bard, Dr.-Ing. Markus Bell, Dr.-Ing. Felix Berkel, M.Sc. Xiang Chen, M.Sc. Patarachai Chevathamnon, Dr.-Ing. Yanhao He, Dipl.-Ing. Adrian Herbst, Dr. Mennatallah Ibrahim, M.Sc. Muhammad Ikhsan, M.Sc. Kashif Iqbal, Dr.-Ing. Christoph Mark, Dr.-Ing. Bashar Melhem, Dr. Shivaraj S. Mohite, M.Sc. Qingshan Pan, Dr.-Ing. Tim Steiner, Dr.-Ing. Alan Turnwald, Dr.-Ing. Hengyi Wang, Dr.-Ing. Min Wu, and Dr.-Ing. Wei Wu. My warm appreciation also goes to the skillful technicians Swen Becker and Thomas Janz and to the relentless secretary Annegret Stabel for providing a good technical and administrative environment. Moreover, I would like to thank the associated professors Dr. Ricardo Luis and Dr. Pedro Fonte at Polytechnic University of Lisbon for the fruitful discussions and valuable suggestions.

During my journey, I had the privilege to work and guide brilliant students, among them a special thanks for your contributions goes to M.Sc. Marcel Wingert, M.Sc. Shrikant Kharade, M.Sc. Kristjan Lleshaj, M.Sc. Wesley Mateus Becker and M.Sc. Jonas Weires.

I am very thankful to my parents Cristina and Eduardo, my brother Diogo and his wife Carina, my auntie Alexandra and cousin Manuel, for the unconditional love and support throughout all the years. Special gratitude goes to my "KL-family" Angjela, Damjan, Laura, Diego, Simon and João. Last but not least, I would like to thank my lovely fiancée Mariana for being a leading example to me and standing by my side all the way. This thesis is dedicated to them.

Pedro

Abstract

Driven by rising global energy demand and the urgent need to reduce carbon emissions, large-scale electrification has become a critical objective – particularly through the integration of renewable energy sources and energy storage systems. These technologies are inherently Direct Current (DC) in nature, challenging the long-standing dominance of Alternating Current (AC) infrastructure and naturally promoting a structural change towards DC and hybrid AC/DC power systems. This transformation is made feasible by advancements in power electronics, where multilevel converter topologies such as the Modular Multilevel Converter (MMC) may play a key enabling role due to their scalability, efficiency, and operational flexibility. This thesis explores two innovative capabilities of the MMC that enhance its functionality as an interconnecting element between distinct power networks. The first contribution introduces the concept of power decoupling between AC and DC grids. By leveraging the MMC's flexible energy storage, the system enables independently shaped transient responses on both grid sides—offering a valuable opportunity to strengthen the interface between weak or mismatched networks. A hierarchical control structure is developed, combining Input-Output Feedback Linearization (IOFL) based controller, an extended disturbance observer, and a 2-Degree-of-Freedom (DOF) outer loop controller, validated through hardware implementation on a laboratory MMC prototype. A long-horizon Model Predictive Controller (MPC) is also introduced to handle system constraints, with its real-time feasibility evaluated in a Processor-in-the-Loop (PiL) environment. The second contribution presents a high step-down MMC-based DC to DC Converter (DC-DC) converter designed specifically for heavy-duty agricultural electrification, a sector traditionally difficult to electrify. In this application, a Medium-Voltage Direct Current (MVDC) microgrid supplies power to mobile agricultural machines. The converter uses an unconventional configuration of permanently inserted submodules to achieve transformerless operation and increased power density. A 300 kW hardware demonstrator is designed to experimentally validate the converter operation. A reduced-order model is developed to support the design of an adaptive controller, capable of maintaining a stable and uniformly responsive behavior under rapidly changing load conditions. In summary, this work demonstrates how the MMC – when paired with advanced control strategies can be a critical component of for future grid architectures and enable electrification in challenging applications. The proposed approaches contribute to the development of robust, flexible, and scalable power conversion systems essential for realizing the next generation of energy infrastructure.

Kurzfassung

Angetrieben durch den weltweit steigenden Energiebedarf und die dringende Notwendigkeit zur Reduktion von CO₂-Emissionen, rückt die großflächige Elektrifizierung zunehmend in den Fokus – insbesondere durch die Integration erneuerbarer Energiequellen und Energiespeichersysteme. Diese Technologien sind von Natur aus Gleichstrom-basiert, was die traditionelle Dominanz von Wechselstrom-Infrastrukturen infrage stellt und einen strukturellen Wandel hin zu Gleichstrom-(DC) und hybriden AC/DC-Energiesystemen begünstigt. Diese Transformation wird durch Fortschritte in der Leistungselektronik ermöglicht, wobei mehrstufige Wandler-Topologien wie der Modular Multilevel Umrichter (MMC) aufgrund ihrer Skalierbarkeit, Effizienz und betrieblichen Flexibilität eine zentrale Rolle einnehmen. Diese Arbeit stellt zwei bislang unerforschte Fähigkeiten des MMC vor, die seine Funktionalität als Verbindungselement zwischen verschiedenen Energienetzen erweitern. Der erste Beitrag führt das Konzept der Leistungsentkopplung zwischen AC- und DC-Netzen ein. Durch die Nutzung der flexiblen Energiespeicherung des MMC können transiente Reaktionen auf beiden Netzseiten unabhängig voneinander gestaltet werden – was eine wertvolle Möglichkeit darstellt, die Schnittstelle zwischen schwachen oder nicht abgestimmten Netzen zu stärken. Es wird eine hierarchische Regelstruktur entwickelt, die Input-Output-Feedback-Linearisation, einen erweiterten Störbeobachter und einen 2-DOF-Außenregelkreis kombiniert. Die Umsetzung und Validierung erfolgte an einem im Labor aufgebauten MMC-Prototyp. Zusätzlich wurde ein Model Predictive Controller (MPC) mit langem Planungshorizont eingeführt, dessen Echtzeitfähigkeit in einer Processor-in-the-Loop-Umgebung getestet wurde. Der zweite Beitrag behandelt die Entwicklung eines MMC-basierten DC-DC-Wandlers mit hohem Spannungsabsenkungsverhältnis, speziell konzipiert für die Elektrifizierung schwerer landwirtschaftlicher Maschinen – ein Bereich, der bisher als schwer zu elektrifizieren galt. In diesem Szenario versorgt ein MVDC-Mikronetz mehrere mobile landwirtschaftliche Maschinen. Der Wandler nutzt eine unkonventionelle Konfiguration dauerhaft eingesetzter Submodule, um eine transformatorlose Betriebsweise mit hoher Leistungsdichte zu ermöglichen. Ein 300-kW-Hardware-Demonstrator wurde zur experimentellen Validierung des Wandlers entwickelt. Ein reduziertes Ordnungsmodell dient als Grundlage für die Entwicklung eines adaptiven Reglers, der ein stabiles und einheitlich dynamisches Verhalten bei schnell wechselnden Lastbedingungen gewährleistet. Zusammenfassend zeigt diese Arbeit, dass MMCs in Kombination mit fortschrittlichen Regelungsverfahren eine entscheidende Komponente zukünftiger Netzarchitekturen darstellen und die Elektrifizierung anspruchsvoller Anwendungen ermöglichen können. Die vorgestellten Ansätze leisten einen Beitrag zur Entwicklung robuster, flexibler und skalierbarer Wandlerlösungen, die für die nächste Generation der Energieinfrastruktur von zentraler Bedeutung sind.

Contents

Acknowledgment

Abstract

List of Figures **V**

List of Tables **IX**

Abbreviations **XI**

1 Introduction **1**

- 1.1 General motivation 2
 - 1.1.1 Macro – Energy transition 2
 - 1.1.2 Micro – Key to green power 5
 - 1.1.3 Nano – Multilevel converters 12
- 1.2 Overview 17
 - 1.2.1 Outline 17
 - 1.2.2 Contributions 18

2 Modular Multilevel Converters **21**

- 2.1 Basic concepts 21
 - 2.1.1 Submodule 21
 - 2.1.2 Arm 25
 - 2.1.3 Average model 26
 - 2.1.4 Energy framework 28
- 2.2 Circuit analysis 29
- 2.3 State-space model 34
 - 2.3.1 Linear model 34
 - 2.3.2 Nonlinear model 35
- 2.4 Open-loop control 38
- 2.5 Closed-loop control 42

3 Power Decoupling Capability **47**

- 3.1 Concept 47
- 3.2 Current controller 49
 - 3.2.1 Feedback linearization 50

3.2.2	Internal dynamics	54
3.2.3	Linear controller	56
3.3	Extended disturbance observer	61
3.4	Outer controller – Loop Shaping	65
3.4.1	Current reference generation	65
3.4.2	Power controller	67
3.4.3	Energy controller	68
3.5	Outer controller – Model Predictive Control	81
3.5.1	State-space model	82
3.5.2	Linear MPC	84
3.5.3	Design of unconstrained MPC	88
3.5.4	Design of constrained MPC	90
3.6	Results	92
3.6.1	Simulation results	92
3.6.2	Experimental results	97
4	High Step-Down Transformerless Capability	109
4.1	Concept	109
4.1.1	Complementary motivation	109
4.1.2	Mobile Side Converter	110
4.1.3	Voltage step-down	111
4.2	Block modulation	115
4.3	MSC operation modes	116
4.3.1	Output voltage	117
4.3.2	Output power	120
4.4	Adaptive control strategy	132
4.4.1	Reduced order model	132
4.4.2	Controller design	133
4.5	Results	135
5	Hardware Setups	143
5.1	Low-power prototype	143
5.2	Open Processor-in-the-Loop (OPiL)	148
5.3	High-power demonstrator	149
6	Conclusion	155
6.1	Summary	155
6.2	Future Work	157
A	Auxiliary Math	159
A.1	Reference frames	159
A.2	Auxiliary transformations	160
A.3	Trigonometry	162

B	Arm Power Flow	163
C	Discretization	169
	C.1 Transfer functions	169
	C.2 State-space representations	169
D	Remaining MSC Operation Ratios	173
	D.1 Ratio 1	173
	D.1.1 DCM1	174
	D.1.2 DCM2	175
	D.1.3 DCM3	176
	D.1.4 CCM1	177
	D.1.5 CCM2	178
	D.1.6 CCM3	179
	D.1.7 CCM4	180
	D.1.8 CCM5	181
	D.2 Ratio 2	182
	D.2.1 DCM1	183
	D.2.2 CCM1	184
	D.2.3 CCM2	185
	D.2.4 CCM3	186
	D.2.5 CCM4	187
	D.2.6 CCM5	188
	D.3 Ratio 4	189
	D.3.1 DCM1	189
	D.3.2 DCM2	190
	D.3.3 CCM1	190
	Bibliography	193

List of Figures

1.1	United Nations – Sustainable Development Goals [1]	1
1.2	Human population growth over time by region [3]	2
1.3	World energy demand [4]	3
1.4	Greenhouse Gases (GHGs) emissions over time by region [4]	3
1.5	Global temperature change over time [7]	3
1.6	Current GHGs emissions by sector [10]	4
1.7	Electricity produced by renewable sources over time [12]	5
1.8	Power converter overview: functions and internal structure	7
1.9	Single-phase DC to AC converters	8
1.10	DC to DC converters	8
1.11	Bidirectional non-isolated Buck-Boost converter	9
1.12	Bidirectional isolated Buck-Boost converter	9
1.13	Single-phase AC to AC converters	10
1.14	Possible connections of isolated DC-DC converters	11
1.15	Hybrid AC/DC grid – Adding DC (in green) to an existing AC grid	13
1.16	Generic Multilevel Converters (MLC) representation as controllable voltage source with LC low-pass filter and examples for nearest level modulation	14
1.17	Influence of multilevel concept and switching frequency on LC filter current and voltage waveform for a single-phase inverter [80]	15
1.18	Conventional MLC topologies (5L)	16
1.19	Number of components in three-phase MLC topologies	17
2.1	Grid connected Modular Multilevel Converter	22
2.2	Most common submodules used in the MMC	23
2.3	Half-Bridge Submodule (HB-SM) switching states	23
2.4	Stacked submodules generating arm multilevel waveform	25
2.5	Stacked submodules represented as Arm Average Model (AAM)	27
2.6	Modular Multilevel Converter Arm Average Model	30
2.7	MMC Kirchhoff Current Law (KCL) analysis	31
2.8	MMC Kirchhoff Voltage Law (KVL) analysis	33
2.9	External and internal MMC equivalent circuits: DC-side, Circulating Current (Z)-side and AC-side	33
2.10	Nonlinear state space model block diagram	36
2.11	Arm voltage modulation overview	39

2.12	Balancing algorithm for submodule voltage balancing	40
2.13	Arm voltage modulation resulting waveforms	41
2.14	Balancing algorithm effect on Submodule (SM) voltage for an arm	42
2.15	Comparison between AAM and Switching Model (SWM) models .	43
2.16	Cascaded control structure of grid-connected MMC	44
3.1	Simplified representation of the MMC energy buffering capability	48
3.2	Power decoupling concept for a power dispatch	49
3.3	Research topic of this section	50
3.4	Block diagram of Single-Input-Single-Output (SISO) Input-Output Feedback Linearization	51
3.5	Block diagram of Multiple-Input-Multiple-Output (MIMO) Input- Output Feedback Linearization applied to the MMC model	54
3.6	Current reference tracking independent closed-loops	57
3.7	Resulting step response with different desired transient times . . .	58
3.8	AC-grid current controller block diagram	60
3.9	Resulting step response for the AC-grid controller	60
3.10	Block diagram of Extended Disturbance Observer (Extended Dis- turbance Observer (EDOB))	64
3.11	Block diagram of closed-loop system	64
3.12	Research topic of this section	65
3.13	Step responses of 1 st and 2 nd order systems	69
3.14	Main objective of the energy controller	69
3.15	2-DOF control architecture block diagram for total energy control	70
3.16	Step responses of 1 st -, 2 nd - and 4 th -order Bessel filters with $k_b = 0.25$	73
3.17	Impulse responses of 1 st -, 2 nd - and 4 th -order Bessel filters with $k_b = 0.25$	73
3.18	Impulse responses of 4 th -order Bessel filters for different k_b	74
3.19	Normalized peak time between adjusted 2 nd -, 3 rd and 4 th -order Bessel filters at different k_b	74
3.20	Bandwidth adjustment factor for achieving the settling time of a 1 st -order system in 2 nd -, 3 rd and 4 th -order Bessel filters at different k_b	75
3.21	Normalized amplitude drop in adjusted 2 nd -, 3 rd and 4 th -order Bessel filters at different k_b , related to its 1 st -order	75
3.22	Total energy settling time dependent on chosen ω_{ac} and ω_{dc}	76
3.23	Resulting peak energy deviation dependent on chosen ω_{ac} and ω_{dc}	76
3.24	Time instant of peak total energy deviation dependent on chosen ω_{ac} and ω_{dc}	77
3.25	Resultant available peak voltage drop dependent on installed C_{arm} and resulting T_{set}	78
3.26	Total energy reference tracking and disturbance rejection with and without $G_{st}(s)$	78

3.27	50Hz notch filter magnitude with different damping coefficients . . .	80
3.28	50Hz notch filter phase-shift with different damping coefficients . .	80
3.29	Controller block diagram: Outer loop designed via Loop Shaping .	81
3.30	General concept of Model Predictive Control with Moving Horizon	82
3.31	Block diagram of Continuous-Control-Set (CCS)-MPC	88
3.32	Tuning unconstrained MPC: Resulting closed-loop bandwidth with $N_p = 20$ and varying r_w and N_c	89
3.33	Tuning unconstrained MPC: Resulting closed-loop phase-margin with $N_p = 20$ and varying r_w and N_c	89
3.34	MMC controller block diagram: Outer loop designed via MPC . .	92
3.35	Simulated test setup for loop shaped controller – original states .	95
3.36	Simulated test setup for loop shaped controller - $\Sigma\Delta$ energy states in abc frame	96
3.37	Power decoupling capability with loop shaping controller	97
3.38	Current reference step response: 1.5 A to 3.5 A	98
3.39	Power decoupling during a step response: 1.5 A to 3.5 A	98
3.40	Energy disturbance response during step response: 1.5 A to 3.5 A	99
3.41	Current reference step response: 3.5 A to 1.5 A	100
3.42	Power decoupling during a step response: 3.5 A to 1.5 A	100
3.43	Energy disturbance response during step response: 3.5 A to 1.5 A	101
3.44	EDOB response during at 16% unbalanced load:	101
3.45	EDOB effect on energy disturbance at 16% unbalanced load . . .	102
3.46	PiL test setup for MPC – original states	104
3.47	PiL test setup for MPC – power decoupling	105
3.48	PiL test setup for MPC – horizontal and vertical energy	106
4.1	Project GridCON – System overview	110
4.2	Mobile Side Converter Mobile Side Converter (MSC)	111
4.3	Nearest Level Modulation principle - full submodule usage	112
4.4	Nearest Level Modulation principle - partial submodule usage . .	114
4.5	Block Modulation: Resulting upper, lower and differential voltage	116
4.6	Equivalent model of MSC for operation mode analysis	117
4.7	Differential, line-line and rectified voltage at $m_u = 0.25$	118
4.8	Differential, line-line and rectified voltage at $m_u = 0.5$	119
4.9	Differential, line-line and rectified voltage at $m_u = 0.75$	120
4.10	DCM13	123
4.11	Discontinuous Conduction Mode (DCM)23	125
4.12	DCM33	126
4.13	Continuous Conduction Mode (CCM)13	128
4.14	CCM23	129
4.15	CCM33	131
4.16	Comparison between switching and reduced equivalent models . .	133
4.17	Reduced model of MSC for control purposes	133

4.18	Block diagram of ideal linear controller	134
4.19	Block diagram of proposed adaptive controller	135
4.20	Hardware demonstrator – Input and output voltage	136
4.21	Simulation demonstrator – Resulting arm voltage in phase B . . .	136
4.22	Hardware demonstrator – Resulting arm voltage in phase B . . .	137
4.23	Simulation demonstrator – Resulting arm current in phase B . . .	137
4.24	Hardware demonstrator – Resulting arm current in phase B . . .	137
4.25	Simulation demonstrator – Resulting circulating and input currents	138
4.26	Load step change – voltage response	139
4.27	Load step change – modulation index response	139
4.28	Reference change at low load – voltage response	140
4.29	Reference change at low load – modulation index response	140
4.30	Reference change at high load – voltage response	140
4.31	Reference change at high load – modulation index response	141
5.1	MMC 1 kW prototype	144
5.2	Prototype half- and full-bridge submodule	145
5.3	Central Field Programmable Gate Array (FPGA) controller board	146
5.4	Master controller	147
5.5	Block diagram of prototype’s system architecture	148
5.6	Example of control system implementation in a System-On-Chip .	150
5.7	Concept of Open Processor-in-the-Loop (Open Processor-in-the- Loop (OPiL))	150
5.8	Mobile Side Converter – 300 kW Demonstrator	151
5.9	Demonstrator half-bridge submodule	152
5.10	Control platform – dSPACE , central FPGA and user interface . .	152
A.1	Relationships between the Park and Clarke transformations	159

List of Tables

1.1	Component count for Multilevel topologies	17
2.1	Half-Bridge submodule - Conduction states	24
2.2	Full-Bridge submodule - Conduction states	24
2.3	Summary of control objectives in MMC	44
3.1	Proportional gain for vertical current generation [103]	67
3.2	Simulated plant - circuit parameter of medium voltage MMC . . .	93
3.3	Control parameter used for simulation tests of loop shaping controller	94
3.4	Desired closed-loop bandwidth for unconstrained MPC design . .	103
3.5	MPC Test performance metrics (Execution times in ms)	107
4.1	Impact of partial submodule usage	115
4.2	Operation modes for different voltage ratios	121
4.3	Boundary conditions	122
4.4	Current equations for i_{sa} in DCM1	123
4.5	Current equations for i_{sa} in DCM2	125
4.6	Current equations for i_{sa} in DCM3	127
4.7	Current equations for i_{sa} in CCM1	128
4.8	Current equations for i_{sa} in CCM2	130
4.9	Current equations for i_{sa} in CCM3	131
4.10	Average rectified current I_R for each operation mode	132
4.11	MSC modulation index m_u for each desired operation	135
5.1	Communication channels between Master and Central Field Programmable Gate Array (CFPGA)	147
5.2	MMC prototype - circuit parameter of low voltage MMC	149
5.3	Circuit parameter of medium voltage MSC Demonstrator	153
D.1	Boundary conditions for Ratio 1	173
D.2	Current equations for i_{sa} in DCM1	174
D.3	Current equations for i_{sa} in DCM2	175
D.4	Current equations for i_{sa} in DCM3	176
D.5	Current equations for i_{sa} in CCM1	177
D.6	Current equations for i_{sa} in CCM2	178
D.7	Current equations for i_{sa} in CCM3	179

D.8	Current equations for i_{sa} in CCM4	180
D.9	Current equations for i_{sa} in CCM5	181
D.10	Boundary conditions for Ratio 2	182
D.11	Current equations for i_{sa} in DCM1	183
D.12	Current equations for i_{sa} in CCM1	184
D.13	Current equations for i_{sa} in CCM2	185
D.14	Current equations for i_{sa} in CCM3	186
D.15	Current equations for i_{sa} in CCM4	187
D.16	Current equations for i_{sa} in CCM5	188
D.17	Boundary conditions for Ratio 4	189
D.18	Current equations for $i_{sa}(\varphi)$ in DCM1	189
D.19	Current equations for i_{sa} in DCM2	190
D.20	Current equations for i_{sa} in CCM3	191

Abbreviations

AAM	Arm Average Model
AC	Alternating Current
AC-DC	AC to DC Converter: Rectifier
ADC	Analog-to-Digital Converter
BESS	Battery Energy Storage Systems
BIBO	Bounded Input Bounded Output
BM	Block Modulation
CCM	Continuous Conduction Mode
CCS	Continuous-Control-Set
CFPGA	Central Field Programmable Gate Array
CM	Common-Mode
DAB	Dual-Active-Bridge
DC	Direct Current
DC-AC	DC to AC Converter: Inverter
DC-DC	DC to DC Converter
DCM	Discontinuous Conduction Mode
DOB	Disturbance Observer
DOF	Degree-of-Freedom
EDOB	Extended Disturbance Observer
EMC	Electromagnetic compatibility
ESO	Extended State Observer
ESS	Energy Storage Systems
EV	Electrical Vehicle
FBL	Feedback Linearization Law
FB	Full-Bridge
FB-SM	Full-Bridge Submodule
FC	Flying Capacitor Converter

FPGA	Field Programmable Gate Array
GHGs	Greenhouse Gases
HB	Half-Bridge
HB-SM	Half-Bridge Submodule
HVDC	High-Voltage Direct Current
IGBT	Insulated-Gate Bipolar Transistor
IMP	Internal Model Principle
IOFL	Input-Output Feedback Linearization
IPC	Interconnecting Power Converter
KCL	Kirchhoff Current Law
KVL	Kirchhoff Voltage Law
LFPGA	Local Field Programmable Gate Array
LQR	Linear Quadratic Regulator
LTI	Linear Time-Invariant
LVDC	Low-Voltage Direct Current
MIMO	Multiple-Input-Multiple-Output
MLC	Multilevel Converters
MMC	Modular Multilevel Converter
MOSFET	Metal-Oxide-Semiconductor Field-Effect Transistor
MPC	Model Predictive Controller
MPPT	Maximum Power Point Tracking
MSC	Mobile Side Converter
MVAC	Medium-Voltage Alternate Current
MVDC	Medium-Voltage Direct Current
NDOB	Nonlinear Disturbance Observer
NLM	Nearest Level Modulation
NPC	Neutral-Point Clamped Converter
OPiL	Open Processor-in-the-Loop
OPP	Optimized Pulse Patterns
PEBB	Power Electronic Building Block
PI	Proportional Integral
PiL	Processor-in-the-Loop

PL	Programmable Logic
PLL	Phase-Locked-Loop
PR	Proportional Resonant
PS	Processing System
PWM	Pulse-Width Modulation
PV	Solar Photovoltaics
QP	Quadratic Programming
RES	Renewable Energy Sources
SAB	Single-Active-Bridge
SSC	Supply Side Converter
SDGs	Sustainable Development Goals
SISO	Single-Input-Single-Output
SM	Submodule
SOA	Safe Operation Area
SoC	System-On-Chip
SVM	Space Vector Modulation
SWM	Switching Model
UART	Universal Asynchronous Receive Transmit
UN	United Nations
VFD	Variable Frequency Drives
Z	Circulating Current
ZOH	Zero-Order Hold

1 Introduction

Every research journey starts from a higher-level perspective, this thesis is no different. Besides my personal fascination for field of power electronics (from the design to control of power converters), I would like take this opportunity the reveal some of the arguments, which led me to this research path. My motivation starts with the Sustainable Development Goals (SDGs) established by the United Nations (UN) in 2015 [1] and ends on a very important power electronics topology, as solution to help reach these goals. Afterwards, the objectives of this thesis are explained and brief outline of every chapter here included is provided. Finally, it ends with a list of outcomes and contributions for the scientific world.



Figure 1.1: United Nations – Sustainable Development Goals [1]

1.1 General motivation

1.1.1 Macro – Energy transition

Technological and health advances have been driving world population growth, since after the second world war [2]. In 2023 the world has reached 8 Billion people (Figure 1.2) and the UN expects global population to reach its peak at around 10.3 billion in the mid-2080's [3]. As the population grows, the demand for basic services, such as housing, transportation, food production, and water supply, increases, all of which require energy, as historically shown in Figure 1.3. Furthermore, the growth of households, businesses, and infrastructure directly raises the amount of energy needed for heating, cooling, lighting, and powering machines. In the last 50 years, this has been more evident in the Asiatic continent, specially in China and India. However nowadays, still around 10% of the population does not have direct access to electricity. Reducing this number, is one main priorities of the UN, which further foresees a higher energy demand.

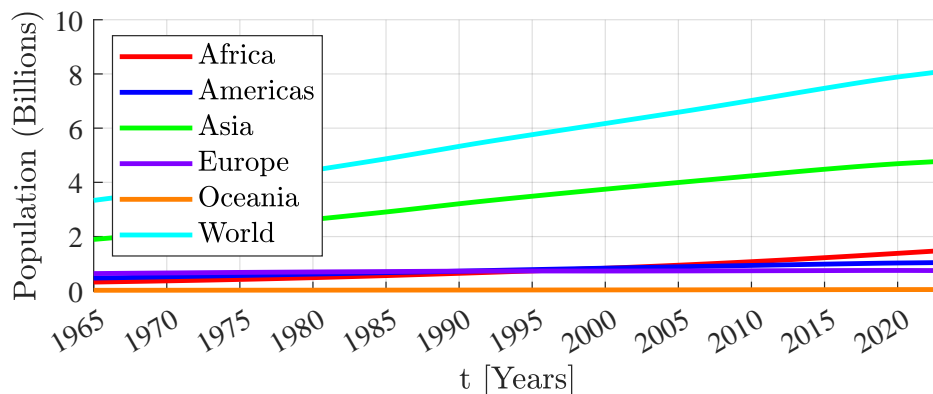


Figure 1.2: Human population growth over time by region [3]

The industrial revolution sparked the large-scale use of coal for heating, industry, and transport, with oil and gas joining in the 19th and 20th centuries to meet energy demands [5]. The reason is simple to understand. Fossil fuels are burned to generate heat, which is then converted into mechanical or electrical energy, but the efficiency is limited by the second law of thermodynamics, resulting in significant heat waste and the release of pollutants like methane (CH_4), sulfur dioxide (SO_2), and nitrogen oxides (NO_x). This results in a higher concentration of the so-called Greenhouse Gases (GHGs) in Earth's atmosphere, which increases the greenhouse effect. Early studies had already warned that burning fossil fuels would raise carbon dioxide (CO_2) levels and eventually lead to global warming. [6].

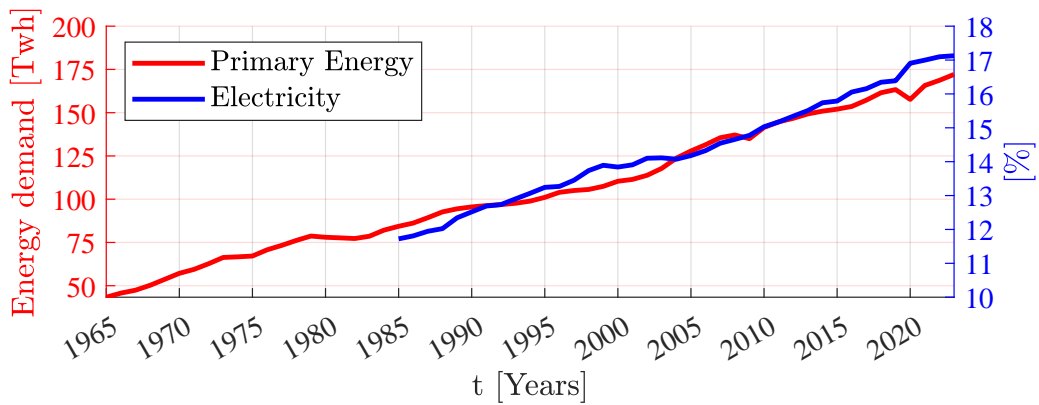


Figure 1.3: World energy demand [4]

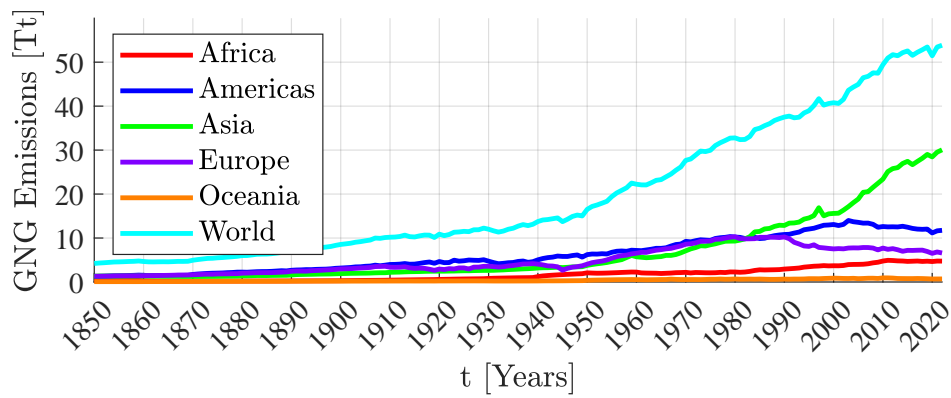


Figure 1.4: GHGs emissions over time by region [4]

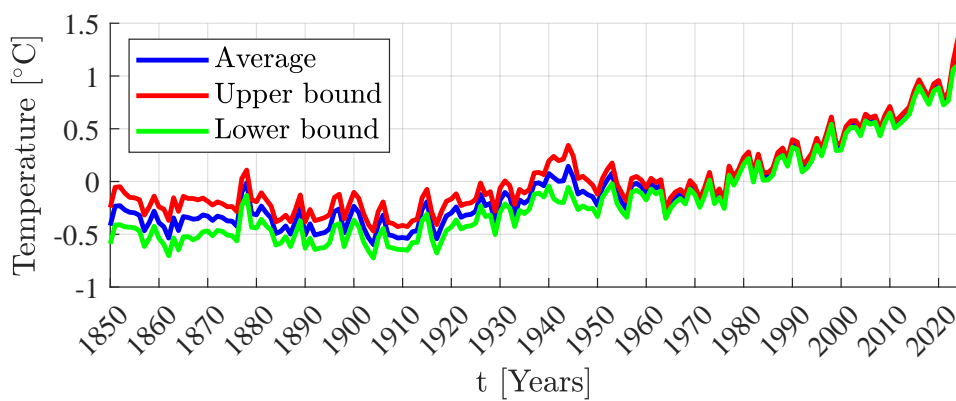


Figure 1.5: Global temperature change over time [7]

It is widely recognized that global warming affects the Earth's ecosystems in numerous ways. Its impacts are continually assessed alongside the scientific understanding of climate change, which includes an analysis of future risks and strategies for adaptation and mitigation [8]. Besides efforts of worldwide governments and international agency plans [9], the CO₂ levels are still growing and our planet continuous to warm up, as recorded in Figure 1.4 and Figure 1.5.

Most recent data [10] points out that almost three-quarters of GHGs emissions are directly from energy demand across sectors such industry (in general), transportation and residential buildings, while almost one fifth of the emissions is produced by the agriculture and forestry sectors. A more detailed overview of each sector contribution is given in Figure 1.6. Electrification is a consensual worldwide solu-

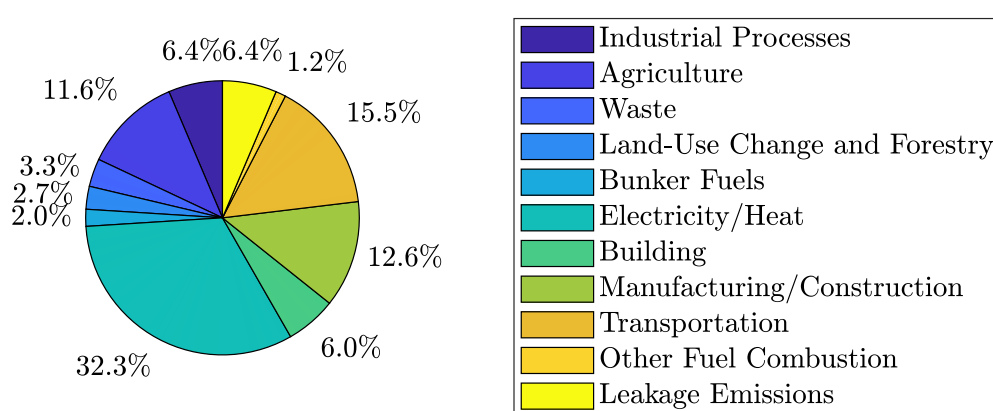


Figure 1.6: Current GHGs emissions by sector [10]

tion [1],[8],[9] to fully decarbonize the major part of the responsible sectors. The electrification itself can be divided into distinct groups:

- **Easy-to-electrify sectors** – are those where energy needs can be met with electricity using existing or rapidly advancing technologies, which are often supported by falling costs. These include heating, cooling, and cooking in residential building through electric appliances and heat pumps or the adoption of Electrical Vehicle (EV)s and electrified public transport systems offering reducing emissions and fuel costs.
- **Hard-to-electrify sectors** – include heavy industries such as steel, cement, and chemicals; long-distance transport like aviation, maritime shipping, heavy-duty trucking and high-temperature industrial processes. These sectors face challenges due to their reliance on high-energy-density fuels, the need for specific chemical processes, or the difficulty of adapting existing infrastructure to electrification [11].

To achieve meaningful decarbonization, it is essential that the energy used to power electrified systems comes from clean, renewable sources. The current global

energy mix shows that less than one-fifth of the world's energy consumption is electricity (Figure 1.3), and less than a third of this electricity comes from Renewable Energy Sources (RES), as shown in Figure 1.7.

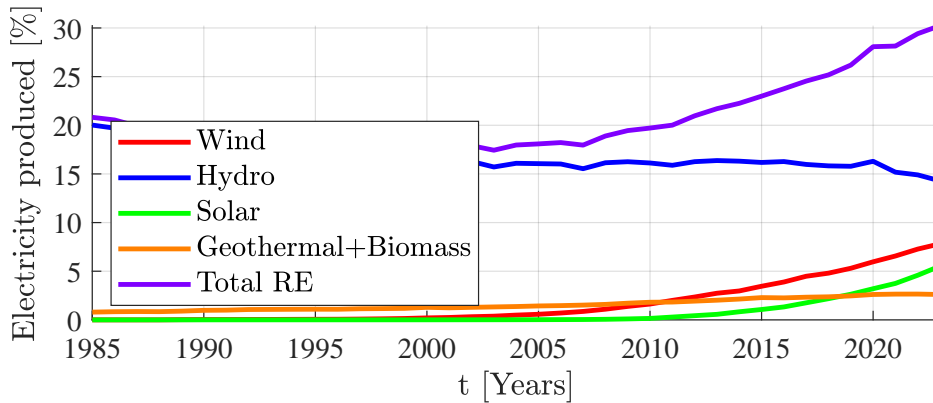


Figure 1.7: Electricity produced by renewable sources over time [12]

Therefore, without a substantial increase in the share of clean electricity, the environmental benefits of electrification may be undermined by continued reliance on fossil-fuel-based power generation. However, there is a promising outlook, as the rapid cost reductions in RES technologies are driving significant progress. For instance, the deployment of Solar Photovoltaics (PV), combined with Energy Storage Systems (ESS) like batteries, has seen an exponential rise, with an 80% growth in 2023 alone. This trend is expected to continue, positioning solar energy as the leading RES in the coming years, largely due to the abundant availability of materials such as silicon for PV cells, which supports scalable and cost-effective production [13].

Nevertheless, a successful energy transition and decarbonization depend heavily on critical areas such as overall energy efficiency and the sustainable use of material resources. These aspects are identified as key enablers in reports by several leading consulting firms and international agencies [14, 15].

1.1.2 Micro – Key to green power

The path to reach the All-Electric-Society is not straightforward. The deployment of RES and electrification introduce new global challenges [14, 16, 17]:

- Intermittency – due to the nature of RES, its availability is not fully controllable but instead predictable via weather forecasts;
- Fossil-fuel dependency – due to the availability risk, the traditional non-RES must still be taken into account on the energy mix;

- Operation costs – for many heavy-industries, relying on electricity produced by fossil-fuels is still as much cost effective option;
- System overload – as the consumption of electricity increases, so the transmission capacity requirements;
- Infrastructure upgrades - deployment of RES and new electrified loads alone is not compatible with the electrical grid requirements;
- Non-uniform policymaking – commitment to energy transition is not equal around the world. In many countries, clear long-term targets, specific strategies and complex/non-existent supporting legislation repel private investment;

From a technological perspective, these challenges can be addressed through the implementation of three pivotal technologies, which are discussed in this subsection [13].

Energy storage systems

ESS are critical for enabling a reliable and decarbonized energy future, especially these are able to solve several of the challenges above mentioned [13, 18]. By storing excess energy during peak generation periods and releasing it during times of low production, ESS reduce dependence on fossil fuels, provide grid stabilization function for the grid, and improve overall energy efficiency [19]. This functionality is vital, considering that the solar energy reaching Earth in just one hour could meet global annual energy demand [20], yet much of it is lost without adequate storage.

Batteries, particularly lithium-ion types, are currently the most widely adopted storage technology due to their ability to provide sustained energy over longer durations and decreasing cost. Supercapacitors, on the other hand, are well-suited for short-term applications requiring rapid charge and discharge cycles, such as smoothing power fluctuations. Together, they address different needs across residential, commercial, and utility-scale systems.

While demand-side solutions like flexible load management have potential, they often face barriers related to user participation and data privacy [21]. In contrast, ESS operate independently of consumer behavior, offering a passive yet powerful solution that can also enhance system resilience. At the grid level, utilities are increasingly investing in Battery Energy Storage Systems (BESS) for their modularity, fast response, and ability to provide ancillary services [22]. Many of these advancements stem from progress in electric vehicle battery technology, now being applied to energy systems [23]. A variety of storage solutions are available,

and their strategic integration is key to building a flexible and future-ready power infrastructure [24, 19].

Power electronics

Power electronics focuses on controlling and efficiently converting electrical energy through the use of electronic switches, such as power semiconductors. Power converters execute the required energy conversion through these power semiconductors, which are driven by specially designed gate drivers and controlled either digitally or in an analog manner. These devices enable the modification of voltage, current, frequency, and phase configuration (e.g. single-phase input to three-phase output) in electrical circuits across a wide range of systems, from low to high power. To ensure compliance with grid codes and maintain power quality, reactive elements, such as inductors and capacitors, are integrated into power converters as filters or short-term storage elements. These components help mitigate harmonics, stabilize voltage, and ensure compatibility with standards governing voltage and frequency. Applications of power converters span various sectors, including industrial processes, household appliances, and mobility solutions [25]. Figure 1.8 provides an overview of the conversion category and the internal structure of a power converter. Power converters are crucial for integrating RES and

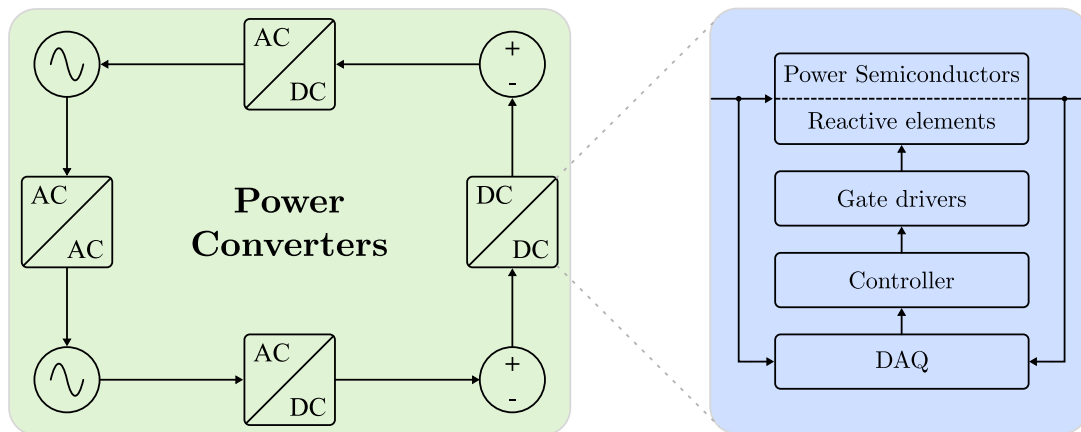


Figure 1.8: Power converter overview: functions and internal structure

ESS into the AC-grid. To ensure compatibility, all sources and loads must adhere to grid codes, particularly regarding voltage and frequency standards [26],[27]. Since most RES and ESS inhere a DC nature, direct connection to the grid is not feasible and requires the use of power converters to enable proper interfacing. The power converter interfacing the PV with the grid is typically formed by a two separate stages [28]:

- DC to AC Converter: Inverter (DC-AC) – Converts a regulated DC voltage

into an alternating waveform. An example of a single-phase inverter electrical circuit diagram is given in Figure 1.9a. In order to charge a BESS from the grid, the inverse logic is applied to the same circuitry [29]. An AC to DC Converter: Rectifier (AC-DC) (Figure 1.9b) is used to obtain a DC voltage from a alternating voltage. Operation details are well documented in [25].

- DC-DC – adjusts PV’s varying DC voltage to a stable level, to meet the inverter’s operating requirements. This stage often incorporates a Maximum Power Point Tracking (MPPT) algorithm, ensuring PV panels always operate at a maximizing power extraction point under varying environmental conditions. A commonly used methodology is given in [30].

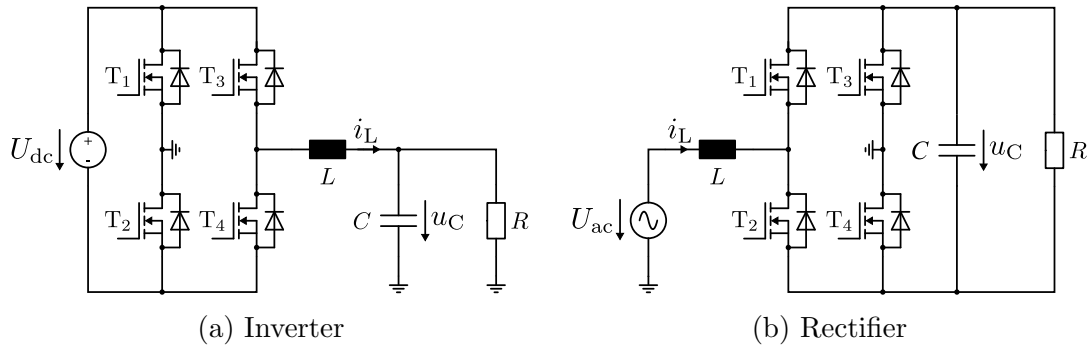


Figure 1.9: Single-phase DC to AC converters

Additionally, it is important to highlight the step-up and step-down capabilities of power converters. This refers to the ability of a circuit, to increase (step-up) or decrease (step-down) voltage levels. These capabilities are essential for efficiently adapting voltage levels to suit different parts of an electrical system. For a DC-DC stage, the most simple step-down (Buck) and step-up (Boost) converters are shown in Figure 1.10a and Figure 1.10b. By combining both circuits, a Buck-Boost converter is obtained as represented in Figure 1.11. The last is widely used as DC-DC stage in PV applications to perform MPPT [31].

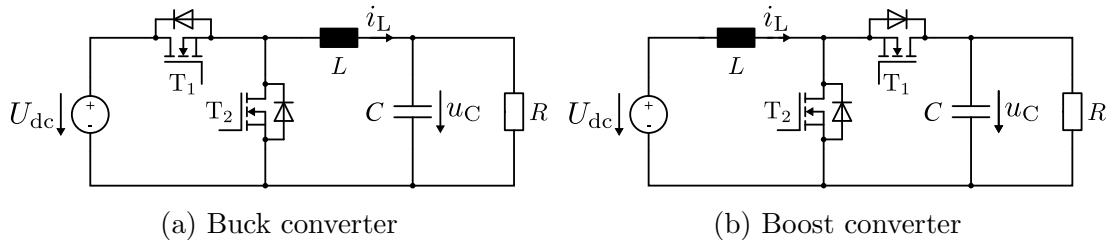


Figure 1.10: DC to DC converters

In several applications, i.e. incorporating ESS, it is desired to include a galvanic

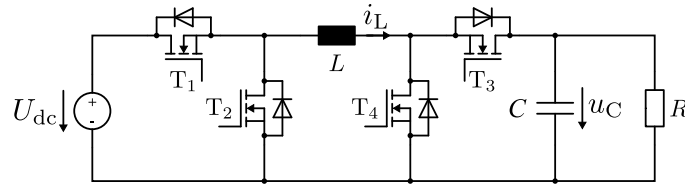


Figure 1.11: Bidirectional non-isolated Buck-Boost converter

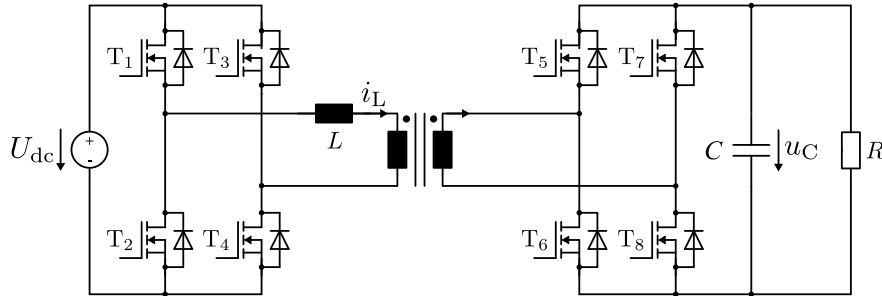


Figure 1.12: Bidirectional isolated Buck-Boost converter

isolation stage in the power converter [32, 33, 34, 35]. This protects users and sensitive components from faults such as ground loops, short circuits, or overvoltage conditions. For ESS, without isolation, differences in ground potential between the battery and other parts of the system can create ground loops. These loops can cause unwanted currents, leading to noise, interference, and potential damage to sensitive electronics. In high-power applications requiring wide voltage conversion ratios, galvanic isolation with an appropriate transformer turns ratio can improve feasibility, efficiency and reduce total system cost, particularly when safety isolation is required [36, 37]. An example of an isolated DC-DC with bidirectional power flow capability is given in Figure 1.12, named Dual-Active-Bridge (DAB) [38], include all the functions introduced so far.

The same principles apply to direct AC to AC conversion through the use of the so-called Matrix Converter. By employing power semiconductors in an anti-series configuration, the Matrix Converter enables stepping up or down the amplitude and frequency of the alternating voltage [39]. An illustrative example of this converter is shown in Figure 1.13. Unlike traditional back-to-back converters used in mixed-frequency power systems or wind power plants, which consist of a rectifier stage, an inverter stage, and a bulky capacitor for DC-link energy storage, the Matrix Converter is a storageless solution. This design eliminates the bulky capacitor, one of the most common failure points in such applications, resulting in a more compact and efficient system, at the cost of increased circuit and control complexity [40]. Further insights into advancements and applications within this conversion category can be found in [41].

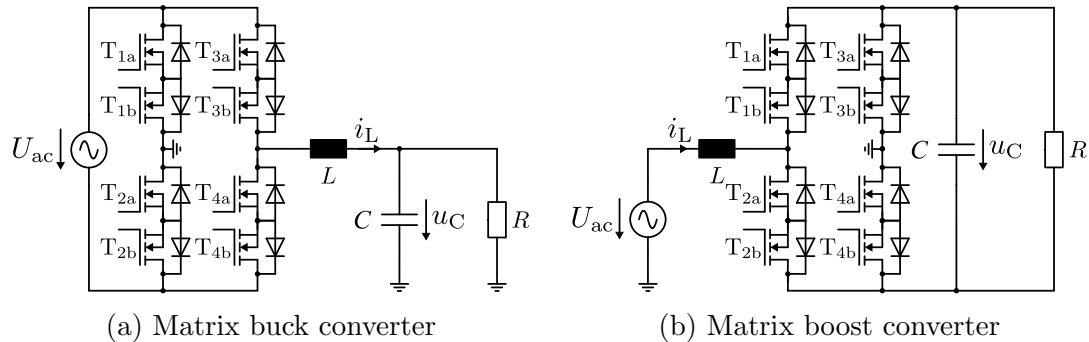


Figure 1.13: Single-phase AC to AC converters

Advancements in power semiconductors have introduced new technologies with superior switching characteristics, such as silicon carbide (SiC) Metal-Oxide-Semiconductor Field-Effect Transistor (MOSFET)s and gallium nitride (GaN) transistors. These innovations enable higher switching frequencies at elevated voltages (>1 kV) in high-power converters, resulting in more compact and potentially more efficient power conversion systems. This progress directly supports the advancement of electrification while significantly reducing the production footprint. A comprehensive review of exemplary designs is provided in [42]. Notably, a 5 kV/5 MVA transformer operating at 1 kHz was developed, as detailed in [43]. In comparison, a conventional 50 Hz transformer weighs 11,500 kg (2.5 kg/kVA), whereas the medium-frequency transformer achieves a significantly reduced weight of 675 kg (0.14 kg/kVA) [44].

It is also possible to create configurations through the interconnection of modules in series or parallel groups. This approach forms a fully modular system, built on a standardized Power Electronic Building Block (PEBB), which can be flexibly interconnected to suit specific applications [43]. Such a design enhances modularity and scalability. For increased current capability, modules are connected in parallel, while higher voltage capability is achieved through series connections. A combination of both configurations is also feasible but is typically implemented only in isolated converter systems and represented in Figure 1.14.

Hybrid-grids

On September 4, 1882, Thomas Edison showcased the first electrical grid powered in a DC format. However, the invention of the transformer brought the ability to transmit electricity over vast distances leading to the dominance of AC in global power infrastructure. Today, most power transmission systems still rely on fossil fuel-based generators that produce AC electricity. Unavoidably, losses occur during transmission and distribution through power lines, which are estimated

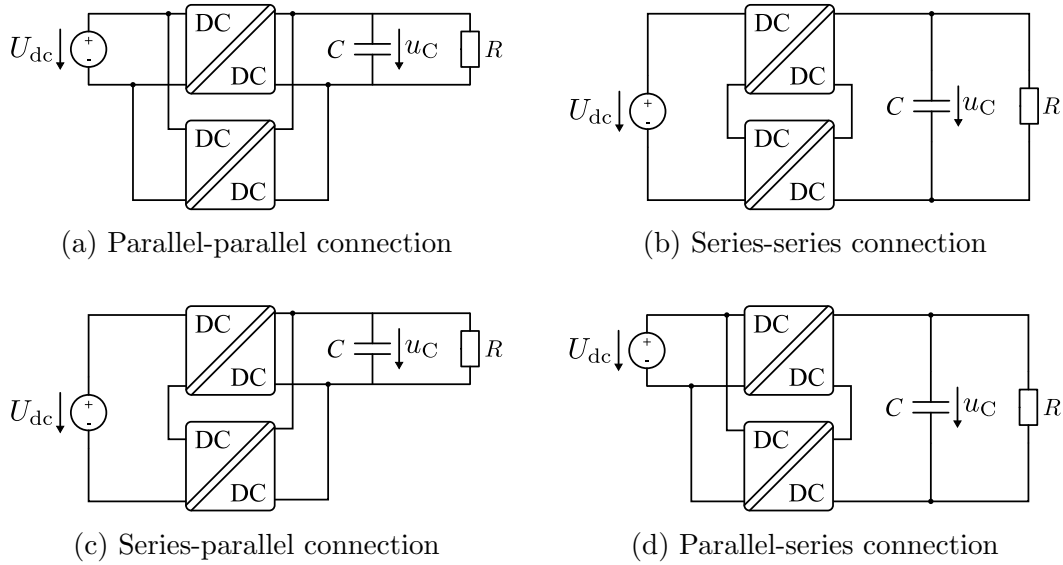


Figure 1.14: Possible connections of isolated DC-DC converters

to result in slightly less than 3% of global CO₂ emissions [15]. In the European power system network, the transmission-related losses are in average around 2%, while in distribution this number increases up to 8%, according to latest reports in [45]. This is normal, since in distribution networks, the working voltage is lower and current higher, resulting in higher losses. As previously emphasized, the urgent transition from fossil fuels to RES has become increasingly critical. Moreover, emerging loads such as EVs chargers, data centers, LED lighting, and Variable Frequency Drives (VFD) motor appliances inherently operate on DC power. Coupled with advancements in power electronics, which offer improved efficiency and a smaller footprint, this raises the question of whether the development of new DC power grids should now be considered. In comparison with traditional AC-grids the following benefits should be highlighted [46, 47]:

- Discard frequency control – power flow is online dependent of voltage amplitude level. This includes several benefits: easier controlability, standardization, component integration, scalability and connection between grids.
- Higher cable utilization – skin effect is not present in DC system, which increases the utilization of the cable cross-section. In another view, the same cable has a smaller effective resistance [48].
- Smaller footprint – one conductor less than in three-phase systems. Due to modern loads, less conversion stages are necessary. As these are converter-interfaced, increased switching frequency leads higher power density.

At the high-voltage transmission level, there are several point-to-point industrial projects proving the benefits and economical feasibility of applying DC tech-

nology, especially on systems requiring long-distance power transmission lines, submarine cables and interconnection of asynchronous grids [49, 50, 51, 52, 53]. Several technological problems under research are related with insulation, protection and stability of multi-terminal High-Voltage Direct Current (HVDC) systems [54, 55, 56].

On the low-voltage and medium-voltage levels, the advantageous of DC technology have also been shown in many applications: Agriculture [57], Aerospace [58, 59], Maritime[60], Commercial buildings[61] and factories[62], Households[63], Mining[64] and Railway[65]. It is important to notice, these applications are mainly standalone, point-to-point, islanded or a separate branch of the distribution grid. In another words, these are DC-microgrids. Up to the author's best knowledge, DC-based distributed network is still up today in practice a research topic. A survey of existing pilot projects is given in [66].

Although DC technology presents great opportunities, it lacks in maturity and standards, where investments are risky and highly state-subsidized. As in the automotive industry, to achieve a smoother transition from internal combustion cars (IEC) to EVs, hybrid solutions were and still are required. For distribution networks, a similar path has been followed in latest years. Cooperative projects involving industry and academic partners have been carried out to develop hybrid AC/DC grids, and hence, explore the potential DC grid technologies directly connected to existing AC distribution networks. Examples of ongoing projects and their results can be found in [67, 68, 69]. Such hybrid approach aims to maximize the usage of existing infrastructure, while introducing and maturing the prospective advantages of the DC technology. Additionally, it increases security of supply by enhancing grid inter-connectivity. This is exemplified in Figure 1.15 [70], where a MVDC line creates an additional path between two original grid sectors. This is only possible due to presence of Interconnecting Power Converter (IPC)s, which regulate power transfer between DC- and AC-grids, while maintaining the power system stability [71].

1.1.3 Nano – Multilevel converters

Power converters are a key element for proliferation of DC technology in distributed grids. Referring back to Figure 1.15, it is necessary to develop high-power converters to convert from Medium-Voltage Alternate Current (MVAC) to MVDC, as well as from MVDC to Low-Voltage Direct Current (LVDC). Conventional isolated and non-isolated power converter topologies, well described in [25], operate on two-level (2L) principle, i.e. one transistor must be able to switch the entire input voltage. According to traditional grid codes [72], the MV range lies in between voltage levels of 1 kV and 60 kV. However power semiconductors

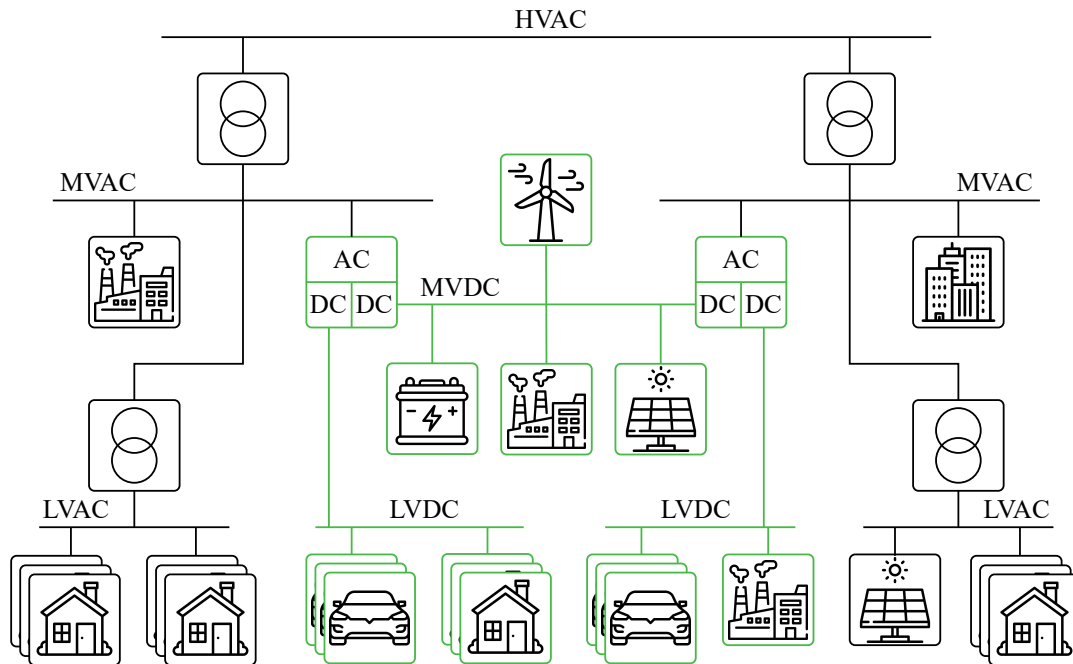


Figure 1.15: Hybrid AC/DC grid – Adding DC (in green) to an existing AC grid

with active turn-on and -off capabilities are limited to 6.5 kV blocking voltage [73]. The series connection of active semiconductors poses significant risks due to the inherent challenges associated with uneven voltage distribution caused by differences in device parameters and circuit asymmetries. This issue is further enhanced by the fast switching transient behavior, which make dynamic voltage equalization difficult to achieve, thereby compromising the safe operation of the circuit [74]. Increasing the blocking voltage of SiC-Metal-Oxide-Semiconductor Field-Effect Transistor (MOSFET)s is a topic under investigation, with promising results [75]. So far no commercial solutions are available in the market. To achieve higher voltage capability, the connection of series-parallel PEBBs (Figure 1.14) and Multilevel Converters (MLC) topologies have been proposed as successful alternative solutions [42, 76].

A conventional 2L converter achieves higher voltage capability mainly by using higher-rated devices or by series-connecting semiconductors to withstand the required blocking voltage. In contrast, MLCs increase voltage capability by splitting the total DC-link voltage across multiple devices and voltage levels, thereby reducing the voltage stress on each semiconductor. As an IPC, the MLC operation relies on synthesizing a staircase waveform that closely approximates a sinusoidal shape, offering enhanced power quality and reduced harmonic distortion compared to traditional 2L converters. An illustrative example of the nearest level approximation of a sinusoidal reference for 2L and 5L single-phase inverters is shown in Figure 1.16. To further improve the voltage waveform quality, higher-

frequency techniques such as Pulse-Width Modulation (PWM) or Space Vector Modulation (SVM) are commonly employed [77, 78].

As the number of active semiconductors in multilevel converters increases, so do the conduction and switching losses. This requires a trade-off between switching frequency and waveform quality. Optimized Pulse Patterns (OPP) offer a promising solution by enabling the generation of high-quality waveforms at switching frequencies near the fundamental frequency (50 Hz). These patterns are pre-optimized offline through computationally intensive processes, limiting their practical application to converters with a low number of levels [79]. Despite their benefits, PWM-based modulation remains the preferred choice in most applications due to its ease of implementation and high flexibility. As the PWM

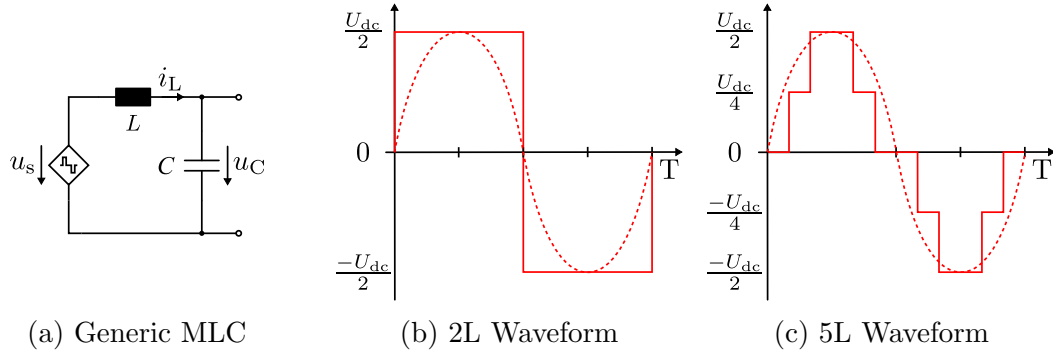


Figure 1.16: Generic MLC representation as controllable voltage source with LC low-pass filter and examples for nearest level modulation

waveform inherently contains harmonics that must be filtered to achieve a high quality sinusoidal output, an LC low-pass filter is essential to meet AC grid code requirements [26]. The inductor (L) smooths the current, while the capacitor (C) attenuates harmonic voltage content, ensuring the voltage is filtered to an acceptable level. A generic representation of a MLC is depicted in Figure 1.16a. Regardless of the application, the high-frequency components of current and voltage around the fundamental waveform are described by (1.1) and (1.2), which are inversely related to the size of the LC filter. An analysis of normalized values, presented in Figure 1.17, clearly demonstrates that increasing the number of levels has a greater impact on reducing filter size compared to increasing the switching frequency. In comparison with a 2L topology, the filter size decreases, however the conduction and switching losses increase, due to the higher number of active semiconductors. Although this represents an enormous potential decreasing the footprint of MV and HV converter, a trade-off must be made, depending on the application. In [80], it is shown that a LV single-phase AC-DC converter requires seven voltage levels to achieve an efficiency comparable to that of a traditional 2L solution. A similar study has been done for motor applications in [81].

$$\Delta i_L = \frac{U_{dc}}{4N_L^2 f_{sw} L}, \quad (1.1)$$

$$\Delta u_C = \frac{U_{dc}}{32N_L^2 f_{sw}^2 LC}. \quad (1.2)$$

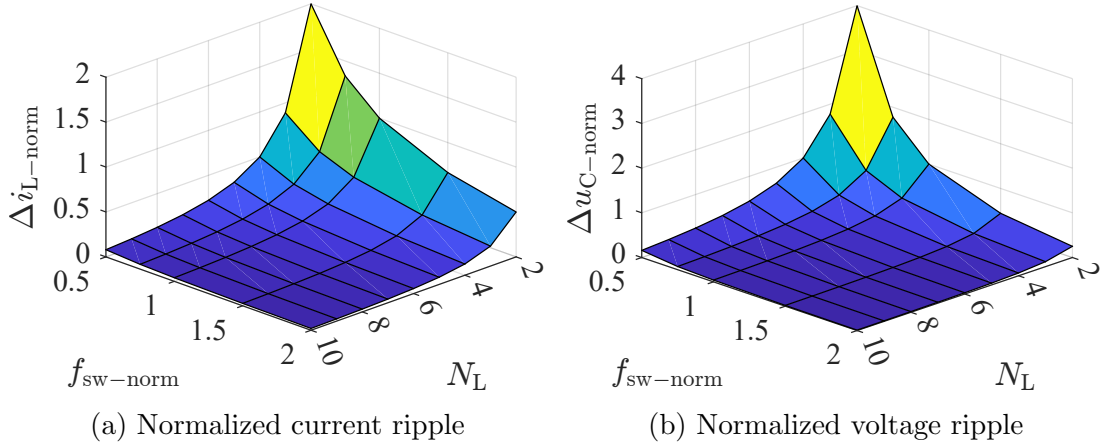


Figure 1.17: Influence of multilevel concept and switching frequency on LC filter current and voltage waveform for a single-phase inverter [80]

The main advantages of multilevel converters are [82]:

- Lower voltage waveform distortion, leads to reduced the harmonic losses.
- Reduced effort to comply with Electromagnetic compatibility (EMC) standards.
- Increased number of switching combinations for the same voltage levels enables redundant operation.

All the aforementioned advantages arise from the increased DOF in multilevel topologies. This comes at the cost of greater system complexity, particularly in the control system design. Nevertheless, this complexity also creates opportunities for innovation and optimization in system design and operation [83].

MLCs are classified based on the method used to generate voltage levels. A comprehensive review of the most commonly employed topologies and their operating principles can be found in [84]. These topologies, namely Neutral-Point Clamped Converter (NPC), Flying Capacitor Converter (FC) and MMC are illustrated for a 5L application in Figure 1.18. To evaluate the scalability of MLC topologies, the required components are compared across different numbers of levels, as summarized in Table 1.1. Notably, the MMC topology stands out as it does not require

additional diodes (beyond those integrated into the active semiconductors) or DC-link capacitors.

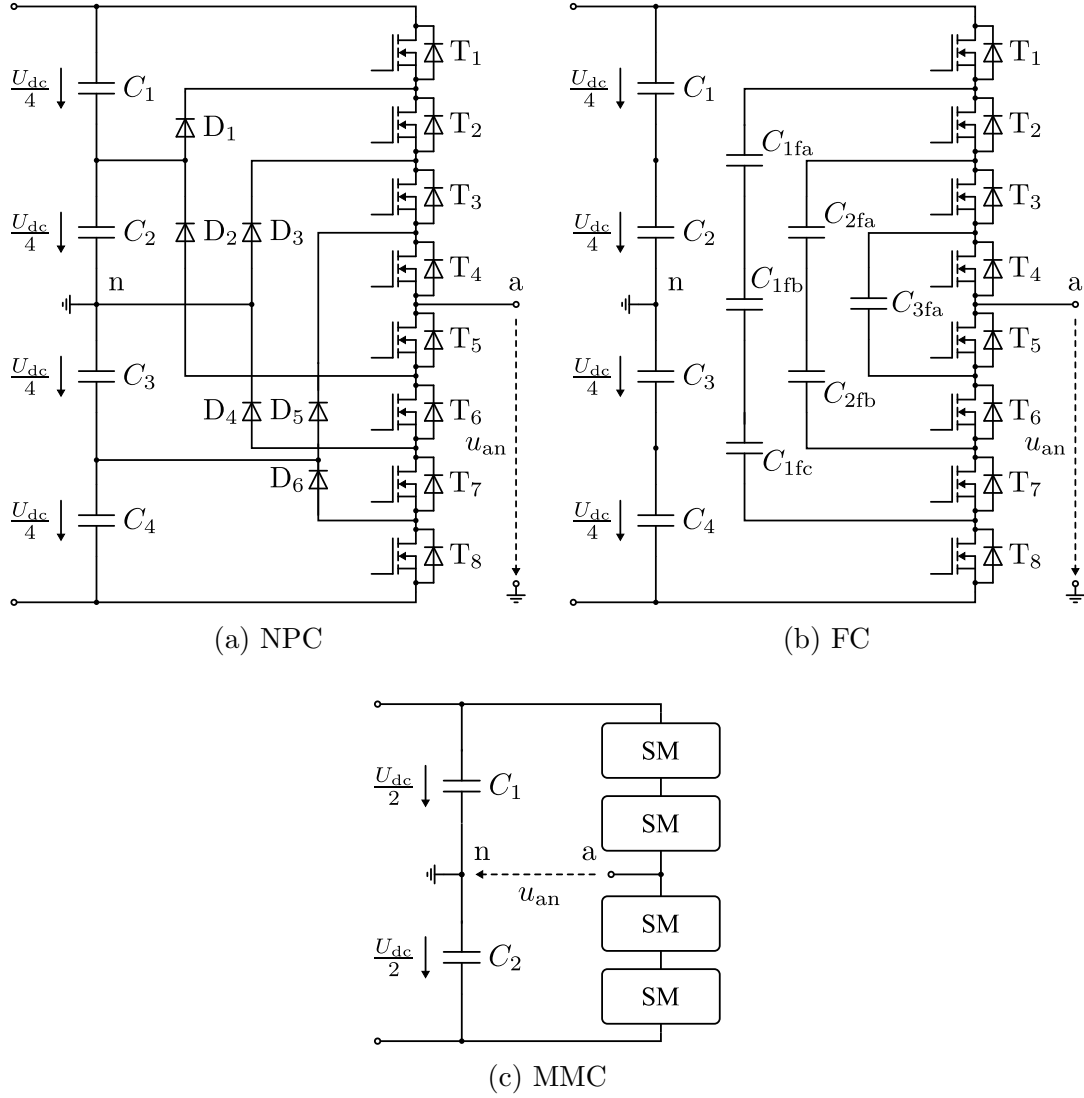


Figure 1.18: Conventional MLC topologies (5L)

As expected, the number of components increases with the number of levels (N_L) in all MLC, as well as the number of phases (N_{Ph}). However, the MMC structure stands out as its component count grows linearly with the number of levels. Figure 1.19 provides a comparison of the required components per level. For a higher number of levels, the MMC emerges as the most advantageous topology. Studies such as [85, 86] evaluate the efficiency benefits of various multilevel topologies in different applications, including medium-voltage solar inverters and variable-speed drives. Among these, the MMC demonstrates the best overall performance.

Table 1.1: Component count for Multilevel topologies

	NPC	FCC	MMC
Transistors	$2 \cdot (N_L - 1) \cdot N_{Ph}$	$2 \cdot (N_L - 1) \cdot N_{Ph}$	$4 \cdot (N_L - 1) \cdot N_{Ph}$
Diodes	$(N_L - 1) \cdot (N_L - 2) \cdot N_{Ph}$	0	0
Capacitors	0	$\frac{(N_L - 2) \cdot (N_L - 1)}{2} \cdot N_{Ph}$	$2 \cdot (N_L - 1) \cdot N_{Ph}$
DC-Link	$N_L - 1$	$N_L - 1$	0

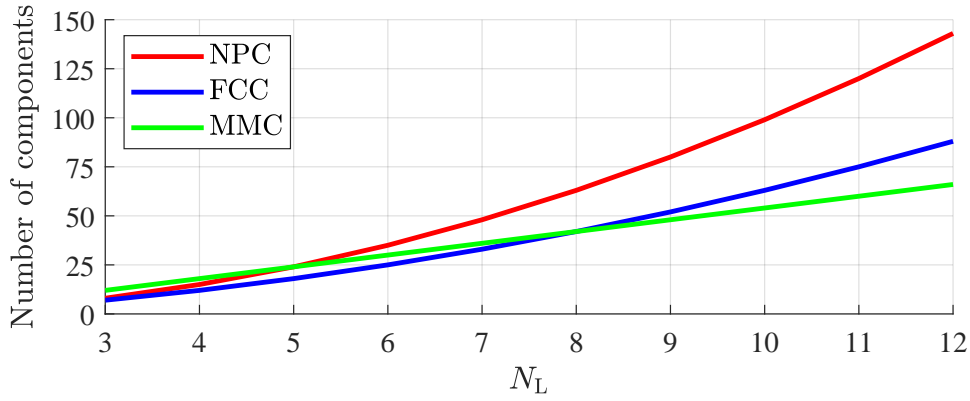


Figure 1.19: Number of components in three-phase MLC topologies

1.2 Overview

The modular structure of the MMC topology offers several DOF that can be systematically exploited. The primary objective of this thesis is to explore two innovative capabilities that enhance the interconnection of distinct power networks, i.e. in the hybrid-grid represented in Figure 1.15. These capabilities are realized by leveraging the MMC's topological flexibility into the design of dedicated control algorithms.

1.2.1 Outline

In Chapter 1, the thesis begins by examining the global shift towards electrification, primarily driven by the increasing integration of renewable energy sources

and energy storage systems. This chapter discusses the inherent direct current (DC) nature of these technologies and the consequent need to transition from traditional AC grids to DC or hybrid AC/DC grid architectures. It highlights the role of advancements in power electronics, particularly MLC topologies, in facilitating this transition.

In chapter 2, the MMC topology is analyzed by deconstructing it into its fundamental building blocks, with particular emphasis on its flexible energy storage capabilities. A comprehensive circuit analysis of the topology is conducted, serving as the foundation for deriving well representative mathematical models. These will serve as basis for control design. A literature review of control strategies applied to the MMC finalizes this chapter.

Chapter 3 introduces the concept of power decoupling between AC and DC grids, leveraging the flexible energy storage capabilities of the MMC to provide distinct transient responses to a common power reference change on both the DC and AC sides. Furthermore, the control algorithms enabling this functionality are described in detail.

Chapter 4 presents the development of a high step-down MMC-based DC-DC converter, tailored for heavy-duty agricultural electrification. In this chapter the proposed converter is explained and their operation modes are deeply explored. Furthermore, the control algorithms enabling this functionality are described in detail.

Chapter 5 provides details on the hardware developed to support the research findings presented in this thesis. This includes the design and construction of a low-power MMC prototype and an additional 300 kW demonstrator, tailored to validate the proposed control strategies and operational concepts.

In the final chapter, a comprehensive conclusion is presented, summarizing the main findings and results of this research. Additionally, potential directions for future work are discussed, highlighting areas where further investigation could build upon the contributions of this study.

1.2.2 Contributions

The research conducted throughout this thesis has resulted in the following peer-reviewed publications. While a few of these directly support the core contributions of the thesis, others emerged as valuable by-products of the broader investigative process:

1. “Adaptive Control for Enhanced Performance in Grid-Connected Agricultural Machines,” *2024 IEEE 15th International Symposium on Power Elec-*

tronics for Distributed Generation Systems (PEDG)

2. “Decoupled Current Control via Feedback Linearization Technique for a Grid-Connected Modular Multilevel Converter,” *IECON 2023 – 49th Annual Conference of the IEEE Industrial Electronics Society*
3. “Optimized Pulse Pattern with Half-Wave Symmetry for 5-Level Converter,” *2022 24th European Conference on Power Electronics and Applications (EPE'22 ECCE Europe)*.
4. “Volume Optimization of a 300kW MMC-Based DC-DC Converter for a DC Grid Connected Agricultural Machine,” *PCIM Asia 2021*.
5. “Experimental Evaluation of a High Power Medium Voltage Converter for a DC Grid Connected Agricultural Machine,” *PCIM Europe Digital Days 2020*.
6. “Flexible and General Strategy of Space Vector Modulation for Multilevel Converters,” *PCIM Asia 2020*.

2 Modular Multilevel Converters

The Modular Multilevel Converter (MMC), initially introduced in 2003 [87], has since evolved into a key technology for various emerging application fields. This includes more efficient utilization of large drive systems, integration of solar and wind power sources, and the enhancement of grid infrastructure—particularly in multi-terminal HVDC and MVDC networks. While the advantages of this topology over their peer-topologies are highlighted in the previous chapter, this chapter is focused on its working principle, mathematical model and operation, which serves as common-ground for the following chapters.

2.1 Basic concepts

2.1.1 Submodule

The structure of a grid-connected MMC is provided in Figure 2.1. Its main building block is the so-called submodule (SM), typically composed by a storage capacitor (C_{sm}) and a standard simple switching topology. Most commonly, Half-Bridge (HB) and Full-Bridge (FB) submodules are considered, both represented in Figure 2.2. Alternative submodule configurations are reviewed in [88, 89]. Regardless of the switching configuration and the active power semiconductors employed, the submodule can be regarded as a controllable voltage source. Consequently, its terminal voltage is determined by the switching function (s_{T}) and the available voltage ($u_{C_{\text{sm}}}$), as given for the HB-SM in (2.1), where the subscript T denotes the applied submodule topology. The switching function determines, how the submodule contributes in the generation of the multilevel waveform. Additionally, it influences the dynamics of the stored energy in each submodule, by dynamically allowing current to flow in and out of the submodule, as provided in (2.2). Furthermore, the capacitor voltage $u_{C_{\text{sm}}}(t)$ consists of an average component representing the stored energy level and a periodic component resultant from the switching action, as given in (2.3)

$$u_{\text{sm}}(t) = s_{\text{T}}(t) \cdot u_{C_{\text{sm}}}(t) \quad \text{where,} \quad s_{\text{HB}}(t) = \begin{cases} 0 & \text{if bypassed} \\ 1 & \text{if inserted} \end{cases} \quad (2.1)$$

$$\dot{u}_{C_{sm}}(t) = \frac{i_{sm}(t)}{C_{sm}} = s_{HB}(t) \cdot \frac{i_{arm}(t)}{C_{sm}} \quad (2.2)$$

$$u_{C_{sm}}(t) = U_{C_{sm}0} + \tilde{u}_{C_{sm}}(t) \quad (2.3)$$

The switching states and submodule dynamics for an HB configuration are depicted in Figure 2.3 and summarized in Table 2.1. Due to the higher number of semiconductors, the Full-Bridge Submodule (FB-SM) offers higher DOF, as summarized in Table 2.2.

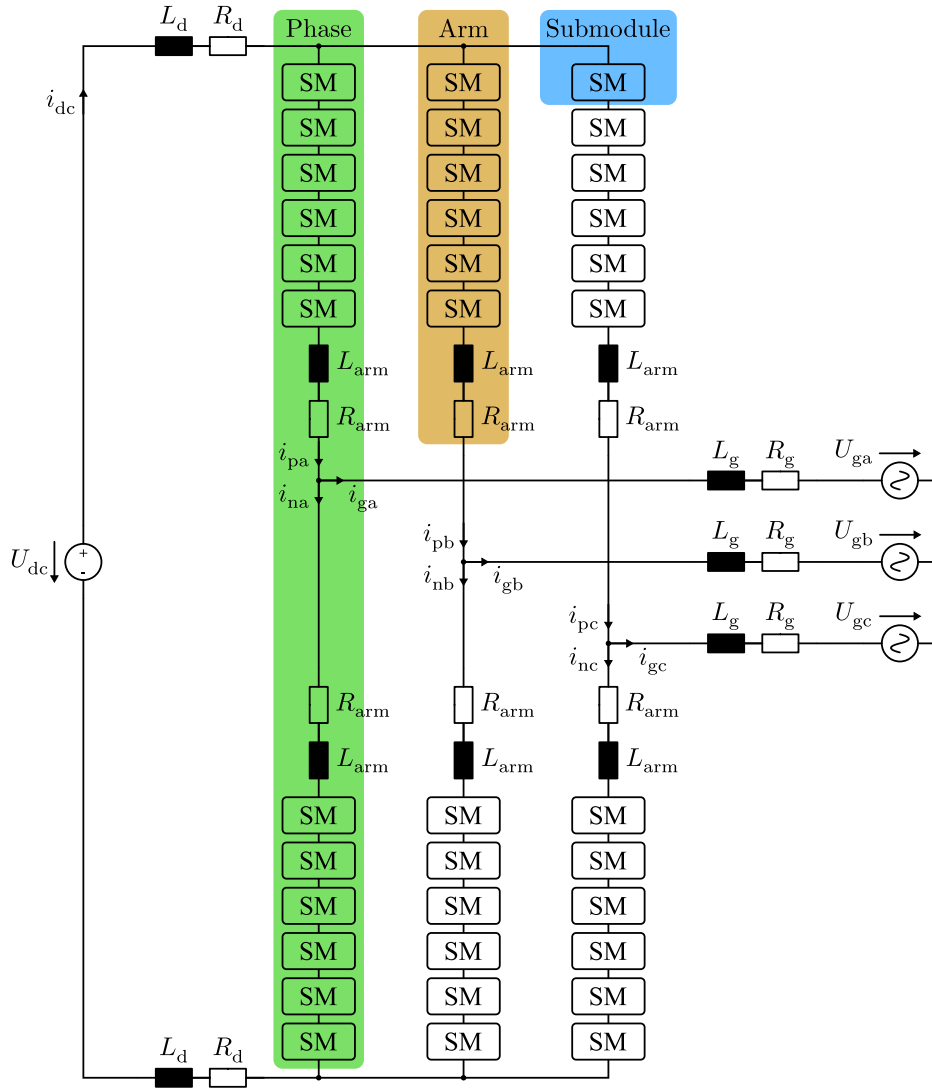
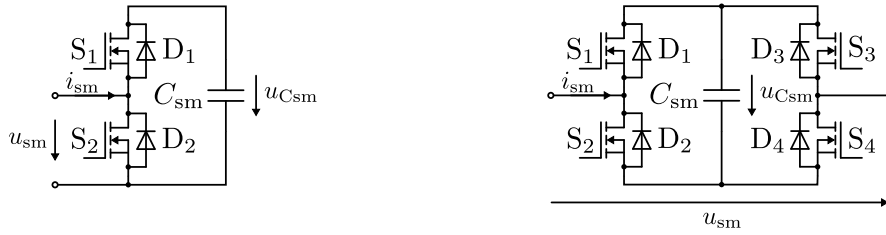


Figure 2.1: Grid connected Modular Multilevel Converter

When selecting a submodule configuration, the following factors should be considered:



(a) Half-Bridge submodule (HB-SM)

(b) Full-Bridge submodule (FB-SM)

Figure 2.2: Most common submodules used in the MMC

- **Cost:** The number of semiconductors and auxiliary circuitry in the submodule directly affects the overall system cost. HB configurations are more cost-effective, while FB configurations are more expensive.
- **Power density:** The additional components in FB-SM increase system size and weight compared to HB configurations.
- **Efficiency:** HB-SM have lower conduction and switching losses due to fewer semiconductors, while FB-SM experience higher losses.
- **Voltage Levels:** FB-SM offer a wider range of output voltage levels, enabling greater operational flexibility compared to HB-SM.
- **Fault Handling:** FB-SM provide inherent DC fault-blocking capability, which may eliminate the need for additional protection devices, whereas HB-SM require external fault protection mechanisms.

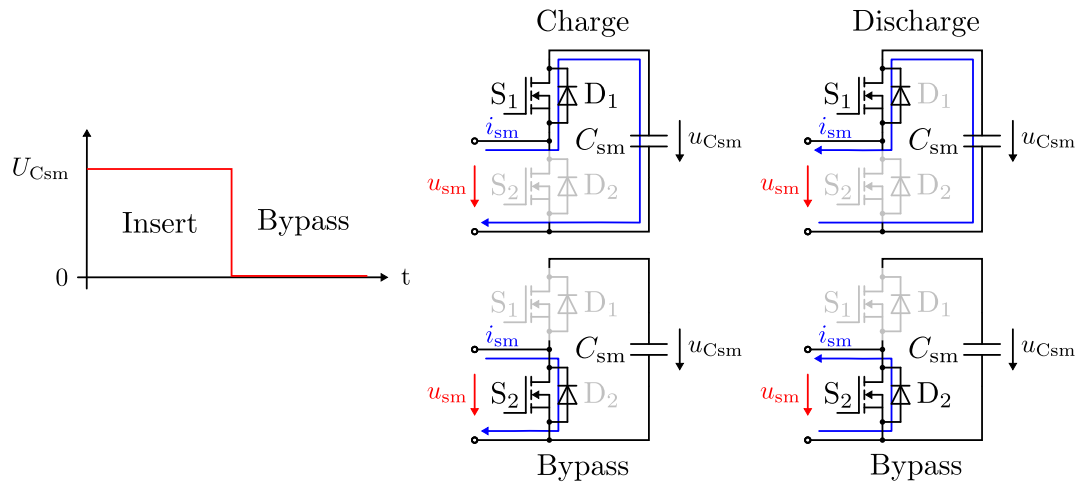


Figure 2.3: HB-SM switching states

Table 2.1: Half-Bridge submodule - Conduction states

State	s_{HB}	(S_1, S_2)	Conducts	u_{sm}	i_{arm}	$\frac{du_{\text{Csm}}}{dt}$
Insert	1	1 0	S_1	$+u_{\text{Csm}}$	> 0	> 0
				$+u_{\text{Csm}}$	< 0	< 0
Bypass	0	0 1	S_2	0	> 0	$= 0$
				0	< 0	$= 0$
Passive	X	0 0	D_1	$+u_{\text{Csm}}$	> 0	> 0
			D_2	0	< 0	$= 0$

Table 2.2: Full-Bridge submodule - Conduction states

State	s_{FB}	(S_1, S_2, S_3, S_4)	Conducts	u_{sm}	i_{arm}	$\frac{du_{\text{Csm}}}{dt}$
Insert +	1	1 0 0 1	S_1, S_4	$+u_{\text{Csm}}$	> 0	> 0
				$+u_{\text{Csm}}$	< 0	< 0
Insert -	-1	0 1 1 0	S_2, S_3	$-u_{\text{Csm}}$	> 0	< 0
				$-u_{\text{Csm}}$	< 0	> 0
Bypass	0	1 0 1 0	S_1, S_3	0	> 0	$= 0$
				0	< 0	$= 0$
Bypass	0	0 1 0 1	S_2, S_4	0	> 0	$= 0$
				0	< 0	$= 0$
Passive	X	0 0 0 0	D_1, D_4	$+u_{\text{Csm}}$	> 0	> 0
			D_2, D_3	$-u_{\text{Csm}}$	< 0	> 0

2.1.2 Arm

The multilevel capability is realized by connecting submodules in series. A series configuration of installed submodules (N_{sm}) is referred to as an arm, as depicted in Figure 2.1. The arm output voltage, u_{arm} , is determined by summing the capacitor voltages of all the inserted submodules in the series connection, as expressed in (2.4). An example of this equation for an arm comprising six HB-SMs is illustrated in Figure 2.4. Assuming all submodules are ideal and well balanced, each contributes equally due to similar insertion time.

$$u_{\text{arm}}(t) = \sum_{k=1}^{N_{\text{sm}}} s_{T,k}(t) u_{C_{\text{sm},k}}(t) \quad (2.4)$$

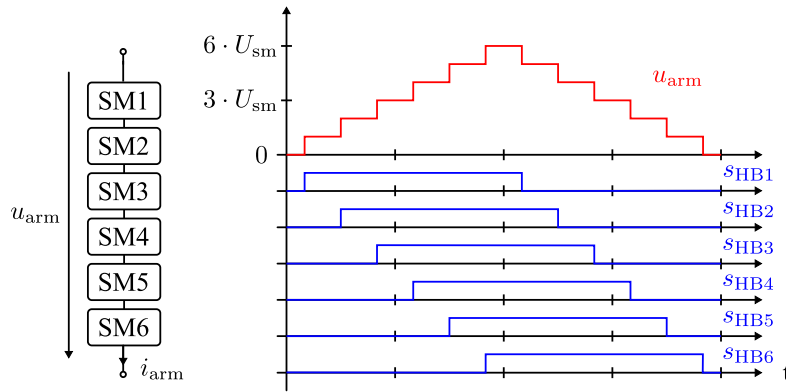


Figure 2.4: Stacked submodules generating arm multilevel waveform

The current flowing through the entire series stack of submodules is commonly referred to as the arm current (i_{arm}). Its waveform is influenced by the contributions of inserted submodules as well as the interactions at the terminal interface with other arms, sources, or loads. Consequently, the voltage dynamic equation within a single arm ($\dot{u}_{C_{\text{arm}}}$), as expressed in (2.5), are determined by the contributions of the inserted submodules. In the bypassed state their charge state remains unchanged.

$$\dot{u}_{C_{\text{arm}}}(t) = \sum_{k=1}^{N_{\text{sm}}} \frac{s_{T,k}(t)}{C_{\text{sm}}} i_{\text{arm}}(t) \quad (2.5)$$

Regardless of their switching state, the available arm voltage ($u_{C_{\text{arm}}}$), as the total electrical charge stored in all submodules within one arm ($u_{C_{\text{sm}}}^{\Sigma}$) is defined in (2.6).

$$u_{C_{\text{arm}}}(t) = U_{C_{\text{arm}0}} + \tilde{u}_{C_{\text{arm}}}(t) \quad (2.6)$$

Fundamentally, the arm output voltage represents a specific fraction of the total available voltage. Building on this concept, (2.5) and (2.6) are combined in

(2.7) to define this relationship and normalize the proportion of instantaneously inserted submodules relative to N_{sm} . Such relation is commonly named as modulation index, whereas $m = 0$ bypasses all submodules, while $m = 1$ inserts them all.

$$m(t) = \frac{\sum_{k=1}^{N_{\text{sm}}} s_{\text{T},k}(t)}{N_{\text{sm}}} = \frac{u_{\text{arm}}(t)}{u_{\text{Carm}}(t)} \quad (2.7)$$

Each arm includes an inductance (L_{arm}) and a parasitic resistance (R_{arm}). Fundamentally, it limits the current maximum amplitude and transient behavior, to protect the converter and associated equipment [90]. Despite being application dependent, its design should take into consideration the following operative aspects [91]:

- **Fault current limitation:** To protect the converter by limiting fault current levels during DC or AC faults.
- **Ripple current reduction:** Switching of submodules induce high-frequency components, i.e. ripples. The arm inductance acts as filter reducing stress on components and extending their lifespan.
- **Voltage balancing:** limiting the current transient behavior, enable balancing of the submodules and hence stable operation.
- **Dynamic performance and resonance avoidance:** Prevents system resonance and helps maintaining stability.

Although the design of the arm inductance is beyond the scope of this thesis, its design methodology, associated trade-offs, and optimization strategies are thoroughly reviewed in [92, 93, 94]. The same principles apply to both DC- and AC-filter inductance, referred to as L_{d} and L_{g} .

2.1.3 Average model

Assuming a very large N_{sm} or a substantially higher submodule switching frequency as well as an even voltage distribution among the submodules during operation, the arm can be approximated by an equivalent continuous model [95, 96]. Now, only a single arm capacitance is used and the modulation index becomes the control variable. This simplifies the dynamic behavior of the converter by focusing on averaged quantities rather than the detailed switching behavior of individual submodules. Additionally, it allows for faster simulations and easier analysis of the system, especially in scenarios where the exact switching dynamics are not critical [97]. Combining (2.5) and (2.7) the arm available voltage dynamics are updated in (2.8), where C_{arm} refers to the series connections of all stacked

submodules.

$$\dot{u}_{C_{\text{arm}}}(t) = \frac{m(t) \cdot i_{\text{arm}}(t) \cdot N_{\text{sm}}}{C_{\text{sm}}} = \frac{m(t) \cdot i_{\text{arm}}(t)}{C_{\text{arm}}} \quad (2.8)$$

This forms a continuous model representing a variable capacitance and in the remaining topology perspective, a controllable voltage source rearranging (2.7) as

$$u_{\text{arm}}(t) = m(t) \cdot u_{C_{\text{arm}}}(t) \quad (2.9)$$

Substituting (2.9) into (2.7) reveals that the dynamics of the available voltage in the arm are directly dictated by the instantaneous power flow within the arm itself. Since $u_{\text{arm}}(t)$ is commanded $m(t)$, a complex, intertwined non-linear relationship becomes evident.

$$\dot{u}_{C_{\text{arm}}}(t) = \frac{u_{\text{arm}}(t) \cdot i_{\text{arm}}(t)}{C_{\text{arm}} \cdot u_{C_{\text{arm}}}(t)} = \frac{P_{\text{arm}}(t)}{C_{\text{arm}} \cdot u_{C_{\text{arm}}}(t)} \quad (2.10)$$

In summary, this concept is well represented by the meshed equivalent circuit in Figure 2.5.

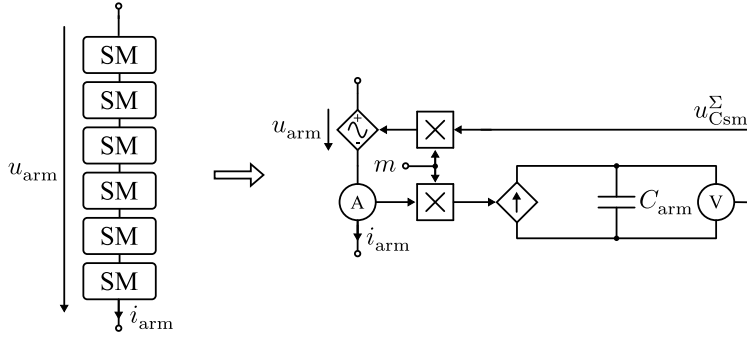


Figure 2.5: Stacked submodules represented as AAM

Naturally, the requested voltage cannot be greater than available voltage within the arm, therefore the following physical constraints should be yielded in operation,

$$0 \leq u_{\text{arm}}(t) \leq u_{C_{\text{arm}}}(t) \quad (2.11)$$

In case FB-SM are considered, negative requested voltages are allowed, therefore the constraint is extended to

$$-u_{C_{\text{arm}}}(t) \leq u_{\text{arm}}(t) \leq u_{C_{\text{arm}}}(t) \quad (2.12)$$

By adjusting the insertion and bypass intervals, the number of inserted submodules as well as the average capacitor voltage levels are controlled, enabling arm voltages above or below U_{dc} . Hence, unlike other MLC topologies, the available arm voltage can deviate from the input DC voltage and may be either lower or

higher than U_{dc} , depending on the operational requirements. This relation is represented by the scaling factor k_c in (2.13). This flexibility arises from the variable capacitance capabilities of the system [98].

$$U_{C_{arm}} = k_c \cdot U_{dc} \quad (2.13)$$

A comparable voltage boosting principle is known from Marx generators [99], where charged capacitors are reconfigured in series to obtain an increased output voltage. This feature will be further explored in subsequent sections of this thesis.

2.1.4 Energy framework

The submodules can be seen as controllable energy storages, where each capacitor stores it in form of electrical field. The energy stored in each capacitor is represented by

$$W_{sm}(t) = \frac{1}{2} C_{sm} u_{C_{sm}}^2(t) \quad (2.14)$$

Similarly, using the AAM principle, the energy stored within one arm yields,

$$W_{arm}(t) = \frac{1}{2} C_{arm} u_{C_{arm}}^2(t) \quad (2.15)$$

The dynamics of the energy stored in the arm are determined by its rate of change, which directly corresponds to the fundamental definition of active power flow. Differentiating on (2.15) the following representation is obtained,

$$P_{arm}(t) = \dot{W}_{arm}(t) = C_{arm} u_{C_{arm}}(t) \dot{u}_{C_{arm}}(t) \quad (2.16)$$

which matches (2.10), proving the veracity of this representation. For each phase $x \in \{a, b, c\}$ there is an upper (p) and lower (n) arm. In each, a separate energy storage is available. The energy stored per phase is given by,

$$\forall x \in \{a, b, c\}, \quad W_{\Sigma x} = W_{px} + W_{nx} \quad (2.17)$$

and the energy difference between upper and lower arms yields,

$$\forall x \in \{a, b, c\}, \quad W_{\Delta x} = W_{px} - W_{nx} \quad (2.18)$$

Furthermore it is also useful to consider the entire energy stored in the MMC as

$$W_{MMC} = \sum_{x \in \{a, b, c\}} W_{px} + \sum_{x \in \{a, b, c\}} W_{nx} \quad (2.19)$$

Alternatively, (2.19) can be expressed by the total MMC capacitance

$$C_{MMC} = 3 \cdot C_{arm} \quad (2.20)$$

and the average available voltage in the six arms

$$W_{\text{MMC}} = \frac{C_{\text{MMC}} U_{\text{Carm}}^2}{2} \quad (2.21)$$

Due to potential mismatches among the submodule capacitors [100], the energy states should be represented by the voltage available in each arm. Nonetheless, the energy-based framework is highly effective in grid-connected converters, where the power exchanged with the grid can be directly linked to the energy dynamics, as further discussed in Section 3.1.

2.2 Circuit analysis

A three-phase grid-connected MMC incorporates six arms, as represented in Figure 2.1. Based on the AAM principle, the stacked submodules are modeled as a controllable voltage source. This simplifies the MMC representation, as shown in Figure 2.6. Furthermore a clearer circuit analysis of this topology can be carried on. For each phase $x \in \{a, b, c\}$ there is an upper (p) and lower (n) arm, with the correspondent arm current and voltage. Additionally, variables and parameters associated with the AC grid are labeled as gx , while those related to the DC grid interface are labeled as dc . Typically, both grids are interfaced via an inductance with its internal resistance and are here considered for the following circuit analysis. For clarity, the MMC is considered in inverter mode, hence transferring power from DC to AC side.

By applying KCL at nodes a, b, c and n of Figure 2.7 it results in

$$\forall x \in \{a, b, c\}, \quad i_{gx} = i_{px} - i_{nx} \quad (2.22)$$

$$\sum_{x \in \{a, b, c\}} i_{gx} = 0 \quad (2.23)$$

and at the nodes d_p and d_n in

$$i_{dc} = \sum_{x \in \{a, b, c\}} i_{px} = \sum_{x \in \{a, b, c\}} i_{nx} \quad (2.24)$$

The arm currents are a superposition of both grid side currents and an additional circulating current (i_{zx}). Ideally these are symmetrically divided among the six arms. Hence, the arm currents are defined as in (2.25) and (2.26).

$$i_{px} = \frac{i_{dc}}{3} + \frac{i_{gx}}{2} + i_{zx} \quad (2.25)$$

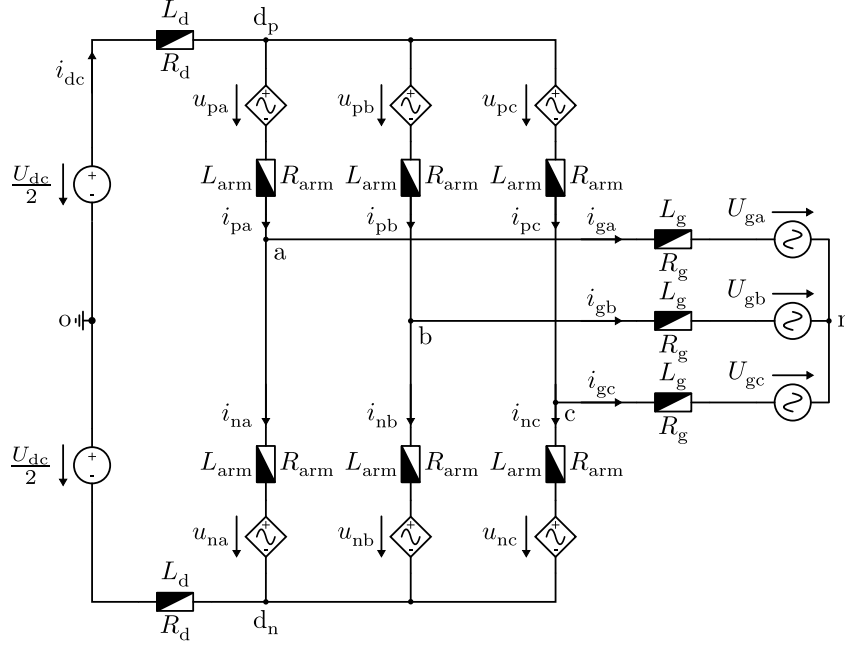


Figure 2.6: Modular Multilevel Converter Arm Average Model

$$i_{nx} = \frac{i_{dc}}{3} - \frac{i_{gx}}{2} + i_{zx} \quad (2.26)$$

The circulating current originates from voltage imbalances and harmonic interaction between the upper and lower arms, as well as imperfections in component design. Its value is obtained from the Common-Mode (CM) current definition between upper and lower arms in each phase, yielding

$$i_{cmx} = \frac{i_{px} + i_{nx}}{2} = \frac{i_{dc}}{3} + i_{zx} \quad (2.27)$$

Furthermore, the CM-currents consist of two parts: DC-current which is equally distributed over all three phases and the circulating current. Rearranging (2.27), the circulating currents are given by

$$i_{zx} = i_{cmx} - \frac{i_{dc}}{3} \quad (2.28)$$

This current only circulates within the MMC and does not influence its input or output waveforms. Hence the relation in (2.29) yields

$$\sum_{x \in \{a,b,c\}} i_{zx} = 0 \quad (2.29)$$

Referring to the KVL, six different loops are identified and represented in Figure 2.8. The solid lines represent the upper arm related loops (M_{1-3}), while the

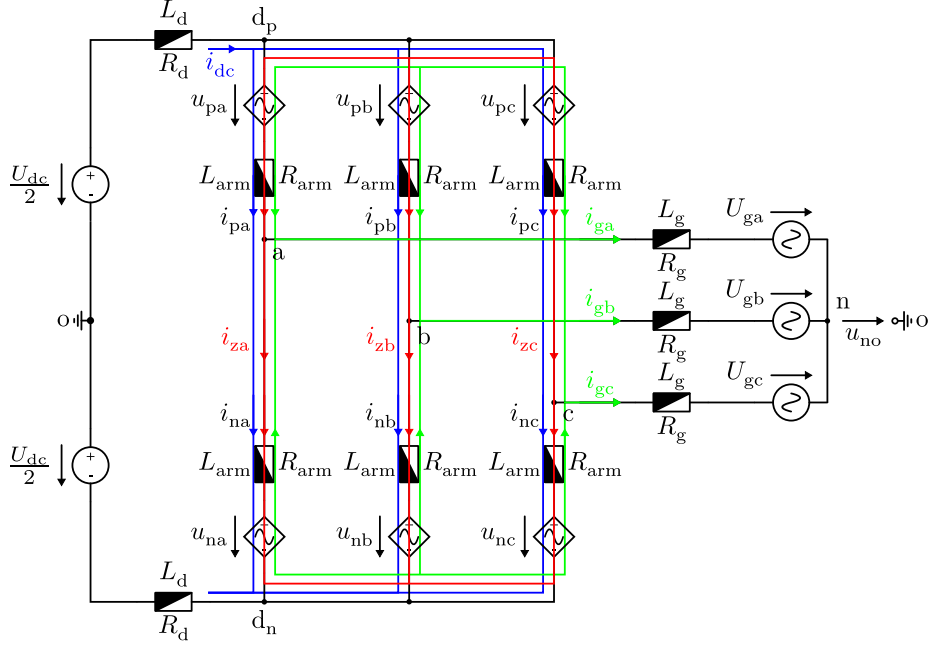


Figure 2.7: MMC KCL analysis

dashed lines, the lower-arm related loops (M_{4-6}). The resulting KVL equations are generically formulated, yielding

$$-\frac{U_{dc}}{2} + L_d \dot{i}_{dc} + R_d i_{dc} + u_{px} + L_{arm} \dot{i}_{px} + R_{arm} i_{px} + L_g \dot{i}_{gx} + R_g i_{gx} + U_{gx} + u_{no} = 0 \quad (2.30)$$

$$-\frac{U_{dc}}{2} + L_d \dot{i}_{dc} + R_d i_{dc} + u_{nx} + L_{arm} \dot{i}_{nx} + R_{arm} i_{nx} - L_g \dot{i}_{gx} - R_g i_{gx} - U_{gx} - u_{no} = 0 \quad (2.31)$$

The summation of (2.30) and (2.31) yields

$$-U_{dc} + 2L_d \dot{i}_{dc} + 2R_d i_{dc} + u_{px} + u_{nx} + L_{arm} (\dot{i}_{px} + \dot{i}_{nx}) + R_{arm} (i_{px} + i_{nx}) = 0 \quad (2.32)$$

and using the relation in (2.27)

$$-U_{dc} + u_{px} + u_{nx} + \left(2L_d + \frac{2L_{arm}}{3}\right) \dot{i}_{dc} + \left(2R_d + \frac{2R_{arm}}{3}\right) i_{dc} + 2L_{arm} \dot{i}_{zx} + 2R_{arm} i_{zx} = 0 \quad (2.33)$$

is obtained. Similarly through subtraction of (2.30) and (2.31)

$$(u_{px} - u_{nx}) + L_{arm} (\dot{i}_{px} - \dot{i}_{nx}) + R_{arm} (i_{px} - i_{nx}) + 2L_g \dot{i}_{gx} + 2R_g i_{gx} + 2U_{gx} + 2u_{no} = 0 \quad (2.34)$$

and further use of (2.22) yields,

$$u_{px} - u_{nx} + (L_{arm} + 2L_g) \dot{i}_{gx} + (R_{arm} + 2R_g) i_{gx} + 2U_{gx} + 2u_{no} = 0 \quad (2.35)$$

For control purposes, it is beneficial to separate the DC, Z, and AC components, allowing their dynamics to be analyzed and characterized independently. The decoupling of DC current is obtained by summing (2.33) for all phases, resulting in

$$-U_{dc} + \sum_{x \in \{a,b,c\}} \frac{u_{px} + u_{nx}}{3} + \left(2L_d + \frac{2L_{arm}}{3}\right) \dot{i}_{dc} + \left(2R_d + \frac{2R_{arm}}{3}\right) i_{dc} = 0 \quad (2.36)$$

The circulating current in each phase is obtained by substituting (2.36) into (2.33), leading to

$$\left(u_{px} + u_{nx} - \sum_{x \in \{a,b,c\}} \frac{u_{px} + u_{nx}}{3}\right) + 2L_{arm} \dot{i}_{zx} + 2R_{arm} i_{zx} = 0 \quad (2.37)$$

Finally, the AC current dynamic is contained in (2.35). Nevertheless, there is here a dependency on u_{no} , which is the average voltage of the three-phase outputs with respect to the reference DC virtual ground [101] and is defined as

$$u_{no} = \sum_{x \in \{a,b,c\}} \frac{-u_{px} + u_{nx}}{6} \quad (2.38)$$

Furthermore, consider the following relations, which simplify the dynamic equations above written. The passive elements are rearranged as,

$$L_{dc} = 2L_d + \frac{2L_{arm}}{3} \quad R_{dc} = 2R_d + \frac{2R_{arm}}{3} \quad (2.39)$$

$$L_z = 2L_{arm} \quad R_z = 2R_{arm} \quad (2.40)$$

$$L_{ac} = \frac{L_{arm}}{2} + L_g \quad R_{ac} = \frac{R_{arm}}{2} + R_g \quad (2.41)$$

It is also helpful to define the CM voltage for the arm voltages of each as

$$u_{d0} = \sum_{x \in \{a,b,c\}} \frac{u_{px} + u_{nx}}{3} \quad (2.42)$$

which drives i_{dc} . Similarly, the differential arm voltages are used to drive i_{gx} , yielding

$$\forall x \in \{a, b, c\}, \quad u_{sx} = \frac{-u_{px} + u_{nx}}{2} \quad (2.43)$$

Lastly, the voltage driving the circulating currents for each phase is defined as

$$\forall x \in \{a, b, c\}, \quad u_{zx} = u_{px} + u_{nx} - \sum_{x \in \{a,b,c\}} \frac{u_{px} + u_{nx}}{3} \quad (2.44)$$

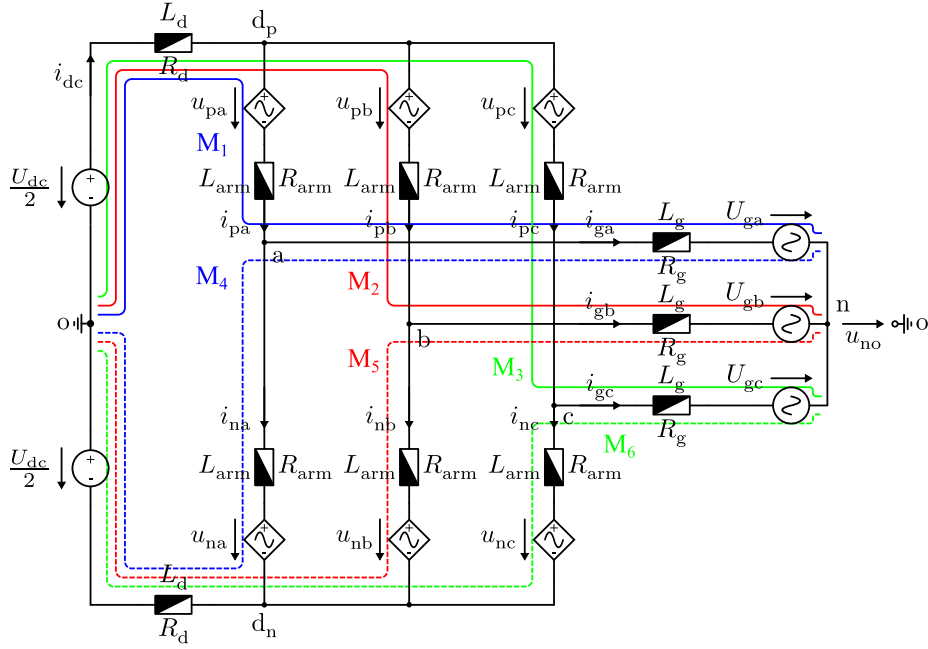


Figure 2.8: MMC KVL analysis

Ultimately, the current dynamics are reduced to the following,

$$L_{dc} \dot{i}_{dc} = -R_{dc} i_{dc} + U_{dc} - u_{d0} \quad (2.45)$$

$$\forall x \in \{a, b, c\}, \quad L_z \dot{i}_{zx} = -R_z i_{zx} - u_{zx} \quad (2.46)$$

$$\forall x \in \{a, b, c\}, \quad L_{ac} \dot{i}_{gx} = -R_{ac} i_{gx} + u_{sx} - u_{no} - U_{gx} \quad (2.47)$$

and form the simple equivalent circuits represented in Figure 2.9. It is worth noting that, although the equivalent circuits describe seven different currents, only five are controllable. This limitation arises from the circuit constraints in (2.23) and (2.29).

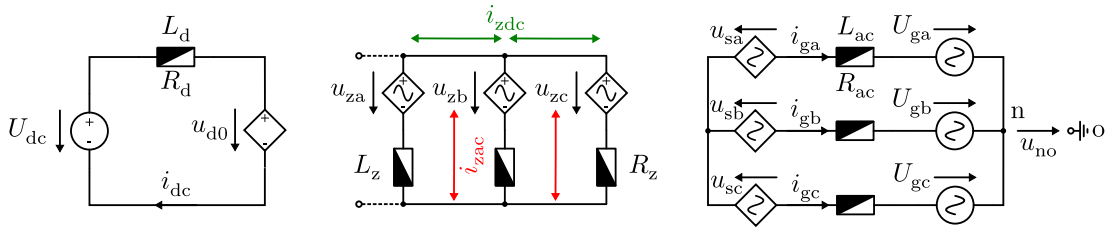


Figure 2.9: External and internal MMC equivalent circuits: DC-side, Z-side and AC-side

2.3 State-space model

The MMC is a meshed MIMO system. In this section a state-space model is developed, which serves as basis for development of a control algorithm.

2.3.1 Linear model

Building on the circuit analysis from the previous section, a Linear Time-Invariant (LTI) state-space model in the form of (2.48) is developed to represent the current dynamics. This derivation assumes that the arm voltages driving the current dynamics operate as ideal controllable voltage sources.

$$\begin{aligned}\dot{\mathbf{x}}_i(t) &= \mathbf{A}_i \mathbf{x}_i(t) + \mathbf{B}_i \mathbf{u}_i(t) + \mathbf{E}_i \mathbf{v}_i(t), \\ \mathbf{y}_i(t) &= \mathbf{C}_i \mathbf{x}_i(t).\end{aligned}\tag{2.48}$$

The physical current model includes seven current states (\mathbf{x}_i), six inputs, the arm voltages (\mathbf{u}_i) and four measurable disturbances (\mathbf{v}_i), both being the AC- and DC-grid voltages. Therefore, the following state, input and disturbance vectors are defined as below.

$$\begin{aligned}\mathbf{x}_{i,abc} &= [i_{ga}, i_{gb}, i_{gc}, i_{za}, i_{zb}, i_{zc}, i_{dc}]^T \\ \mathbf{u}_{i,abc} &= [u_{pa}, u_{pb}, u_{pc}, u_{na}, u_{nb}, u_{nc}]^T \\ \mathbf{v}_{i,abc} &= [U_{ga}, U_{gb}, U_{gc}, 0, 0, U_{dc}]^T\end{aligned}\tag{2.49}$$

Both circulating and AC current components have an oscillating nature. Therefore, a change of coordinates via transformation between abc, stationary $\alpha\beta 0$ or rotating dq0 reference-frames can be applied. This reduces the system order to be equal to the number of controllable currents. A geometrical interpretation of these reference frames is given in [102], while the necessary transformation is listed in Appendix A. As in previous works [103, 104, 105] stationary reference frame is chosen and based on (A.1) and (A.3), (2.49) is updated accordingly,

$$\begin{aligned}\mathbf{x}_{i,\alpha\beta} &= [i_{g\alpha}, i_{g\beta}, i_{z\alpha}, i_{z\beta}, i_{dc}]^T \\ \mathbf{u}_{i,\alpha\beta} &= [u_{p\alpha}, u_{p\beta}, u_{n\alpha}, u_{n\beta}, u_{d0}]^T \\ \mathbf{v}_{i,\alpha\beta} &= [U_{g\alpha}, U_{g\beta}, 0, 0, U_{dc}]^T\end{aligned}\tag{2.50}$$

Consequently, the corresponding dynamic equations are updated, which are finally written in the vector form of (2.48). Hence, the system (\mathbf{A}_i), input (\mathbf{B}_i) and disturbance (\mathbf{E}_i) matrices are defined as in (2.51). All current states are

measurable or easily obtained from available measurements, therefore $\mathbf{y}_i = \mathbf{x}_i$.

$$\begin{aligned}
\mathbf{A}_i &= -diag \left(\left[\frac{R_{ac}}{L_{ac}}, \frac{R_{ac}}{L_{ac}}, \frac{R_z}{L_z}, \frac{R_z}{L_z}, \frac{R_{dc}}{L_{dc}} \right] \right) \\
\mathbf{B}_i &= \begin{bmatrix} -\frac{1}{2L_{ac}} & 0 & \frac{1}{2L_{ac}} & 0 & 0 \\ 0 & -\frac{1}{2L_{ac}} & 0 & \frac{1}{2L_{ac}} & 0 \\ -\frac{1}{L_z} & 0 & -\frac{1}{L_z} & 0 & 0 \\ 0 & -\frac{1}{L_z} & 0 & -\frac{1}{L_z} & 0 \\ 0 & 0 & 0 & 0 & -\frac{1}{L_{dc}} \end{bmatrix} \\
\mathbf{E}_i &= -diag \left(\left[\frac{1}{L_{ac}}, \frac{1}{L_{ac}}, 0, 0, -\frac{1}{L_{dc}} \right] \right) \\
\mathbf{C}_i &= \mathbf{I}
\end{aligned} \tag{2.51}$$

Analyzing the state matrix (2.51), it is clear that all system eigenvalues have negative real parts and as a result the system is asymptotically stable [106].

2.3.2 Nonlinear model

Assuming the arm voltages to be ideally controllable sources simplifies the analysis of current states in the MMC topology. However, in practice, arm voltages are limited in availability, as detailed in subsection 2.1.2. These voltages must be actively controlled for the proper operation of the MMC. As a result, six additional energy states (\mathbf{x}_w) must be incorporated into the model, representing the energy stored in each arm. As shown in (2.8), these energy states are influenced by the arm currents and the percentage of available voltage in each arm, expressed through the modulation index (m) in (2.9). This modulation index serves as the ambiguous control input for all states, making it logical to update the input vector accordingly.

$$\begin{aligned}
\mathbf{x}_w &= [u_{cpa}, u_{cpb}, u_{cpc}, u_{cna}, u_{cnb}, u_{cnc}]^T \\
\mathbf{u} &= [m_{pa}, m_{pb}, m_{pc}, m_{na}, m_{nb}, m_{nc}]^T
\end{aligned} \tag{2.52}$$

Consider the auxiliary vector containing the six arm currents \mathbf{i}_{pn} .

$$\mathbf{i}_{pn} = [i_{pa}, i_{pb}, i_{pc}, i_{na}, i_{nb}, i_{nc}]^T \tag{2.53}$$

Now (2.8) can be written in a vectored form, yielding

$$\dot{\mathbf{x}}_w = \frac{\mathbf{u} \odot \mathbf{i}_{pn}}{C_{arm}}. \quad (2.54)$$

Making use of transformation in (A.16), the energy state dynamics become dependent on the control input and chosen current state vectors, leading to

$$\dot{\mathbf{x}}_w = \frac{\mathbf{u} \odot (\mathbf{T}_{xi,pn} \mathbf{x}_{i,\alpha\beta})}{C_{arm}}. \quad (2.55)$$

The element-wise multiplication between both vectors is non-linear. Now the entire MMC model state vector is given by

$$\mathbf{x} = \begin{bmatrix} \mathbf{x}_{i,\alpha\beta} \\ \mathbf{x}_w \end{bmatrix}, \quad (2.56)$$

while control input and disturbance ($\mathbf{v} = \mathbf{v}_{i,\alpha\beta}$) vectors remain unchanged. Unlike the previous linear model, the energy states only includes a forced component, having no characteristic equation. As a result, the state equations for the entire model are linear in the control inputs, making the system a control-affine system. Further details on this class of dynamical systems can be found in [107, 108]. The state-space representation of such systems yields

$$\begin{aligned} \dot{\mathbf{x}}(t) &= \mathbf{A}\mathbf{x}(t) + \mathbf{B}(\mathbf{x}(t))\mathbf{u}(t) + \mathbf{E}\mathbf{v}(t), \\ \mathbf{y}(t) &= \mathbf{C}\mathbf{x}(t). \end{aligned} \quad (2.57)$$

where the input matrix is state-dependent and is further expressed as the Kronecker product between system states and control inputs. Its block diagram representation is given in Figure 2.10.

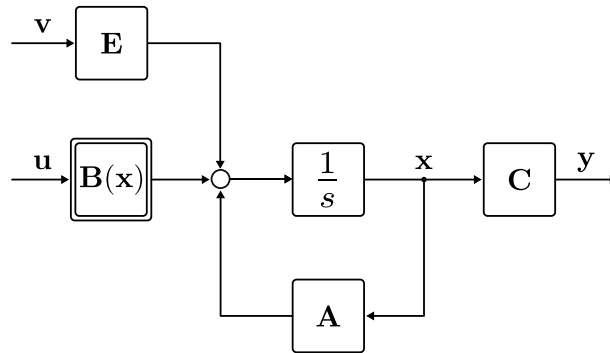


Figure 2.10: Nonlinear state space model block diagram

Due to the introduction of (2.52), current dynamics are similarly affected. While the unforced component of LTI model remains the same, the forced component

must return to the abc frame to comply with the chosen energy states. This is achieved using the transformation (A.17) and equations (2.9), it yields

$$\mathbf{u}_{i,abc} = \mathbf{T}_{iC,ui} \cdot \mathbf{u}_{i,\alpha\beta}, \quad (2.58)$$

For a three-phase four-wire system, an additional state i_{g0} must be included in the current state vector, and the transformation in (2.55) is replaced by (A.15). Finally, the entire state, input, disturbance and output matrices, describing the entire system dynamics are given below.

$$\mathbf{A}_i = -diag \left(\left[\frac{R_{ac}}{L_{ac}}, \frac{R_{ac}}{L_{ac}}, \frac{R_{no}}{L_{no}}, \frac{R_z}{L_z}, \frac{R_z}{L_z}, \frac{R_{dc}}{L_{dc}} \right] \right) \quad (2.59)$$

$$\mathbf{A} = \begin{bmatrix} \mathbf{A}_i & \mathbf{0}_{6 \times 6} \\ \mathbf{0}_{6 \times 6} & \mathbf{0}_{6 \times 6} \end{bmatrix}$$

$$\mathbf{E}_i = -diag \left(\left[\frac{1}{L_{ac}}, \frac{1}{L_{ac}}, \frac{1}{L_{no}}, 0, 0, -\frac{1}{L_{dc}} \right] \right) \quad (2.60)$$

$$\mathbf{E} = \begin{bmatrix} \mathbf{E}_i & \mathbf{0}_{6 \times 6} \\ \mathbf{0}_{6 \times 6} & \mathbf{0}_{6 \times 6} \end{bmatrix}$$

$$\mathbf{C} = \mathbf{C}_i \quad (2.61)$$

The matrices $\mathbf{B}_m(\mathbf{x})$ represent the state-dependent contribution of the modulation signal of the m -th arm to the bilinear term. Therefore the index m denotes the arm index of the MMC and identifies the modulation input vector u_m . For $m \in \{1, \dots, 6\}$, the indices correspond to the arms pa , pb , pc , na , nb , and nc , respectively.

$$\mathbf{B}(\mathbf{x})\mathbf{u} = \sum_{m=1}^6 \mathbf{B}_m(\mathbf{x})u_m,$$

$$\mathbf{B}_m(\mathbf{x}) = \begin{bmatrix} \mathbf{0}_{6 \times 6} & [\mathbf{0}_{6 \times (m-1)} & \mathbf{B}_{mi} & \mathbf{0}_{6 \times (6-m)}] \\ \begin{bmatrix} \mathbf{0}_{(m-1) \times 6} \\ \mathbf{B}_{mw} \\ \mathbf{0}_{(6-m) \times 6} \end{bmatrix} & \mathbf{0}_{6 \times 6} \end{bmatrix} \cdot \begin{bmatrix} \mathbf{x}_i \\ \mathbf{x}_w \end{bmatrix}$$

$$\mathbf{B}_{1i} = \left[-\frac{1}{3L_{ac}}, 0, -\frac{1}{6L_{ac}}, -\frac{2}{3L_z}, 0, -\frac{1}{3L_{dc}} \right]^T$$

$$\mathbf{B}_{2i} = \left[\frac{1}{6L_{ac}}, -\frac{\sqrt{3}}{6L_{ac}}, -\frac{1}{6L_{ac}}, \frac{1}{3L_z}, -\frac{\sqrt{3}}{3L_z}, -\frac{1}{3L_{dc}} \right]^T$$

$$\mathbf{B}_{3i} = \left[\frac{1}{6L_{ac}}, \frac{\sqrt{3}}{6L_{ac}}, -\frac{1}{6L_{ac}}, \frac{1}{3L_z}, \frac{\sqrt{3}}{3L_z}, -\frac{1}{3L_{dc}} \right]^T$$

$$\begin{aligned}
\mathbf{B}_{4i} &= \left[\frac{1}{3L_{ac}}, 0, \frac{1}{6L_{ac}}, -\frac{2}{3L_z}, 0, -\frac{1}{3L_{dc}} \right]^T \\
\mathbf{B}_{5i} &= \left[-\frac{1}{6L_{ac}}, \frac{\sqrt{3}}{6L_{ac}}, \frac{1}{6L_{ac}}, \frac{1}{3L_z}, -\frac{\sqrt{3}}{3L_z}, -\frac{1}{3L_{dc}} \right]^T \\
\mathbf{B}_{6i} &= \left[-\frac{1}{6L_{ac}}, -\frac{\sqrt{3}}{6L_{ac}}, \frac{1}{6L_{ac}}, \frac{1}{3L_z}, \frac{\sqrt{3}}{3L_z}, -\frac{1}{3L_{dc}} \right]^T \\
\mathbf{B}_{1w} &= \frac{1}{C_{arm}} \left[\frac{1}{2}, 0, \frac{1}{2}, 1, 0, \frac{1}{3} \right] \\
\mathbf{B}_{2w} &= \frac{1}{C_{arm}} \left[-\frac{1}{4}, \frac{\sqrt{3}}{4}, \frac{1}{2}, -\frac{1}{2}, \frac{\sqrt{3}}{2}, \frac{1}{3} \right] \\
\mathbf{B}_{3w} &= \frac{1}{C_{arm}} \left[-\frac{1}{4}, -\frac{\sqrt{3}}{4}, \frac{1}{2}, -\frac{1}{2}, -\frac{\sqrt{3}}{2}, \frac{1}{3} \right] \\
\mathbf{B}_{4w} &= \frac{1}{C_{arm}} \left[-\frac{1}{2}, 0, -\frac{1}{2}, 1, 0, \frac{1}{3} \right] \\
\mathbf{B}_{5w} &= \frac{1}{C_{arm}} \left[\frac{1}{4}, -\frac{\sqrt{3}}{4}, -\frac{1}{2}, -\frac{1}{2}, \frac{\sqrt{3}}{2}, \frac{1}{3} \right] \\
\mathbf{B}_{6w} &= \frac{1}{C_{arm}} \left[\frac{1}{4}, \frac{\sqrt{3}}{4}, -\frac{1}{2}, -\frac{1}{2}, -\frac{\sqrt{3}}{2}, \frac{1}{3} \right]
\end{aligned} \tag{2.62}$$

2.4 Open-loop control

The accuracy of the AAM principle is fundamentally dependent on precise arm voltage modulation [109]. Similar to other inverter and rectifier topologies, PWM is typically employed to achieve the desired voltage modulation. A comparative review of various carrier-based PWM algorithms is presented in [77], highlighting differences in voltage quality under varying operating conditions. Despite these differences, all modulation strategies essentially implement (2.7). The digital implementation of these strategies plays a critical role in determining their precision [110]. Furthermore, accurate voltage modulation is unattainable without ensuring proper balancing of the capacitor voltages within the arm [111]. Commonly, sorting-based algorithms are responsible for this task [112] and are embedded in the arm modulation process as illustrated in Figure 2.11.

A flowchart illustrating the balancing algorithm is shown in Figure 2.12. Within each arm, during every switching period (T_{sw}), the submodule capacitor voltages and arm current are measured. The modulator determines the number of sub-

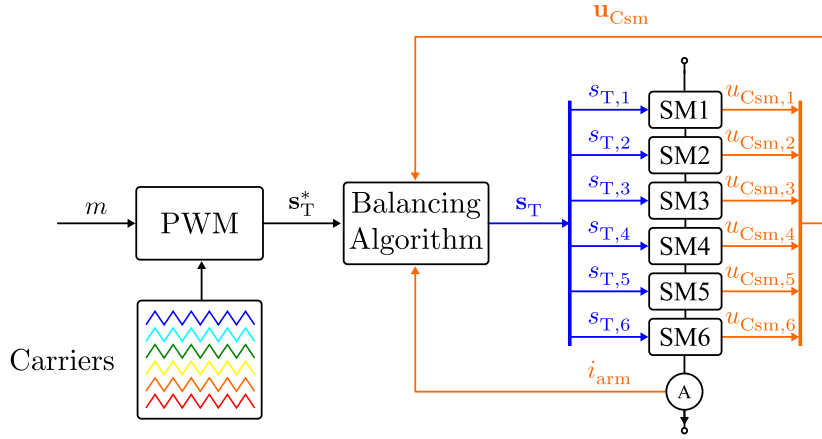


Figure 2.11: Arm voltage modulation overview

modules to be inserted in that switching period. Referring to Table 2.1, for an arm containing HB-SM, the direction of the current dictates the sorting order of the submodules. The sorting algorithm ranks the submodules based on their charge levels, producing a list of indices. Subsequently, the switching functions are reassigned accordingly. For example, when the arm current is positive, the submodules with the lowest charge levels are assigned the highest priority indices, leading to their insertion for charging. In contrast, for negative currents, the opposite occurs. In the case of FB-SM, an inverse logic is applied when negative arm voltages are required (Table 2.2).

The design and implementation of balancing algorithms is itself a research topic. Further proposed analysis, methodologies and improvements are presented in [113, 114, 115, 116, 117, 118].

To confirm the suitability of the arm modulator and balancing algorithm, a comparison between an AAM and SWM is carried out. The SWM is an accurate representation of a real MMC system, as it takes into account the switching actions of the number of submodules used per arm. Therefore it embeds the structure in Figure 2.11. Consider now the MMC prototype in section 5.1, supplying a resistive load connected its AC terminals in open-loop operation. In order to supply a sinusoidal current, the modulation index of each are chosen accordingly [119], yielding

$$\begin{aligned} m_{\text{px}}(t) &= \frac{1 - m_{\text{sx}}(t)}{2} \\ m_{\text{nx}}(t) &= \frac{1 + m_{\text{sx}}(t)}{2} \end{aligned} \quad (2.63)$$

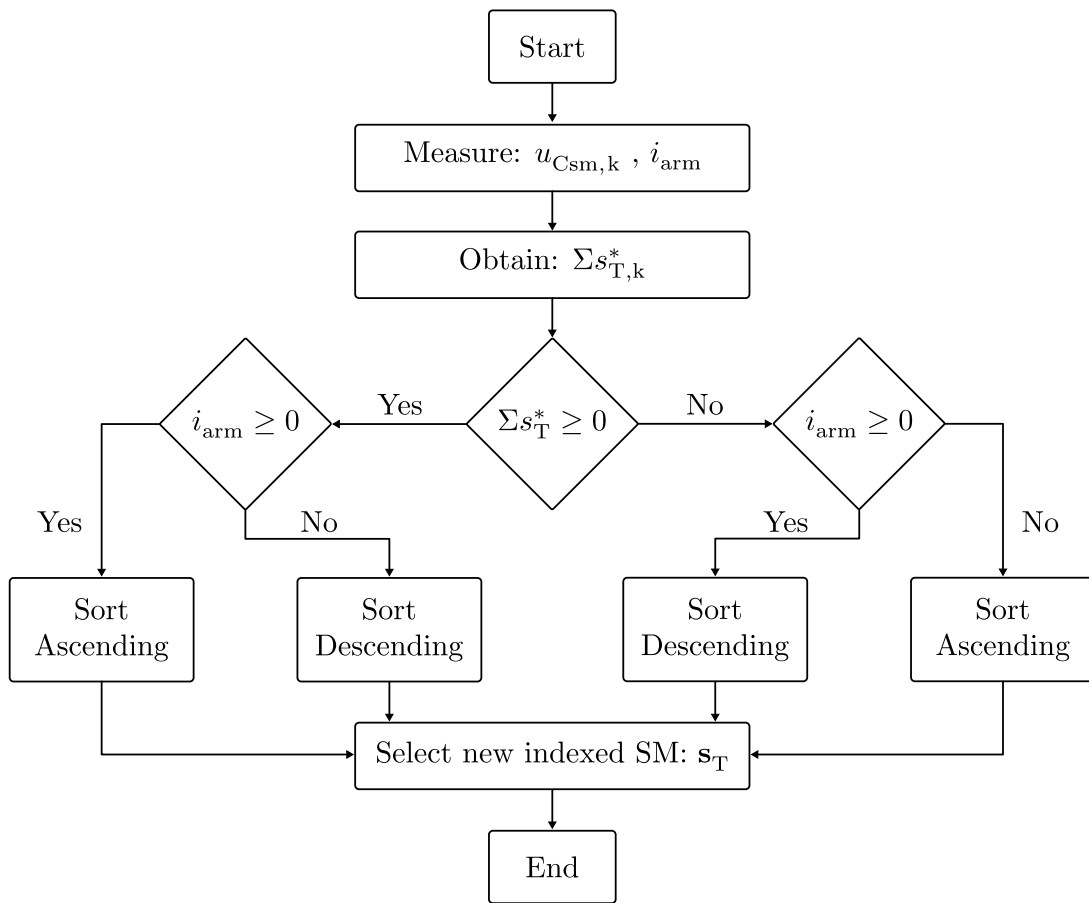


Figure 2.12: Balancing algorithm for submodule voltage balancing

where as

$$\begin{aligned} m_{sa}(t) &= \hat{m}_s \cos(\omega t) \\ m_{sb}(t) &= \hat{m}_s \cos\left(\omega t - \frac{2\pi}{3}\right). \\ m_{sc}(t) &= \hat{m}_s \cos\left(\omega t + \frac{2\pi}{3}\right) \end{aligned} \quad (2.64)$$

Essentially, the MMC common-mode voltage u_{d0} is regulated close to U_{dc} , while the differential-mode voltage u_{sx} follows the references in (2.63). Its peak amplitude depends on the chosen modulation index and can reach at most $\frac{u_{d0}}{2}$. The prototype is modeled using the software PLECS [120] as AAM and SWM. Both simultaneously receive the reference (2.63) with $\hat{m}_s = 0.75$. The resulting arm voltages are given in Figure 2.13 for phase a . Due to the limited 7L resolution of each arm, the SMs must be switched at a much higher frequency than the fundamental to be able to achieve the waveform quality performance of the AAM. Naturally, as the N_{sm} increases, less switching actions are necessary. Typically in HVDC application, where each arm includes $N_{sm} \geq 100$, the Nearest Level Modulation (NLM) is followed and the submodules switch at the fundamental frequency [121, 122, 123].

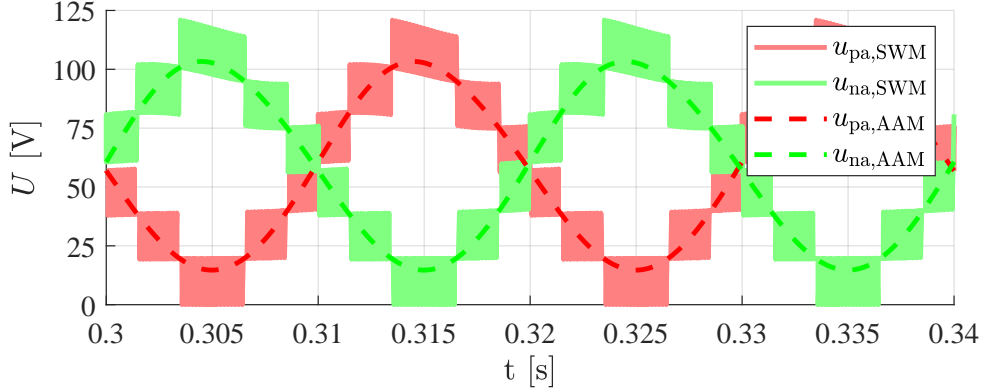


Figure 2.13: Arm voltage modulation resulting waveforms

The balancing algorithm described in Figure 2.12 is chosen to operate at an average switching frequency of 1 kHz, assures all six submodules are well balanced, as inspected in Figure 2.14 for the upper arm in phase a . It worth to notice, the average capacitor voltage in the arm ($u_{sm,Avg}$) reassembles very closely the available arm voltage u_{Carm} . Furthermore the resulting currents and changes in the available arm voltages of both models are compared in Figure 2.15. At first, one notices both models perform very similarly. Ideally, only DC- and AC-side

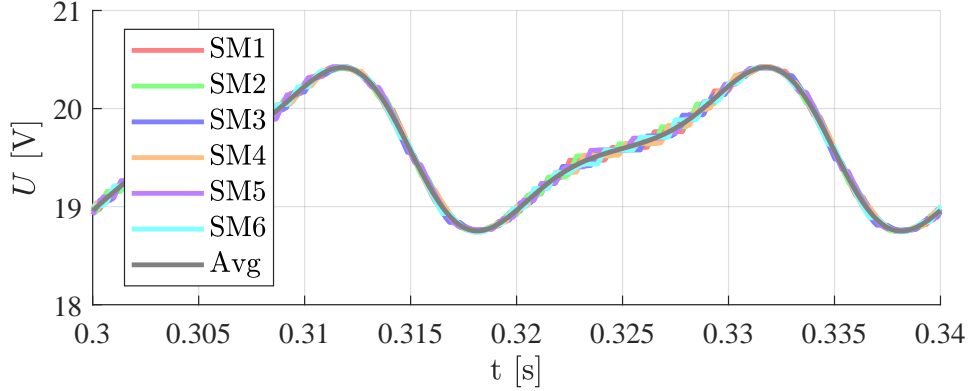


Figure 2.14: Balancing algorithm effect on SM voltage for an arm

currents would be expected. In that case the arm currents would yield,

$$\begin{aligned} i_{pa}(t) &= \frac{I_{dc}}{3} + \frac{\hat{I}_g}{2} \cos(\omega t) \\ i_{na}(t) &= \frac{I_{dc}}{3} - \frac{\hat{I}_g}{2} \cos(\omega t) \end{aligned} \quad (2.65)$$

for phase a (as an example). Inserting (2.63) and (2.65) in (2.8) would origin a second harmonic ripple in u_{Carm} when integrated. This is explained by trigonometric relations highlighted in (A.20), (A.21) and visible in Figure 2.14. Furthermore this second harmonic will induce a second harmonic component in the circulating current, visible in Figure 2.15. This interaction between oscillating components further results in less significant higher harmonic content on the available arm voltage and circulating currents. This is well presented in [124]. Lastly, the switching actions in the SWM lead to high frequency components in the current waveforms, which is unavoidable [125, 126]. However, both average and fundamental components, hence the main interesting components, remain unaffected. In summary, the AAM represents well the SWM. Therefore, for next sections only AAM will be considered, avoiding the burden and details of the SWM.

2.5 Closed-loop control

The previous analysis was carried out for an arbitrary modulation reference, disregarding state or output tracking functionality, enough to verify the MMC steady-state operation. Depending on the application, several reference waveform are to be tracked. To achieve this, a proper control algorithm must be designed. In general any control algorithm should offer the following features [106]:

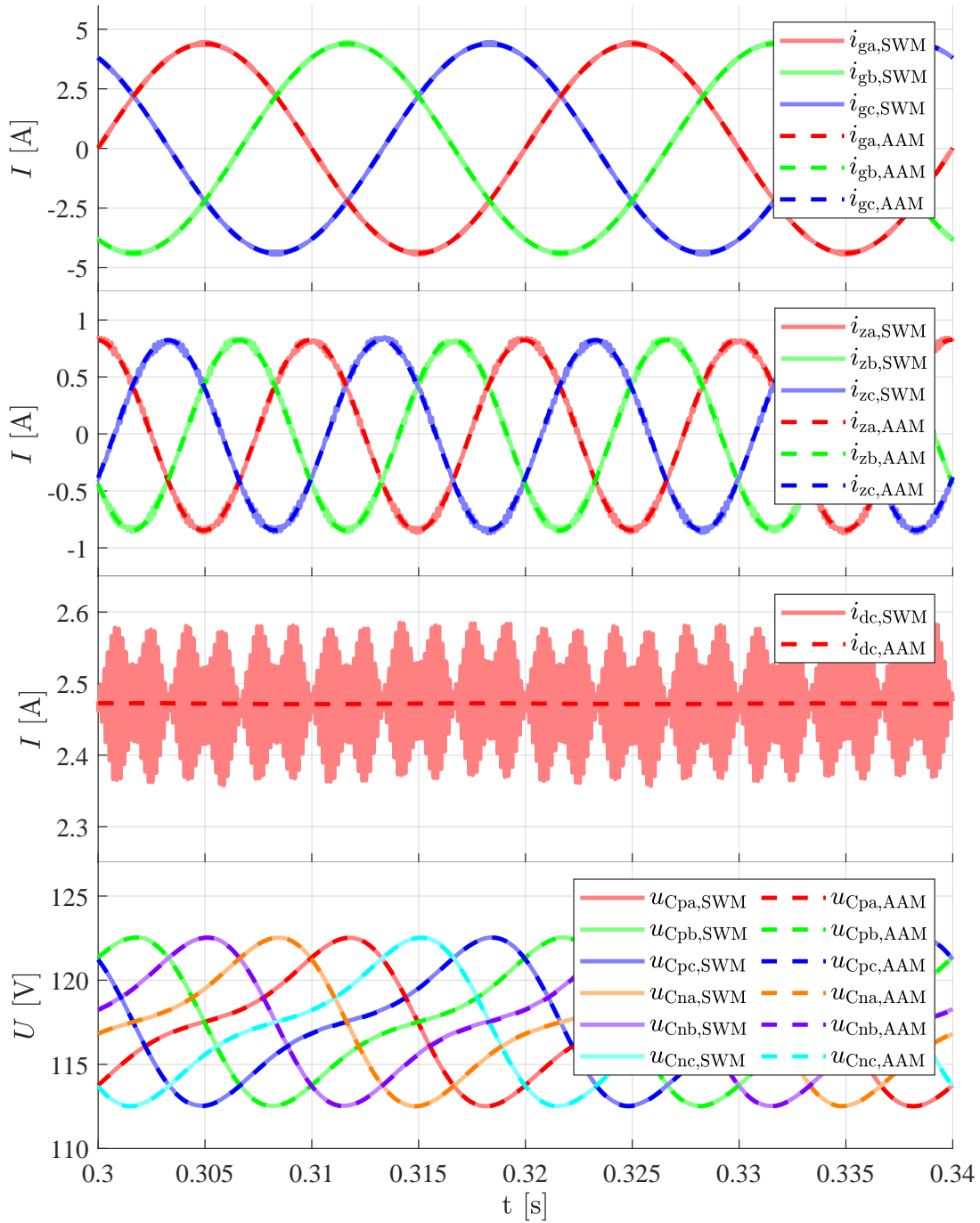


Figure 2.15: Comparison between AAM and SWM models

Table 2.3: Summary of control objectives in MMC

Reference	Nature	Objective	DOF
i_{gx}	AC	Tracking	2
i_{zx}	DC+AC	Regulation + Tracking	2
i_{dc}	DC	Tracking	1
u_{px}	DC+AC	Tracking	3
u_{nx}	DC+AC	Tracking	3

- Stability – ensure the system returns to equilibrium or desired operation after a disturbance.
- Accuracy – achieve the desired reference value with minimal error.
- Robustness – ability to maintain performance despite uncertainties, parameter variations, or external disturbances.
- Responsiveness – desired transient response, avoiding overshoots.

Ideally, the 3PH-MMC main control objectives and available DOF can be summarized in Table 2.3 [127, 128, 129]. Besides being a highly meshed non-linear system, the mixed nature of its references requires a complex control strategies.

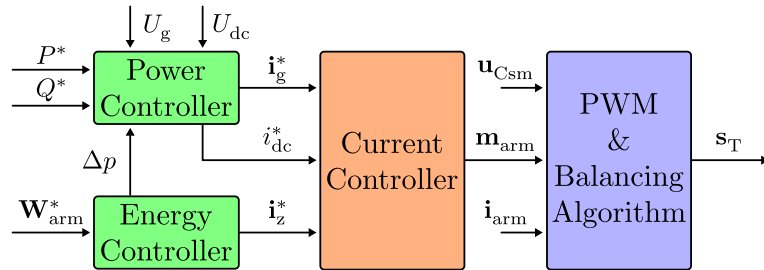


Figure 2.16: Cascaded control structure of grid-connected MMC

Based on the assumption that the energy dynamics are slower than the current dynamics, the linear cascaded-control structure represents the majority of control schemes applied to a grid-connected MMC [130]. A block diagram of this cascaded structure is represented in Figure 2.16. In such, an energy-power outer loop generates the current references to be tracked by an inner loop, which typically contains Proportional Integral (PI) or Proportional Resonant (PR) based linear controllers [131]. Each PI or PR controller generates a voltage reference to be modulated [132], which will reduce the difference between the measured current and its reference. Alternatively, linear state-feedback-based MIMO controllers consider the current coupling terms and improve the overall system behavior [133]. In both cases, zero error steady-state is achieved, while good dynamic per-

formance is only obtained at a limited linear range around an operation point. To attain high dynamic performance across the entire operation range, the nonlinear nature of the topology must be taken into account.

The use of MPC to design a multi-variable optimal controller, has been reported as a promising strategy to deal with the MMC model nonlinearities, providing fast dynamics and constrained operation [134]. However, MPC strategies implemented so far have a high computational burden and therefore haven't been implemented in practice for longer horizons [135]. Widely proposed, are single-prediction step implementations. However these are restricted to a low N_{sm} . A higher N_{sm} , results in a large integer optimization problem not easily solvable on-line, despite many efforts reducing its computational burden [136]. A piecewise Linear Quadratic Regulator (LQR) solution with similar performance [134] is presented in [137]. A similar solution, Lyapunov-based state feedback is presented in [138]. In the previous schemes, the response to an energy imbalance situation is not reported. An identical approach with an integrated strategy for current control, energy control, and energy balancing is presented in [139]. These last two methods are based on optimal state-dependent feedback around linearized energy operating points, resulting in a rather complicated tuning process.

Relying on the widely used cascaded structure, a current control strategy for a single-phase (1PH) MMC based on IOFL technique has been proposed in [140]. Using this technique both linear and nonlinear terms are decoupled for the whole operation range and the controller design becomes straightforward for the resulting linearized system. For a three-phase (3PH) MMC, the authors in [141] use IOFL to decouple the MMC's internal dynamics and directly control the grid power exchange. Opposite to [142], 3PH modelling philosophy is considered. In the per-phase modelling philosophy, the MMC phases are independently modelled so as the resulting circulating current dynamics. This modelling philosophy highly simplifies the Feedback Linearization Law (FBL) derivation. However, it is only useful in perfectly balanced situations [143]. Despite of increasing the model complexity, by considering 3PH philosophy, the coupling between phases is considered and the effect of energy- and grid- unbalances are taken into account. For this case, the FBL has not been considered so far and shall be investigated in the next section.

3 Power Decoupling Capability

This section explores a unique feature of the MMC, focusing on its capability to achieve power decoupling between DC and AC grids. Unlike conventional DC-AC converter topologies, this functionality allows the power input and output sides to exhibit distinct dynamic behaviors in response to transient phenomena. The discussion begins with an overview of the general concept, followed by an explanation of the selected control algorithm, to simply achieve the proposed function. Additionally, simulation and experimental results are presented to validate the introduced concepts.

3.1 Concept

As mention in 1.1.2, interfacing DC and AC grids is done with IPCs. Besides the difference in nature of both grids, its interface should be seamless and resilient [71]. Opposite to traditional DC-AC converter topologies [144], the MMC offers extra DOF (energy states) with its distributed capacity energy storage. Through control, these can generate controlled circulating currents capable of canceling continuous or oscillating components originated either from the DC- or AC-grids and avoid their propagation from one side to another [145]. Alternatively, the topology can be seen as an aggregation of a DC-DC converter with a separate DC-AC converter interfaced by a self-regulated energy storage system [146]. Taking into account the total capacitance of the MMC in (2.20) and the equivalent circuits represented in Figure 2.9, a simplified representation of energy buffering capability is given in Figure 3.1. Mathematically this concept is demonstrated by (3.1), where as P_{in} and P_{out} depend on the power flow direction.

$$P_{\text{in}} = P_{\text{out}} + P_{\text{MMC}} + P_{\text{loss}} \quad (3.1)$$

For simplicity, a lossless inverter mode operation is considered, i.e. $P_{\text{in}} = P_{\text{dc}}$ and $P_{\text{out}} = P_{\text{ac}}$. In rectification mode, the roles of input and output power are simply reversed. Considering (2.21), (3.1) is rewritten as

$$\dot{W}_{\text{MMC}} = P_{\text{MMC}} = P_{\text{dc}} - P_{\text{ac}}, \quad (3.2)$$

demonstrates that the rate of energy stored in MMC is dependent on a balanced power flow between both grids. By manipulation of the modulation indexes within vector \mathbf{u} , u_{d0} and u_{sx} are simultaneously adjusted, s.t. the desired power flow is achieved in both grid interface circuits. Furthermore, adjusting u_{zx} will assure that circulating currents balance the energy in the arms. In previous works, this capability has primarily been utilized to dampen low-frequency oscillations (0.1–25 Hz) in the AC grid, while preventing their propagation to the DC side [145, 147, 148]. Similar advantages have been demonstrated in [127, 130] during unbalanced grid operation. This buffering functionality has been reported to enhance grid-forming operations provided by wind turbine collectors in [146, 149]. Authors in [150, 151] have mitigated the high-amplitude harmonic content induced by high-power DC pulsed loads in the AC grid, using the distributed energy storage capability.

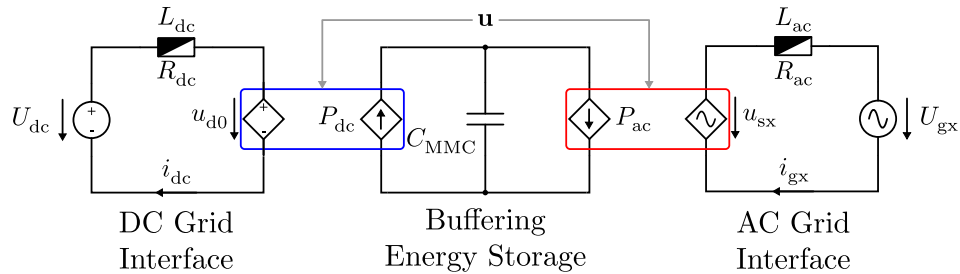
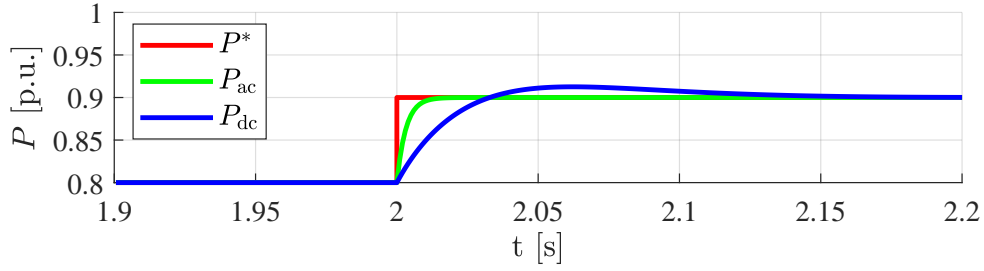


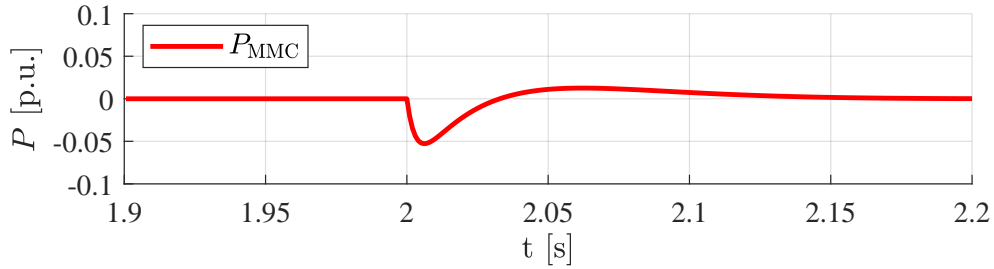
Figure 3.1: Simplified representation of the MMC energy buffering capability

During power dispatches or disturbances, conventional DC-AC converter topologies cause both grids to experience identical transient responses. This section explores how the buffering storage capability of the MMC can be utilized to decouple these responses, enabling distinct transient behavior on each side of the grid. A generic example, shown in Figure 3.2, illustrates the simplicity of this approach. Consider a controlled grid-connected MMC capable of tracking any specified power reference. During a power dispatch event, the AC grid demands a fast transient response, while the DC grid interprets it as a load disturbance, benefiting more from a slower response. Nevertheless, the principle of power balance must remain intact. Here, the MMC would manage this deficit by rapidly compensating the difference using the energy stored in its capacitors. This energy is then restored gradually, allowing the system to return to its steady-state reference.

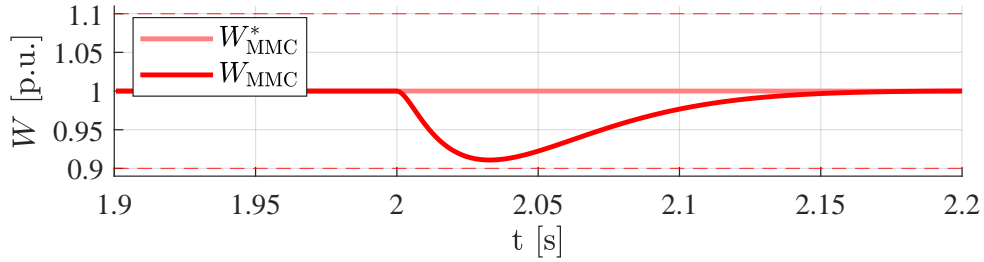
To achieve this behavior, the grid-connected MMC must behave as the equivalent circuit shown in Figure 3.1. In other words, it must be fully controlled such that the desired references are independently tracked with the desired dynamic performance. Simultaneously, the energy stored must not overpass its limitations, i.e. violate (2.11) nor surpass the capacitors rated voltage. This applies for all six arms. Therefore it is foreseen, that the initial timing of the power step response



(a) Step responses from the AC and DC grids



(b) Power flow within the MMC



(c) Energy stored in the MMC

Figure 3.2: Power decoupling concept for a power dispatch

disrupts the stored energy in the arms unevenly. Consequently, a precise energy controller is essential. The following sections will present the control algorithm, capable of validating the power decoupling feature.

3.2 Current controller

As the MMC is a highly coupled MIMO nonlinear system, classical linear controllers only achieve zero steady-state error and good dynamic performance at a limited linear range around an operation point. Else, its dynamic performance highly depreciates. As represented in Figure 3.3, in this section the Input-Output Feedback Linearization technique is used to decouple the meshed state-dependent inputs of the grid-connected MMC current dynamics model. Afterwards, the

controller design is much simpler, which will impact the design of outer loop controller. This method allows independent control the of DC-, AC-, and Z- currents with desired performance through the whole operation range.

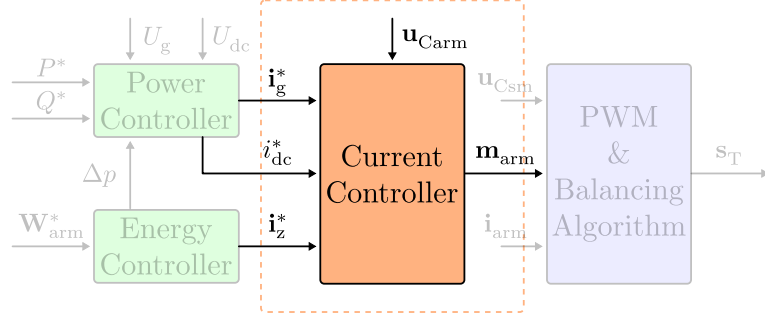


Figure 3.3: Research topic of this section

3.2.1 Feedback linearization

The system given in subsection 2.3.2 describes the MMC as a meshed control-affine MIMO system. Alternatively, such can be generically represented by

$$\begin{aligned}\dot{\mathbf{x}} &= f(\mathbf{x}) + \sum_1^m \mathbf{g}_m(\mathbf{x}) u_m \\ \mathbf{y} = \mathbf{h}(\mathbf{x}) &= [h_1(\mathbf{x}) \quad \dots \quad h_p(\mathbf{x})]^T\end{aligned}\quad (3.3)$$

where $x \in \mathbb{R}^n$, $u \in \mathbb{R}^m$ and $y \in \mathbb{R}^p$. The idea behind the IOFL technique is to find a feedback law for the inputs \mathbf{u} such that the dynamic relation between the outputs \mathbf{y} and virtual inputs $\boldsymbol{\gamma}$ are linear [107, 108]. For the SISO case ($m = p = 1$), the feedback linearization law is given by

$$u = \alpha(x) + \beta(x)\gamma \quad (3.4)$$

Differentiating of the output once yields

$$\dot{y} = \frac{\partial h}{\partial x} [f(x) + g(x)u] = L_f h(x) + L_g h(x)u, \quad (3.5)$$

where $L_f h(x)$, $L_g h(x)$ are Lie derivatives. For $L_g h(x) \neq 0$, (3.4) can be used to linearize input-output relation. If $L_g h(x) = 0$, the output y is independent of u and the differentiation of y has to be repeated until the control input u appears in the ρ th-order derivative of y . Hence, ρ is called the relative degree of the

dynamic system. In case $\rho < n$, there exist $n - \rho$ unobservable states which have no influence on y . These states are called internal dynamics and must be further investigated. The linearized closed loop system is said to be stable, if the internal dynamics are asymptotically stable. In case $\rho = n$, no internal dynamics exist and the system is exactly input–output linearizable. Furthermore, after applying the feedback linearization law, the linearized system is equivalent to a ρ th-order chain of integrators. Afterwards, a linear controller can be designed to bring the system to the desired reference point. This is well represented in Figure 3.4. An application of the IOFL for a SISO system (Boost Converter) is given in [152].

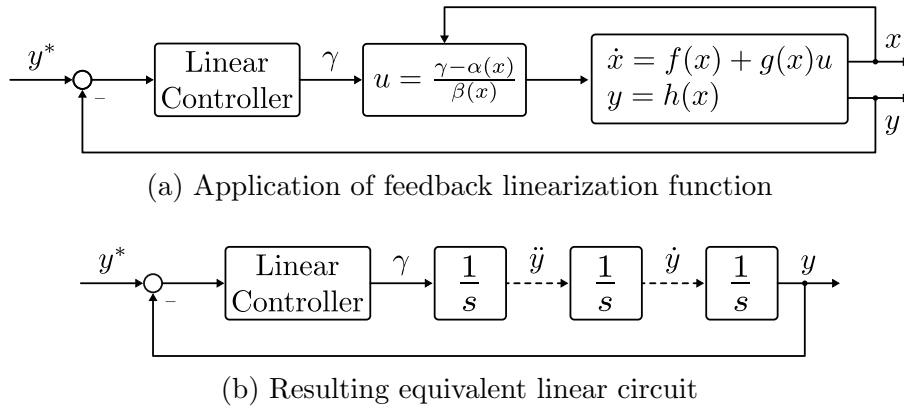


Figure 3.4: Block diagram of SISO Input-Output Feedback Linearization

The IOFL technique can be extended for MIMO systems [153], where the feedback control law is given by

$$\begin{aligned}
 \mathbf{u} &= \mathbf{D}_L(\mathbf{x})^{-1} [\boldsymbol{\gamma} - \mathbf{A}_L(\mathbf{x})] \\
 \mathbf{A}_L(\mathbf{x}) &= [L_f^{\rho_1} h_1(x) \quad \dots \quad L_f^{\rho_m} h_p(x)]^T \\
 \mathbf{D}_L(\mathbf{x}) &= \begin{bmatrix} L_{g_1} L_f^{\rho_1-1} h_1(\mathbf{x}) & \dots & L_{g_m} L_f^{\rho_1-1} h_1(\mathbf{x}) \\ \vdots & \ddots & \vdots \\ L_{g_1} L_f^{\rho_m-1} h_p(\mathbf{x}) & \dots & L_{g_m} L_f^{\rho_m-1} h_p(\mathbf{x}) \end{bmatrix} \\
 \boldsymbol{\gamma} &= [\gamma_1 \quad \dots \quad \gamma_m]^T
 \end{aligned} \tag{3.6}$$

where ρ_1, \dots, ρ_m are the relative degrees of the outputs y_1, \dots, y_m . Note that the matrix $\mathbf{D}_L(\mathbf{x})$ has to be non-singular such that the inverse of the matrix exists.

When applying the IOFL technique to the bilinear MMC system, the number of linearizable outputs cannot exceed the number of inputs, i.e. $p = m$. Due to the fact that the current states have faster dynamics than the energy related states, the current states are the target outputs for the IOFL. As a result the output function $\mathbf{h}(\mathbf{x})$ is given by

$$\mathbf{h}(\mathbf{x}) = [\mathbf{I}_{6 \times 6} \quad \mathbf{0}_{(6 \times 6)}] \begin{bmatrix} \mathbf{x}_i \\ \mathbf{x}_w \end{bmatrix} \quad (3.7)$$

For the given $\mathbf{h}(\mathbf{x})$, differentiating \mathbf{y} yields

$$\dot{\mathbf{y}} = \dot{\mathbf{x}}_i \quad (3.8)$$

where the control input u appears in the first derivative, giving a relative degree for each input-output relation equals to one. By comparing (2.57) with (3.3), $\mathbf{f}(\mathbf{x})$ and $\sum_1^m \mathbf{g}_m(\mathbf{x})u_m$ has to be equal to

$$\begin{aligned} \mathbf{f}(\mathbf{x}) &= \mathbf{A}\mathbf{x} + \mathbf{E}\mathbf{v} \\ \sum_1^m \mathbf{g}_m(\mathbf{x})u_m &= \sum_1^m \mathbf{B}_m(\mathbf{x})u_m \end{aligned} \quad (3.9)$$

For $m = p = 6$ and $\rho_1, \dots, \rho_6 = 1$, the structures of $\mathbf{A}_L(\mathbf{x})$ and $\mathbf{D}_L(\mathbf{x})$ are given by

$$\begin{aligned} \mathbf{A}_L(\mathbf{x}) &= [L_f h_1(\mathbf{x}) \quad L_f h_2(\mathbf{x}) \quad L_f h_3(\mathbf{x}) \quad L_f h_4(\mathbf{x}) \quad L_f h_5(\mathbf{x}) \quad L_f h_6(\mathbf{x})]^T \quad (3.10) \\ \mathbf{D}_L(\mathbf{x}) &= \begin{bmatrix} L_{g_1} h_1(\mathbf{x}) & L_{g_2} h_1(\mathbf{x}) & L_{g_3} h_1(\mathbf{x}) & L_{g_4} h_1(\mathbf{x}) & L_{g_5} h_1(\mathbf{x}) & L_{g_6} h_1(\mathbf{x}) \\ L_{g_1} h_2(\mathbf{x}) & L_{g_2} h_2(\mathbf{x}) & L_{g_3} h_2(\mathbf{x}) & L_{g_4} h_2(\mathbf{x}) & L_{g_5} h_2(\mathbf{x}) & L_{g_6} h_2(\mathbf{x}) \\ L_{g_1} h_3(\mathbf{x}) & L_{g_2} h_3(\mathbf{x}) & L_{g_3} h_3(\mathbf{x}) & L_{g_4} h_3(\mathbf{x}) & L_{g_5} h_3(\mathbf{x}) & L_{g_6} h_3(\mathbf{x}) \\ L_{g_1} h_4(\mathbf{x}) & L_{g_2} h_4(\mathbf{x}) & L_{g_3} h_4(\mathbf{x}) & L_{g_4} h_4(\mathbf{x}) & L_{g_5} h_4(\mathbf{x}) & L_{g_6} h_4(\mathbf{x}) \\ L_{g_1} h_5(\mathbf{x}) & L_{g_2} h_5(\mathbf{x}) & L_{g_3} h_5(\mathbf{x}) & L_{g_4} h_5(\mathbf{x}) & L_{g_5} h_5(\mathbf{x}) & L_{g_6} h_5(\mathbf{x}) \\ L_{g_1} h_6(\mathbf{x}) & L_{g_2} h_6(\mathbf{x}) & L_{g_3} h_6(\mathbf{x}) & L_{g_4} h_6(\mathbf{x}) & L_{g_5} h_6(\mathbf{x}) & L_{g_6} h_6(\mathbf{x}) \end{bmatrix} \end{aligned} \quad (3.11)$$

with $L_f^{\rho_m-1} h_p(\mathbf{x}) = h_p(\mathbf{x})$, since $\rho_m = 1$ for $m = 1, 2, \dots, 6$. Exemplary, the first elements of $\mathbf{A}_L(\mathbf{x})$ and $\mathbf{D}_L(\mathbf{x})$ can be calculated as

$$L_f h_1(\mathbf{x}) = \frac{\partial h_1(\mathbf{x})}{\partial \mathbf{x}} \mathbf{f}(\mathbf{x}) = [1 \quad 0 \quad 0 \quad 0 \quad 0 \quad 0] \mathbf{f}(\mathbf{x}) = -\frac{R_{ac}}{L_{ac}} i_{g\alpha} \quad (3.12)$$

$$L_{g_1} h_1(\mathbf{x}) = \frac{\partial h_1(\mathbf{x})}{\partial \mathbf{x}} \mathbf{g}_1(\mathbf{x}) = [1 \quad 0 \quad \dots \quad 0] \mathbf{B}_1(\mathbf{x}) = -\frac{u_{cpa}}{3L_{ac}} \quad (3.13)$$

and repeating the previous calculation for all elements, $\mathbf{A}_L(\mathbf{x})$ and $\mathbf{D}_L(\mathbf{x})$ are given by

$$\mathbf{A}_L(\mathbf{x}) = \begin{bmatrix} -\frac{R_{ac}}{L_{ac}} i_{g\alpha} - \frac{1}{L_{ac}} U_{g\alpha} \\ -\frac{R_{ac}}{L_{ac}} i_{g\beta} - \frac{1}{L_{ac}} U_{g\beta} \\ -\frac{R_{no}}{L_{no}} i_{g0} - \frac{1}{L_{no}} U_{g0} \\ -\frac{R_z}{L_z} i_{z\alpha} \\ -\frac{R_z}{L_z} i_{z\beta} \\ -\frac{R_{dc}}{L_{dc}} i_{dc} + \frac{1}{L_{dc}} U_{dc} \end{bmatrix} \quad (3.14)$$

$$\mathbf{D}_L(\mathbf{x}) = \begin{bmatrix} -\frac{u_{cpa}}{3L_{ac}} & \frac{u_{cpb}}{6L_{ac}} & \frac{u_{cpc}}{6L_{ac}} & \frac{u_{cna}}{3L_{ac}} & -\frac{u_{cnb}}{6L_{ac}} & -\frac{u_{cnc}}{6L_{ac}} \\ 0 & -\frac{\sqrt{3}u_{cpb}}{6L_{ac}} & \frac{\sqrt{3}u_{cpc}}{6L_{ac}} & 0 & \frac{\sqrt{3}u_{cnb}}{6L_{ac}} & -\frac{\sqrt{3}u_{cnc}}{6L_{ac}} \\ -\frac{u_{cpa}}{6L_{no}} & -\frac{u_{cpb}}{6L_{no}} & -\frac{u_{cpc}}{6L_{no}} & \frac{u_{cna}}{6L_{no}} & \frac{u_{cnb}}{6L_{no}} & \frac{u_{cnc}}{6L_{no}} \\ -\frac{2u_{cpa}}{3L_z} & \frac{u_{cpb}}{3L_z} & \frac{u_{cpc}}{3L_z} & -\frac{2u_{cna}}{3L_z} & \frac{u_{cnb}}{3L_z} & \frac{u_{cnc}}{3L_z} \\ 0 & -\frac{\sqrt{3}u_{cpb}}{3L_z} & \frac{\sqrt{3}u_{cpc}}{3L_z} & 0 & -\frac{\sqrt{3}u_{cnb}}{3L_z} & \frac{\sqrt{3}u_{cnc}}{3L_z} \\ -\frac{u_{cpa}}{3L_{dc}} & -\frac{u_{cpb}}{3L_{dc}} & -\frac{u_{cpc}}{3L_{dc}} & -\frac{u_{cna}}{3L_{dc}} & -\frac{u_{cnb}}{3L_{dc}} & -\frac{u_{cnc}}{3L_{dc}} \end{bmatrix} \quad (3.15)$$

Inserting (3.14) and (3.15) into (3.6) yields

$$\mathbf{u} = \begin{bmatrix} m_{ap} \\ m_{bp} \\ m_{cp} \\ m_{an} \\ m_{bn} \\ m_{cn} \end{bmatrix} = \begin{bmatrix} -\frac{L_{ac}}{u_{cpa}} & 0 & -\frac{L_{no}}{u_{cpa}} & -\frac{L_z}{2u_{cpa}} & 0 & -\frac{L_{dc}}{2u_{cpa}} \\ \frac{L_{ac}}{2u_{cpb}} & -\frac{\sqrt{3}L_{ac}}{2u_{cpb}} & -\frac{L_{no}}{u_{cpb}} & \frac{L_z}{4u_{cpb}} & -\frac{\sqrt{3}L_z}{4u_{cpb}} & -\frac{L_{dc}}{2u_{cpb}} \\ \frac{L_{ac}}{2u_{cpc}} & \frac{\sqrt{3}L_{ac}}{2u_{cpc}} & -\frac{L_{no}}{u_{cpc}} & \frac{L_z}{4u_{cpc}} & \frac{\sqrt{3}L_z}{4u_{cpc}} & -\frac{L_{dc}}{2u_{cpc}} \\ \frac{L_{ac}}{u_{cna}} & 0 & \frac{L_{no}}{u_{cna}} & -\frac{L_z}{2u_{cna}} & 0 & -\frac{L_{dc}}{2u_{cna}} \\ -\frac{L_{ac}}{2u_{cnb}} & \frac{\sqrt{3}L_{ac}}{2u_{cnb}} & \frac{L_{no}}{u_{cnb}} & \frac{L_z}{4u_{cnb}} & -\frac{\sqrt{3}L_z}{4u_{cnb}} & -\frac{L_{dc}}{2u_{cnb}} \\ -\frac{L_{ac}}{2u_{cnc}} & -\frac{\sqrt{3}L_{ac}}{2u_{cnc}} & \frac{L_{no}}{u_{cnc}} & \frac{L_z}{4u_{cnc}} & \frac{\sqrt{3}L_z}{4u_{cnc}} & -\frac{L_{dc}}{2u_{cnc}} \end{bmatrix} \cdot \begin{bmatrix} \gamma_1 \\ \gamma_2 \\ \gamma_3 \\ \gamma_4 \\ \gamma_5 \\ \gamma_6 \end{bmatrix} - \begin{bmatrix} -\frac{R_{ac}}{L_{ac}} i_{g\alpha} - \frac{1}{L_{ac}} U_{g\alpha} \\ -\frac{R_{ac}}{L_{ac}} i_{g\beta} - \frac{1}{L_{ac}} U_{g\beta} \\ -\frac{R_{no}}{L_{no}} i_{g0} - \frac{1}{L_{no}} U_{g0} \\ -\frac{R_z}{L_z} i_{z\alpha} \\ -\frac{R_z}{L_z} i_{z\beta} \\ -\frac{R_{dc}}{L_{dc}} i_{dc} + \frac{1}{L_{dc}} U_{dc} \end{bmatrix} \quad (3.16)$$

Finally, it is feasible to apply the IOFL law in the form of (3.6), such that the nonlinearities and phase relations are decoupled within the MMC current model. For this case, the resultant transformation is given as (3.16). Note that the available arm voltages are a common denominator and must be greater than 0 for the transformation to be valid. Physically, if no energy is available in the arms, there won't be enough usable voltage to drive the desired currents. After

applying (3.16) a simple independent linear relation is obtained between the new control inputs to choose and each output current, yield a new equivalent system,

$$\begin{bmatrix} \dot{y}_1 \\ \dot{y}_2 \\ \dot{y}_3 \\ \dot{y}_4 \\ \dot{y}_5 \\ \dot{y}_6 \end{bmatrix} = \begin{bmatrix} \dot{i}_{g\alpha} \\ \dot{i}_{g\beta} \\ \dot{i}_{g0} \\ \dot{i}_{z\alpha} \\ \dot{i}_{z\beta} \\ \dot{i}_{dc} \end{bmatrix} = \begin{bmatrix} \gamma_1 \\ \gamma_2 \\ \gamma_3 \\ \gamma_4 \\ \gamma_5 \\ \gamma_6 \end{bmatrix} \quad (3.17)$$

accomplishing the desired linear input-output relation. Similar to the SISO case, the corresponding block diagram is given in Figure 3.5.

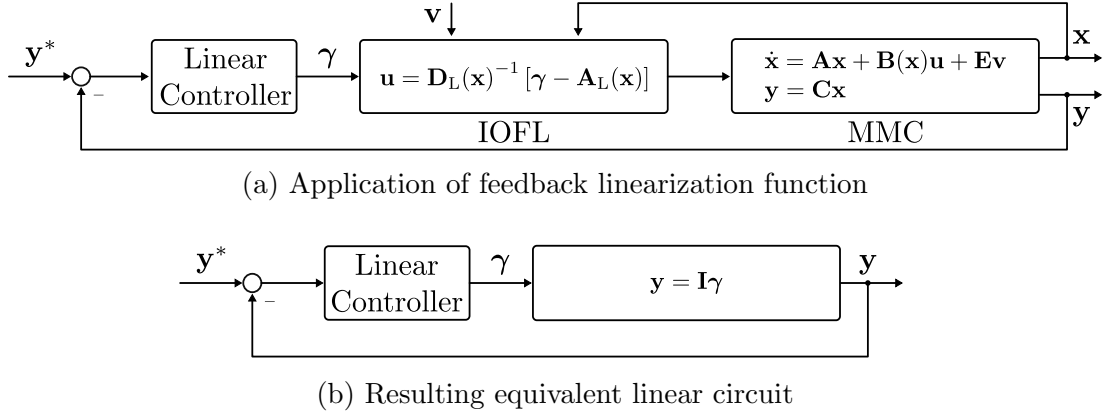


Figure 3.5: Block diagram of MIMO Input-Output Feedback Linearization applied to the MMC model

The new virtual inputs are chosen as the corrected error between desired references (\mathbf{y}^*) and measured outputs, as given in (3.18).

$$\gamma_m := G_{cm} (y_m^* - y_m), \quad \forall m \quad (3.18)$$

where G_{cm} denotes the function of the independent controller for the m -th output. The design of G_{cm} is discussed in a coming subsection. However first, the internal dynamics of the remaining states must be verified to validate the usage of the derived IOFL law.

3.2.2 Internal dynamics

Once the IOFL is derived, it is essential to confirm the stability of the internal dynamics. The nonlinear model of the MMC is $n = 12$ dimensional and its relative

degree $\rho = \sum \rho_i = 6$. Hence there are $n - \rho = 6$ unobserved states to investigate, which are the energy-related states (\mathbf{x}_w). To accomplish this, the influence of the output vector is disregarded. As the \mathbf{x}_w have no unforced component, an inconclusive result is obtained (3.19), in terms of pure stability analysis.

$$\begin{aligned} \mathbf{y} = \mathbf{0} &\implies \mathbf{x}_i = \mathbf{0} \\ \mathbf{x}_w = \frac{\mathbf{x}_i \cdot \mathbf{u}}{C_{\text{arm}}} &\implies \mathbf{x}_w = \mathbf{0} \end{aligned} \quad (3.19)$$

Alternatively, the resultant IOFL law (3.16) is applied to the original system (2.57) as state feedback yielding

$$\dot{\mathbf{x}} = \mathbf{A}\mathbf{x} + \mathbf{B}(\mathbf{x}) (\mathbf{D}_L(\mathbf{x})^{-1} [\boldsymbol{\gamma} - \mathbf{A}_L(\mathbf{x})]) + \mathbf{E}\mathbf{v} \quad (3.20)$$

Isolating \mathbf{x}_w in (3.20) results in

$$\dot{\mathbf{x}}_w = \mathbf{B}(\mathbf{x}) (\mathbf{D}_L(\mathbf{x})^{-1} [\boldsymbol{\gamma} - \mathbf{A}_L(\mathbf{x})]) \quad (3.21)$$

Assuming the deployed controller tracks well the current references ($\dot{\mathbf{y}} = \boldsymbol{\gamma} = \mathbf{0}$), the internal dynamics are expressed by (3.22).

$$\dot{\mathbf{x}}_w = -\mathbf{B}(\mathbf{x}) \mathbf{D}_L(\mathbf{x})^{-1} \mathbf{A}_L(\mathbf{x}) \quad (3.22)$$

A well-balanced open star point at the AC-grid side is assumed, and circulating current references are set to zero. Else, a more complete derivation is given in Appendix B. Furthermore, the following conditions yield,

$$\begin{aligned} U_{g\alpha} &= \hat{U}_g \cos(\omega t) \\ U_{g\beta} &= \hat{U}_g \sin(\omega t) \\ U_{g0} &= 0 \\ i_{g0} &= 0 \\ i_{z\alpha} &= 0 \\ i_{z\beta} &= 0 \end{aligned} \quad (3.23)$$

For simplicity, only the first energy-related state is extended for this analysis. However, the following methodology can be similarly applied to the rest of the vector \mathbf{x}_w .

$$\begin{aligned} \dot{u}_{\text{cpa}} &= \frac{1}{C_{\text{arm}} u_{\text{cpa}}} \left(\frac{U_{\text{dc}} i_{\text{dc}}}{2} - \frac{R_{\text{ac}} i_{g\alpha}^2}{2} - \frac{R_{\text{dc}} i_{\text{dc}}^2}{2} - \frac{U_{g\alpha} i_{g\alpha}}{2} \right. \\ &\quad \left. + \frac{U_{\text{dc}} i_{g\alpha}}{4} - U_{g\alpha} i_{d0} - R_{\text{ac}} i_{g\alpha} i_{\text{dc}} - \frac{R_{\text{dc}} i_{g\alpha} i_{\text{dc}}}{4} \right) = \frac{P_{\text{pa}}}{C_{\text{arm}} u_{\text{cpa}}} \end{aligned} \quad (3.24)$$

Assuming an operation point $u_{\text{cpa}} \neq 0$ and taking into consideration the trigonometric relations (A.20) and (A.21), it is clear that the instantaneous power flowing in the arm is only responsible for the change of the available voltage in its own arm capacitors. In (3.25) the power flow in one arm is further expressed in DC- and AC-terms.

$$\begin{aligned}
 P_{\text{ap}} &= \bar{P}_{\text{ap}} + \tilde{P}_{\text{ap}} \\
 P_{\text{ap}} &= \underbrace{\frac{P_{\text{dc}}}{6} - P_{\text{loss}} - \frac{P_{\text{ac}}}{6}}_{P_{\text{ap-DC}}} + \underbrace{P_{50} + P_{100} + P_{\text{hof}}}_{P_{\text{ap-AC}}} \quad (3.25)
 \end{aligned}$$

As long as the input power compensates for the output power transferred to the AC grid and the generated conduction losses, i.e. power balance, no DC-terms will appear in (3.24), preventing a change in average voltage, which is coherent with (3.1). The remaining oscillating power, mainly at 50 Hz and 100 Hz, leads to periodic oscillations around the average voltage, as exemplified in Figure 2.14. These oscillations are limited in amplitude, keeping the internal dynamics of the system stable when power is balanced. In other words, since P_{arm} is bounded in amplitude and results in a bounded voltage oscillation, the system can be assumed as Bounded Input Bounded Output (BIBO) stable [154]. In summary, the MMC internal dynamics are BIBO-stable under power-balanced conditions. Additionally from (3.25) a byproduct of this analysis are the conduction losses in each arm for steady-state operation.

3.2.3 Linear controller

In this subsection a linear controller for the solely purpose of reference tracking with desired transient performance is designed, according to Table 2.3. Assuming the currents in α and β should perform equally, three independent controllers are to be designed and their resulting close loops are represented in the figure below.

It is desired that every closed-loop behaves as a first order system. This provides simplicity, no overshoot during transient responses and a single tuning parameter for each loop [155].

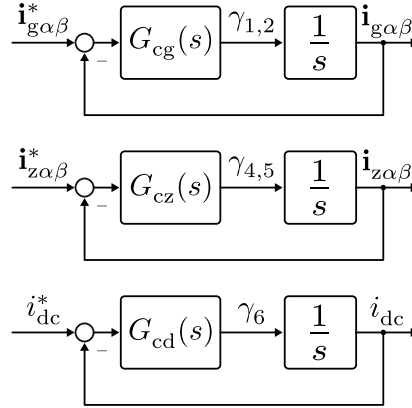


Figure 3.6: Current reference tracking independent closed-loops

DC-grid current

Starting with the DC current loop, its closed-loop,

$$G_{id}(s) = \frac{\frac{G_{cd}(s)}{s}}{1 + \frac{G_{cd}(s)}{s}} \quad (3.26)$$

is to be matched with the desired closed loop transfer function

$$G_{id}^*(s) = \frac{\omega_{dc}}{s + \omega_{dc}}, \quad (3.27)$$

Solving for $G_{cd}(s)$, the controller yields,

$$G_{cd}(s) = \omega_{dc} = 2\pi f_{dc} = \frac{2\pi}{t_{dc}} \quad (3.28)$$

which results in a simple proportional term. Simultaneously, this is the only tuning parameter. Hence, t_{dc} denotes the desired settling time of the current in the step response. For instance, by choosing $f_{dc} = 50$ Hz, the desired current reaches its steady state after 20 ms. The step responses for arbitrarily different transient responses are shown in Figure 3.7.

AC-grid current

For the AC-grid currents it would be desirable to apply the same procedure as outlined in the previous section. However, the Internal Model Principle (IMP) states that to achieve precise tracking of a particular class of signals, a control system must embed within its structure a representation of the dynamics that characterize those signals. In the case of sinusoidal signals, this implies that the

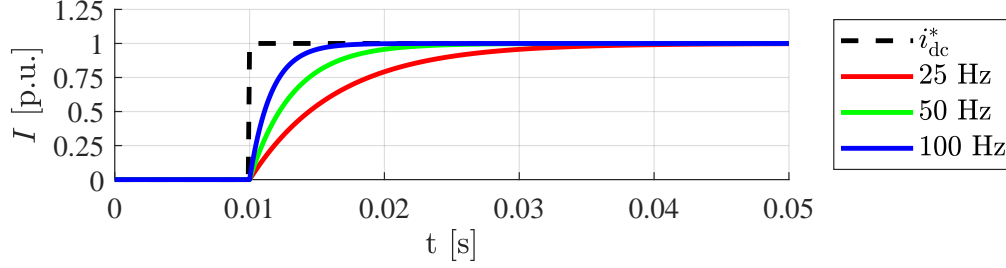


Figure 3.7: Resulting step response with different desired transient times

controller must incorporate the inherent dynamics responsible for producing the sinusoidal behavior [156]. Although resonant controllers are a common choice, these require additional terms to obtain the desired transient performance as in the previous subsection [155]. Furthermore, it is not straightforward for digital implementation [157]. Alternatively, a change of reference frame is a widely adopted solution [158].

Using the coordinate transformation (A.5), the current sub-vector is mapped from the stationary $\alpha\beta$ frame to the rotating dq frame as:

$$\mathbf{i}_{gdq} = \mathbf{T}_{R,1+} \mathbf{i}_{g\alpha\beta}. \quad (3.29)$$

Differentiating and using the product rule, it yields:

$$\dot{\mathbf{i}}_{gdq} = \dot{\mathbf{T}}_{R,1+} \mathbf{i}_{g\alpha\beta} + \mathbf{T}_{R,1+} \dot{\mathbf{i}}_{g\alpha\beta}. \quad (3.30)$$

Substituting the relation of (3.17) in (3.30)

$$\dot{\mathbf{i}}_{gdq} = \dot{\mathbf{T}}_{R,1+} \mathbf{i}_{g\alpha\beta} + \mathbf{T}_{R,1+} \boldsymbol{\gamma}_{1,2}, \quad (3.31)$$

and rewritten as

$$\dot{\mathbf{i}}_{gdq} = \dot{\mathbf{T}}_{R,1+} \mathbf{T}_{R,1-} \mathbf{i}_{gdq} + \mathbf{T}_{R,1+} \boldsymbol{\gamma}_{1,2}. \quad (3.32)$$

Computing the product,

$$\dot{\mathbf{T}}_{R,1+} \mathbf{T}_{R,1-} = \dot{\theta} \begin{bmatrix} -\sin(\theta) & \cos(\theta) \\ -\cos(\theta) & -\sin(\theta) \end{bmatrix} \begin{bmatrix} \cos(\theta) & -\sin(\theta) \\ \sin(\theta) & \cos(\theta) \end{bmatrix} \quad (3.33)$$

which simplified yields,

$$\dot{\mathbf{T}}_{R,1+} \mathbf{T}_{R,1-} = \omega \begin{bmatrix} 0 & -1 \\ 1 & 0 \end{bmatrix}, \quad (3.34)$$

where $\omega = \dot{\theta}$ is the angular speed of the rotating frame, commonly estimated using Phase-Locked-Loop (PLL) algorithms. A comprehensive review of existing

techniques can be found in [159]. Substituting (3.34) into (3.32) results,

$$\dot{\mathbf{i}}_{\text{gdq}} = \omega \begin{bmatrix} 0 & -1 \\ 1 & 0 \end{bmatrix} \mathbf{i}_{\text{gdq}} + \mathbf{T}_{\text{R},1} \boldsymbol{\gamma}_{1,2}. \quad (3.35)$$

Let $\boldsymbol{\gamma}_{\text{gdq}} = \mathbf{T}_{\text{R},1} \boldsymbol{\gamma}_{1,2}$, the control inputs transformed into the dq frame. The final dynamics become:

$$\dot{\mathbf{i}}_{\text{gdq}} = \omega \begin{bmatrix} 0 & -1 \\ 1 & 0 \end{bmatrix} \mathbf{i}_{\text{gdq}} + \mathbf{I} \boldsymbol{\gamma}_{\text{gdq}}. \quad (3.36)$$

After this change of coordinates, the original sinusoidal reference signals are now DC in nature. Therefore a controller similar to the one designed in the previous subsection can be designed. The new system (3.36) is in the state-space form and in order for closed-loop system to behave as a first-order system, a state feedback

$$\boldsymbol{\gamma}_{\text{gdq}} = -\mathbf{K}_{\text{sg}} \mathbf{i}_{\text{gdq}}, \quad (3.37)$$

should applied such,

$$\mathbf{A}_{\text{cl,gdq}} = (\mathbf{A}_{\text{gdq}} - \mathbf{B}_{\text{gdq}} \mathbf{K}_{\text{sg}}) = \mathbf{I} \omega_{\text{ac}}, \quad (3.38)$$

where ω_{ac} is the tuning parameter for this loop. Solving for \mathbf{K}_{sg} the state feedback matrix gains are obtained:

$$\mathbf{K}_{\text{sf}} = \begin{bmatrix} \omega_{\text{ac}} & \omega \\ -\omega & \omega_{\text{ac}} \end{bmatrix} \quad (3.39)$$

The chosen state feedback modifies the system dynamics to place poles at desired locations. However, it does not guarantee that the output follows the reference $\mathbf{i}_{\text{gdq}}^*$. Using the feedforward term

$$\mathbf{K}_{\text{fg}} = -(\mathbf{C}_{\text{gdq}} (\mathbf{A}_{\text{gdq}} - \mathbf{B}_{\text{gdq}} \mathbf{K}_{\text{fg}})^{-1} \mathbf{B}_{\text{gdq}})^{-1} = \begin{bmatrix} \omega_{\text{ac}} & 0 \\ 0 & \omega_{\text{ac}} \end{bmatrix}, \quad (3.40)$$

ensures accurate reference tracking without steady-state error [106]. Notice, the decoupling terms in \mathbf{K}_{sg} are only dependent on the measured angular frequency and not on the plant parameters, as typically found in most controllers working in the rotating dq frame. This makes the reference tracking controller less susceptible to plant uncertainties [160]. A block of the overall resulting structure is given below.

Considering the chosen controller and a desired transient response $f_{\text{ac}} = 50$ Hz, the obtained step responses are illustrated in both rotating and stationary frames in Figure 3.9, match the same performance as in Figure 3.7.

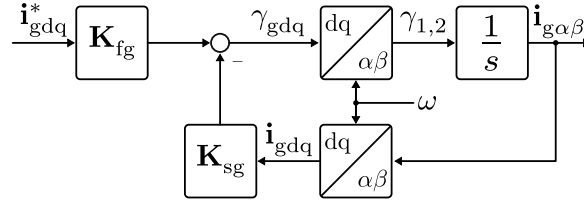
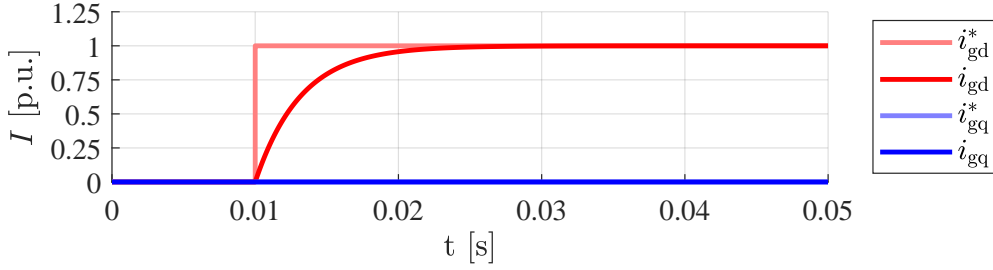
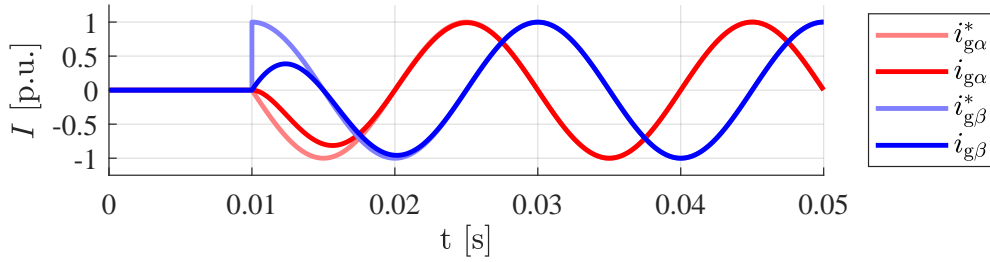


Figure 3.8: AC-grid current controller block diagram



(a) Rotating reference frame



(b) Stationary reference frame

Figure 3.9: Resulting step response for the AC-grid controller

Circulating current

The control of the circulating current is divided in two parts. The current responsible for energy exchange in between phases has a DC nature and therefore is designed according to (3.28). For the correct vertical energy exchange, only pure AC currents are allowed. Therefore, the structure in Figure 3.8 is considered. Afterwards, the output of both is combined in a single output for each phase $\gamma_{4,5}$. As reviewed in [161], the parallel combination of both DC and AC components implies a challenging control design for a desired performance under reference tracking. However, most important is to stabilize the circulating current through correct pole placement, i.e. the tuning parameter ω_z . The energy controller is responsible for defining the current reference to be followed, as it be explained in the next sections. Nevertheless, during operation the circulating current is not expected to be non-zero at steady state.

3.3 Extended disturbance observer

The feedback control law and controller design, based on the feedback-linearized model, were derived under the assumption that the system parameters were known. However, in practice, deviations from the nominal parameter values—referred to as parameter uncertainties—are inevitable. To address this, a Disturbance Observer (DOB) [162] is employed to enhance the robustness of the IOFL. By estimating and compensating for external disturbances and modeling uncertainties, the DOB ensures that the control system remains robust and effective, even in the presence of these challenges. Ideally, given the inherently nonlinear nature of the original system, a Nonlinear Disturbance Observer (NDOB) could have been implemented. However, the research conducted in [163] resulted in a state-dependent solution that proved to be highly complex and non-intuitive to design. Alternatively, an EDOB is considered, which utilizes the feedback-linearized model obtained via IOFL, simplifying the design procedure.

Since the target outputs of the IOFL are the current states, the disturbance observer is formulated on the corresponding output dynamics. To account for external disturbances and internal disturbances caused by model uncertainties [164], the MIMO system in (2.57) is augmented by a lumped disturbance term

$$\dot{\mathbf{x}} = \mathbf{A}\mathbf{x} + \mathbf{B}(\mathbf{x})\mathbf{u} + \mathbf{E}\mathbf{v} + \mathbf{B}_d\mathbf{d}. \quad (3.41)$$

With the output definition

$$\mathbf{y} = \mathbf{x}_i = \mathbf{C}_i\mathbf{x}, \quad (3.42)$$

the disturbed output dynamics are obtained as

$$\dot{\mathbf{x}}_i = \mathbf{C}_i\mathbf{A}\mathbf{x} + \mathbf{C}_i\mathbf{B}(\mathbf{x})\mathbf{u} + \mathbf{C}_i\mathbf{E}\mathbf{v} + \mathbf{C}_i\mathbf{B}_d\mathbf{d}. \quad (3.43)$$

Substituting the control law from (3.16), the nominal dynamics are transformed by IOFL into

$$\dot{\mathbf{x}}_i = \boldsymbol{\gamma} + \mathbf{d}_\ell, \quad (3.44)$$

where

$$\mathbf{d}_\ell := \mathbf{C}_i\mathbf{B}_d\mathbf{d} = \mathbf{B}_d\mathbf{d}. \quad (3.45)$$

Assuming current-wise decoupling, the disturbance contribution in each state is represented by an equivalent lumped disturbance term [165], such that its dynamics become

$$\dot{x}_{i,m} = \gamma_m + \mathbf{B}_{dm}\mathbf{d}_{\ell,m}, \quad m = 1, 2, \dots, 6. \quad (3.46)$$

For estimating the lumped disturbance in each channel, an Extended State Observer (ESO) is designed. Firstly, the state space model is augmented to include the lumped disturbances $\boldsymbol{\rho}_m = \mathbf{d}_{\ell,m}$, yielding

$$\begin{bmatrix} \dot{x}_{i,m} \\ \dot{\boldsymbol{\rho}}_m \end{bmatrix} = \begin{bmatrix} \mathbf{A}_m & \mathbf{B}_{dm} \\ \mathbf{0} & \mathbf{A}_{\rho m} \end{bmatrix} \begin{bmatrix} x_{i,m} \\ \boldsymbol{\rho}_m \end{bmatrix} + \begin{bmatrix} \mathbf{B}_m \\ \mathbf{0} \end{bmatrix} \gamma_m, \quad y_m = \begin{bmatrix} C_m & \mathbf{0} \end{bmatrix} \begin{bmatrix} x_{i,m} \\ \boldsymbol{\rho}_m \end{bmatrix} \quad (3.47)$$

where $\mathbf{A}_{\rho m}$ is a model of the disturbances and \mathbf{B}_{dm} describe how the disturbance vector influences the current state. For describing DC- and AC-disturbances, the disturbance state $\boldsymbol{\rho}_m$ is further expanded by states including constant disturbances $\bar{\rho}_m$ and harmonic disturbances, where ρ_{m,ω_g} corresponds to disturbances at the fundamental grid frequency ω_g , and $\rho_{m,2\omega_g}$ captures second-order harmonic disturbances. Therefore, an oscillator based model is utilized describing the constant and harmonic disturbances [161]. In relation to the IOFL, the resulting independent plant for each current provides a major advantage with the original solution, as the design of the ESO can be done independently for each current state.

$$\mathbf{A}_{\rho m} = \begin{bmatrix} 0 & 0 & 0 & 0 & 0 \\ 0 & 0 & 0 & 1 & 0 \\ 0 & 0 & 0 & 0 & 1 \\ 0 & -\omega_g^2 & 0 & 0 & 0 \\ 0 & 0 & -4\omega_g^2 & 0 & 0 \end{bmatrix} \quad (3.48)$$

The extended disturbance state is given by

$$\boldsymbol{\rho}_m = \begin{bmatrix} \bar{\rho}_m \\ \rho_{m,\omega_g} \\ \rho_{m,2\omega_g} \\ \dot{\rho}_{m,\omega_g} \\ \dot{\rho}_{m,2\omega_g} \end{bmatrix} \quad (3.49)$$

and the state space model in (3.47) with (3.48) and (3.49) results in

$$\begin{bmatrix} \dot{x}_{i,m} \\ \dot{\boldsymbol{\rho}}_m \end{bmatrix} = \begin{bmatrix} 0 & 1 & 1 & 1 & 0 & 0 \\ 0 & 0 & 0 & 0 & 0 & 0 \\ 0 & 0 & 0 & 0 & 1 & 0 \\ 0 & 0 & 0 & 0 & 0 & 1 \\ 0 & 0 & -\omega_g^2 & 0 & 0 & 0 \\ 0 & 0 & 0 & -4\omega_g^2 & 0 & 0 \end{bmatrix} \begin{bmatrix} x_{i,m} \\ \boldsymbol{\rho}_m \end{bmatrix} + \begin{bmatrix} 1 \\ \mathbf{0}_{(5 \times 1)} \end{bmatrix} \gamma_m \quad (3.50)$$

$$y_m = \begin{bmatrix} 1 & \mathbf{0}_{(1 \times 5)} \end{bmatrix} \begin{bmatrix} x_{i,m} \\ \boldsymbol{\rho}_m \end{bmatrix} \quad (3.51)$$

Next, the disturbance observer for estimating the states is defined as

$$\begin{aligned}
\begin{bmatrix} \dot{\hat{x}}_{i,m} \\ \dot{\hat{\rho}}_m \end{bmatrix} &= \begin{bmatrix} 0 & 1 & 1 & 1 & 0 & 0 \\ 0 & 0 & 0 & 0 & 0 & 0 \\ 0 & 0 & 0 & 0 & 1 & 0 \\ 0 & 0 & 0 & 0 & 0 & 1 \\ 0 & 0 & -\omega_g^2 & 0 & 0 & 0 \\ 0 & 0 & 0 & -4\omega_g^2 & 0 & 0 \end{bmatrix} \begin{bmatrix} \hat{x}_{i,m} \\ \hat{\rho}_m \end{bmatrix} + \begin{bmatrix} 1 \\ \mathbf{0}_{(5 \times 1)} \end{bmatrix} \gamma_m \\
&+ \mathbf{L}_m (\hat{y}_m - y_m) \\
&= \mathbf{A}_m \begin{bmatrix} \hat{x}_{i,m} \\ \hat{\rho}_m \end{bmatrix} + \mathbf{B}_m \gamma_m + \mathbf{L}_m (\hat{y}_m - y_m)
\end{aligned} \tag{3.52}$$

where $\mathbf{L}_m = [L_1 \ \mathbf{L}_2]^T = [L_1 \ L_{21} \ L_{22} \ L_{23} \ L_{24} \ L_{25}]^T$ is the observer gain matrix, $\hat{y}_m = [1 \ \mathbf{0}_{(1 \times 5)}] [\hat{x}_{i,m} \ \hat{\rho}_m]^T$ are the estimated outputs and $y_m = [1 \ \mathbf{0}_{(1 \times 5)}] [x_{i,m} \ \rho_m]^T$ are the system outputs. Defining the estimation error as

$$\begin{bmatrix} e_{x_{i,m}} \\ \mathbf{e}_{\rho_m} \end{bmatrix} = \begin{bmatrix} x_{i,m} - \hat{x}_{i,m} \\ \rho_m - \hat{\rho}_m \end{bmatrix}, \tag{3.53}$$

the dynamics of the estimation error are given by

$$\begin{aligned}
\begin{bmatrix} \dot{e}_{x_{i,m}} \\ \dot{\mathbf{e}}_{\rho_m} \end{bmatrix} &= \begin{bmatrix} 0 & 1 & 1 & 1 & 0 & 0 \\ 0 & 0 & 0 & 0 & 0 & 0 \\ 0 & 0 & 0 & 0 & 1 & 0 \\ 0 & 0 & 0 & 0 & 0 & 1 \\ 0 & 0 & -\omega_g^2 & 0 & 0 & 0 \\ 0 & 0 & 0 & -4\omega_g^2 & 0 & 0 \end{bmatrix} \begin{bmatrix} e_{x_{i,m}} \\ \mathbf{e}_{\rho_m} \end{bmatrix} + \begin{bmatrix} L_1 \\ \mathbf{L}_2 \end{bmatrix} [1 \ \mathbf{0}_{(1 \times 5)}] \begin{bmatrix} e_{x_{i,m}} \\ \mathbf{e}_{\rho_m} \end{bmatrix} \\
&= \begin{bmatrix} -L_1 & 1 & 1 & 1 & 0 & 0 \\ -L_{21} & 0 & 0 & 0 & 0 & 0 \\ -L_{22} & 0 & 0 & 0 & 1 & 0 \\ -L_{23} & 0 & 0 & 0 & 0 & 1 \\ -L_{24} & 0 & -\omega_g^2 & 0 & 0 & 0 \\ -L_{25} & 0 & 0 & -4\omega_g^2 & 0 & 0 \end{bmatrix} \begin{bmatrix} e_{x_{i,m}} \\ \mathbf{e}_{\rho_m} \end{bmatrix} = \mathbf{A}_{em} \begin{bmatrix} e_{x_{i,m}} \\ \mathbf{e}_{\rho_m} \end{bmatrix}
\end{aligned} \tag{3.54}$$

Essentially, from (3.54) the observer gain matrix \mathbf{L}_m is designed such that the matrix \mathbf{A}_{em} is Hurwitz, i.e. the estimation error is asymptotically stable and converges to zero. In addition, for the DOB to be effective, its dynamics must be faster than the closed-loop system induced by the feedback-linearization law. This ensures rapid convergence of the disturbance estimates and accurate com-

pensation, while preserving the feedback-linearized plant dynamics. The total disturbance estimation can be extracted from the estimated states by

$$\hat{d}_m = [0 \ 1 \ 1 \ 1 \ 0 \ 0] \begin{bmatrix} \hat{x}_{i,m} \\ \hat{\rho}_m \end{bmatrix} = \mathbf{L}_{\hat{d}} \begin{bmatrix} \hat{x}_{i,m} \\ \hat{\rho}_m \end{bmatrix} \quad (3.55)$$

and to compensate the disturbance, the input γ_m is changed to

$$\gamma_m = \gamma_m^* - \hat{d}_m \quad (3.56)$$

where γ_m^* is the output of the feedback controller. The block diagram of the EDOB is depicted in Figure 3.10, where $\hat{\mathbf{x}}_m = \begin{bmatrix} \hat{x}_{i,m} \\ \hat{\rho}_m \end{bmatrix}$.

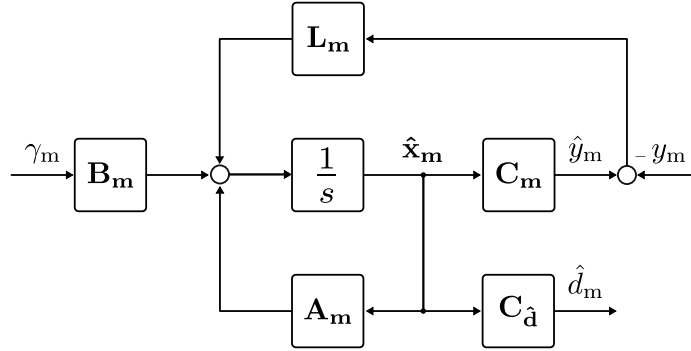


Figure 3.10: Block diagram of Extended Disturbance Observer (EDOB)

For each current state, an independent EDOB is deployed. Hence the resulting close-loop block diagram for each state is represented in Figure 3.11.

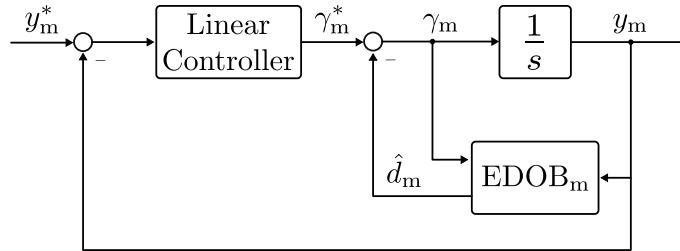


Figure 3.11: Block diagram of closed-loop system

3.4 Outer controller – Loop Shaping

The previous section established a desired linear behavior for the current dynamics. However, these constitute a means to achieve a more important outcome, i.e. desired power transfer between grids and energy storage levels in the MMC. Hence, this section is dedicated to the outer-loop responsible of tracking the power, energy references and achieve the proposed power decoupling capability. This objective is highlighted in Figure 3.12.

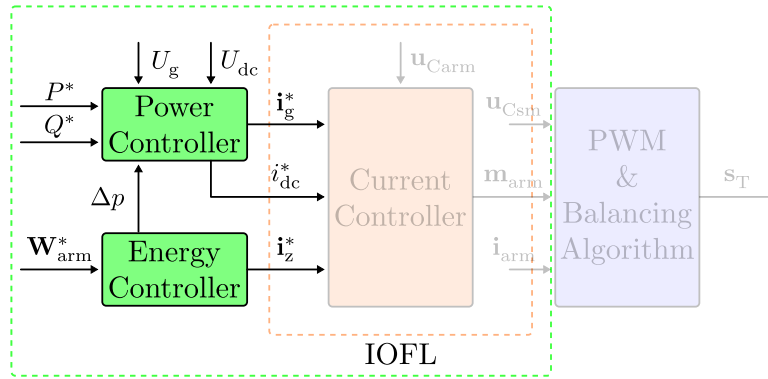


Figure 3.12: Research topic of this section

3.4.1 Current reference generation

For an IPC, the desired references are given as power and not currents. For the DC-grid current reference,

$$i_{dc}^* = \frac{P_{dc}^*}{U_{dc}} \quad (3.57)$$

is used. From the instantaneous power theory [166], the current references are related to the desired active and reactive power transfer, yielding

$$\begin{bmatrix} i_{g\alpha}^* \\ i_{g\beta}^* \end{bmatrix} = \frac{2}{3} \cdot \frac{1}{U_{g\alpha}^2 + U_{g\beta}^2} \begin{bmatrix} U_{g\alpha} & U_{g\beta} \\ U_{g\beta} & -U_{g\alpha} \end{bmatrix} \begin{bmatrix} P_{ac}^* \\ Q^* \end{bmatrix}. \quad (3.58)$$

Regarding the circulating current references, it is necessary to isolate the terms that generate non-periodic power flow from the equations derived in Appendix B. Under nominal conditions, assuming negligible power losses and reactive power terms, only the active power components remain, which are responsible for altering the average energy stored in the arm's capacitors. Hence,

$$P_{\Sigma\alpha} = U_{dc} i_{z\alpha} \quad (3.59)$$

$$P_{\Sigma\beta} = U_{\text{dc}} i_{z\beta} \quad (3.60)$$

$$P_{\Sigma 0} = \frac{U_{\text{dc}} i_{\text{dc}}}{3} - \frac{U_{g\alpha} i_{g\alpha}}{2} - \frac{U_{g\beta} i_{g\beta}}{2} \quad (3.61)$$

$$P_{\Delta\alpha} = U_{g\beta} i_{z\beta} - U_{g\alpha} i_{z\alpha} \quad (3.62)$$

$$P_{\Delta\beta} = U_{g\beta} i_{z\alpha} + U_{g\alpha} i_{z\beta} \quad (3.63)$$

$$P_{\Delta 0} = -U_{g\beta} i_{z\beta} - U_{g\alpha} i_{z\alpha} \quad (3.64)$$

The energy states are now considered in $\alpha\beta 0$ frame and as Σ, Δ terms, which establishes less meshed relations and facilitates the reference generation. Equation (3.61) mirrors the initial relation established in (3.2). Due to reference frame transformation consider $P_{\text{MMC}} = 3 \cdot P_{\Sigma 0}$. Furthermore, there is only active power in $P_{\Sigma\alpha}$ and $P_{\Sigma\beta}$, iff circulating currents have a DC component. Therefore, the DC reference for the Z currents is generated accordingly,

$$\begin{bmatrix} i_{z\alpha, \text{DC}}^* \\ i_{z\beta, \text{DC}}^* \end{bmatrix} = \frac{1}{U_{\text{dc}}} \begin{bmatrix} 1 & 0 \\ 0 & 1 \end{bmatrix} \begin{bmatrix} P_{\Sigma\alpha}^* \\ P_{\Sigma\beta}^* \end{bmatrix} \quad (3.65)$$

For the Δ components, other approach is necessary. Assume both positive and negative components in the circulating currents. A DC component would not be tolerated, as it would lead to an offset on the AC grid currents. Using the rotation transformations (A.5) and (A.6) the circulating currents are expressed in the rotating reference frame, yielding

$$i_{z\alpha, \omega} = i_{z\alpha, \omega+} + i_{z\alpha, \omega-} = \cos(\theta) (i_{z\text{d}+} + i_{z\text{d}-}) - \sin(\theta) (i_{z\text{q}+} - i_{z\text{q}-}) \quad (3.66)$$

$$i_{z\beta, \omega} = i_{z\beta, \omega+} + i_{z\beta, \omega-} = \sin(\theta) (i_{z\text{d}+} - i_{z\text{d}-}) + \cos(\theta) (i_{z\text{q}+} + i_{z\text{q}-}) \quad (3.67)$$

Considering the same rotating frame for the grid voltages operating in a well balanced way ($q = 0$), and replacing them in the equations above, the active power flow equations are rewritten in terms of positive and negative components.

$$P_{\Delta\alpha} = U_{g\beta} i_{z\beta} - U_{g\alpha} i_{z\alpha} = -U_{\text{gd}+} i_{z\text{d}-} \quad (3.68)$$

$$P_{\Delta\beta} = U_{g\beta} i_{z\alpha} + U_{g\alpha} i_{z\beta} = U_{\text{gd}+} i_{z\text{q}-} \quad (3.69)$$

$$P_{\Delta 0} = -U_{g\beta} i_{z\beta} - U_{g\alpha} i_{z\alpha} = -U_{\text{gd}+} i_{z\text{d}+} \quad (3.70)$$

The circulating currents should flow only within the MMC. However (3.70) violates this condition. As originally proposed in methods 1 [167] and 2 [168], the

Table 3.1: Proportional gain for vertical current generation [103]

Method	K_{zp}	K_{zn}
1	$\frac{1}{\sqrt{3}}$	$\frac{1}{\sqrt{2}}$
2	$\frac{2}{\sqrt{6}}$	1

zero component is embedded in the α and β components to solve the problem. Accordingly, the current references are given in (3.71). The proportional terms K_{zp} and K_{zn} , provided in Table 3.1 result from an harmonization of the original techniques, investigated in [103]. In summary, method 1 shapes the current references to ensure that the balancing action occurs specifically within the phase that requires correction. In contrast, method 2 distributes the generated balancing current evenly across all phases, regardless of where the imbalance originates. The choice between these methods presents a trade-off in terms of power losses: The first method typically results in higher current amplitudes in a single phase, potentially leading to lower switching losses but higher conduction losses in all six arms. Opposite, the second method, with its more evenly distributed balancing current, generates lower amplitude per phase, which may reduce conduction losses but increase switching losses. Further investigation into this topic would be beneficial. From a control perspective, both methods lead to very similar results.

$$\begin{bmatrix} i_{z\alpha,AC}^* \\ i_{z,\beta AC}^* \end{bmatrix} = \frac{1}{\hat{U}_g} \begin{bmatrix} -K_{zn} \cos(\omega t) & K_{zn} \sin(\omega t) & -K_{zp} \cos(\omega t) \\ K_{zn} \sin(\omega t) & K_{zn} \cos(\omega t) & -K_{zp} \sin(\omega t) \end{bmatrix} \begin{bmatrix} P_{\Delta\alpha}^* \\ P_{\Delta\beta}^* \\ P_{\Delta 0}^* \end{bmatrix} \quad (3.71)$$

By inserting the new references in the vertical power flow equations above derived, leads to a decoupled loop, where each average power component can be controlled independently.

3.4.2 Power controller

In normal conditions, an extra power controller that generates the output current references is unnecessary. The setup in Figure 3.11 is sufficient, where the EDOB compensates for parameter uncertainties and/or grid voltage changes. In this circumstances, the closed-loop for power reference tracking is simply represented by the current transfer function in (3.72). Therefore, the design is as described

in 2.3.1, leading to a first-order system behavior.

$$G_{ig}(s) = \frac{i_g(s)}{i_g^*(s)} = \frac{\omega_{ac}}{s + \omega_{ac}} \quad (3.72)$$

However, in a first-order response, the maximum slope occurs at the initial stage, whereas in a second-order response, the steepest slope appears later in the transient process. Hence, the last may be preferred. Adding an integral term and following the same principle as in (3.26), the new closed-loop transfer yields

$$G_{pd}(s) = \frac{P_{ac}(s)}{P_{ac}^*(s)} = \frac{K_i \cdot \omega_{ac}}{s^2 + \omega_{ac}s + K_i \cdot \omega_{ac}} \implies \frac{\omega_{pd}^2}{s^2 + 2\zeta_{pd}\omega_{pd}s + \omega_{pd}^2}. \quad (3.73)$$

For the proposed application, it is still desirable to avoid an underdamped response to a reference change, i.e. $\zeta_{pd} \geq 1$ to obtain a smooth transition at the desired transient time. Matching the coefficients in (3.73), the relations,

$$\begin{aligned} \omega_{ac} &= \omega_{pd} \cdot 2\zeta_{pd} \\ K_i &= \frac{\omega_{ac}}{4\zeta_{pd}^2} \end{aligned}$$

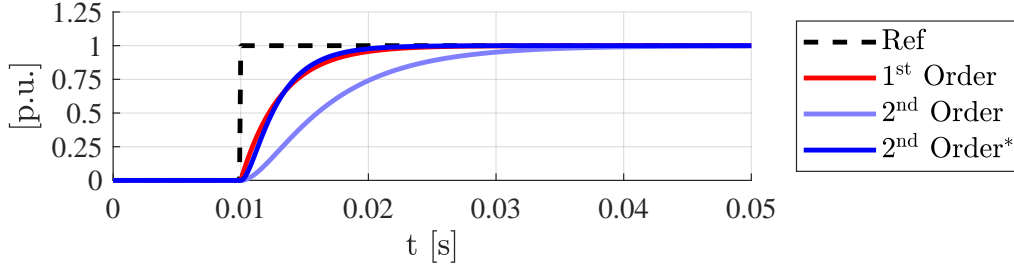
are obtained. Now ζ_{pd} and ω_{pd} are the tuning variables. Increasing the damping coefficient of the desired closed-loop system increases its phase margin, hence its robustness. However, the system natural frequency ω_{pd} must be adjusted accordingly to maintain the desired transient time $t_{pd}^* = 2\pi/\omega_{pd}^*$ (as in (3.28)). This relation is given by (3.74) [169].

$$\omega_{pd} = \frac{1}{\sqrt{\sqrt{4\zeta_{pd}^4 + 1} - 2\zeta_{pd}^2}} \cdot \omega_{pd}^* \quad (3.74)$$

This is also illustrated in Figure 3.13, where a step response comparison between (3.72) and (3.73) is shown. After using (3.74), the second-order system, denoted by * in the legend, exhibits the desired transient time. In practice, this is limited by the resulting ω_{ac} .

3.4.3 Energy controller

The energy controller is the key layer for achieving power decoupling. Its primary function is to maintain and evenly distribute the desired energy level across all six arms while ensuring compliance with the constraint defined in (2.11). Only its average component is aimed to be controlled, while the amplitude of the oscillating do not contribute for the desired feature. Most commonly, depending

Figure 3.13: Step responses of 1st and 2nd order systems

on the instantaneous AC grid angle, a sudden power shift can cause an imbalance in the MMC energy distribution, leading to uneven discharge among the arms, with one being affected more than the others. The energy controller is responsible for regulating the energy back to its original levels. This situation is illustrated in Figure 3.14.

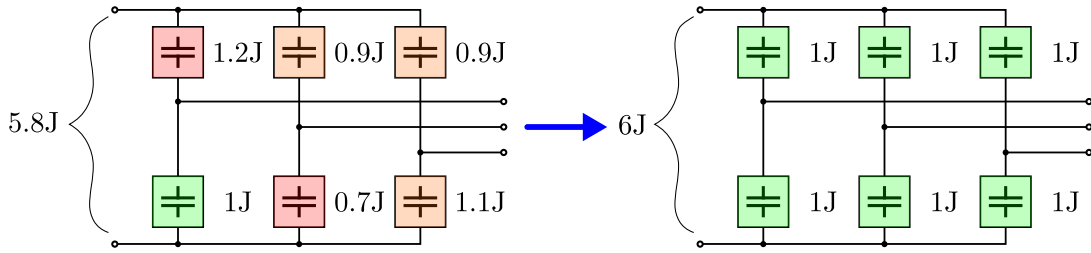


Figure 3.14: Main objective of the energy controller

As demonstrated in Appendix B, a change of coordinates is beneficial to control the arm storage energies. Considering $\Sigma\Delta$ in the $\alpha\beta$ frame, yielding

$$\begin{bmatrix} W_{\Sigma\alpha} \\ W_{\Sigma\beta} \\ W_{\Sigma 0} \end{bmatrix} = \mathbf{T}_{C0} \cdot \begin{bmatrix} W_{pa} + W_{na} \\ W_{pb} + W_{nb} \\ W_{pc} + W_{nc} \end{bmatrix} \quad (3.75)$$

$$\begin{bmatrix} W_{\Delta\alpha} \\ W_{\Delta\beta} \\ W_{\Delta 0} \end{bmatrix} = \mathbf{T}_{C0} \cdot \begin{bmatrix} W_{pa} - W_{na} \\ W_{pb} - W_{nb} \\ W_{pc} - W_{nc} \end{bmatrix}, \quad (3.76)$$

are the new energy states to be controlled.

Total energy controller

The desired power decoupling behavior illustrated in Figure 3.2 is investigated through the design of the total energy controller. Building on this concept, the controller is designed to shape the buffer contribution during a power reference

change. From a control perspective, this change is treated as a disturbance affecting the total stored energy. Afterwards, power is injected to recharge the arm capacitors to its original reference. Furthermore, this controller tracks a given desired energy reference. In classical control theory, this is achieved with a 2-DOF control architecture as represented in Figure 3.15. In contrast to standard PIs or 1-DOF controller, 2-DOF allow independent tuning of the reference tracking and disturbance rejection capabilities [170].

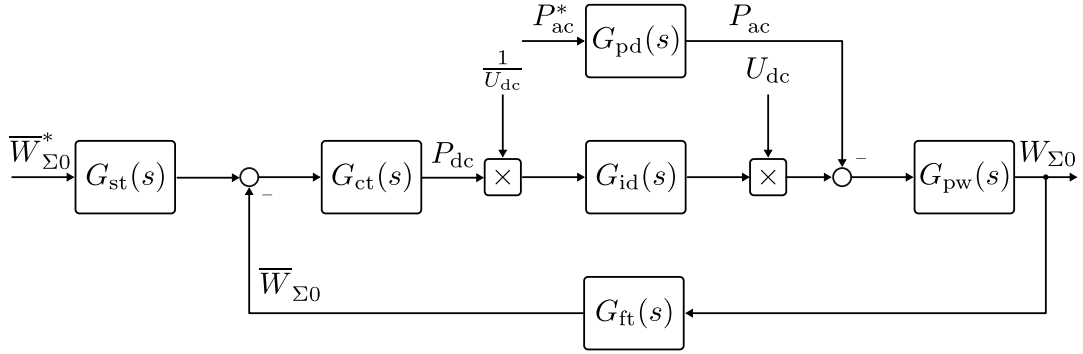


Figure 3.15: 2-DOF control architecture block diagram for total energy control

Examining the effect of disturbance the following closed-loop transfer is obtained,

$$G_{\text{wtd}}(s) = \frac{W_{\Sigma 0}(s)}{P_{ac}^*(s)} = -\frac{G_{id}(s)G_{pw}(s)G_{pd}(s)}{1 + G_{ct}(s)G_{ft}(s)G_{id}(s)G_{pw}(s)} \quad (3.77)$$

where $G_{pw}(s) = \frac{1}{s}$ and $G_{ft}(s)$ is a filter targeted to reject the arm energy oscillating components. Due to the coordinate changes, the zero components only contain low amplitude high frequency terms, which are negligible for this case. Hence $G_{ft} = 1$ is considered for the following case.

Considering the grid active power measurement (and its known dynamic) as a feedforward term and a proportional gain in $G_{ct}(s)$ to regulate the total energy storage, the resulting transfer functions are expressed as (3.78) or (3.79). Opposite to (3.73), for higher-order systems, it is highly complex to obtain a meaningful analytical expression capable representing the desired behavior. Simply placing the poles, s.t. the denominator polynomial is Hurwitz (stable), becomes highly non-intuitive to obtain a certain dynamic performance.

$$G_{\text{wtd},3}(s) = -\frac{s\omega_{ac}}{a_3s^3 + a_2s^2 + a_1s + a_0}, \quad \text{where} \quad (3.78)$$

$$a_3 = 1,$$

$$a_2 = \omega_{dc} + \omega_{ac},$$

$$\begin{aligned} a_1 &= \omega_{dc} (K_{ct} + \omega_{ac}), \\ a_0 &= K_{ct} \omega_{dc} \omega_{ac}. \end{aligned}$$

$$G_{\text{wtd},4}(s) = -\frac{s\omega_{pd}^2}{a_4s^4 + a_3s^3 + a_2s^2 + a_1s + a_0}, \quad \text{where} \quad (3.79)$$

$$\begin{aligned} a_4 &= 1, \\ a_3 &= 2\zeta_{pd}\omega_{pd} + \omega_{dc}, \\ a_2 &= \omega_{pd}^2 + 2\zeta_{pd}\omega_{dc}\omega_{pd} + K_{ct}\omega_{dc}, \\ a_1 &= \omega_{dc}\omega_{pd}^2 + 2K_{ct}\zeta_{pd}\omega_{dc}\omega_{pd}, \\ a_0 &= K_{ct}\omega_{dc}\omega_{pd}^2. \end{aligned}$$

To design the control loop for achieving the desired disturbance rejection performance, Bessel polynomials [171] are employed as reference transfer functions. Due to their maximally flat group delay and minimal overshoot, Bessel filters are well-suited for shaping closed-loop responses where preserving signal integrity and achieving smooth, well-damped transient behavior are prioritized over bandwidth and rapid response. This advantage extends to higher-order systems. The transfer function of the normalized Bessel filter is given by

$$T_{n+1}(s) = \frac{D_{n+1}(s)|_{s=0}}{D_{n+1}(s)} = \frac{d_0}{s^{n+1} + d_n s^n + \dots + d_1 s + d_0} \quad (3.80)$$

The denominator of the filter in (3.80) is defined as

$$D_{n+1}(s) = s^n w_{n+1}(s) - k_b n w_n(s) \quad (3.81)$$

where

$$w_n(s) = \sum_{k=0}^n \frac{(n+k)!}{(n-k)!k!(2s)^k} \quad (3.82)$$

is the n -th order Bessel polynomial. As investigated in [172] an additional parameter (k_b) is used to further adjust the filter overshoot. Substituting s in (3.80) by $s/\omega_{c,n+1}$, one obtains

$$\begin{aligned}
T'_{n+1}(s) &= T_{n+1}(s)|_{s=s/\omega_{c,n+1}} = \frac{D_{n+1}(s/\omega_{c,n+1})|_{s/\omega_{c,n+1}=0}}{D_{n+1}(s/\omega_{c,n+1})} \\
&= \frac{d_0}{\left(\frac{s}{\omega_{c,n+1}}\right)^{n+1} + d_n\left(\frac{s}{\omega_{c,n+1}}\right)^n + \dots + d_1\left(\frac{s}{\omega_{c,n+1}}\right) + d_0}
\end{aligned} \tag{3.83}$$

where $\omega_{c,n+1}$ is the bandwidth of the Bessel filter. Using (3.83), the first-order Bessel filter up to the fourth-order filter are given by

$$\begin{aligned}
T'_1(s) &= \frac{\omega_{c,1}}{s + \omega_{c,1}} \\
T'_2(s) &= \frac{(3 - k_b)\omega_{c,2}^2}{s^2 + (3 - k_b)\omega_{c,2}s + (3 - k_b)\omega_{c,2}^2} \\
T'_3(s) &= \frac{(15 - 6k_b)\omega_{c,3}^3}{s^3 + (6 - 2k_b)\omega_{c,3}s^2 + (15 - 6k_b)\omega_{c,3}^2s + (15 - 6k_b)\omega_{c,3}^3} \\
T'_4(s) &= \frac{(105 - 45k_b)\omega_{c,4}^4}{s^4 + (10 - 3k_b)\omega_{c,4}s^3 + (45 - 18k_b)\omega_{c,4}^2s^2 + (105 - 45k_b)\omega_{c,4}^3s + (105 - 45k_b)\omega_{c,4}^4}
\end{aligned} \tag{3.84}$$

The goal is to approximate the transient behavior of a first-order system using higher-order Bessel filters. Since identical responses cannot be achieved due to the increased system order, the cutoff frequencies are scaled with the following factors

$$\begin{aligned}
\omega_{c2} &= \frac{T_{\text{set},2}}{T_{\text{set},1}}\omega_{c1} = k_{\omega_{c2}}\omega_{c1} \\
\omega_{c3} &= \frac{T_{\text{set},3}}{T_{\text{set},1}}\omega_{c1} = k_{\omega_{c3}}\omega_{c1} \\
\omega_{c4} &= \frac{T_{\text{set},4}}{T_{\text{set},1}}\omega_{c1} = k_{\omega_{c4}}\omega_{c1}
\end{aligned} \tag{3.85}$$

such that a comparable settling time is obtained. The required scaling factors are determined numerically, as the relationship between cutoff frequency and settling time depends on the filter order. The impact of bandwidth scaling on the transient response is illustrated in Figure 3.16 through a comparison of a second- and fourth-order Bessel filters with and without scaling.

The result shows that the higher-order filter maintains the same transient time as the first-order filter, thereby achieving the desired transient response while requiring less bandwidth after adjustment. The target transfer function to design (3.79), includes a zero at the origin. From a structural perspective, the zero at

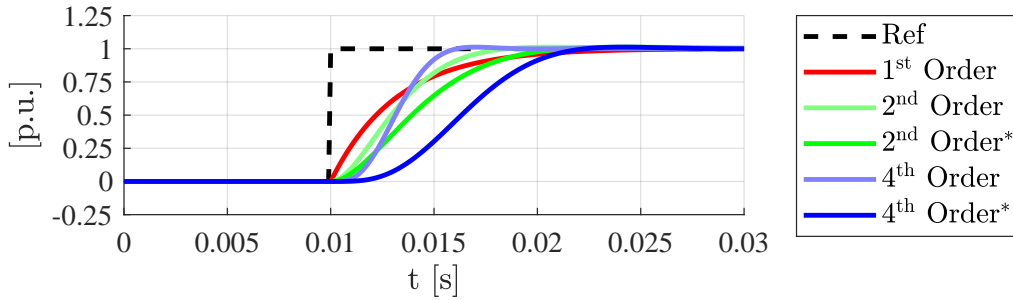


Figure 3.16: Step responses of 1st-, 2nd- and 4th-order Bessel filters with $k_b = 0.25$

the origin leads to a step response similar to a disturbance rejection behavior, with the output converging to the reference. This matches the desired transient behavior of the total energy storage in the MMC. Accordingly, the Bessel filters response is provided in Figure 3.17¹. In step response analysis, the damping coefficient can directly limit the peak value to ensure it does not exceed a desired reference. Additionally, a unity DC gain must be guaranteed. In contrast, the impulse response represents the system’s intrinsic dynamics without a reference level, making peak amplitudes less directly related to design specifications such as overshoot. While the settling time is defined identically to the step response, the peak deviation from the origin is determined by the pole locations and chosen DC gain. As shown in Figure 3.17, higher-order systems delay the peak time while maintaining the same settling time after bandwidth adjustment. The parameter k_b plays a crucial role in shaping the damping characteristics, even in higher-order systems. This was previously explored for a very narrow range of values in [172]. Expanding this range further, the comparison in Figure 3.18 reveals that negative k_b values lead to an overdamped response, whereas positive values shift poles to the right-half plane, resulting in instability.

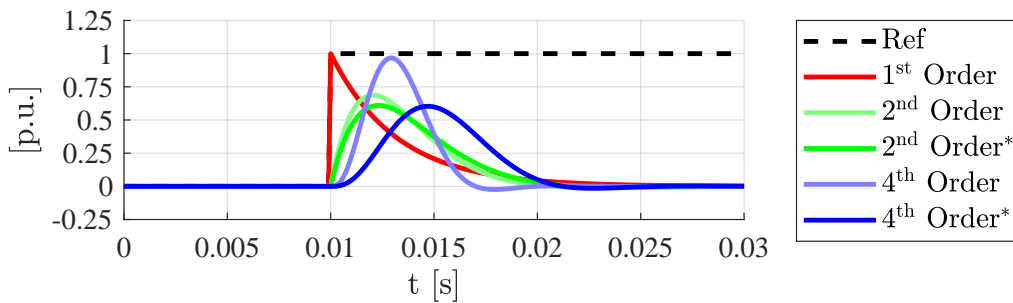


Figure 3.17: Impulse responses of 1st-, 2nd- and 4th-order Bessel filters with $k_b = 0.25$

¹The result should display a negative drop; however, for visual clarity and alignment with the step reference, the signal has been inverted.

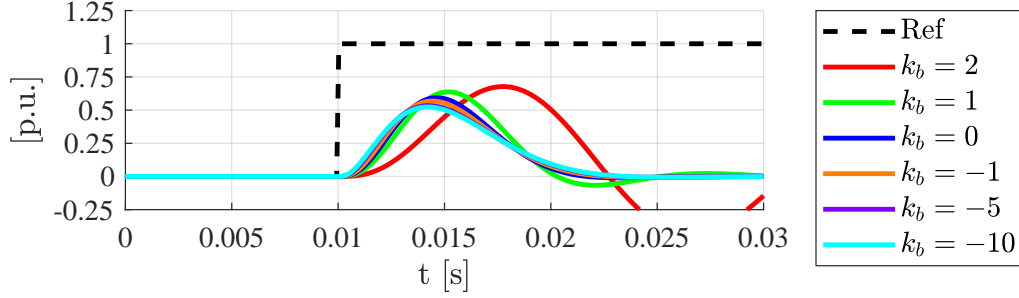


Figure 3.18: Impulse responses of 4th-order Bessel filters for different k_b

An analytical solution for the second-order Bessel filter is straightforward to derive and can be used to shape the energy disturbance response. The influence of the scaling factor k_b on the peak time of higher-order filters is illustrated in Figure 3.19, where k_b effectively serves as a scaling parameter that relates the second-order filter to higher-order implementations. Using (3.85), this concept is extended to adjust the filter bandwidth. Notably, decreasing k_b increases the damping, leading to a more overdamped system with one or more dominant poles.

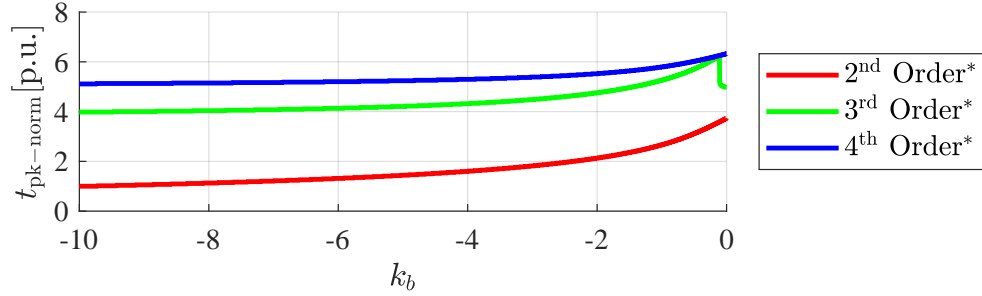


Figure 3.19: Normalized peak time between adjusted 2nd-, 3rd and 4th-order Bessel filters at different k_b

For simplicity, the third-order filter is selected as the desired closed-loop transfer function for disturbance rejection. However the approach can be further extended for higher-order systems. Comparing the denominator of (3.85) and (3.78), the following relations are obtained,

$$\begin{aligned}\omega_{ac} + \omega_{dc} &= (6 - 2k_b) \omega_{c3} \\ \omega_{dc} (K_{ct} + \omega_{ac}) &= (15 - 6k_b) \omega_{c3}^2 \\ \omega_{dc} K_{ct} \omega_{ac} &= (15 - 6k_b) \omega_{c3}^3.\end{aligned}\tag{3.86}$$

There are six variables to choose, however only three equations to solve. While ω_{ac} is chosen in advance, it is enough to fix arbitrarily another variable to obtain the polynomial coefficients. From (3.2), it is intuitive to perform a grid search

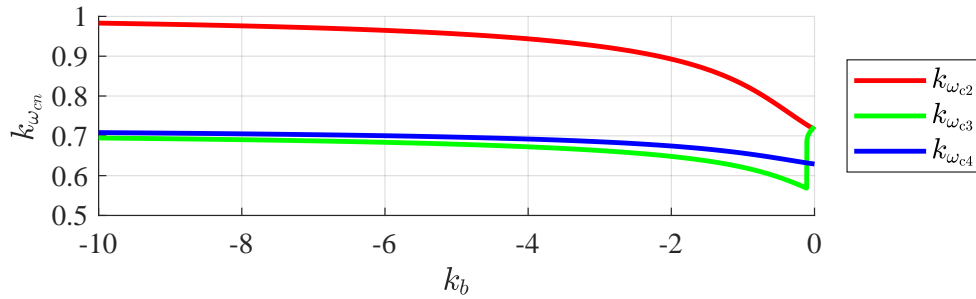


Figure 3.20: Bandwidth adjustment factor for achieving the settling time of a 1st-order system in 2nd-, 3rd and 4th-order Bessel filters at different k_b

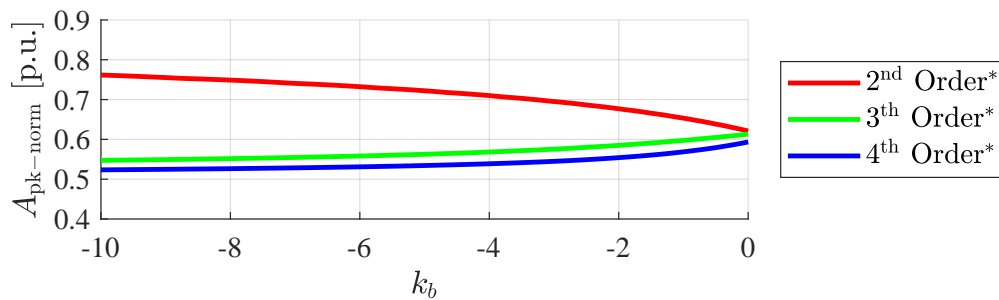


Figure 3.21: Normalized amplitude drop in adjusted 2nd-, 3rd and 4th-order Bessel filters at different k_b , related to its 1st-order

by sweeping $\omega_{ac} \geq 0$ and $\omega_{dc} \geq 0$ across several frequencies. Together with the relations derived in this subsection, the coefficients are found accordingly. The resulting outputs plotted in following figures² are:

- Energy settling time after a power step change
- Peak amplitude of the energy deviation from original reference
- Time instant of peak amplitude deviation after power reference change

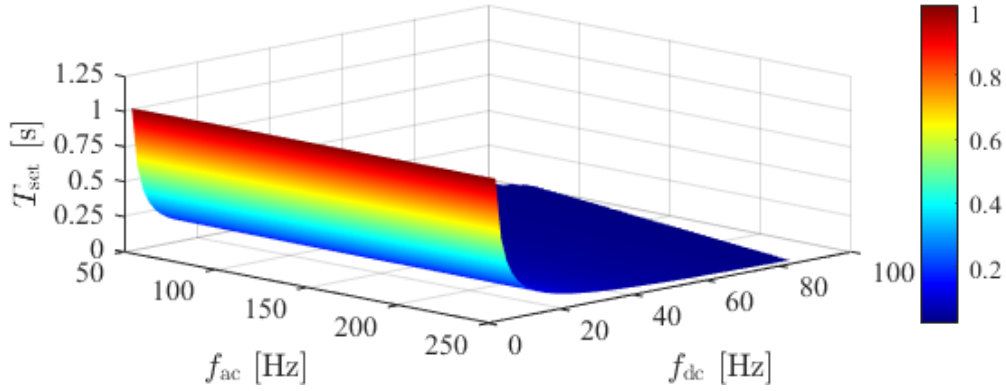


Figure 3.22: Total energy settling time dependent on chosen ω_{ac} and ω_{dc}

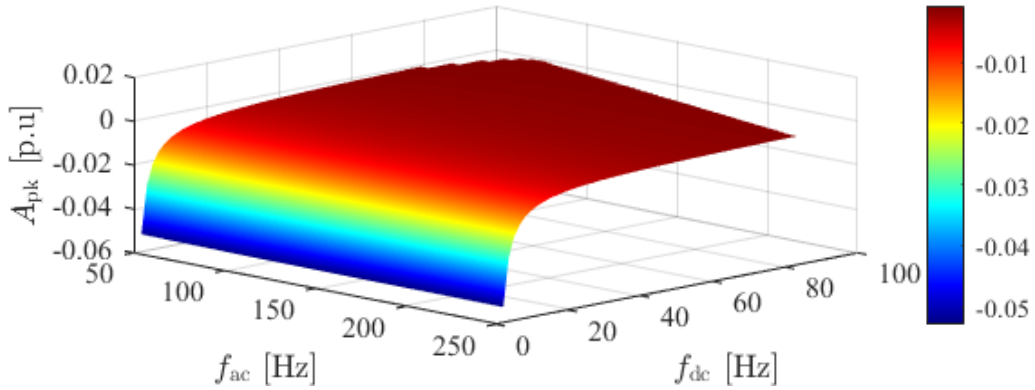


Figure 3.23: Resulting peak energy deviation dependent on chosen ω_{ac} and ω_{dc}

As expected, the greater the amplitude difference between ω_{ac} and ω_{dc} , the more energy in the MMC is used and the more it takes to be regulated back to its origin, whereas the choice of ω_{dc} contributes the most for this difference.

As expected, a larger difference between ω_{ac} and ω_{dc} leads to greater energy deviation in the MMC, resulting in increased effort to restore the system to its

² ω_{dc} limited to 1Hz for better visualization

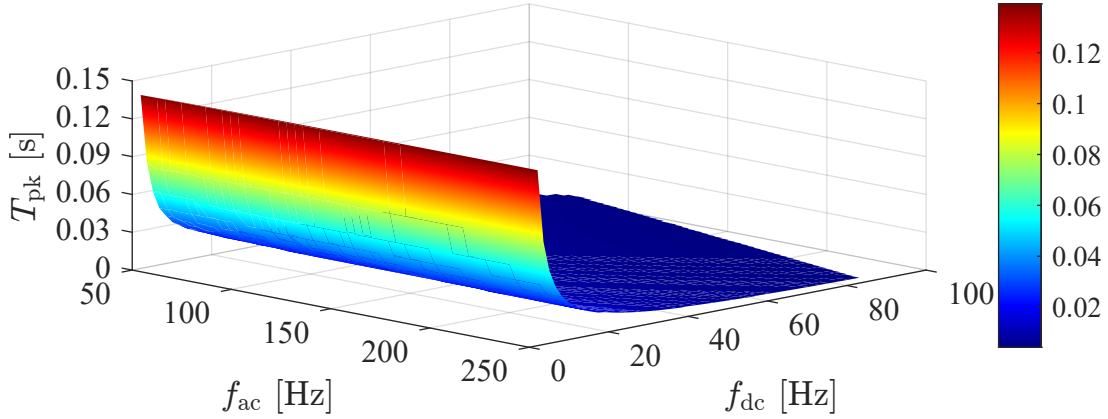


Figure 3.24: Time instant of peak total energy deviation dependent on chosen ω_{ac} and ω_{dc}

nominal state. Among these parameters, the choice of ω_{dc} has the dominant influence on this behavior. This relations have an exponential nature. From the resulting data, it is observed that for ω_{dc} greater than ω_{ac} the settling time is slowly reduced to match $\frac{1}{f_{ac}}$. This is due to the feedforward of the measured power, which settles after $\frac{1}{f_{ac}}$. The decoupling capability is mostly related with the installed capacity within the MMC. Therefore, this results can be used to provide an estimation of the necessary capacitance to avoid violating the condition (2.11). Based on (2.20) (2.21), the average available voltage deviation is obtained, yielding

$$\Delta U_{C_{arm}} = \sqrt{\frac{2\Delta W_{MMC}}{6C_{arm}}}. \quad (3.87)$$

Sweeping between possible arm capacitance values, the resultant available peak voltage drop for $P_{ac}^* = 1W$ is provided graphically in Figure 3.25. As expected, lower installed capacitance leads to higher voltage drops, which is opposite to settling time imposed. Accordingly, the amplitude of available voltage drop is scaled with P_{ac}^* .

It is also desired to track references for total energy stored. Using the chosen proportional controller, the closed-loop transfer yields,

$$G_{wtr}(s) = \frac{W_0(s)}{W_0^*(s)} = \frac{G_{ct}(s)G_{id}(s)G_{pw}(s)}{1 + G_{ct}(s)G_{ft}(s)G_{id}(s)G_{pw}(s)} = \frac{\omega_{dc}}{s^2 + s\omega_{dc} + K_{ct}\omega_{dc}}, \quad (3.88)$$

which is a second-order system. In its current form, the transfer function does not exhibit unity DC gain. Similar to (3.40), this is addressed by adding a feedforward gain that guarantees zero steady-state error during reference tracking. However, its dynamic is still dependent on the chosen disturbance response. Adding shaping

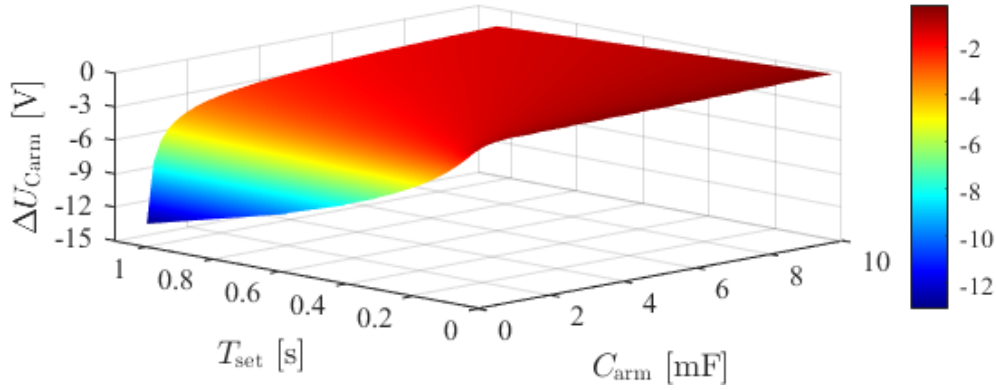


Figure 3.25: Resultant available peak voltage drop dependent on installed C_{arm} and resulting T_{set}

function $G_{\text{st}}(s)$ as in Figure 3.15 to (3.88), influences how the closed-loop perceives the energy reference. The new desired closed-loop yields,

$$G_{\text{wtr}}^*(s) = G_{\text{st}}(s)G_{\text{wtr}}(s) = \frac{\omega_{\text{rt}}^2}{s^2 + 2\omega_{\text{dc}} + K_{\text{ct}}\omega_{\text{dc}}}, \quad (3.89)$$

which can be design as in the subsection 3.4.2. Consequently, the shaper transfer function must result in

$$G_{\text{st}}(s) = \frac{\omega_{\text{tr}}^2}{\omega_{\text{dc}}} \cdot \frac{s^2 + s\omega_{\text{dc}} + K_{\text{ct}}\omega_{\text{dc}}}{s^2 + 2\zeta_{\text{tr}}\omega_{\text{tr}}s + \omega_{\text{tr}}^2}. \quad (3.90)$$

This difference is well illustrated in Figure 3.26. In absence of $G_{\text{st}}(s)$, a 1-DOF controller couples reference tracking and disturbance rejection, leading to similarly fast dynamics in both responses. This may be undesirable in MMC operation. A 2-DOF structure allows independent tuning of the reference step response while preserving the previously designed disturbance rejection behavior.

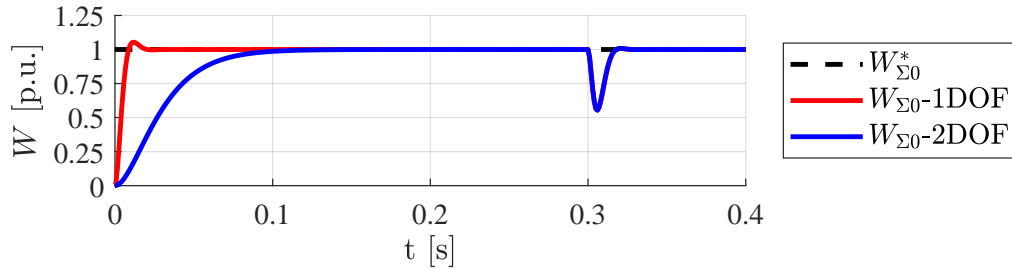


Figure 3.26: Total energy reference tracking and disturbance rejection with and without $G_{\text{st}}(s)$

Horizontal and Vertical energy controllers

Both the horizontal and vertical controllers are responsible for generating the references for (3.65) and (3.71), respectively. Their primary function in this application is to ensure an equal distribution of the energy stored within the arms. Unlike total energy control, the balancing action must respond rapidly to compensate for power reference changes that disproportionately affect one arm over the others. To achieve this, a control structure similar to that of the total energy controller is employed, as any output power reference change inherently disrupts the energy balance among the arms. Consequently, this disturbance follows the same dynamic behavior as described in (3.72). Due to its mixed frequency nature of these energy states, no feedforward term is considered. Thus, the disturbance rejection closed-loop transfer function for W_Σ is given in (3.91), with the Δ component inheriting the exact same transfer function. The denominator design follows the methodology outlined in the previous subsection. However, the introduction of an additional zero results in a more aggressive transient response. Fortunately, since $\omega_z > 0$, this zero ensures a minimum phase transient behavior.

$$G_{w\Sigma d,3}(s) = \frac{W_{\Sigma\alpha\beta}}{P_{ac}^*} = -\frac{\omega_{ac}(s + \omega_z)}{a_3s^3 + a_2s^2 + a_1s + a_0}, \quad \text{where} \quad (3.91)$$

$$a_3 = 1,$$

$$a_2 = \omega_z + \omega_{ac},$$

$$a_1 = \omega_z(K_{c\Sigma} + \omega_{ac}),$$

$$a_0 = K_{c\Sigma}\omega_z\omega_{ac}.$$

Referring to Figure 3.15, it is evident that $G_{ft}(s)$ cannot be neglected. Under balanced conditions, no DC components are present, meaning that both $\alpha\beta$ states consist only of oscillating components, which do not directly impact the control objective. However, their amplitude remains sufficiently high to introduce perturbations into the system. To mitigate these disturbances, notch filters are incorporated into the control loop. The corresponding filter transfer function is given by:

$$G_{nf}(s) = \frac{s^2 + \omega_{nf}^2}{s^2 + 2\zeta_{nf}\omega_{nf}s + \omega_{nf}^2}, \quad (3.92)$$

For $W_{\Delta\alpha\beta 0}$, the dominant oscillating component occurs at 50 Hz, and the notch filter is specifically designed to attenuate this frequency. Ideally, this component should be suppressed as much as possible. However, stronger attenuation comes at the cost of increased phase shift, which affects the closed-loop phase margin, thereby influencing the overall dynamic behavior and robustness of the system. This trade-off is illustrated in Figure 3.27 and Figure 3.28, where the filter damping coefficient determines the balance between attenuation and stability. For

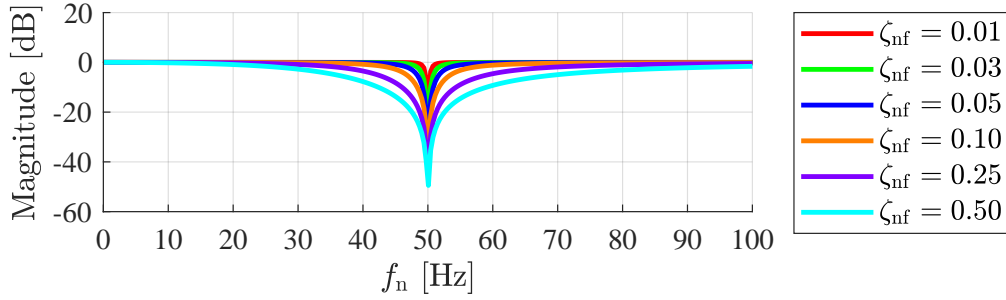


Figure 3.27: 50Hz notch filter magnitude with different damping coefficients

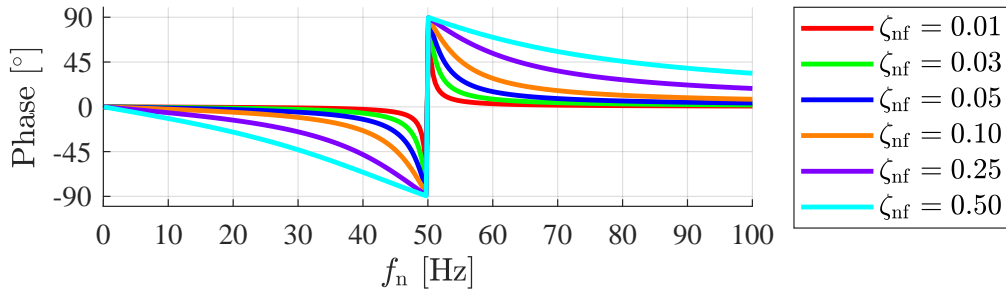


Figure 3.28: 50Hz notch filter phase-shift with different damping coefficients

$W_{\Sigma\alpha\beta}$, the dominant frequency component is 100 Hz, and the notch filter is adjusted accordingly. Alternatively, a higher-order notch or low-pass filters could be used to achieve better suppression. However, these approaches introduce greater design complexity and implementation challenges, making a standard notch filter the preferred choice in most cases.

In summary, Figure 3.29 presents the block diagram of the entire control structure, highlighting the loop shaping design technique for the outer loop.

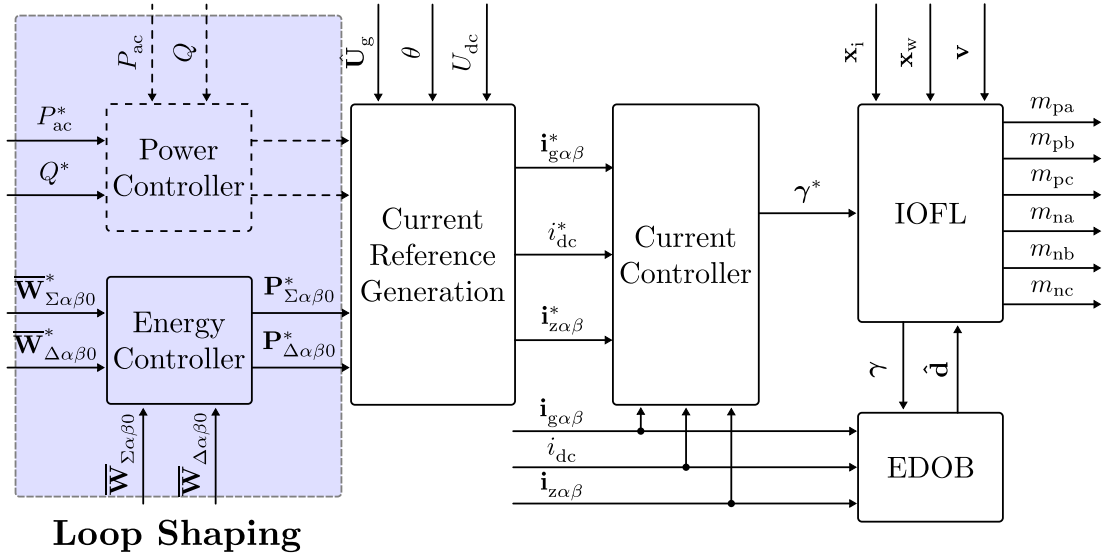


Figure 3.29: Controller block diagram: Outer loop designed via Loop Shaping

3.5 Outer controller – Model Predictive Control

The linear (MPC) algorithm is explored here as an alternative to the loop-shaping approach. Its primary objective is to constrain energy and, indirectly, current amplitudes to ensure the MMC operates within its critical safe region. This choice is motivated by several factors:

- **Submodule capacitors:** While they cannot exceed their rated DC voltage, they can tolerate higher peak voltages as long as these are periodic and bounded (i.e., within acceptable ripple limits).
- **Arm voltage:** The total available arm voltage must remain within specific limits to prevent over-modulation, inrush currents, and excessive arm current.
- **Arm current:** The maximum allowable arm current should align with the semiconductor's Safe Operation Area (SOA) to prevent damage.
- **Current limits in AC- and DC-grids:** Constraints must account for both grid sides to ensure that voltage sags do not induce overcurrent in the MMC.

MPC is an advanced control strategy that optimizes future control actions based on a predictive model of the system. The core concept of MPC with a moving horizon is illustrated in Figure 3.30. At each discrete time step k , the controller uses the current state x_0 as the initial condition and predicts the system's future behavior over a finite time window known as the prediction horizon, spanning

from $k + 1$ to $k + N_p$, where N_p denotes the prediction horizon length. Based on this forecast, the controller solves an optimization problem to compute a sequence of control inputs that minimize a predefined cost function while satisfying system constraints, which are enforced over a constraint horizon length N_c .

Only the first control input from the optimized sequence is applied to the system. At the next time step, the horizon advances, the system state is updated, and the optimization is resolved. This receding horizon strategy allows the controller to continuously adapt its actions to the most recent state information, ensuring robust performance without violating the desired constraints. However, a major limitation of MPC is its relatively high computational demand compared to classical control methods, due to the need for real-time optimization [173].

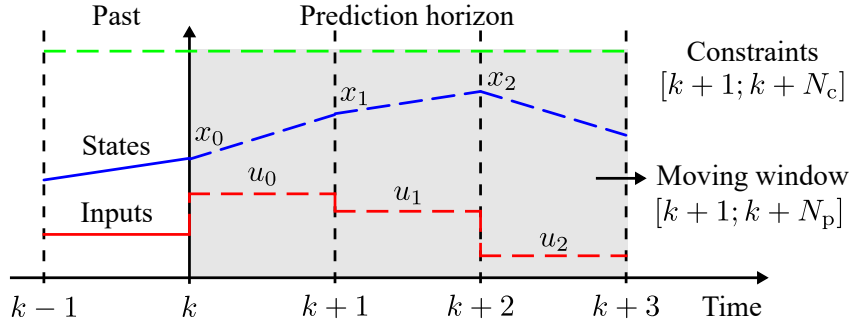


Figure 3.30: General concept of Model Predictive Control with Moving Horizon

3.5.1 State-space model

The design of a MPC control algorithm requires a state-space model of the system. Considering controlled currents, generated from power references in the previous subsections, the states, inputs and outputs are defined as

$$\begin{aligned}
 \mathbf{x} &= [P_{ac}, Q, P_{dc}, W_{\Sigma 0}, P_{\Sigma\alpha}, P_{\Sigma\beta}, W_{\Sigma\alpha}, W_{\Sigma\beta}, P_{\Delta\alpha}, P_{\Delta\beta}, P_{\Delta 0}, W_{\Delta\alpha}, W_{\Delta\beta}, W_{\Delta 0}]^T \\
 \mathbf{u} &= [P^*, Q^*, P_{\Sigma 0}^*, P_{\Sigma\alpha}^*, P_{\Sigma\beta}^*, P_{\Delta\alpha}^*, P_{\Delta\beta}^*, P_{\Delta 0}^*]^T \\
 \mathbf{y}_i &= [P_{ac}, Q, W_{\Sigma 0}, W_{\Sigma\alpha}, W_{\Sigma\beta}, W_{\Delta\alpha}, W_{\Delta\beta}, W_{\Delta 0}]^T
 \end{aligned} \tag{3.93}$$

Following the structure in (2.48), for the inverter operation the state matrix yields,

$$\mathbf{A}_{W,i} = \begin{bmatrix} \mathbf{A}_{T,i} & \mathbf{0} & \mathbf{0} \\ \mathbf{0} & \mathbf{A}_{\Sigma} & \mathbf{0} \\ \mathbf{0} & \mathbf{0} & \mathbf{A}_{\Delta} \end{bmatrix}, \quad \text{where} \quad \mathbf{A}_{T,i} = \begin{bmatrix} -\omega_{ac} & 0 & 0 & 0 \\ 0 & -\omega_{ac} & 0 & 0 \\ \omega_{dc} & 0 & -\omega_{dc} & 0 \\ -1 & 0 & 1 & 0 \end{bmatrix} \tag{3.94}$$

$$\mathbf{A}_\Sigma = \begin{bmatrix} -\omega_c \mathbf{I}_{2 \times 2} & \mathbf{0}_{2 \times 2} \\ \mathbf{I}_{2 \times 2} & \mathbf{0}_{2 \times 2} \end{bmatrix}, \quad \mathbf{A}_\Delta = \begin{bmatrix} -\omega_z \mathbf{I}_{3 \times 3} & \mathbf{0}_{3 \times 3} \\ \mathbf{I}_{3 \times 3} & \mathbf{0}_{3 \times 3} \end{bmatrix}$$

The input matrix is given by,

$$\mathbf{B}_{W,i} = \begin{bmatrix} \mathbf{B}_{T,i} & \mathbf{0} & \mathbf{0} \\ \mathbf{0} & \mathbf{B}_\Sigma & \mathbf{0} \\ \mathbf{0} & \mathbf{0} & \mathbf{B}_\Delta \end{bmatrix}, \quad \text{where } \mathbf{B}_{T,i} = \begin{bmatrix} \omega_{ac} & 0 & 0 \\ 0 & \omega_{ac} & 0 \\ 0 & 0 & \omega_{dc} \\ 0 & 0 & 0 \end{bmatrix} \quad (3.95)$$

$$\mathbf{B}_\Sigma = \begin{bmatrix} \omega_c \mathbf{I}_{2 \times 2} \\ \mathbf{0}_{2 \times 2} \end{bmatrix}, \quad \mathbf{B}_\Delta = \begin{bmatrix} \omega_c \mathbf{I}_{3 \times 3} \\ \mathbf{0}_{3 \times 3} \end{bmatrix}$$

and the output matrix yields

$$\mathbf{C}_{W,i} = \begin{bmatrix} 1 & 0 & 0 & 0 & 0 & 0 & 0 & 0 & 0 & 0 & 0 & 0 & 0 & 0 & 0 \\ 0 & 1 & 0 & 0 & 0 & 0 & 0 & 0 & 0 & 0 & 0 & 0 & 0 & 0 & 0 \\ 0 & 0 & 0 & 1 & 0 & 0 & 0 & 0 & 0 & 0 & 0 & 0 & 0 & 0 & 0 \\ 0 & 0 & 0 & 0 & 0 & 0 & 1 & 0 & 0 & 0 & 0 & 0 & 0 & 0 & 0 \\ 0 & 0 & 0 & 0 & 0 & 0 & 0 & 1 & 0 & 0 & 0 & 0 & 0 & 0 & 0 \\ 0 & 0 & 0 & 0 & 0 & 0 & 0 & 0 & 0 & 0 & 1 & 0 & 0 & 0 & 0 \\ 0 & 0 & 0 & 0 & 0 & 0 & 0 & 0 & 0 & 0 & 0 & 1 & 0 & 0 & 0 \\ 0 & 0 & 0 & 0 & 0 & 0 & 0 & 0 & 0 & 0 & 0 & 0 & 1 & 0 & 0 \end{bmatrix} \quad (3.96)$$

For the rectifier mode, the output vector changes slightly,

$$\mathbf{y}_r = [Q, P_{dc}, W_{\Sigma 0}, W_{\Sigma \alpha}, W_{\Sigma \beta}, W_{\Delta \alpha}, W_{\Delta \beta}, W_{\Delta 0}]^T \quad (3.97)$$

which leads to the following readjustments in the state matrix

$$\mathbf{A}_{W,r} = \begin{bmatrix} \mathbf{A}_{T,r} & \mathbf{0} & \mathbf{0} \\ \mathbf{0} & \mathbf{A}_\Sigma & \mathbf{0} \\ \mathbf{0} & \mathbf{0} & \mathbf{A}_\Delta \end{bmatrix}, \quad \text{where } \mathbf{A}_{T,r} = \begin{bmatrix} -\omega_{ac} & 0 & \omega_{ac} & 0 \\ 0 & -\omega_{ac} & 0 & 0 \\ 0 & 0 & -\omega_{dc} & 0 \\ 1 & 0 & -1 & 0 \end{bmatrix} \quad (3.98)$$

and input matrix

$$\mathbf{B}_{W,r} = \begin{bmatrix} \mathbf{B}_{T,r} & \mathbf{0} & \mathbf{0} \\ \mathbf{0} & \mathbf{B}_\Sigma & \mathbf{0} \\ \mathbf{0} & \mathbf{0} & \mathbf{B}_\Delta \end{bmatrix}, \quad \text{where } \mathbf{B}_{T,r} = \begin{bmatrix} 0 & 0 & \omega_{dc} \\ 0 & \omega_{ac} & 0 \\ \omega_{ac} & 0 & 0 \\ 0 & 0 & 0 \end{bmatrix} \quad (3.99)$$

as well as in the output matrix

$$\mathbf{C}_{w,r} = \begin{bmatrix} 0 & 1 & 0 & 0 & 0 & 0 & 0 & 0 & 0 & 0 & 0 & 0 & 0 & 0 \\ 0 & 0 & 1 & 0 & 0 & 0 & 0 & 0 & 0 & 0 & 0 & 0 & 0 & 0 \\ 0 & 0 & 0 & 1 & 0 & 0 & 0 & 0 & 0 & 0 & 0 & 0 & 0 & 0 \\ 0 & 0 & 0 & 0 & 0 & 0 & 1 & 0 & 0 & 0 & 0 & 0 & 0 & 0 \\ 0 & 0 & 0 & 0 & 0 & 0 & 0 & 1 & 0 & 0 & 0 & 0 & 0 & 0 \\ 0 & 0 & 0 & 0 & 0 & 0 & 0 & 0 & 0 & 0 & 1 & 0 & 0 & 0 \\ 0 & 0 & 0 & 0 & 0 & 0 & 0 & 0 & 0 & 0 & 0 & 1 & 0 & 0 \\ 0 & 0 & 0 & 0 & 0 & 0 & 0 & 0 & 0 & 0 & 0 & 0 & 1 & 0 \end{bmatrix}. \quad (3.100)$$

3.5.2 Linear MPC

This subsection presents the CCS-MPC algorithm. In this formulation, the system model is augmented with an integrator state to account for model mismatch and parameter uncertainties [174]. Hence the augmented state-space model yields

$$\mathbf{x}(k+1) = \mathbf{A}\mathbf{x}(k) + \mathbf{B}\Delta\mathbf{u}(k) \quad (3.101)$$

$$\mathbf{y}(k) = \mathbf{C}\mathbf{x}(k), \quad (3.102)$$

where

$$\mathbf{x}(k) = [\Delta\mathbf{x}_m(k) \quad \mathbf{y}(k)]^\top, \quad \Delta\mathbf{x}_m(k) = \mathbf{x}_m(k) - \mathbf{x}_m(k-1),$$

$$\Delta\mathbf{u}(k) = \mathbf{u}(k) - \mathbf{u}(k-1)$$

and the matrices \mathbf{A} , \mathbf{B} , \mathbf{C} are defined as,

$$\mathbf{A} = \begin{bmatrix} \mathbf{A}_d & \mathbf{0}_{14 \times 8} \\ \mathbf{C}_d \mathbf{A}_d & \mathbf{I}_8 \end{bmatrix}, \quad \mathbf{B} = \begin{bmatrix} \mathbf{B}_d \\ \mathbf{C}_d \mathbf{B}_d \end{bmatrix}, \quad \mathbf{C} = [\mathbf{0}_{8 \times 14} \quad \mathbf{I}_8],$$

where the matrices \mathbf{A}_d , \mathbf{B}_d , and \mathbf{C}_d are obtained by discretizing the model given in previous subsection. The discretization method is Zero-Order Hold (ZOH), as described in Appendix C. Considering a desired prediction horizon N_p and control horizon N_c , and assuming the initial state is known, a prediction model is obtained. First, the future control action and predicted output vectors are defined as

$$\mathbf{Y} = [\mathbf{y}(k_i+1) \quad \mathbf{y}(k_i+2) \quad \mathbf{y}(k_i+3) \quad \dots \quad \mathbf{y}(k_i+N_p)]^T,$$

$$\Delta\mathbf{U} = [\Delta\mathbf{u}(k_i) \quad \Delta\mathbf{u}(k_i+1) \quad \Delta\mathbf{u}(k_i+2) \quad \dots \quad \Delta\mathbf{u}(k_i+N_c-1)]^T,$$

and a condensed form of the prediction model

$$\mathbf{Y} = \mathbf{F}\mathbf{x}(k_i) + \Phi\Delta\mathbf{U} \quad (3.103)$$

where,

$$\mathbf{F} = \begin{bmatrix} \mathbf{CA} \\ \mathbf{CA}^2 \\ \mathbf{CA}^3 \\ \vdots \\ \mathbf{CA}^{N_p} \end{bmatrix}; \quad \Phi = \begin{bmatrix} \mathbf{CB} & 0 & 0 & \dots & 0 \\ \mathbf{CAB} & \mathbf{CB} & 0 & \dots & 0 \\ \mathbf{CA}^2\mathbf{B} & \mathbf{CAB} & \mathbf{CB} & \dots & 0 \\ \vdots & & & & \\ \mathbf{CA}^{N_p-1}\mathbf{B} & \mathbf{CA}^{N_p-2}\mathbf{B} & \mathbf{CA}^{N_p-3}\mathbf{B} & \dots & \mathbf{CA}^{N_p-N_c}\mathbf{B} \end{bmatrix}.$$

The control objective is to minimize the tracking error, i.e. the difference between the outputs $\mathbf{y}(k)$ and their corresponding references $\mathbf{r}(k)$, which is represented by the cost function J

$$J = \sum_{i=0}^{N_p-1} \|\mathbf{r}(k_i + i + 1) - \mathbf{y}(k_i + i + 1)\|^2 + \mathbf{R}_w \|\Delta\mathbf{u}(k_i + i)\|^2, \quad (3.104)$$

where k_i is the sampling instant and \mathbf{R}_w is the weight that determines the trade-off between tracking performance and control effort. The same cost function can be written as a function of the initial state, system matrices (condensed formulation) and future control actions, yielding

$$J = (\mathbf{R}_s - \mathbf{Y})^T (\mathbf{R}_s - \mathbf{Y}) + \Delta\mathbf{U}^T \bar{\mathbf{R}}_w \Delta\mathbf{U} \quad (3.105)$$

where the reference vector is defined as

$$\mathbf{R}_s^T = [\mathbf{I}_{n_y \times N_p}] \mathbf{r}(k_i),$$

and $\bar{\mathbf{R}}_w$ is the block-diagonal weighting with dimensions $(n_u \times N_c) \times (n_u \times N_c)$. Both n_u and n_y denote the dimensions of the system's input and output vectors, respectively. By inserting (3.103) into (3.105), the optimization problem can be further rewritten as a standard unconstrained Quadratic Programming (QP) problem of the form

$$\min_{\Delta\mathbf{U}} J = \frac{1}{2} \Delta\mathbf{U}^T \mathbf{H} \Delta\mathbf{U} + \mathbf{f}^T \Delta\mathbf{U}, \quad (3.106)$$

with

$$\mathbf{H} = \Phi^T \Phi + \bar{\mathbf{R}}_w$$

being a symmetric positive semi-definite (Hessian) matrix that defines the quadratic part of the objective function, and

$$\mathbf{f}^T = -\Phi^T (\mathbf{R}_s - \mathbf{F}\mathbf{x}(k_i))$$

a vector defining the linear part of the objective function. For the unconstrained case, an analytical solution is found by taking the gradient of the objective function and setting it to zero

$$\frac{\partial J}{\partial \Delta \mathbf{U}} = 0,$$

from which the optimal solution for the control action to deploy is found as

$$\Delta \mathbf{U}^* = -\mathbf{H}^{-1}\mathbf{f}. \quad (3.107)$$

Due to the receding-horizon implementation, only the first control increment of the optimal input sequence is applied at each sampling instant. For the unconstrained case, the resulting control law has a linear state-feedback structure, analogous to that obtained in LQR, and can be written as

$$\Delta \mathbf{u}(k_i) = [1 \ 0 \ \dots \ 0] \Delta \mathbf{U}^* = \mathbf{K}_y \mathbf{r}(k_i) - \mathbf{K}_s \mathbf{x}(k_i) \quad (3.108)$$

where,

$$\mathbf{K}_y = \mathbf{H}^{-1} \Phi^T \mathbf{R}_s, \quad \mathbf{K}_s = \mathbf{H}^{-1} \Phi^T \mathbf{F}.$$

By applying a receding horizon policy, this problem is solved at every sampling time T_s . Hence, the first element of $\Delta \mathbf{U}^*$ is applied to the system, and the procedure is repeated at the next sampling instant. Another major advantage of the MPC algorithm is the possibility to include constraints without sacrificing the control law performance. However, an analytical optimal solution is not possible to obtain. Hence, modeling constraints is an important aspect of MPC. The bounds do not necessarily have to be constant but can be modeled to depend on the current and future system trajectory. This can be useful, for example, to avoid certain operating regions or nonlinearities. Typically, it is important to impose constraints on the inputs and states; if these remain constant during the prediction horizon, are written as,

$$\begin{bmatrix} \mathbf{u}_{\min} \\ \mathbf{u}_{\min} \\ \vdots \\ \mathbf{u}_{\min} \end{bmatrix} \leq \begin{bmatrix} \mathbf{u}(k_i) \\ \mathbf{u}(k_i + 1) \\ \vdots \\ \mathbf{u}(k_i + N_c - 1) \end{bmatrix} \leq \begin{bmatrix} \mathbf{u}_{\max} \\ \mathbf{u}_{\max} \\ \vdots \\ \mathbf{u}_{\max} \end{bmatrix} \quad (3.109)$$

$$\begin{bmatrix} \mathbf{x}_{\min} \\ \mathbf{x}_{\min} \\ \vdots \\ \mathbf{x}_{\min} \end{bmatrix} \leq \begin{bmatrix} \mathbf{x}(k_i + 1) \\ \mathbf{x}(k_i + 2) \\ \vdots \\ \mathbf{x}(k_i + N_c) \end{bmatrix} \leq \begin{bmatrix} \mathbf{x}_{\max} \\ \mathbf{x}_{\max} \\ \vdots \\ \mathbf{x}_{\max} \end{bmatrix} \quad (3.110)$$

where \mathbf{u}_{\min} and \mathbf{u}_{\max} define the input constraints, and \mathbf{x}_{\min} and \mathbf{x}_{\max} define the state constraints. These must be rewritten in terms of $\Delta\mathbf{U}$ due to the formulation of the quadratic problem in (3.106). Referring its definition the input constraints now yield,

$$\begin{bmatrix} \mathbf{u}_{\min} \\ \mathbf{u}_{\min} \\ \vdots \\ \mathbf{u}_{\min} \end{bmatrix} \leq \underbrace{\begin{bmatrix} \mathbf{I} \\ \mathbf{I} \\ \vdots \\ \mathbf{I} \end{bmatrix}}_{\mathbf{T}_I} \mathbf{u}(k_i - 1) + \underbrace{\begin{bmatrix} \mathbf{I} & 0 & 0 & \cdots & 0 \\ \mathbf{I} & \mathbf{I} & 0 & \cdots & 0 \\ \vdots & \vdots & \vdots & \ddots & \vdots \\ \mathbf{I} & \mathbf{I} & \mathbf{I} & \cdots & \mathbf{I} \end{bmatrix}}_{\mathbf{T}_L} \Delta\mathbf{U} \leq \begin{bmatrix} \mathbf{u}_{\max} \\ \mathbf{u}_{\max} \\ \vdots \\ \mathbf{u}_{\max} \end{bmatrix} \quad (3.111)$$

and the same must be done to the state constraints. Referring to the $\Delta\mathbf{x}_m$ definition,

$$\begin{bmatrix} \mathbf{x}_{\min} \\ \mathbf{x}_{\min} \\ \vdots \\ \mathbf{x}_{\min} \end{bmatrix} \leq \mathbf{T}_I \mathbf{x}_m(k_i) + \underbrace{\mathbf{T}_L \begin{bmatrix} \mathbf{A}_d \\ \mathbf{A}_d^2 \\ \vdots \\ \mathbf{A}_d^{N_c-1} \end{bmatrix}}_{\mathbf{F}_x} \Delta\mathbf{x}_m(k_i) + \underbrace{\mathbf{T}_L \begin{bmatrix} \mathbf{B}_d \\ \mathbf{A}_d \mathbf{B}_d \\ \vdots \\ \mathbf{A}_d^{N_c-1} \mathbf{B}_d \end{bmatrix}}_{\mathbf{\Phi}_x} \Delta\mathbf{U} \leq \begin{bmatrix} \mathbf{x}_{\max} \\ \mathbf{x}_{\max} \\ \vdots \\ \mathbf{x}_{\max} \end{bmatrix}. \quad (3.112)$$

Now the optimization problem can include inequality constraints and be written as a standard QP problem of the form,

$$\begin{aligned} \min_{\Delta\mathbf{U}} \quad & \frac{1}{2} \Delta\mathbf{U}^T \mathbf{H} \Delta\mathbf{U} + \Delta\mathbf{U}^T \mathbf{K}, \\ \text{s.t.} \quad & \mathbf{M} \Delta\mathbf{U} \leq \mathbf{y}. \end{aligned} \quad (3.113)$$

By isolating $\Delta\mathbf{U}$ in (3.111) and (3.112), the matrix \mathbf{M} and the vector \mathbf{y} represent the inequality constraints. To summarize, the block diagram of the CCS-MPC is represented in Figure 3.31.

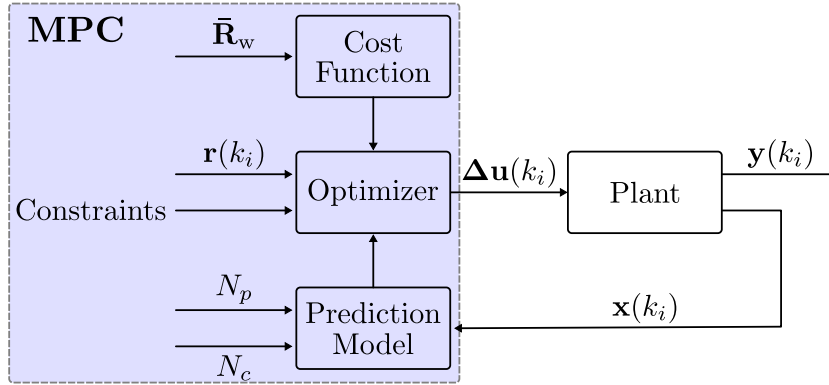


Figure 3.31: Block diagram of CCS-MPC

3.5.3 Design of unconstrained MPC

Designing the MPC algorithm is not straightforward, especially in MIMO systems, due to the high number of DOFs available. However, the following parameters represent the minimal set required for proper tuning:

- Weighting factor on control input – r_w
- Prediction horizon – N_p
- Control horizon – N_c

While the horizons are ambiguous to all states, the weighting factors are tuned separately for each control input. Tuning of MPC is itself a research topic. A review of available methods is provided in [175]. Further optimization technique leads to automated tuning as exemplified in [176]. Alternatively, application-targeted practical guidelines can be explored to simplify this task [177]. For this application, the tuning is done, s.t. the resulting closed-loop offers the desired performances. To do so, first the unconstrained MPC is considered, where the choice of tuning parameters will result in an algebraic optimal solution (3.107). After applying the control law, the closed-loop performance is evaluated.

The main objective of applying MPC to control the average energy in the MMC arms is to ensure the required energy levels, independent of the grid interface action. Hence a long horizon is considered. For instance, with $T_s = 1/250$ Hz, and a $N_p = 20$, it is aimed to fulfill the control objectives within five grid periods. Generically, higher prediction horizons lead to slower dynamics [178]. For the total energy, this would lead to increasing power decoupling effect. However, two tuning parameters remain. Through a grid search of weighting matrix and control horizon, a compromise between robustness and bandwidth is to be obtained. This exemplified for the total energy dynamics (3.94) and (3.95) in Figure 3.32 and

Figure 3.33. Notice, only stable solutions are provided.

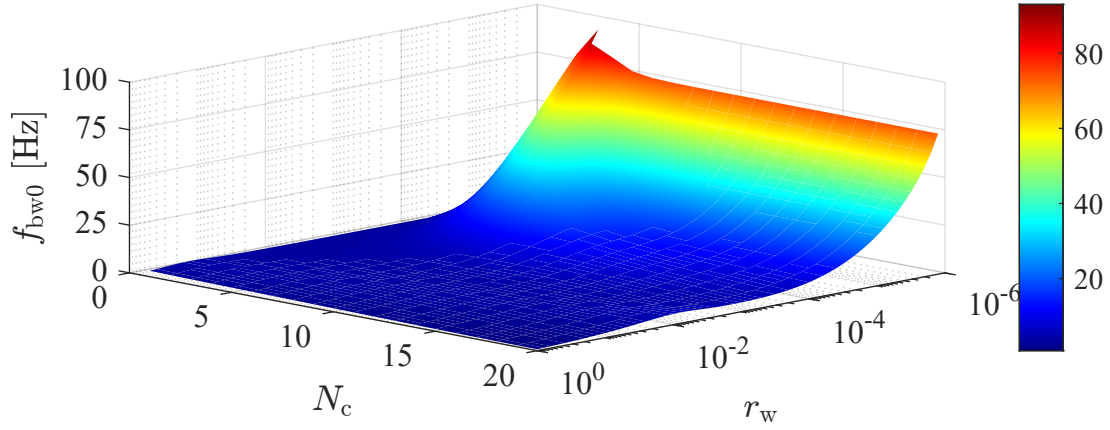


Figure 3.32: Tuning unconstrained MPC: Resulting closed-loop bandwidth with $N_p = 20$ and varying r_w and N_c

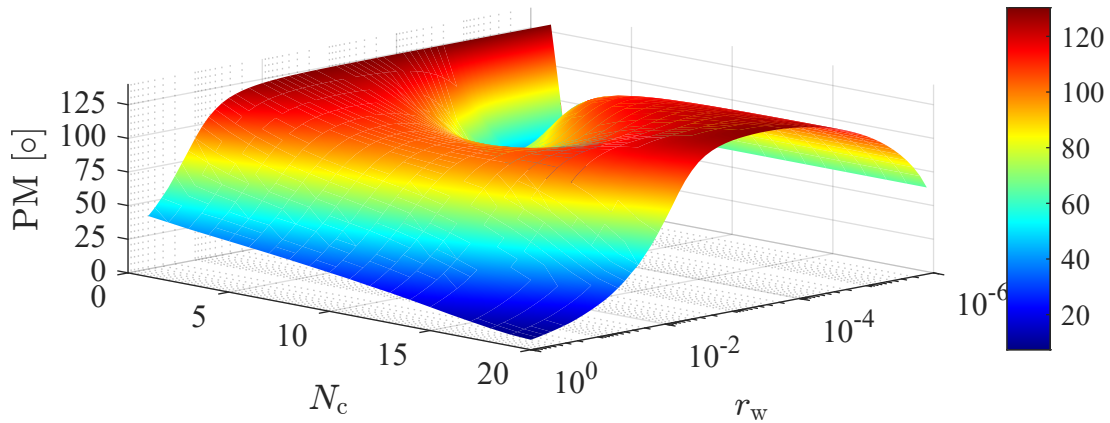


Figure 3.33: Tuning unconstrained MPC: Resulting closed-loop phase-margin with $N_p = 20$ and varying r_w and N_c

oles of the unconstrained closed-loop system

In contrast to the previous subsection, the resulting unconstrained closed-loop system yields two additional zeros in its transfer function, which arise from the inclusion of integral action in the augmented system model. The location of the last depend on the tuning parameters. While the control weight shapes influences both performance and robustness, the control horizon practically relates only to the phase-margin, whereas higher N_c leads to lower robustness. As suggested in [178], low control horizons result in higher robustness. The last is chosen to be $N_c = 5$. Furthermore, after fixing both horizons, the only tuning parameter remaining for rest of the energy states is the r_w . Its choice follows the same methodology.

3.5.4 Design of constrained MPC

In the final MPC implementation, the optimal control increment $\Delta \mathbf{U}$ is initially computed using the analytical solution of the unconstrained problem. As long as all constraints remain inactive, this solution is applied directly. However, the underlying formulation is a constrained MPC problem, and the control input is recomputed by solving the corresponding constrained QP whenever constraints become active. Therefore, choosing the system constraints completes the design of the control algorithm. It is trivial to define the arm energy upper and lower bounds, due to its physical resemblance to the available voltage in the arm. However these must be expressed in the $\alpha\beta$ frame and as $\Sigma\Delta$ components. To achieve this, all possible vector combinations of the upper and lower bounds of the arms are generated. After applying matrix (A.19), the minimum and maximum values are extracted to define the new lower and upper bounds. For instance, considering $\pm 10\%$ on each arm energy per unit would result in

$$\mathbf{W}_{\min} = \begin{bmatrix} W_{\Sigma\alpha,\min} \\ W_{\Sigma\beta,\min} \\ W_{\Sigma 0,\min} \\ W_{\Delta\alpha,\min} \\ W_{\Delta\beta,\min} \\ W_{\Delta 0,\min} \end{bmatrix} = \begin{bmatrix} -0.2667 \\ -0.2309 \\ 1.8000 \\ -0.2667 \\ -0.2309 \\ -0.2000 \end{bmatrix} \quad \mathbf{W}_{\max} = \begin{bmatrix} W_{\Sigma\alpha,\max} \\ W_{\Sigma\beta,\max} \\ W_{\Sigma 0,\max} \\ W_{\Delta\alpha,\max} \\ W_{\Delta\beta,\max} \\ W_{\Delta 0,\max} \end{bmatrix} = \begin{bmatrix} 0.2667 \\ 0.2309 \\ 2.2000 \\ 0.2667 \\ 0.2309 \\ 0.2000 \end{bmatrix}$$

For the state $W_{\Sigma 0}$, the DC and AC power variables are not constrained directly. Instead, their admissible ranges are determined indirectly from time-varying current limits, e.g., during voltage sag conditions. Once these limits are computed, they define lower and upper bounds on the corresponding power variables. Hence, within the MPC formulation, the power constraints are introduced as element-wise inequalities of the form

$$P_{\min} \leq P \leq P_{\max},$$

which constitute box constraints. Although the underlying physical feasibility region is induced by current magnitude limitations and is therefore coupled, its representation in the optimization problem is given by time-varying upper and lower bounds on each power component. Based on (3.57), the reference current saturation function yields

$$I_{\text{dc,max}} = \begin{cases} I_{\text{dc}}^*, & \text{if } |I_{\text{dc}}^*| \leq I_{\text{dc,limit}} \text{ or } I_{\text{dc,limit}} = 0, \\ \text{sign}(I_{\text{dc}}^*) \cdot I_{\text{dc,limit}}, & \text{if } |I_{\text{dc}}^*| > I_{\text{dc,limit}} \text{ and } I_{\text{dc}}^* \neq 0. \end{cases} \quad (3.114)$$

and the upper and lower bound are

$$P_{dc,max} = U_{dc} I_{dc,max} \quad P_{dc,min} = -P_{dc,max}$$

For the active and reactive power limitation, the function (3.114) would simply saturate the peak amplitude of the grid sinusoidal currents. In order to limit the amplitude and maintaining a pure sinusoidal reference, a vector-based current saturation strategy is necessary. Consider $\mathbf{I}_g^* = \begin{bmatrix} I_{g\alpha}^* \\ I_{g\beta}^* \end{bmatrix}$ as the reference current vector from (3.58). Its Euclidean norm yields,

$$\|\mathbf{I}_g^*\| = \sqrt{(I_{g\alpha}^*)^2 + (I_{g\beta}^*)^2} \quad (3.115)$$

and $I_{g,limit}$ as the maximum allowable current magnitude. Considering the smoothing function

$$f(\mathbf{I}^*) = \begin{cases} 1, & \text{if } \|\mathbf{I}^*\| < I_{g,limit}, \\ \frac{I_{g,limit}}{\|\mathbf{I}^*\|}, & \text{otherwise.} \end{cases} \quad (3.116)$$

and applying it to the grid current reference vector

$$\mathbf{I}_{g,max}^* = f(\mathbf{I}^*) \cdot \mathbf{I}_g^* \quad (3.117)$$

scales down the vector while preserving its direction, in case the reference current exceeds the limit. Hence, the upper and lower bounds for the active and reactive power are defined as

$$P_{ac,max} = \frac{3}{2} (U_{g\alpha} I_{g\alpha,max}^* + U_{g\beta} I_{g\beta,max}^*)$$

$$P_{ac,min} = -P_{ac,max}$$

$$Q_{max} = \frac{3}{2} (U_{g\beta} I_{g\alpha,max}^* - U_{g\alpha} I_{g\beta,max}^*)$$

$$Q_{min} = -Q_{max}$$

The input vector can be constrained directly based on operational limits. Alternatively, the remaining $\Sigma\Delta$ components ($P_{\Sigma\alpha}, P_{\Sigma\beta}, P_{\Delta\alpha}, P_{\Delta\beta}, P_{\Delta 0}$) can be constrained indirectly through bounds on the rate of change of the stored energy, thereby ensuring admissible energy dynamics, i.e.,

$$P_{\Sigma\Delta,max} = \frac{\Delta W_{\Sigma\Delta,max}}{T_s} \quad P_{\Sigma\Delta,min} = -P_{\Sigma\Delta,max}$$

However, the last are not considered in this design. Lastly, the QP problem was solved using Hildreth's procedure [179] and a custom-made solver was developed for hardware implementation and tested in a simple Buck converter in [180, 181].

The developed solver includes an user interface for C-code generation for an embedded platform of choice.

In summary, Figure 3.29 is now updated to Figure 3.34 highlight the MPC algorithm responsible for the MMC outer loop.

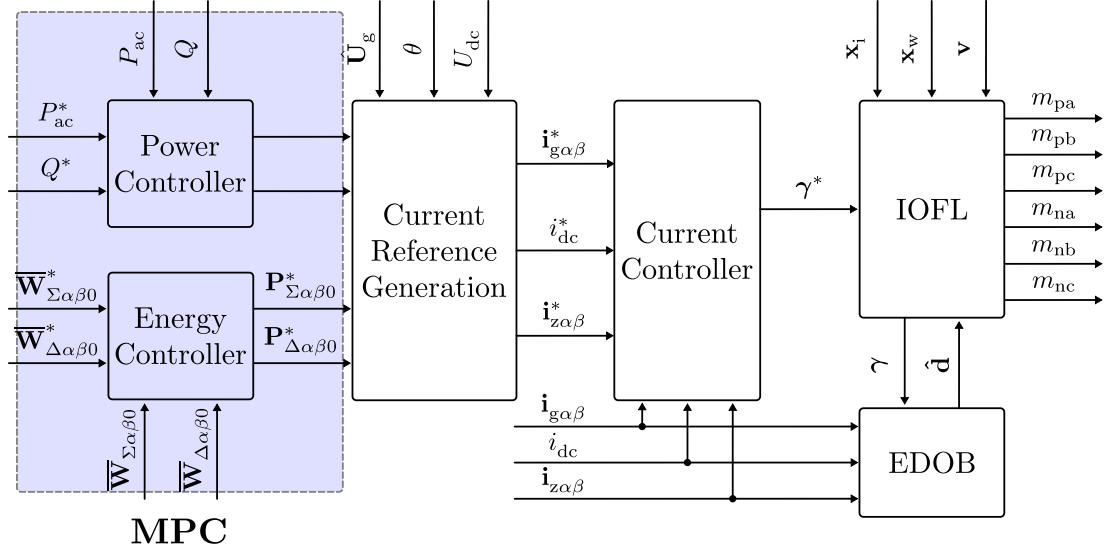


Figure 3.34: MMC controller block diagram: Outer loop designed via MPC

3.6 Results

In this subsection, the simulation and hardware implementation of the designed controllers is presented. Simulations are carried for an IPC between a MVDC and MVAC grids. Hardware demonstration is carried on a low-voltage low-power MMC prototype connected to a passive load. Lastly a PiL scheme is used to bridge simulation results and hardware implementation of control algorithms.

3.6.1 Simulation results

Using simulation, a first validation of the theory presented in this chapter is carried out for the control structure shown in Figure 3.29. The circuit parameters of the simulated IPC plant are provided in Table 3.2, and the control parameters are listed in Table 3.3. The bandwidth of the AC inner closed-loop is selected as 100 Hz. Owing to the feedback-linearized control structure, the current loop is intrinsically stabilized much faster, such that this bandwidth primarily determines the response to reference changes. This choice is consistent with the control architecture, in which the power controller is intentionally implemented as a static

gain to avoid introducing additional dynamics. While most control parameters are kept fixed, three scenarios with different i_{dc} transient performance are considered to demonstrate the power decoupling technique, leading to distinct total energy disturbance responses. The achievable i_{dc} dynamics are constrained by the installed C_{arm} , which is the main factor limiting the power decoupling capability.

Considering the first scenario, the results of a test routine for all desired function is given in Figure 3.35. First, the energy stored in the MMC increases 10% by request, smoothly and at desired transient performance. The response to an active power reference change (200 kW to 1 MW) is shown ($t = 1$ s). At first glance, all currents reach zero error steady-state. The AC-grid current reference is reached within half grid period, as desired. Despite the arm voltage oscillation

Table 3.2: Simulated plant - circuit parameter of medium voltage MMC

Symbol	Description	Value
U_{dc}	DC grid voltage	6000 V
\hat{U}_g	AC grid voltage	$\frac{\sqrt{2}}{\sqrt{3}} \cdot 3300$ V
f_g	AC grid frequency	50 Hz
L_{arm}	Arm inductance	3.19 mH
R_{arm}	Arm resistance	47 m Ω
C_{sm}	SM capacitor	2.3 mF
N_{sm}	Number of SM per arm	8
U_{Csm}	Average SM voltage	825 V

magnitude increase at higher power transfer, its amplitude remains bounded, as expected. The individual arm available voltage change depends on the time instance in respect to the grid period at which the reference change occurs. Hence, the energy controller must bring all arms back to the same reference, which is fully achieved. Additionally, circulating currents are kept entirely within the MMC. This is inspected in zoomed areas of the i_{dc} . Furthermore, both horizontal ($t = 1.5$ s) and vertical ($t = 2.5$ s) energy reference changes are tested.

Table 3.3: Control parameter used for simulation tests of loop shaping controller

Symbol	Scenario 1	Scenario 2	Scenario 3
ω_{dc}	$2\pi 67$ Hz	$2\pi 100$ Hz	$2\pi 150$ Hz
ω_{ac}		$2\pi 100$ Hz	
ω_z		$2\pi 100$ Hz	
ω_{rt0}		$2\pi 10$ Hz	
ζ_{rt0}		1	
$\omega_{rt\Sigma}$		$2\pi 10$ Hz	
$\zeta_{rt\Sigma}$		1	
$\omega_{rt\Delta}$		$2\pi 10$ Hz	
$\zeta_{rt\Delta}$		1	
ω_{dr0}	$2\pi 28$ Hz	$2\pi 42$ Hz	$2\pi 66$ Hz
$\omega_{dr\Sigma}$		$2\pi 50$ Hz	
$\omega_{dr\Delta}$		$2\pi 50$ Hz	

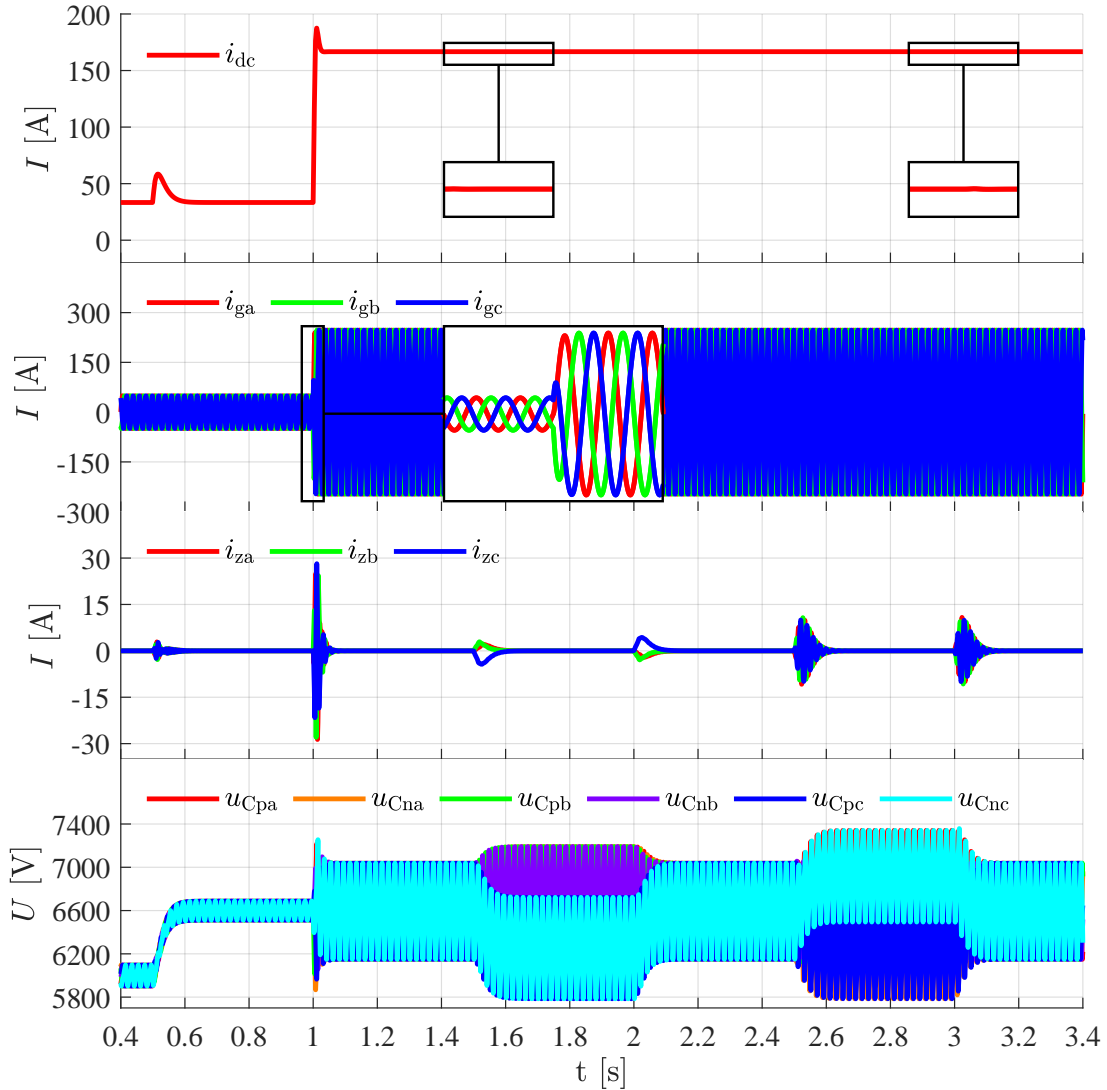


Figure 3.35: Simulated test setup for loop shaped controller – original states

An energy overview is provided in Figure 3.36. First an horizontal change is requested, where 10% of the energy in phase c is distributed equality in both other phases. Afterwards, a vertical reference change is requested. Hence, 5% of stored energy in u_{cna} is shifted to u_{cpa} . The opposite occurs for phase c while b remains at the same levels. In both cases, zero error steady-state is achieved and a smooth response without overshoot is obtained, as in critically damped second-order systems. Since the desired dynamics are achieved for the controller, this verifies the consistency of the IOFL theory. Next, the two alternative scenarios are compared in Figure 3.37. As expected, a higher ω_{dc} results in a shorter decoupling time. Consequently, less energy is drawn from the MMC in response to an active power reference change (from 200 kW to 1 MW). Despite these differences, the overall

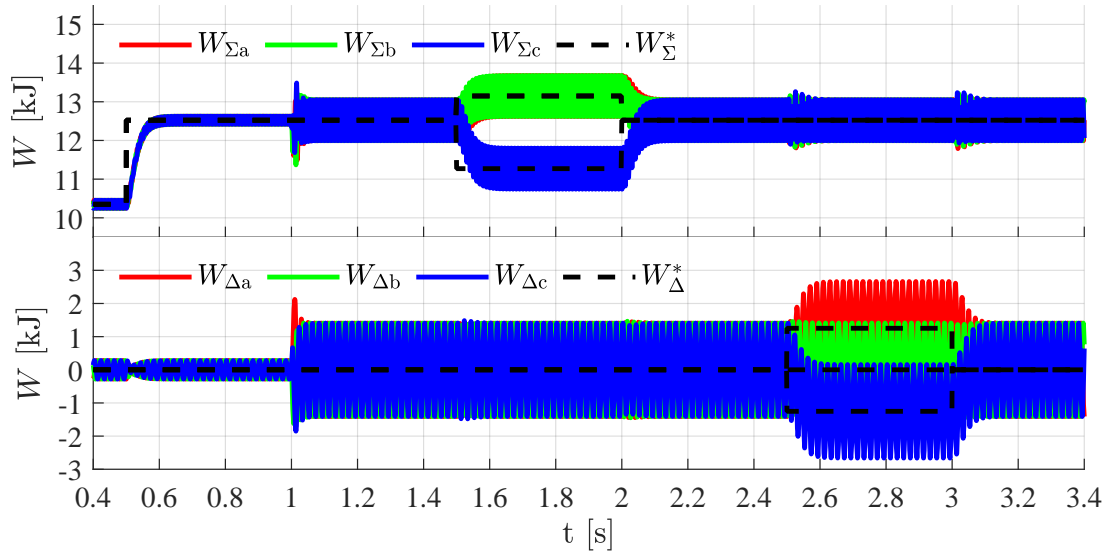


Figure 3.36: Simulated test setup for loop shaped controller - $\Sigma\Delta$ energy states in abc frame

shape of the energy usage profile remains consistent across all cases. The total energy peak deviation and settling time can be selected based on the information provided in Figure 3.23 and Figure 3.22. This enables straightforward tuning of the control parameters to match the specific requirements of the application. For instance, when interfacing weaker grids, the higher power decoupling should be emphasized.

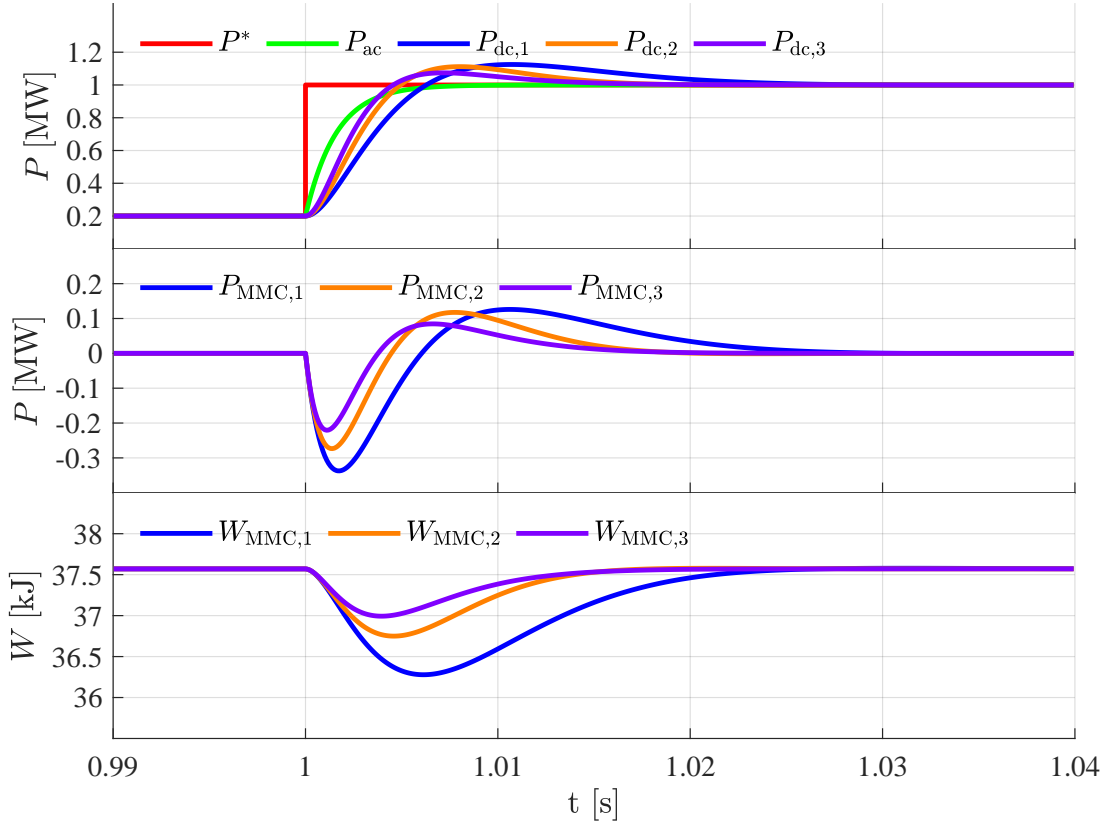


Figure 3.37: Power decoupling capability with loop shaping controller

3.6.2 Experimental results

Loop shaping

Up to this point, the analysis has been carried out for an ideal AAM of the MMC. In the following, the controller is validated on a small-scale hardware prototype, as shown in Figure 5.1. Its parameters are listed in Table 5.2. In the previous model, the effect of losses was not modeled. However for a medium voltage IPC, the line losses do play a major role and can be corrected by an outer controller. In this case, a passive load has been considered instead of an AC-grid. Therefore the current amplitude is directly controlled instead of active power. An additional integral term is assumed and results in the closed-loop behavior obtained in (3.73). Consequentially, fourth-order Bessel polynomial is obtained for the total energy disturbance response. With one additional parameter, the same process is repeated to obtain a similar behavior, as in scenario 1. This is shown in the following figures. Now, a symmetrical current amplitude reference change from 1.5 A to 3.5 A is requested.

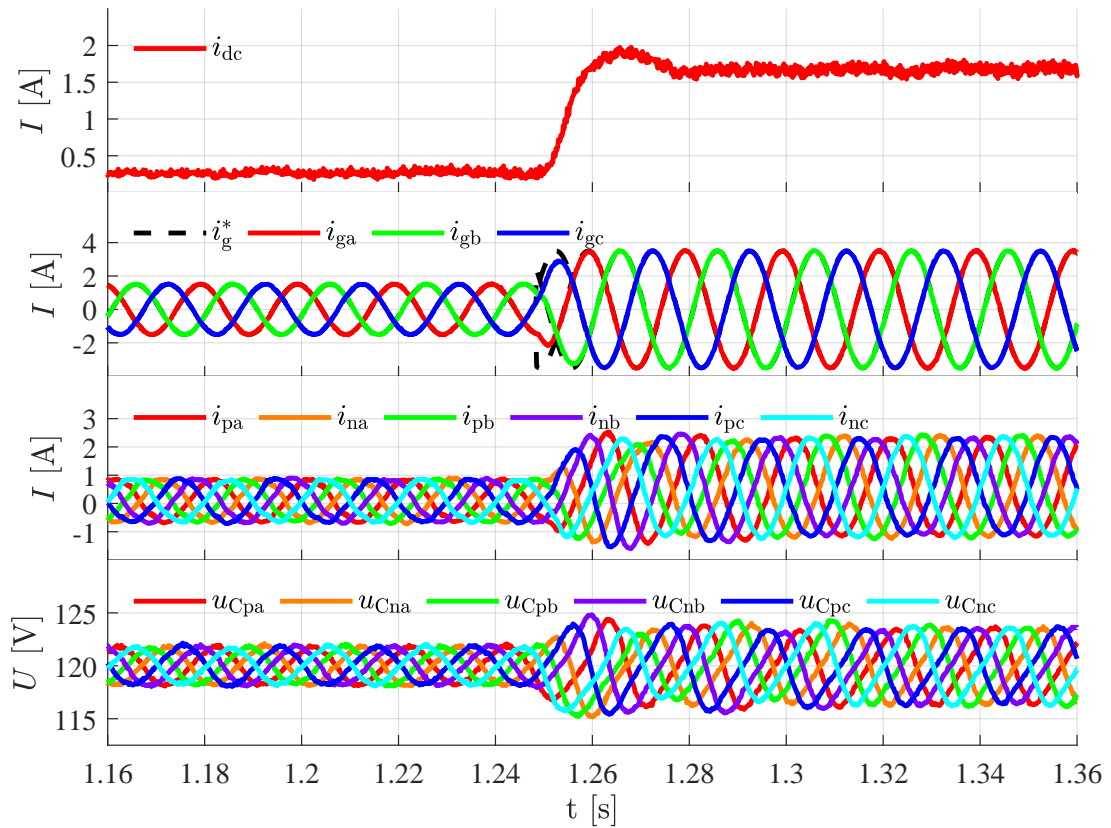


Figure 3.38: Current reference step response: 1.5 A to 3.5 A

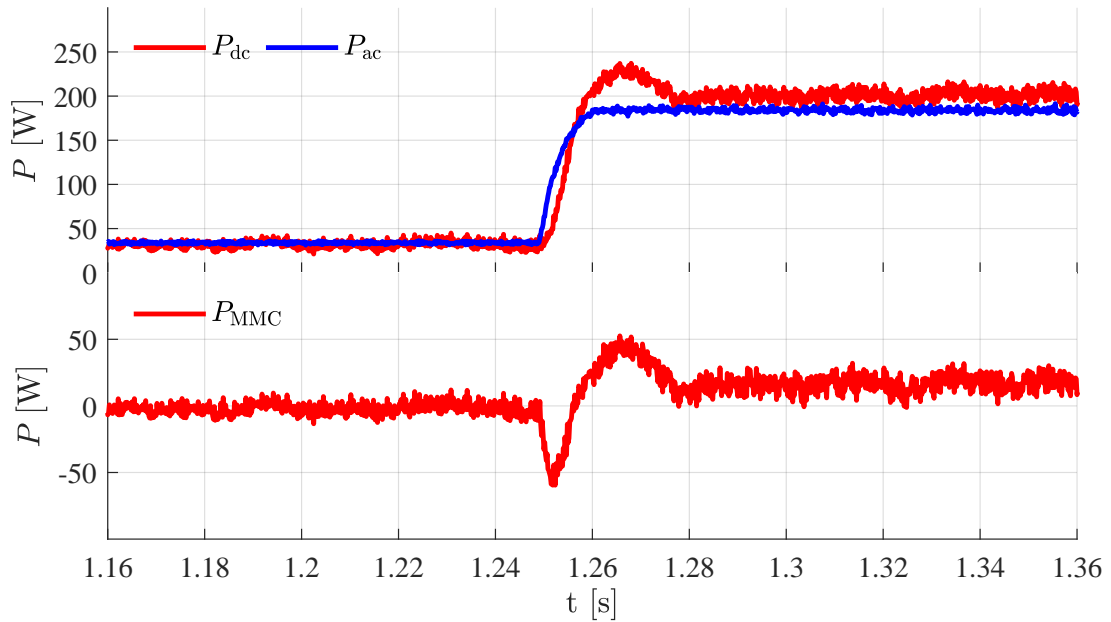


Figure 3.39: Power decoupling during a step response: 1.5 A to 3.5 A

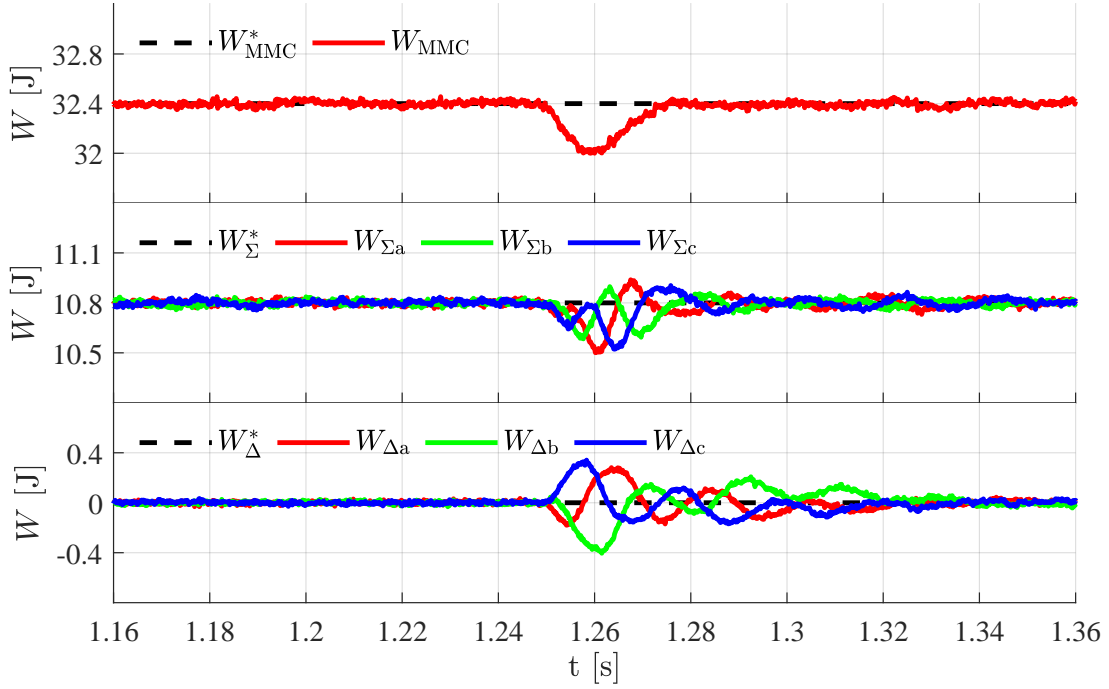


Figure 3.40: Energy disturbance response during step response: 1.5 A to 3.5 A

For the sake of completeness, a reference change is also applied to reduce the power. This ensures a comprehensive evaluation of the controller's response to both power increment and reduction. By analyzing both transitions, the system's performance is validated in practice, confirming the consistency of the IOFL theory across different operating conditions.

Afterward, the results in the following figures will demonstrate that the EDOB effectively maintains IOFL performance even under significant parameter variations. Specifically, in Figure 3.44, a load reduction of approximately 16% in phase c is applied at $t = 0.72$ s, introducing an imbalance in the 3PH load. While stable operation is preserved, this imbalance becomes evident not only in the arm currents but also in the average arm energies. At $t = 0.77$ s, the EDOB is activated, successfully correcting the imbalance and restoring system symmetry. This simple scenario validates the necessity of integrating the EDOB with the IOFL to enhance system performance. Together, they confirm the robustness of the control strategy, ensuring consistent dynamic behavior even under substantial parameter variations.

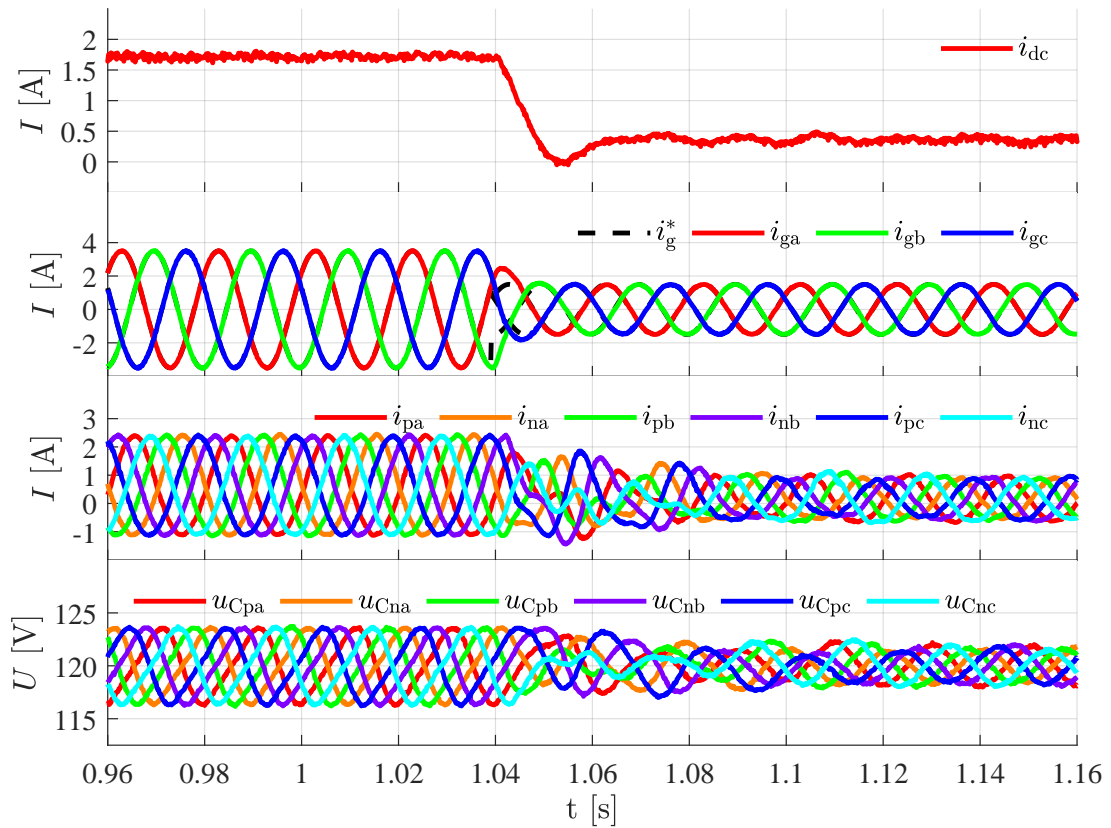


Figure 3.41: Current reference step response: 3.5 A to 1.5 A

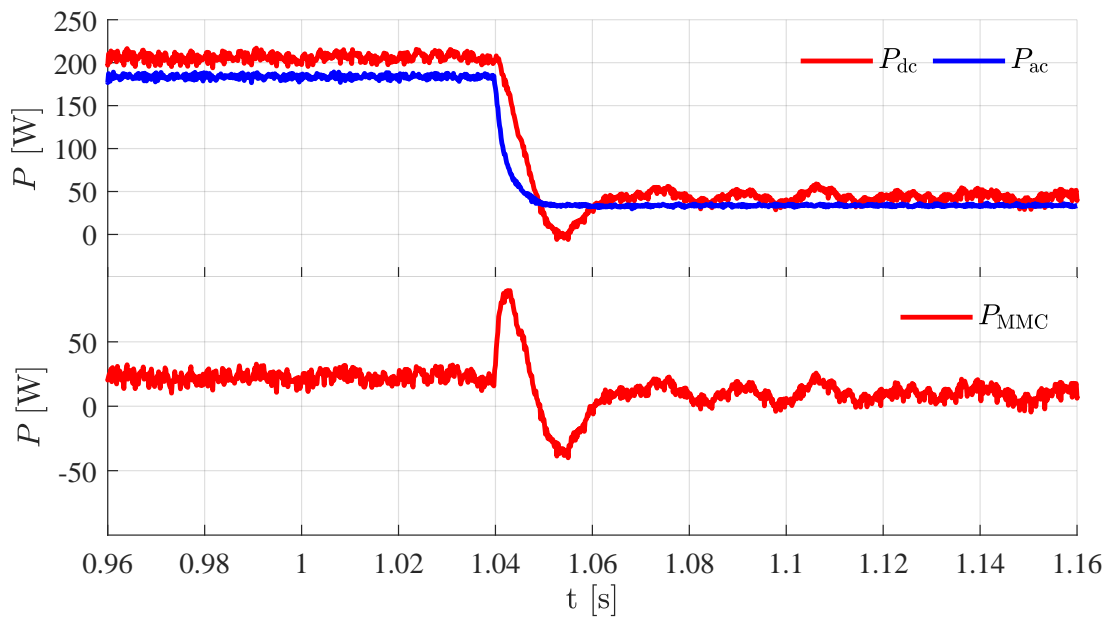


Figure 3.42: Power decoupling during a step response: 3.5 A to 1.5 A

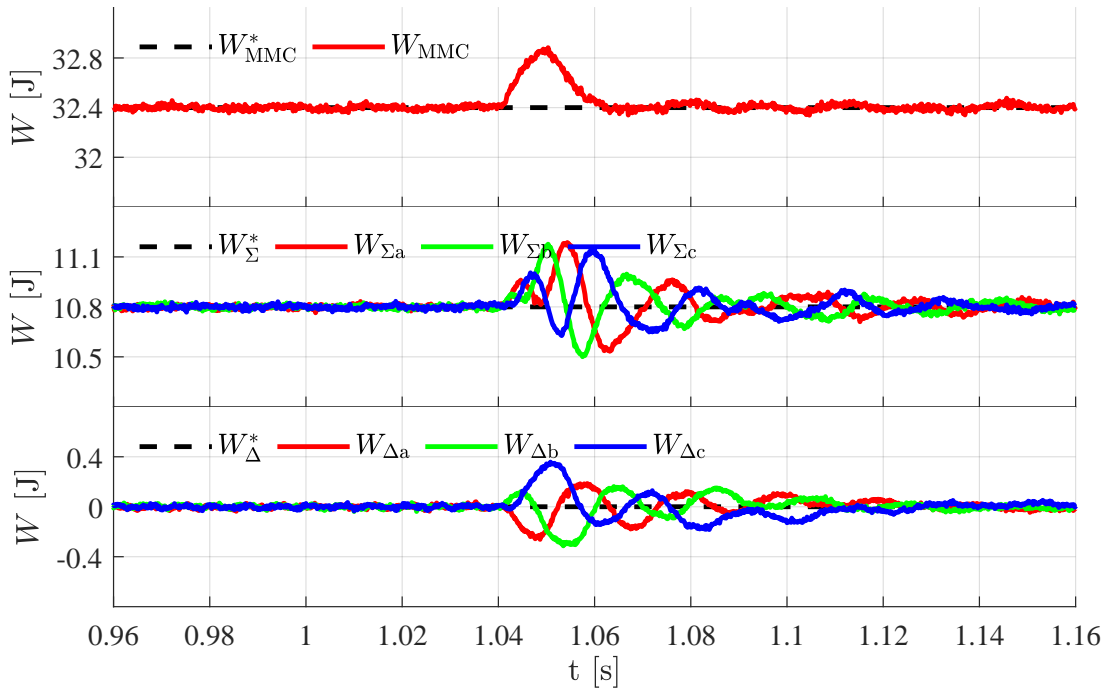


Figure 3.43: Energy disturbance response during step response: 3.5 A to 1.5 A

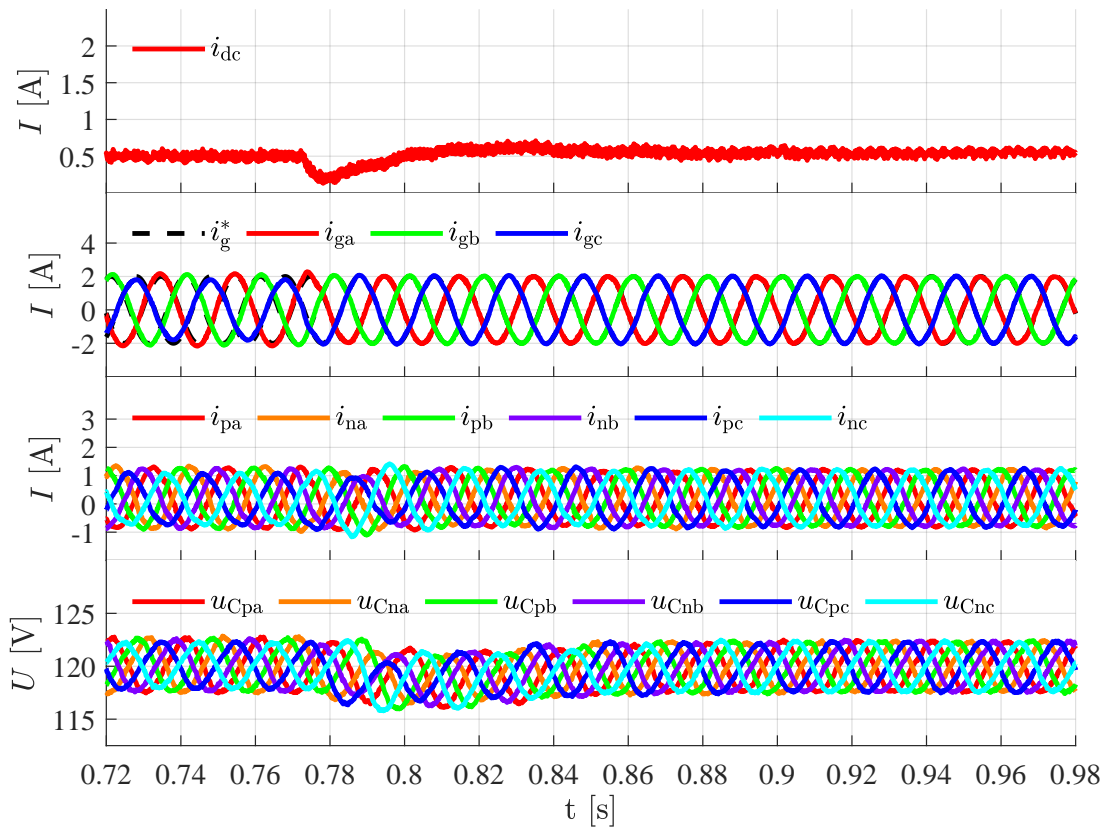


Figure 3.44: EDOB response during at 16% unbalanced load:

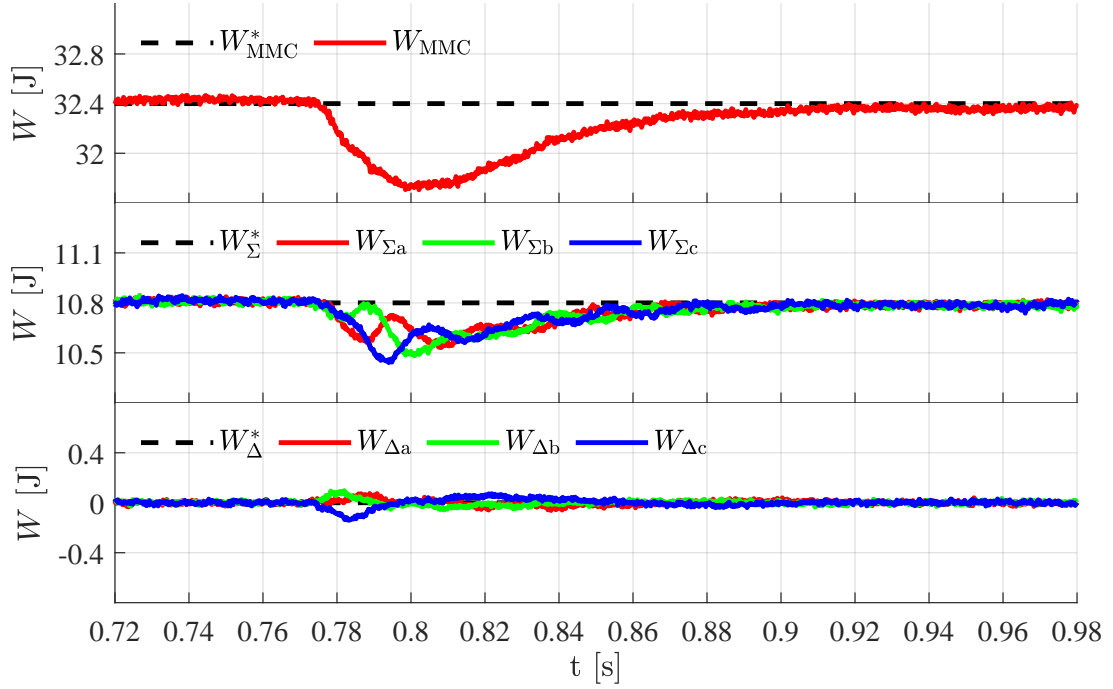


Figure 3.45: EDOB effect on energy disturbance at 16% unbalanced load

Hardware details are provided in Chapter 5. Further investigations and results at different operation points can be visited in [182].

Model Predictive Controller

The last algorithm to be analyzed is the linear MPC as structured in Figure 3.34. The results are obtained via PiL, where the setup is further explained in section 5.2. The sampling frequency is selected as 250 Hz to achieve a prediction horizon of approximately five grid periods. This choice limits the achievable control update rate, and therefore the outer-loop transient performance is reduced to maintain consistency with the simulation scenarios. Using the methodology described in subsection 3.5.3, the resulting tuning variables were chosen as in Table 3.4.

The same simulated test routine presented in Figure 3.35 is now given in Figure 3.46 for the MPC algorithm. Here the following state constraints are imposed:

- P_{ac}, Q_{ac}, P_{dc} do not surpass 5% of its reference value;
- W_{MMC} does differ 3% of its reference value;
- W_{Σ} and W_{Δ} cannot differ more than 12%.

Notice the first half are dynamic constraints, online adapted to the MMC's de-

Table 3.4: Desired closed-loop bandwidth for unconstrained MPC design

Symbol	Scenario 1
ω_{dc}	$2\pi \times 33 \text{ Hz}$
ω_{ac}	$2\pi \times 50 \text{ Hz}$
ω_z	$2\pi \times 50 \text{ Hz}$
ω_0	$2\pi \times 10 \text{ Hz}$
ω_Σ	$2\pi \times 10 \text{ Hz}$
ω_Δ	$2\pi \times 10 \text{ Hz}$
N_p	20
N_c	5
\bar{R}_W	$\begin{bmatrix} 1 & 1 & 0.01 & 0.01 & 0.01 & 0.01 & 0.01 & 0.01 \end{bmatrix}$

sired operation point, while the rest is fixed, as the remaining $\Sigma\Delta$ components ($P_{\Sigma\alpha}, P_{\Sigma\beta}, P_{\Delta\alpha}, P_{\Delta\beta}, P_{\Delta 0}$) are usually regulated to zero.

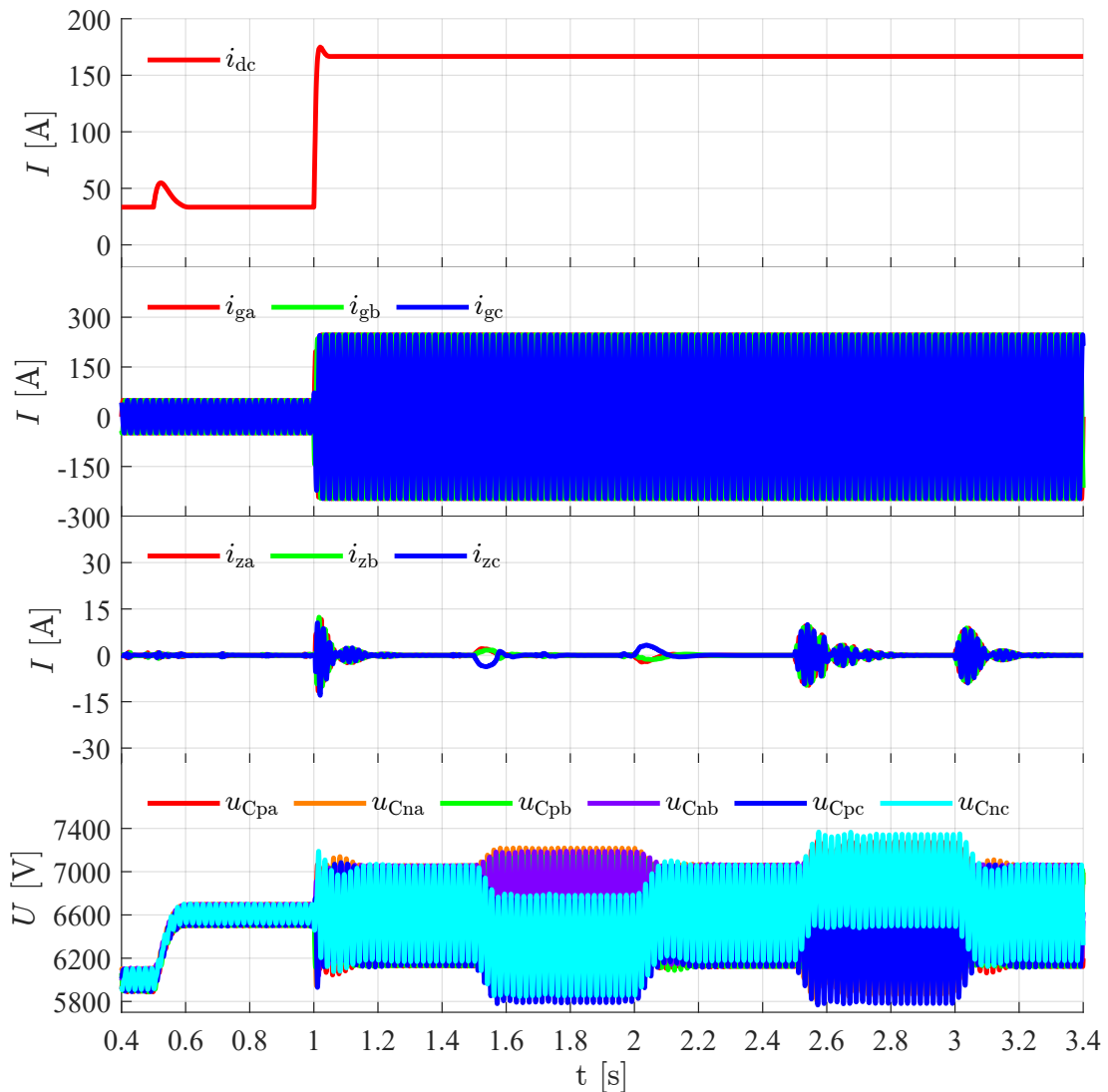


Figure 3.46: PiL test setup for MPC – original states

A detailed view of the response to an active power reference change at $t = 1$ s (200 kW to 1 MW) is shown in Figure 3.47. The results for both constrained (additionally indexed by C) and unconstrained (indexed by U) cases are presented. In both cases the active power reference is well tracked at the desired transient performance and the total energy returns to its reference. However, for the unconstrained case the imposed total energy constraint (in dashed lines) would be surpassed. In the constrained case, the limits are not surpassed. Consequently the power decoupling time is smaller. Since the energy cannot decrease below 3%, the input power must react faster—while still successfully respecting the imposed input power limits. Furthermore, both horizontal and vertical reference changes are investigated in Figure 3.48, which well tracked for both constrained

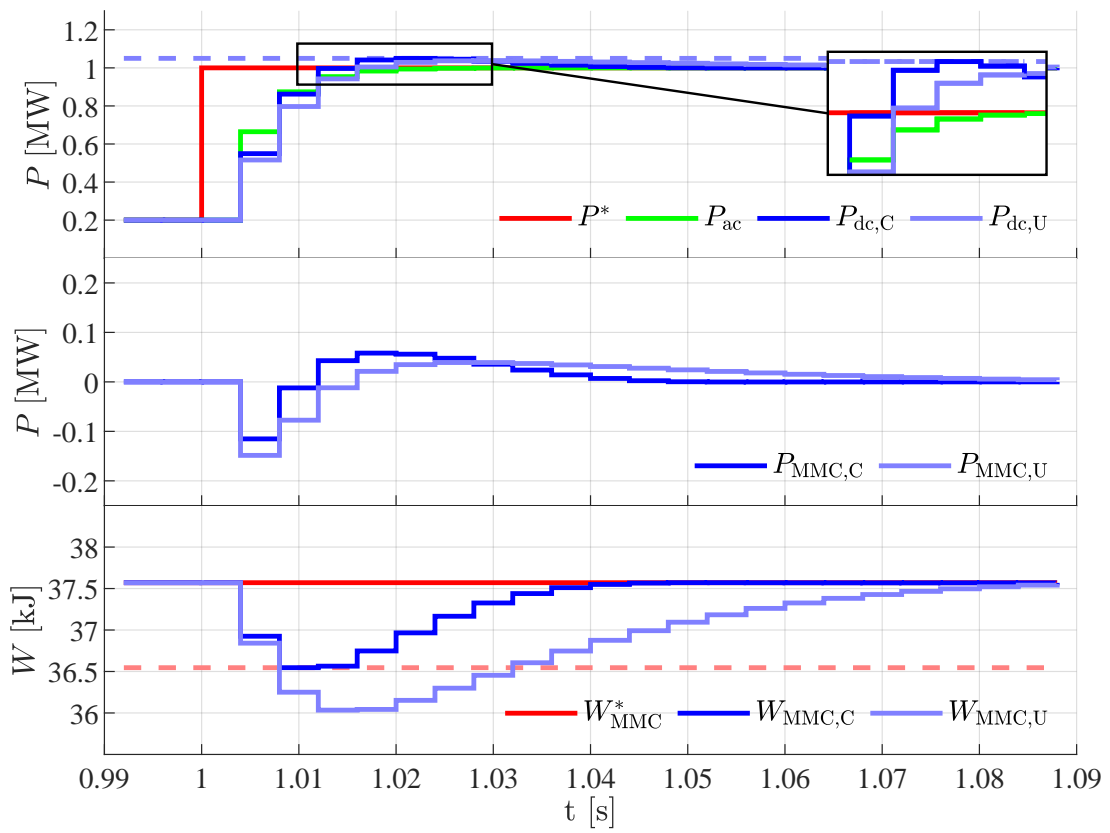


Figure 3.47: PiL test setup for MPC – power decoupling

and unconstrained case. Although, the desired transient time is closely achieved for both cases, a slight overshoot is unavoidable. This is due to the resulting zeros in augmented model used to design the MPC algorithm. Furthermore for both cases a residual steady-state error in the zero vertical component persists. This remains as a point for further investigation.

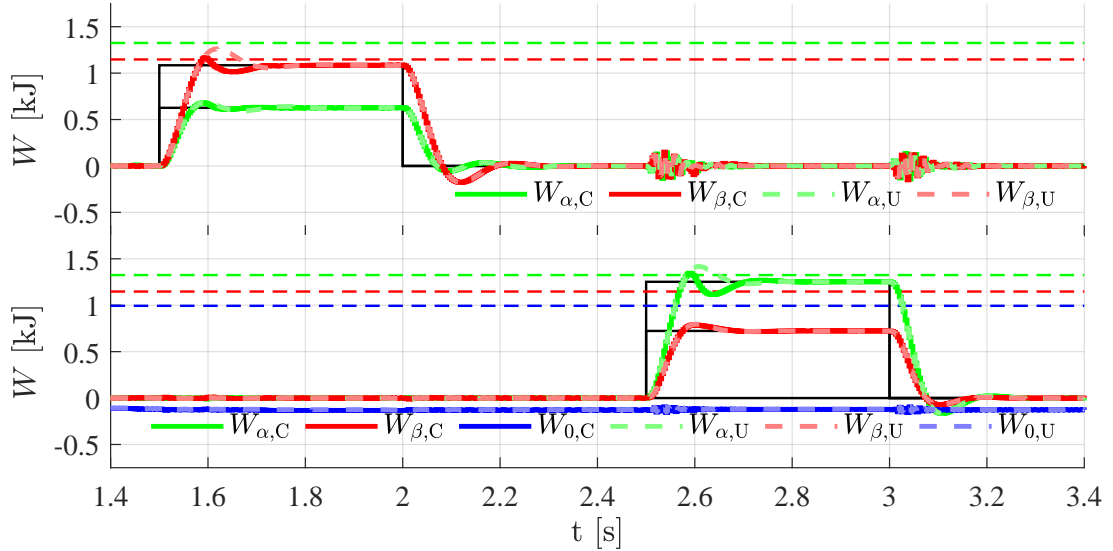


Figure 3.48: PiL test setup for MPC – horizontal and vertical energy

The results originate from the implementation of the MPC algorithm on an embedded target, as C-code running on the processor core of a Zynq-7020 System-On-Chip (SoC). As previously highlighted, the conception of solver algorithm is a research topic itself. Here, the main goal is to assess the performance and feasibility of the designed algorithm in a low-cost platform. Therefore, the test-scenario in Figure 3.46 is carried-out in the PiL test setup, at different prediction and control horizons, all leading to stable operation. Most importantly, the processing time required to execute the MPC algorithm are measured. Here, two distinguishable processing times are highlighted:

- Peak processing time during a transient event – $\hat{T}_{\text{exe},t}$
- Peak processing time during in steady state – $\hat{T}_{\text{exe},s}$

The results are summarized in Table 3.5. In the first four tests, the unconstrained MPC performance was investigated. Here, the processing time never surpasses the controller sampling time ($T_s = 4$ ms) and its processing time remains constant for different prediction and control horizons. As expected, transient events already lead to increased processing times. Nevertheless, it is important to highlight the role of the compiler optimization capability. Simply by using the first level of optimization available (O1), the processing time is reduced to 50%. Further op-

timization levels would require more hardware processing resources, which were not available. Such optimization plays a more important role for constrained cases. Comparing test C1 and C2, the value decreases to approximately one-fourth. Surprisingly to notice, for control horizons closer to the prediction horizon, the processing time increases. The last, naturally increases with control horizon (N_{c1}). Alternatively, the control horizon can remain and the horizons at which the constraints are employed (N_{c2}) can be reduced. This is considered in C7 and C8 and plays a major role on the execution time. Lastly, for lower control horizons a further optimization level was possible to obtain. However comparing C7 and C10, the performance increment is not significant.

Table 3.5: MPC Test performance metrics (Execution times in ms)

Test	N_p	N_{c1}	N_{c2}	$\hat{T}_{\text{exe,t}}$	$\hat{T}_{\text{exe,s}}$	O-Level
U1	20	20	-	2.688	0.019	None
U2	20	20	-	1.015	0.008	O1
U3	15	15	-	1.015	0.008	O1
U4	10	10	-	1.015	0.008	O1
C1	20	5	5	164.215	10.660	None
C2	20	5	5	45.878	3.114	O1
C3	15	5	5	99.749	4.226	O1
C4	10	5	5	111.447	8.671	O1
C5	10	3	3	28.891	1.323	O1
C6	15	3	3	11.145	0.936	O1
C7	20	5	3	5.746	0.744	O1
C8	10	3	2	4.341	0.374	O1
C9	20	2	2	4.542	0.323	O1
C10	20	3	3	5.723	0.682	O2

Although the implementation did not meet real-time constraints on the chosen embedded target, as the execution time exceeded the sampling interval, these results highlight the importance of a PiL test setup to assess hardware suitability and to identify computational bottlenecks in the control algorithm for step-by-step optimization. Nevertheless, the provided results prove the suitability of the MPC algorithm to obtain the power decoupling feature.

4 High Step-Down Transformerless Capability

This section explores another interesting feature of the MMC topology, highlighting its low voltage gain capability in MVDC and HVDC applications. Unlike traditional DC-DC topologies (Figure 1.10a) or series-parallel arrangements of galvanically isolated converters (Figure 1.14c), the MMC enables a configurable step-down operation, allowing a transformer-free interface between MVDC and LVDC grids. Interestingly, its primary motivation originates from the second SDGs in Figure 1.1, which is briefly discussed in the following subsection. Afterwards, the step-down transformerless concept is introduced. Due to the adopted switching scheme, the MMC cannot be directly treated as an AAM—a limitation that is addressed in the proposed solution. However, this led to the development of an accurate reduced-order model, whose derivation is explained in detail. The resulting model enables the implementation of an adaptive control strategy, complementing the control algorithms outlined in previous section. Finally, simulation and experimental results are presented to validate the proposed concepts.

4.1 Concept

4.1.1 Complementary motivation

The global rise in population and urbanization has increased concerns about the preservation of environmental resources and the sustainable production of food. In response, the development of fully automatic, highly efficient and zero-emission agricultural machinery represents a significant progress toward Precision Farming concepts [183]. Traditionally, achieving electrification in such machinery involves the use of substantial battery banks installed on tractors, resulting in a bulky, heavy, and costly setup. Hence belonging to the "Hard-to-electrify" group. As a solution, these machines could remain cable-connected to the electrical grid when working in a limited perimeter and use its battery to move between working fields. A feasibility study exploring this concept is discussed in greater detail in [184]. Given the high power demand in agriculture, this electrification concept benefits

from the deployment RES. Such combination results in semi-stationary energy storage and reduces the main grid dependence, as explained in the introduction chapter. The outcome is a more sustainable and economically viable operation, as elaborated in [185]. For the reasons highlighted in subsection 1.1.2, considering a DC-grid integrating RES, ESS and electrically-driven loads directly offers greater efficiency potential. The project GridCON researches this possibility [186].

4.1.2 Mobile Side Converter

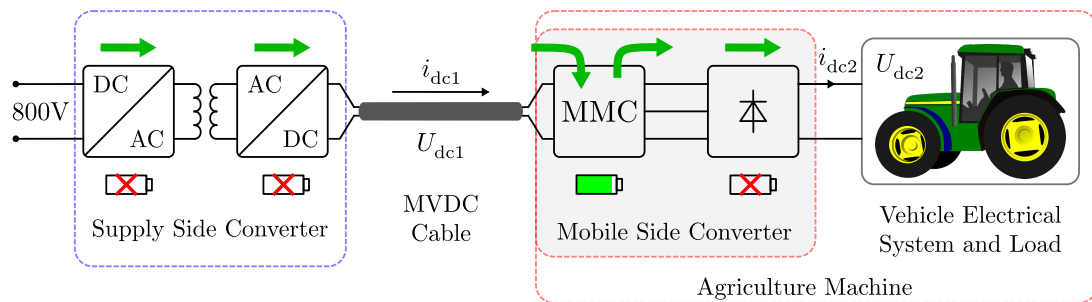


Figure 4.1: Project GridCON – System overview

In this electrification concept, represented in Figure 4.1, each agricultural machine is supplied by a MVDC bus. In this way, transmissions losses throughout the supplying cables are reduced. This isolated DC-microgrid is created with the help of a galvanic isolated boost converter, named Supply Side Converter (SSC). To comply with the vehicle's electrical system requirements, a unidirectional transformerless, MMC-based DC-DC converter is used to step-down the MVDC (U_{dc1}) to a lower DC voltage level (U_{dc2}), here named MSC. This topology, embedding a MMC and diode rectifier is represented in Figure 4.2.

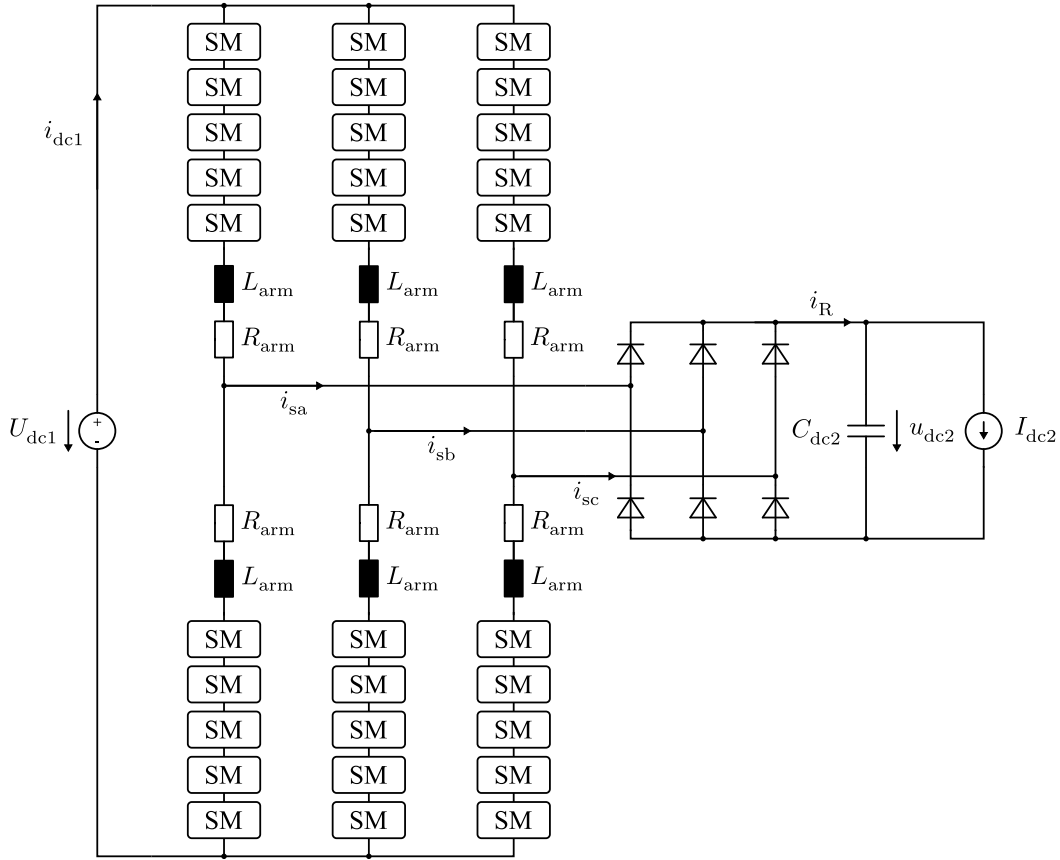


Figure 4.2: Mobile Side Converter MSC

4.1.3 Voltage step-down

To better illustrate the high-voltage step-down capability, consider a more detailed representation of the arm voltage generation, as discussed in Subsections 2.1.2 and 2.1.3. In typical HVDC applications with multiple submodules per arm, NLM is a natural choice due to its minimal switching frequency. When applied to a 7L-MMC, the resulting upper and lower arm voltage waveforms are shown in Figure 4.3. Assuming ideally balanced submodules, the natural switching sequence for both arms in the first half-cycle of the fundamental grid frequency is provided in the same figure.

For a small number of submodules, it is common practice to utilize all available submodules to achieve the highest possible output voltage quality. Essentially, at any given time, half of the available submodules per phase are inserted. From the perspective of U_{dc1} , the MMC effectively operates as virtual a capacitor bank with N_{sm} capacitors in series, resulting in an evenly divided voltage distribution.

Legend:

- SM bypassed (OFF)
- SM inserted (ON)
- Upper Arm voltage - u_{px}
- Lower Arm voltage - u_{nx}
- - - Differential Arm voltage - u_{sx}

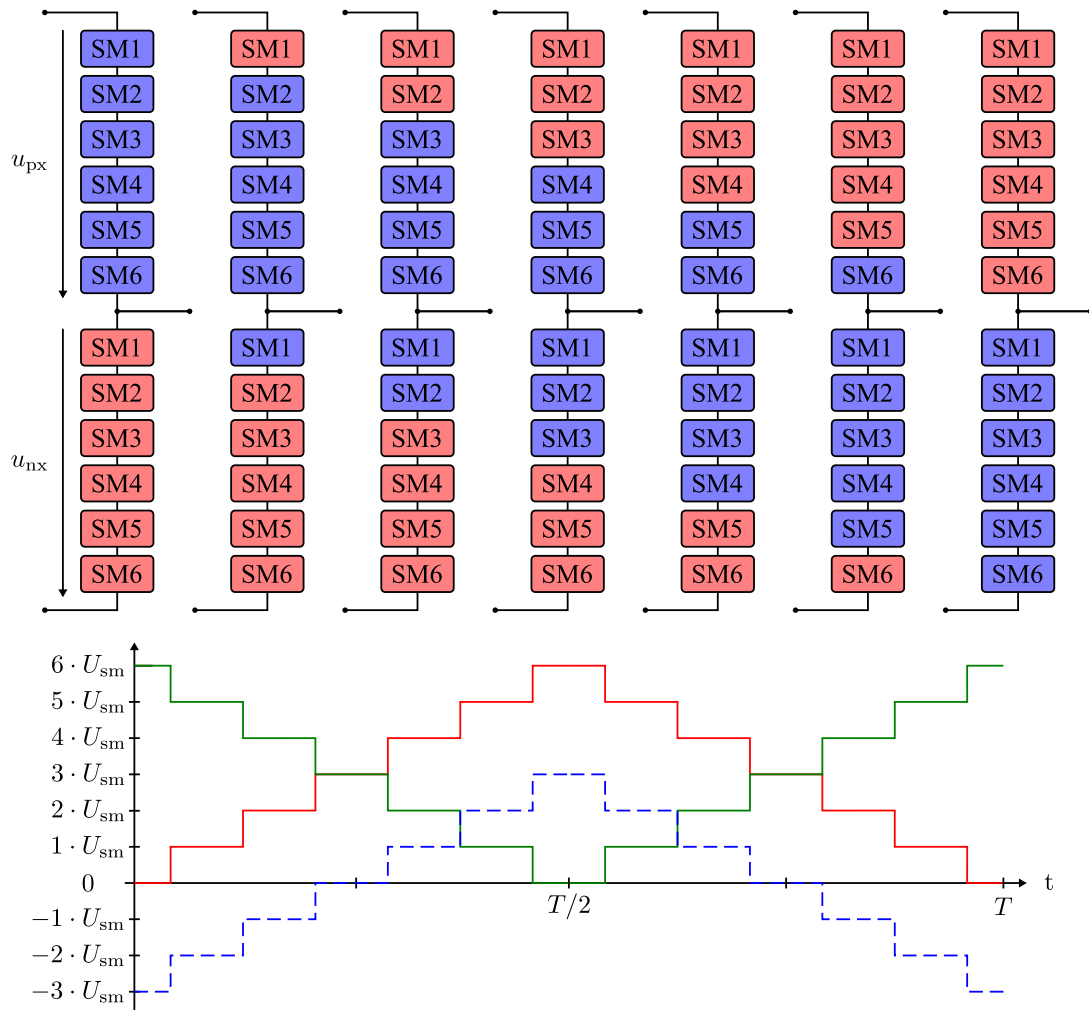


Figure 4.3: Nearest Level Modulation principle - full submodule usage

Hence, the average submodule voltage yields,

$$U_{C_{sm}} = \frac{U_{dc}}{N_{sm}}. \quad (4.1)$$

Additionally, (4.1) normally provides the submodules capacitor rated voltage. Else, for the application presented in the previous chapter, (2.13) should be considered.

Increasing the number of inserted submodules results in a larger number of series-connected capacitors, causing the same U_{dc1} to be distributed across N_{ins} submodules per phase and thereby reducing the voltage stress per submodule. However, this reduces the number of available voltage levels for modulation, leading to a degradation in output voltage resolution, as illustrated in Figure 4.4. Accordingly, the number of achievable levels is now given by

$$N_L = 2N_{sm} - N_{ins} + 1 \quad (4.2)$$

and (2.13) must be updated to include this variation, yielding

$$U_{C_{sm}} = \frac{U_{dc}}{N_{ins}} \quad \text{where, } N_{sm} \leq N_{ins} \leq 2(N_{sm} - 1). \quad (4.3)$$

In this example, the impact of partial submodule usage is presented in Table 4.1. Firstly, inserting more submodules offers an effective lower voltage gain, which is necessary to step from MVDC to LVDC efficiently. Secondly, at the component level, the required submodule-rated voltage decreases with N_{ins} . Therefore, this leads to a reduction in volume, which is particularly beneficial given the importance of power density in this application. Additionally, the same table presents various design options, utilizing different numbers of submodules. As discussed in [187, 188], evaluating the trade-off between volume and cost is essential. The selected design choice is highlighted in Table 4.1

Although the resulting 3L output waveform would not be acceptable for an IPC, this is not the case when the voltage is rectified and the MSC operates as DC-DC converter. In fact, the Single-Active-Bridge (SAB) operates in similar fashion and has been deployed for higher power applications [189, 190]. From the operation point of view, it can only operate in buck mode, which limits its operation voltage range. For most galvanic isolated high-power topologies, deviating much from a unit gain operation, results in design challenges, specially at the power transformer side. In the next section, an alternative simple modulation is introduced to enable the desired output voltage.

Legend:

- SM bypassed (OFF)
- SM inserted (ON)
- Upper Arm voltage - u_{px}
- Lower Arm voltage - u_{nx}
- - - Differential Arm voltage - u_{sx}

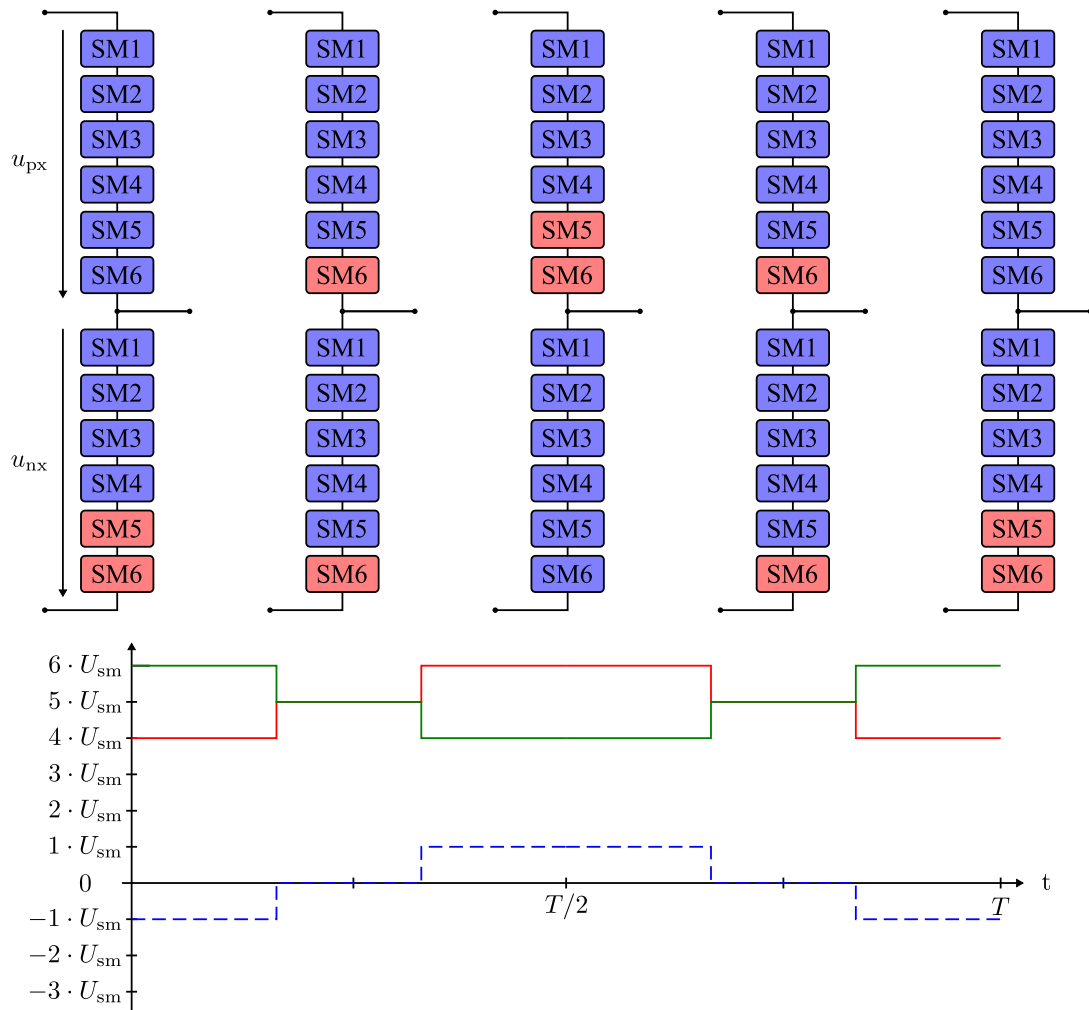


Figure 4.4: Nearest Level Modulation principle - partial submodule usage

Table 4.1: Impact of partial submodule usage

U_{dc} [V]	N_{sm}	N_{ins}	N_L	U_{Csm} [V]
6000	4	4	5	1500
		5	4	1200
		6	3	1000
	5	5	6	1200
		6	5	1000
		7	4	857
		8	3	750
		6	7	1000
	6	7	6	857
		8	5	750
		9	4	667
		10	3	600

4.2 Block modulation

In the MSC, the Block Modulation (BM) technique is employed to simultaneously convert DC voltage into AC voltage while stepping down its amplitude. This modulation effectively enables the MMC to operate equivalently as a 3L controllable voltage source. Essentially, the BM makes use of a single triangular carrier and $N_L - 1$ modulation indexes per phase to obtain the submodule's gating signals. For this application, only two modulation indexes are applied, namely m_{px} for the upper- and m_{nx} for the lower arm. These are kept fixed for an entire carrier period $T = 2\pi/\omega$ for minimal switching actions and ideally share equal amplitude to reduce circulating current and inrush of DC current from the MVDC bus, as explained in section 2.2. Considering an inverse half-wave symmetry, a bipolar square wave with adjustable pulse width is obtained for each arm. This principle and resulting voltage waveforms are given in Figure 4.5 for different modulation amplitudes. Assuming this represents phase a , the remaining phases b and c follow the same logic, however with a phase-shifted triangular carrier by $2\pi/3$ and $4\pi/3$, respectively.

Notice the modulation index width is inversely proportional to the pulse width. Considering all imposed symmetry constraints, it becomes straightforward to use a single control variable, the modulation index amplitude $m_u = 1 - m_{px}$ and

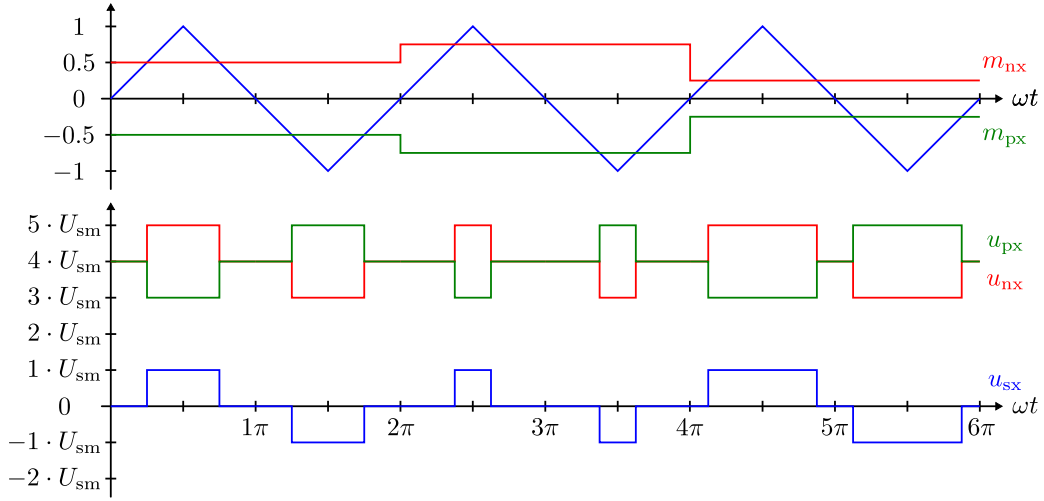


Figure 4.5: Block Modulation: Resulting upper, lower and differential voltage

$m_u = 1 - m_{nx}$, uniformly across all arms. The resulting differential voltage per phase can be expressed with the help of the following switching function,

$$S(\theta) = \begin{cases} 0, & 0 \leq \theta < \frac{\pi}{2}(1 - m_u) \\ +1, & \frac{\pi}{2}(1 - m_u) \leq \theta \leq \frac{\pi}{2}(1 + m_u) \\ 0, & \frac{\pi}{2}(1 + m_u) < \theta < \frac{\pi}{2}(3 - m_u) \\ -1, & \frac{\pi}{2}(3 - m_u) \leq \theta \leq \frac{\pi}{2}(3 + m_u) \\ 0, & \frac{\pi}{2}(3 + m_u) < \theta < 2\pi \end{cases}, \quad (4.4)$$

and assuming well balanced submodules,

$$u_{sx}(\theta) = S_x(\theta)U_{sm} \quad (4.5)$$

Lastly, the resulting RMS voltage yields,

$$U_{sx} = U_{sm} \sqrt{\frac{1}{2\pi} \int_0^{2\pi} S_x^2(\theta) d\theta} = \sqrt{m_u} U_{sm} \quad (4.6)$$

4.3 MSC operation modes

Making use of the derived switching function, the MMC is modeled as 3L controllable voltage source for each phase. The equivalent phase inductors, as defined in (2.41) limit the current flow between the diode bridge and the controllable voltage source as represented in Figure 4.6. Since the diode bridge exhibits switching behavior that depends on the operating conditions [191], achieving the desired

control performance becomes challenging. This will be investigated in this section. A similar analysis of the 3PH-SAB has been presented in [192]. However the SAB only include a HB per phase, resulting in fewer achievable levels. Therefore, a reduced number of DOFs leads to a smaller number of possible operating and conduction modes. For this analysis, the losses and forward voltages in the semiconductors are neglected.

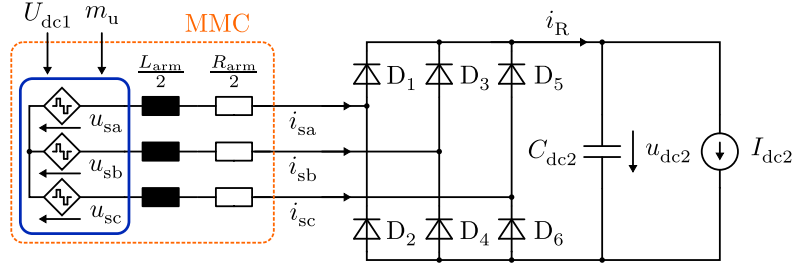


Figure 4.6: Equivalent model of MSC for operation mode analysis

4.3.1 Output voltage

The main objective of the MSC is to regulate the voltage across the output capacitor. First, the MSC voltage gain is investigated. In essence, the line-to-line differential voltages resulting from increase m_u determine the MSC average output voltage. Hence, the rectified voltage is given by

$$u_R = \max(|u_{sa} - u_{sb}|, |u_{sb} - u_{sc}|, |u_{sc} - u_{sa}|). \quad (4.7)$$

Without considering the magnitude of C_{dc2} , the resulting average output voltage yields

$$\bar{U}_{dc2} = \frac{1}{2\pi} \int_0^{2\pi} u_R(\theta) d\theta. \quad (4.8)$$

Furthermore, three different operation ranges are identified:

- Range 1: $0 \leq m_u \leq \frac{1}{3}$
- Range 2: $\frac{1}{3} < m_u \leq \frac{2}{3}$
- Range 3: $\frac{2}{3} < m_u \leq 1$

The main difference between the operating ranges arises from the line-to-line voltage overlap. In the first range, the phase voltages do not overlap. Therefore, the highest obtainable output voltage is U_{sm} . In the second range, the output voltage can be increase up to $2U_{sm}$. In last range, increasing m_u will not lead to

a higher voltage. Combining this information, (4.8) can be simply written as

$$\bar{U}_{dc2} = \begin{cases} 3U_{sm}m_u, & 0 \leq m_u < \frac{2}{3} \\ 2U_{sm}, & \frac{2}{3} \leq m_u \leq 1 \end{cases} \quad (4.9)$$

For each range, an example of the resulting differential, line-to-line and rectified voltages is provided in the figures below.

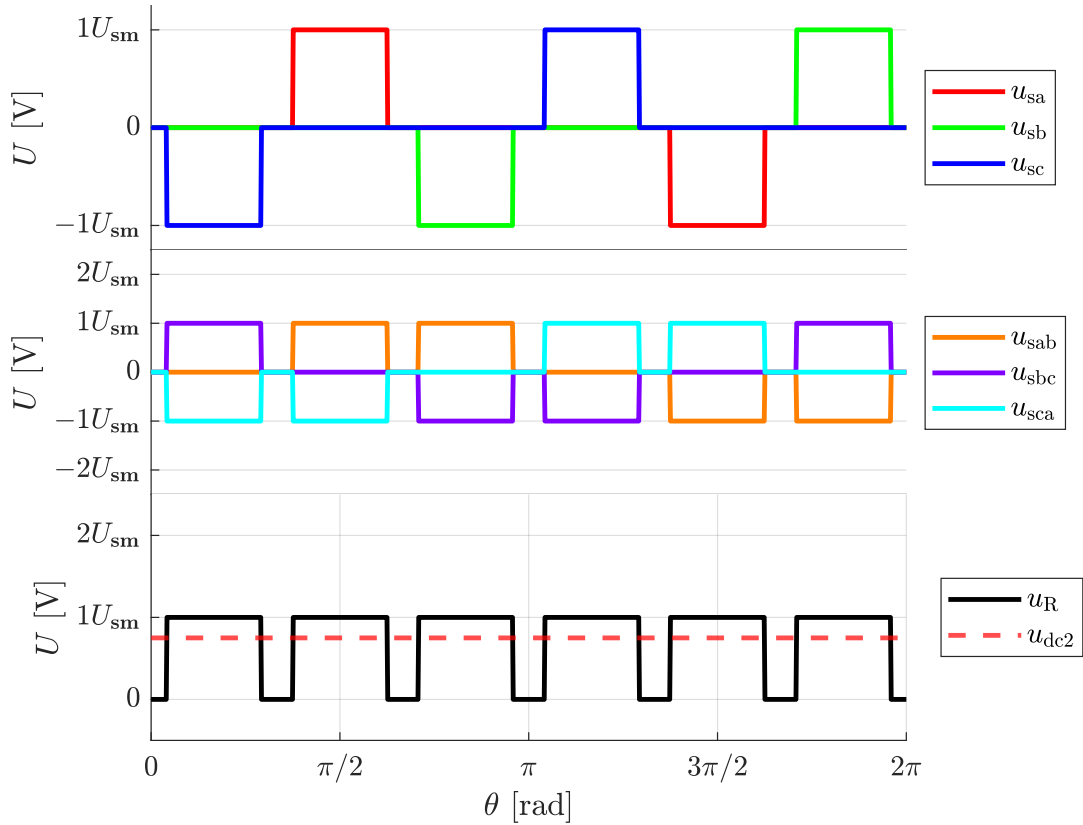
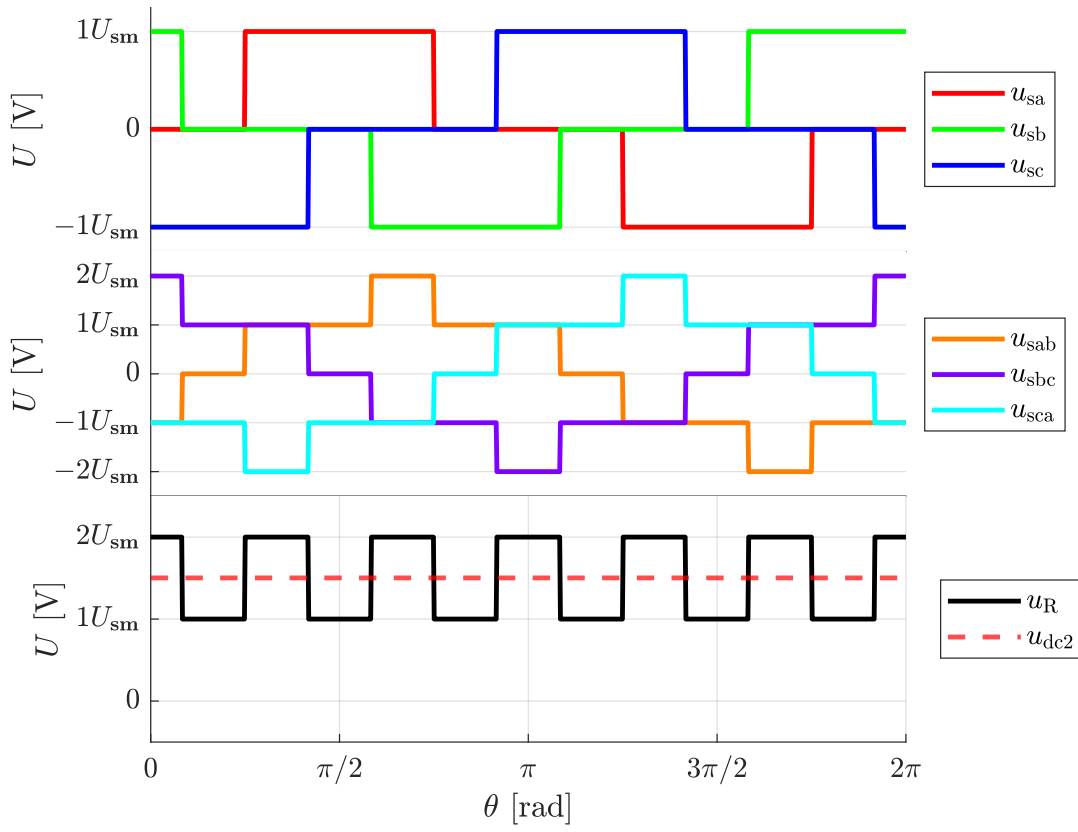


Figure 4.7: Differential, line-line and rectified voltage at $m_u = 0.25$

Figure 4.8: Differential, line-line and rectified voltage at $m_u = 0.5$

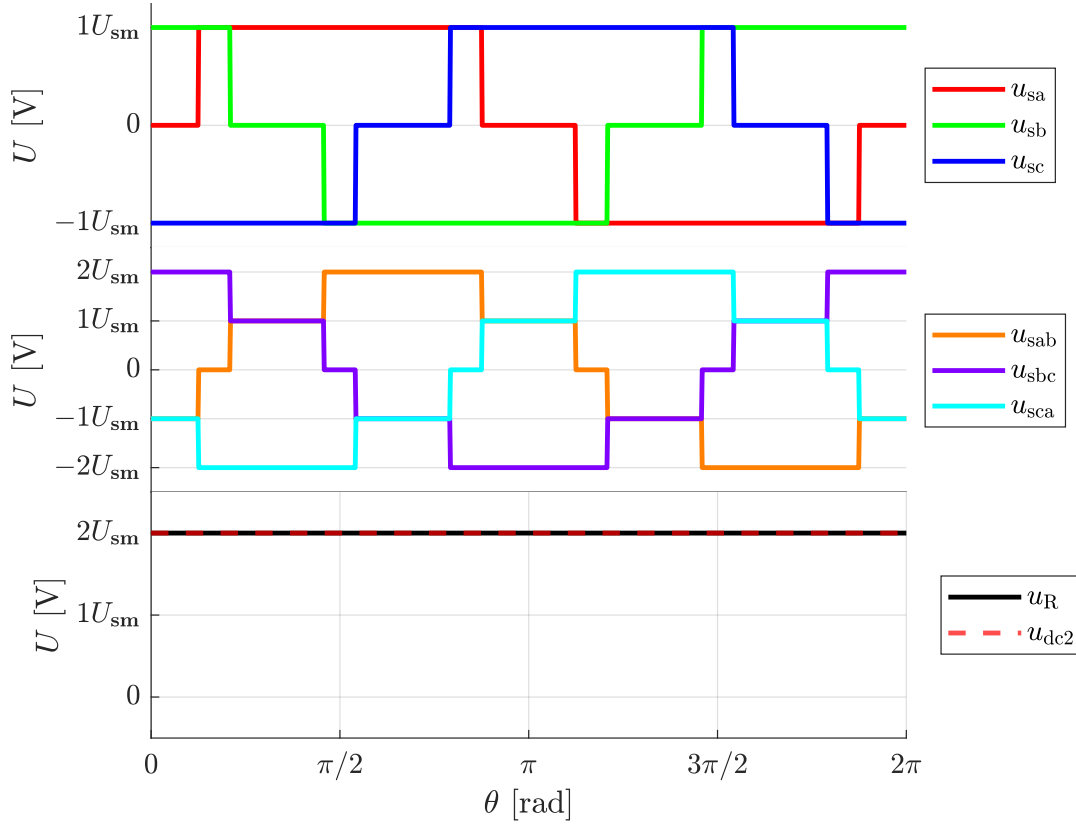


Figure 4.9: Differential, line-line and rectified voltage at $m_u = 0.75$

4.3.2 Output power

The voltage regulation task must be fulfilled at varying power loads. The equivalent phase inductance and output capacitor, will determine the current shape per phase. Since a single diode allows an electric current to pass only in the forward direction, the power flow can only be adjusted by the MMC controllable voltage sources. Hence the MSC operation is investigated here under different load conditions, represented by an ideal current sink. Together with a quite large capacitor, it is now assumed U_{dc2} to be kept at constant desired value for the following analysis. Consequently four different operation voltage modes were identified and outlined, determined by voltage ratios between U_{dc2} and U_{sm} , as listed in Table 4.2. Each ratio defines a unique set of sub-modes in which the operating point is determined by a fixed expression of the control input m_u , subject to specific boundary conditions.

For Ratios 1 and 2, power starts flowing whenever the modulation index m_u exceeds 0. However, in Ratios 3 and 4, currents flow starts at $m_u > 1/3$, attributed to the overlap described in the previous subsection required for gener-

Table 4.2: Operation modes for different voltage ratios

Operation Mode	Voltage Ratio
Ratio 1	$\frac{U_{dc2}}{U_{sm}} < \frac{1}{2}$
Ratio 2	$\frac{1}{2} \leq \frac{U_{dc2}}{U_{sm}} < 1$
Ratio 3	$1 \leq \frac{U_{dc2}}{U_{sm}} < \frac{3}{2}$
Ratio 4	$\frac{3}{2} \leq \frac{U_{dc2}}{U_{sm}} < 2$

ating a phase-to-phase voltage amplitude surpassing U_{dc2} , enabling the diodes to conduct. Each mode is divided in multiple sub-modes, whereas the resulting rectified current i_R becomes a function of m_u . According to the requirements of Project GridCON [193], the MSC is designed to operate at Ratio 3. In practice, this allows a smoother power flow interruption in abnormal circumstances, without a complete shutdown. This is achieved by reducing $m_u \leq 1/3$, which briefly disables the diode-bridge conduction. The extensive analysis is considered for only for Ratio 3 and further extended accordingly for the remaining ratios in Appendix D. Due to the imposed three-phase symmetry, the current equations are only described for phase a , while i_{sb} and i_{sc} are derived by simply phase-shifting i_{sa} . Due to the odd symmetry current function, its sufficient to describe the current slopes in the range from $[0, \pi]$. In total, three discontinuous and three continuous sub-modes were found. Each mode is characterized by a different phase current dynamic and corresponding boundary conditions, are summarized in Table 4.3.

Discontinuous conduction mode 1 (DCM1)

For values of $m_u > 1/3$, the converter works in the DCM1 and therefore, the phase currents have mostly zero values stages. In Table 4.4 the current equations are given in the range from $[0, \pi]$. The waveform of the current, as well as voltages u_{sa} , u_{sb} and u_{sc} are presented in Figure 4.10, for an arbitrary control input within the defined boundary conditions. Applying the inductor voltage-second balance

Table 4.3: Boundary conditions

Sub-mode	Boundary conditions
DCM1	$\frac{1}{3} \leq m_u < \frac{U_{dc2}}{3U_{sm}}$
DCM2	$\frac{U_{dc2}}{3U_{sm}} \leq m_u < \frac{2U_{dc2}}{3(3U_{sm}-U_{dc2})}$
DCM3	$\frac{2U_{dc2}}{3(3U_{sm}-U_{dc2})} \leq m_u < \frac{U_{sm}+2U_{dc2}}{6U_{sm}}$
CCM1	$\frac{U_{sm}+2U_{dc2}}{6U_{sm}} \leq m_u < \frac{2}{3}$
CCM2	$\frac{2}{3} \leq m_u < \frac{5U_{sm}-2U_{dc2}}{3U_{sm}}$
CCM3	$\frac{5U_{sm}-2U_{dc2}}{3U_{sm}} \leq m_u \leq 1$

principle [194], the phase current equations are found in Table 4.4. Notice that i_{sa} is zero at the points:

$$i_0 = i_1 = i_3 = i_4 = i_6 = i_7 = 0 \quad (4.10)$$

From the equation of interval 2 in Table 4.4 and condition (4.10), the angle φ_1 can be calculated by

$$\varphi_1 = \frac{-i_2 2\omega L}{U_{sm} - U_{dc2}}. \quad (4.11)$$

This angle is simply an operation dependent auxiliary variable, representing a current growth/decay subperiod. Replacing i_2 in (4.11) with the equation of interval 3 in Table 4.4, φ_1 is given by

$$\varphi_1 = \pi \frac{U_{dc2} - 2U_{sm}}{U_{sm} - U_{dc2}} \frac{3m_u - 1}{3}. \quad (4.12)$$

If m_u is increased, φ_1 is eventually equal to

$$\varphi_1 = \frac{2\pi}{3} - m_u \pi. \quad (4.13)$$

Therefore, rearranging equation (4.13), it results in the upper bound of m_u for

which the converter works in DCM1 and is given by

$$m_u = \frac{U_{dc2}}{3U_{sm}}. \quad (4.14)$$

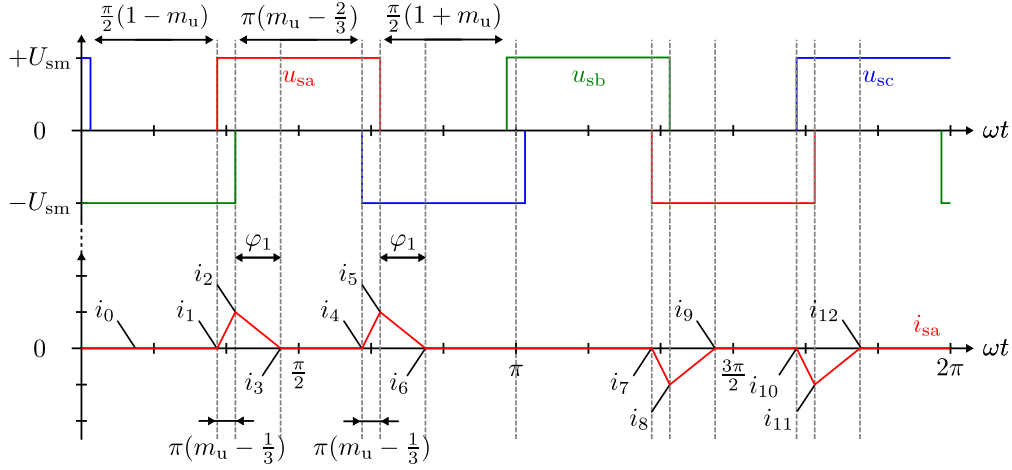


Figure 4.10: DCM13

Table 4.4: Current equations for i_{sa} in DCM1

Interval	Current equations for phase a : i_{sa}
1	$i_1 - i_0 = 0 \left(\frac{\pi}{2} - \frac{m_u \pi}{2} \right)$
2	$i_2 - i_1 = \frac{2U_{sm} - U_{dc2}}{2\omega L} \left(m_u \pi - \frac{\pi}{3} \right)$
3	$i_3 - i_2 = \frac{U_{sm} - U_{dc2}}{2\omega L} \varphi_1$
4	$i_4 - i_3 = 0 \left(\frac{2\pi}{3} - m_u \pi - \varphi_1 \right)$
5	$i_5 - i_4 = \frac{2U_{sm} - U_{dc2}}{2\omega L} \left(m_u \pi - \frac{\pi}{3} \right)$
6	$i_6 - i_5 = \frac{U_{sm} - U_{dc2}}{2\omega L} \varphi_1$
7	$i_0 - i_6 = 0 \left(\frac{\pi}{2} - \frac{m_u \pi}{2} \right)$

Discontinuous conduction mode 2 (DCM2)

For $m_u > \frac{U_{dc2}}{3U_{sm}}$, the converter operates in DCM2 as depicted in Figure 4.11. Unlike in DCM1, the currents have zero stages in DCM2 but not all currents are zero at the same time. Therefore, if one phase current is zero, the diodes corresponding to the other phases are conducting. The current equations of phase a are given in Table 4.5. From Figure 4.11, the current i_{sa} is equal to zero at

$$i_0 = i_1 = i_8 = i_9 = 0 \quad (4.15)$$

Due to the odd symmetry of i_{sa} , it is

$$i_7 = -i_{15} \quad (4.16)$$

and the angle φ_2 is given by

$$\varphi_2 = \frac{-i_7 3\omega L}{U_{dc2}}. \quad (4.17)$$

i_{15} is calculated with Table 4.5 and condition (4.16) to

$$i_{15} = -\frac{3m_u\pi U_{sm} - \pi U_{dc2}}{2\omega L} = -i_7. \quad (4.18)$$

By inserting equation (4.18) in (4.17), φ_2 is

$$\varphi_2 = \pi \frac{3m_u U_{sm} - U_{dc2}}{U_{dc2}}. \quad (4.19)$$

If m_u is large enough, it results in the condition

$$\varphi_2 = m_u\pi - \frac{\pi}{3} \quad (4.20)$$

from which the upper bound of m_u is given as

$$m_u = \frac{2U_{dc2}}{3(3U_{sm} - U_{dc2})}. \quad (4.21)$$

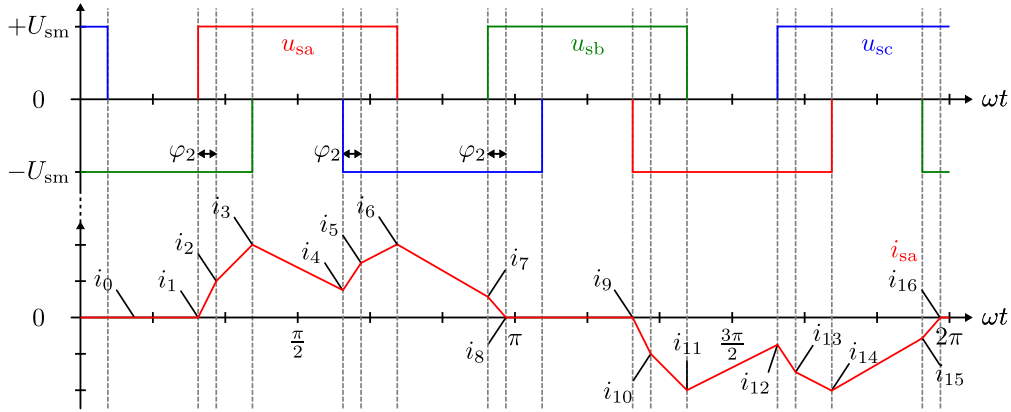


Figure 4.11: DCM23

Table 4.5: Current equations for i_{sa} in DCM2

Interval	Current equations for phase a : i_{sa}
1	$i_1 - i_0 = 0 \frac{\pi}{2} (1 - m_u)$
2	$i_2 - i_1 = \frac{3U_{sm} - U_{dc2}}{3\omega L} \varphi_2$
3	$i_3 - i_2 = \frac{2U_{sm} - U_{dc2}}{2\omega L} (m_u \pi - \frac{\pi}{3} - \varphi_2)$
4	$i_4 - i_3 = \frac{U_{sm} - U_{dc2}}{2\omega L} (\frac{2\pi}{3} - m_u \pi)$
5	$i_5 - i_4 = \frac{3U_{sm} - 2U_{dc2}}{3\omega L} \varphi_2$
6	$i_6 - i_5 = \frac{2U_{sm} - U_{dc2}}{2\omega L} (m_u \pi - \frac{\pi}{3} - \varphi_2)$
7	$i_7 - i_6 = \frac{U_{sm} - U_{dc2}}{2\omega L} (\frac{2\pi}{3} - m_u \pi)$
8	$i_8 - i_7 = -\frac{U_{dc2}}{3\omega L} \varphi_2$
9	$i_0 - i_8 = 0 (\frac{m_u \pi}{2} - \frac{\pi}{6} - \varphi_2)$

Discontinuous conduction mode 3 (DCM3)

Should m_u exceed $\frac{2U_{dc2}}{3(3U_{sm} - U_{dc2})}$, the converter operates in DCM3. The current has zero stages similar to DCM2, but with slightly different slopes as shown in Figure

4.12. All the current equations are given in Table 4.6. By referring to the same figure, the current crosses zero at

$$i_2 = i_3 = 0 \quad (4.22)$$

Due to the odd symmetry of i_{sa} , following in

$$i_1 = -i_{10} \quad (4.23)$$

The angle φ_3 can be calculated with the results from Table 4.6 and condition (4.23) to

$$\varphi_3 = \frac{3m_u U_{sm} - m_u U_{dc2} - \frac{2}{3}U_{dc2}}{U_{sm} + U_{dc2}}. \quad (4.24)$$

In the case, m_u is increased such that

$$\varphi_3 = \frac{2\pi}{3} - m_u \pi \quad (4.25)$$

and the upper bound of m_u results in

$$m_u = \frac{U_{sm} + 2U_{dc2}}{6U_{sm}}. \quad (4.26)$$

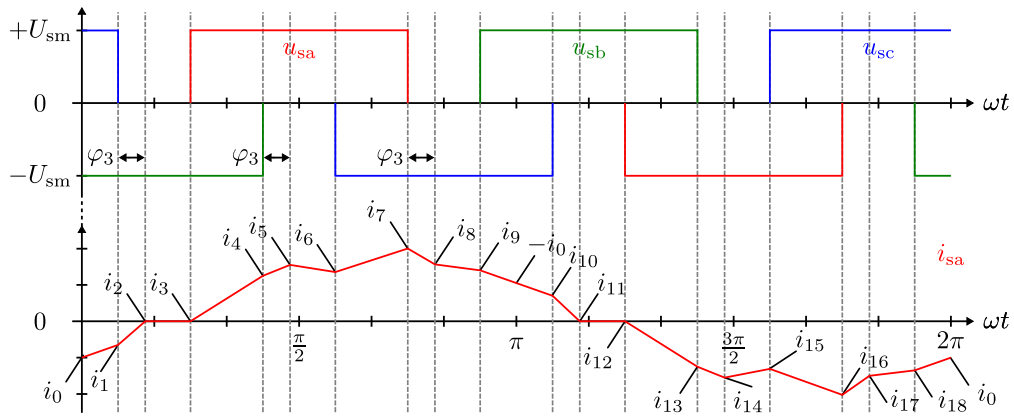


Figure 4.12: DCM33

Table 4.6: Current equations for i_{sa} in DCM3

Interval	Current equations for phase a : i_{sa}
1	$i_1 - i_0 = \frac{U_{dc2}}{3\omega L} \left(\frac{m_u \pi}{2} - \frac{\pi}{6} \right)$
2	$i_2 - i_1 = \frac{U_{sm} + U_{dc2}}{3\omega L} \varphi_3$
3	$i_3 - i_2 = 0 \left(\frac{2\pi}{3} - m_u \pi - \varphi_3 \right)$
4	$i_4 - i_3 = \frac{3U_{sm} - U_{dc2}}{3\omega L} \left(m_u \pi - \frac{\pi}{3} \right)$
5	$i_5 - i_4 = \frac{2U_{sm} - U_{dc2}}{3\omega L} \varphi_3$
6	$i_6 - i_5 = \frac{U_{sm} - U_{dc2}}{2\omega L} \left(\frac{2\pi}{3} - m_u \pi - \varphi_3 \right)$
7	$i_7 - i_6 = \frac{3U_{sm} - 2U_{dc2}}{3\omega L} \left(m_u \pi - \frac{\pi}{3} \right)$
8	$i_8 - i_7 = \frac{U_{sm} - 2U_{dc2}}{3\omega L} \varphi_3$
9	$i_9 - i_8 = \frac{U_{sm} - U_{dc2}}{2\omega L} \left(\frac{2\pi}{3} - m_u \pi - \varphi_3 \right)$
10	$i_{10} - i_9 = -\frac{U_{dc2}}{3\omega L} \left(\frac{m_u \pi}{2} - \frac{\pi}{6} \right)$

Continuous conduction mode 1 (CCM1)

When m_u is in the range $\left[\frac{U_{sm} + 2U_{dc2}}{6U_{sm}}, \frac{2}{3} \right]$, the current is continuous over the complete period and the converter works in continuous conduction mode. In Figure 4.13 the waveform of the current is illustrated. Table 4.7 summarizes all current equations in CCM1. Now, the current crosses zero at

$$i_3 = i_{12} = 0 \quad (4.27)$$

and because of the odd symmetry, it holds

$$i_2 = -i_{11} \quad (4.28)$$

From Table 4.7 and condition (4.28), the angle φ_4 is equal to

$$\varphi_4 = \pi \frac{6m_u U_{sm} - U_{sm} - 2U_{dc2}}{9U_{sm}} \quad (4.29)$$

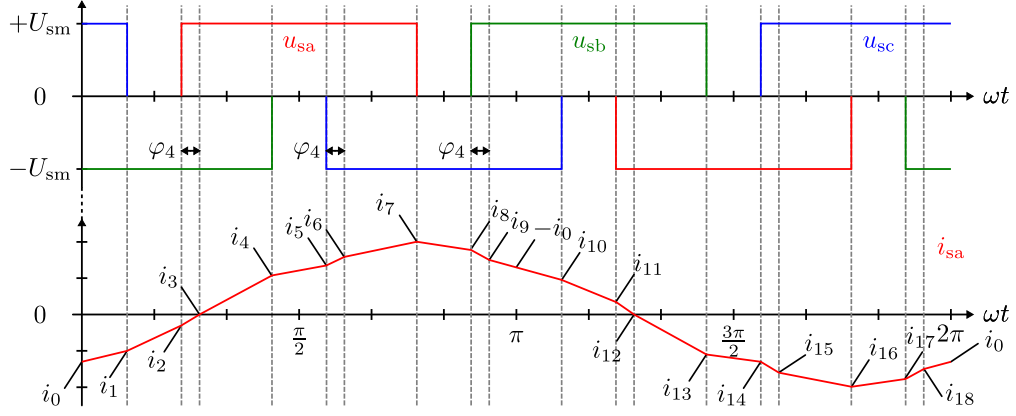


Figure 4.13: CCM13

Table 4.7: Current equations for i_{sa} in CCM1

Interval	Current equations for phase a: i_{sa}
1	$i_1 - i_0 = \frac{U_{dc2}}{3\omega L} \left(\frac{\pi m_u}{2} - \frac{\pi}{6} \right)$
2	$i_2 - i_1 = \frac{U_{sm} + U_{dc2}}{3\omega L} \left(\frac{2\pi}{3} - m_u \pi \right)$
3	$i_3 - i_2 = \frac{3U_{sm} + U_{dc2}}{3\omega L} \varphi_4$
4	$i_4 - i_3 = \frac{3U_{sm} - U_{dc2}}{3\omega L} \left(m_u \pi - \frac{\pi}{3} - \varphi_4 \right)$
5	$i_5 - i_4 = \frac{2U_{sm} - U_{dc2}}{3\omega L} \left(\frac{2\pi}{3} - m_u \pi \right)$
6	$i_6 - i_5 = \frac{3U_{sm} - U_{dc2}}{3\omega L} \varphi_4$
7	$i_7 - i_6 = \frac{3U_{sm} - 2U_{dc2}}{3\omega L} \left(m_u \pi - \frac{\pi}{3} - \varphi_4 \right)$
8	$i_8 - i_7 = \frac{U_{sm} - 2U_{dc2}}{3\omega L} \left(\frac{2\pi}{3} - m_u \pi \right)$
9	$i_9 - i_8 = -\frac{2U_{dc2}}{3\omega L} \varphi_4$
10	$-i_0 - i_9 = -\frac{U_{dc2}}{3\omega L} \left(\frac{m_u \pi}{2} - \frac{\pi}{6} - \varphi_4 \right)$

Table 4.8: Current equations for i_{sa} in CCM2

Interval	Current equations for phase a : i_{sa}
1	$i_1 - i_0 = \frac{U_{dc2}}{3\omega L} \left(\frac{\pi}{2} - \frac{m_u \pi}{2} \right)$
2	$i_2 - i_1 = \frac{2U_{sm} + U_{dc2}}{3\omega L} \left(m_u \pi - \frac{2\pi}{3} \right)$
3	$i_3 - i_2 = \frac{3U_{sm} + U_{dc2}}{3\omega L} \varphi_5$
4	$i_4 - i_3 = \frac{3U_{sm} - U_{dc2}}{3\omega L} \left(\pi - m_u \pi - \varphi_5 \right)$
5	$i_5 - i_4 = \frac{4U_{sm} - U_{dc2}}{3\omega L} \left(m_u \pi - \frac{2\pi}{3} \right)$
6	$i_6 - i_5 = \frac{3U_{sm} - U_{dc2}}{3\omega L} \varphi_5$
7	$i_7 - i_6 = \frac{3U_{sm} - 2U_{dc2}}{3\omega L} \left(\pi - m_u \pi - \varphi_5 \right)$
8	$i_8 - i_7 = \frac{2U_{sm} - 2U_{dc2}}{3\omega L} \left(m_u \pi - \frac{2\pi}{3} \right)$
9	$i_9 - i_8 = -\frac{2U_{dc2}}{3\omega L} \varphi_5$
10	$-i_0 - i_9 = -\frac{U_{dc2}}{3\omega L} \left(\frac{\pi}{2} - \frac{m_u \pi}{2} - \varphi_5 \right)$

Continuous conduction mode 3 (CCM3)

Further increasing m_u in the last boundary region, the converter works in CCM3 as illustrated in Figure 4.15. All the current equations are given in Table 4.9. The current crosses zero at

$$i_2 = i_{11} = 0 \quad (4.34)$$

and because of the odd symmetry, condition (4.35) results therefore.

$$i_1 = -i_{10} \quad (4.35)$$

From Table 4.9 and condition (4.35), the angle φ_6 is equal to

$$\varphi_6 = \pi \frac{3m_u U_{sm} + U_{sm} - 2U_{dc2}}{6U_{sm}} \quad (4.36)$$

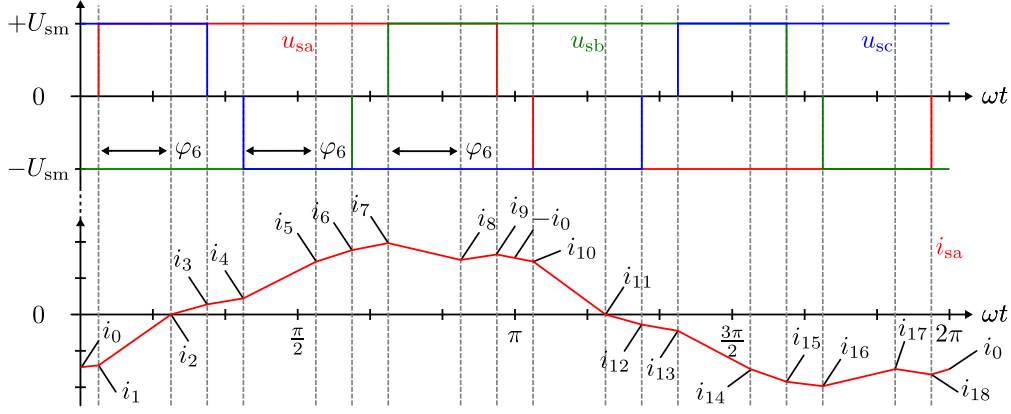


Figure 4.15: CCM3

Table 4.9: Current equations for i_{sa} in CCM3

Interval	Current equations for phase a : i_{sa}
1	$i_1 - i_0 = \frac{U_{dc2}}{3\omega L} \left(\frac{\pi}{2} - \frac{m_u \pi}{2} \right)$
2	$i_2 - i_1 = \frac{2U_{sm} + U_{dc2}}{3\omega L} \varphi_6$
3	$i_3 - i_2 = \frac{2U_{sm} - U_{dc2}}{3\omega L} \left(m_u \pi - \frac{2\pi}{3} - \varphi_6 \right)$
4	$i_4 - i_3 = \frac{3U_{sm} - U_{dc2}}{3\omega L} \left(\pi - m_u \pi \right)$
5	$i_5 - i_4 = \frac{4U_{sm} - U_{dc2}}{3\omega L} \varphi_6$
6	$i_6 - i_5 = \frac{4U_{sm} - 2U_{dc2}}{3\omega L} \left(m_u \pi - \frac{2\pi}{3} - \varphi_6 \right)$
7	$i_7 - i_6 = \frac{3U_{sm} - 2U_{dc2}}{3\omega L} \left(\pi - m_u \pi \right)$
8	$i_8 - i_7 = \frac{2\bar{U}_{sm} - 2U_{dc2}}{3\omega L} \varphi_6$
9	$i_9 - i_8 = \frac{2U_{sm} - U_{dc2}}{3\omega L} \left(m_u \pi - \frac{2\pi}{3} - \varphi_6 \right)$
10	$-i_0 - i_9 = -\frac{U_{dc2}}{3\omega L} \left(\frac{\pi}{2} - \frac{m_u \pi}{2} \right)$

4.4 Adaptive control strategy

4.4.1 Reduced order model

From a circuitry point of view, it would be interesting to separately considered each inductor current. However, only the rectified current i_R , given in (4.37) directly affects the output capacitor voltage. Therefore the average value of i_R over one switching period is used to derive a simplified model of the MSC output behavior, as shown in (4.38).

$$i_R = i_{D1} + i_{D2} + i_{D3} = -(i_{D4} + i_{D5} + i_{D6}) \quad (4.37)$$

$$I_R = \frac{1}{2\pi} \int_0^{2\pi} i_R(\varphi) d\varphi \quad (4.38)$$

For all conduction modes and boundary conditions, I_R is summarized in Table 4.10. Figure 4.16 shows the comparison between simulated switching MSC current i_R and the calculated average values of I_R , validating the presented mathematical derivation. Finally, a reduced model for control purpose is achieved. Represented in Figure 4.17, it mainly simplifies the entire MSC to a single output voltage dynamic is given by (4.39).

$$C_{dc2} \frac{du_{dc2}}{dt} = i_R - i_{dc2} \quad (4.39)$$

Table 4.10: Average rectified current I_R for each operation mode

Mode	Average value of I_R
DCM1	$\frac{\pi}{12\omega L} \frac{U_{sm}(2U_{sm} - U_{dc2})}{U_{dc2} - U_{sm}} (3m_u - 1)^2$
DCM2	$\frac{\pi U_{sm}}{12\omega L U_{dc2}} ((27U_{sm} - 9U_{dc2})m_u^2 - 2U_{dc2})$
DCM3	$\frac{\pi U_{sm}}{\omega L (U_{sm} + U_{dc2})} ((U_{sm} - \frac{U_{dc2}}{3})(3m_u^2 + m_u) - (\frac{U_{sm}}{6} + \frac{5U_{dc2}}{18}))$
CCM1	$\frac{\pi}{27\omega L U_{sm}} (-9U_{sm}m_u^2 + 21U_{sm}^2 m_u - (U_{sm}^2 + 2U_{dc2}^2))$
CCM2	$\frac{\pi}{27\omega L U_{sm}} (-9U_{sm}m_u^2 + 21U_{sm}^2 m_u - (U_{sm}^2 + 2U_{dc2}^2))$
CCM3	$\frac{\pi}{36\omega L U_{sm}} (-9U_{sm}m_u^2 + 18U_{sm}^2 m_u + (7U_{sm}^2 + 4U_{dc2}^2))$

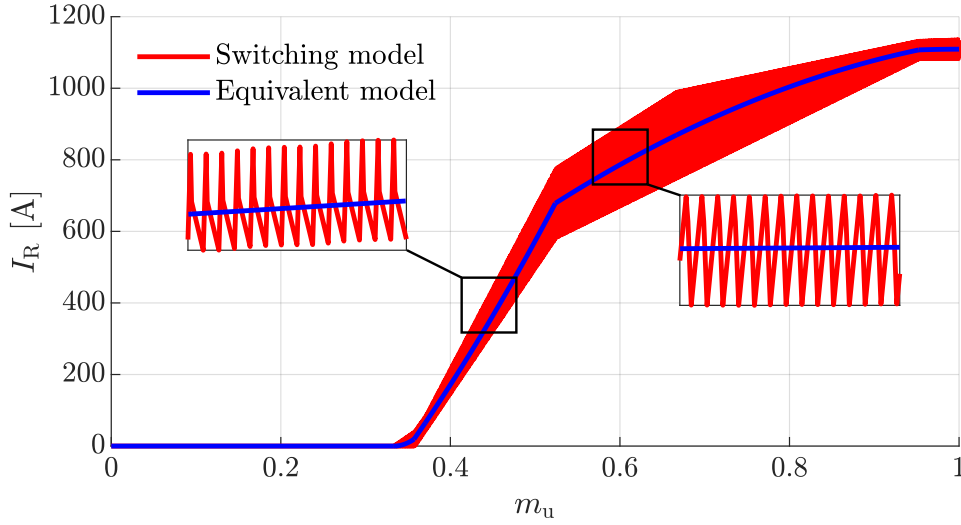


Figure 4.16: Comparison between switching and reduced equivalent models

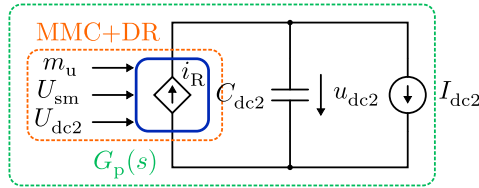


Figure 4.17: Reduced model of MSC for control purposes

4.4.2 Controller design

Now, the main objective of the MSC is to regulate its output capacitor voltage and guarantee a reliable supply for the agricultural machine. Its electrical system and load are modeled as a variable current source (I_{dc2}), which is system disturbance from a control perspective. As in previous chapter, the chosen control structure is a 2-DOF. As first priority, the controller is designed to obtain a closed-loop disturbance response similar to a critically damped ($\zeta > 1$) second-order system, as described by (4.40).

$$G_{dr}^*(s) = \frac{1}{C_{dc2}} \cdot \frac{-s}{s^2 + 2\zeta_d\omega_d s + \omega_d^2} = \frac{U_{dc2}(s)}{I_{dc2}(s)} \quad (4.40)$$

This guarantees a robust and smooth response to a step load change, allowing the voltage to return to its steady-state reference at the desired dynamic ω_d . Consider first the control structure in Figure 4.18, which is designed to instantly track its

rectified current reference (I_R^*). This reference is determined by the control action of $G_c(s)$, which is responsible to regulate the output voltage (U_{dc2}).

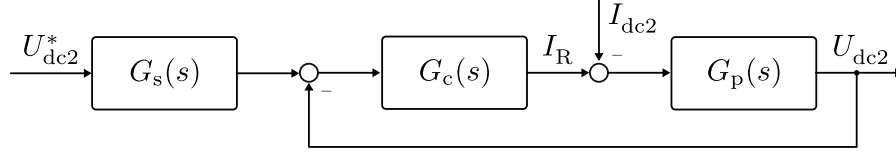


Figure 4.18: Block diagram of ideal linear controller

In order to design G_c , the system closed-loop disturbance response (4.41) is matched to the desired transfer function (4.40). The outcome is a PI structure with coefficients given in (4.42).

$$G_{dr}(s) = -\frac{G_p}{1 + G_c G_p} \quad (4.41)$$

$$K_p = 2\zeta_d \omega_d C_{dc2} \quad K_i = C_{dc2} \omega_d^2 \quad (4.42)$$

Accordingly, the closed-loop step response of this system is given by (4.43), which features the same poles as (4.40), with an undesirable additional zero.

$$G_{sr}(s) = \frac{G_p G_c}{1 + G_c G_p} = \frac{\omega_d(\omega_d + 2\zeta_d s)}{s^2 + 2\zeta_d \omega_d s + \omega_d^2} \quad (4.43)$$

For the agriculture machine, its voltage reference change should be as smooth as possible to avoid high current inrush from the MSC. Therefore the same dynamic response as to a load change is not required. Hence, the desired reference step response is given by the (4.44), where as $\zeta_d \neq \zeta_s$ and $\omega_d \neq \omega_s$.

$$G_{sr}^*(s) = \frac{\omega_s^2}{s^2 + 2\zeta_s \omega_s s + \omega_s^2} = \frac{U_{dc2}(s)}{U_{dc2}^*(s)} \quad (4.44)$$

To accomplish this, an input shaping function is designed, as described in equation (4.45). Following this methodology, the system's disturbance and step response can be independently designed, according to the desired performance.

$$G_{is}(s) = \frac{G_{sr}^*(s)}{G_{sr}(s)} = \frac{\omega_s^2 (s^2 + 2\zeta_d \omega_d s + \omega_d^2)}{\omega_d (\omega_d + 2\zeta_d s) (s^2 + 2\zeta_s \omega_s s + \omega_s^2)} \quad (4.45)$$

Due to the MSC non-linear behavior and limited control bandwidth, a linear controller cannot ensure satisfactory tracking I_R^* across the entire desired operating range. Instead, using the insights gained in the previous circuit analysis, an adaptive feedforward law is obtained, which highly approximates the inverse non-linear characteristic of the MSC, for its entire operation range. This is accomplished by using the functions given in Table 4.11.

Table 4.11: MSC modulation index m_u for each desired operation

Mode	MSC modulation index m_u
DCM1	$\frac{1}{3} + \sqrt{\frac{12\omega LI_R^*}{9\pi} \frac{U_{dc2} - U_{sm}}{U_{sm}(2U_{sm} - U_{dc2})}}$
DCM2	$\sqrt{\frac{12\omega LU_{dc2}I_R^* + 2\pi U_{sm}U_{dc2}}{9\pi U_{sm}(3U_{sm} - U_{dc2})}}$
DCM3	$-\frac{1}{6} + \sqrt{\frac{\pi U_{sm}^2 + \pi U_{sm}U_{dc2} + 4\omega LU_{sm} + U_{dc2}I_R^*}{4\pi U_{sm}(3U_{sm} - U_{dc2})}}$
CCM1	$\frac{7}{6} - \sqrt{\frac{45\pi U_{sm}^2 - 8\pi U_{dc2}^2 - 108\omega LU_{sm}I_R^*}{36\pi U_{sm}^2}}$
CCM2	$\frac{7}{6} - \sqrt{\frac{45\pi U_{sm}^2 - 8\pi U_{dc2}^2 - 108\omega LU_{sm}I_R^*}{36\pi U_{sm}^2}}$
CCM3	$1 - \sqrt{\frac{16\pi U_{sm}^2 - 4\pi U_{dc2}^2 - 36\omega LU_{sm}I_R^*}{9\pi U_{sm}^2}}$

These establish a relation to obtain the modulation index, from the actual operation mode and desired (I_R^*). Furthermore, these are used online, proving a fast adaptation the converter operation mode. Any model inaccuracies are handled by the output voltage controller, which will smoothly adapt the desired (I_R^*), and correct (m_u). The overall designed control block diagram is given in Figure 4.19.

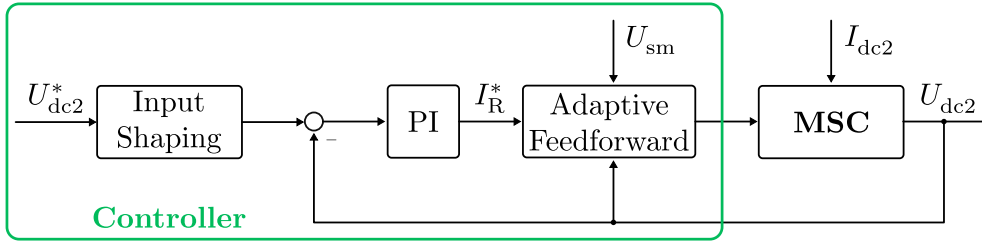


Figure 4.19: Block diagram of proposed adaptive controller

4.5 Results

The controller is now evaluated and simulated against the MSC's switching model. Its parameters are listed in Table 5.3. Details of its design and construction are provided in section 5.3. This model provides a good representation of Hardware used in the project GridCON. As an example, the steady state operation of the

MSC at 125 kW and MVDC bus at 5 kV is given in Figure 4.20. Corresponding waveforms obtained from the switching model are presented in Figure 4.21 and Figure 4.23, demonstrating a close match with the fundamental behavior observed in the hardware measurements.

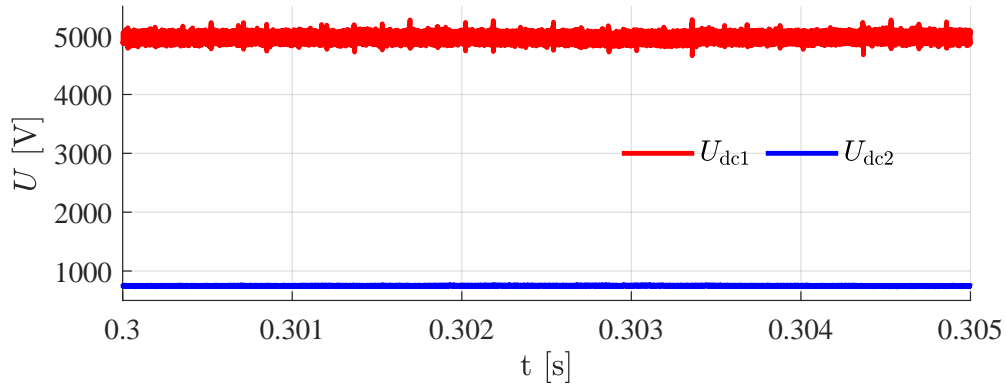


Figure 4.20: Hardware demonstrator – Input and output voltage

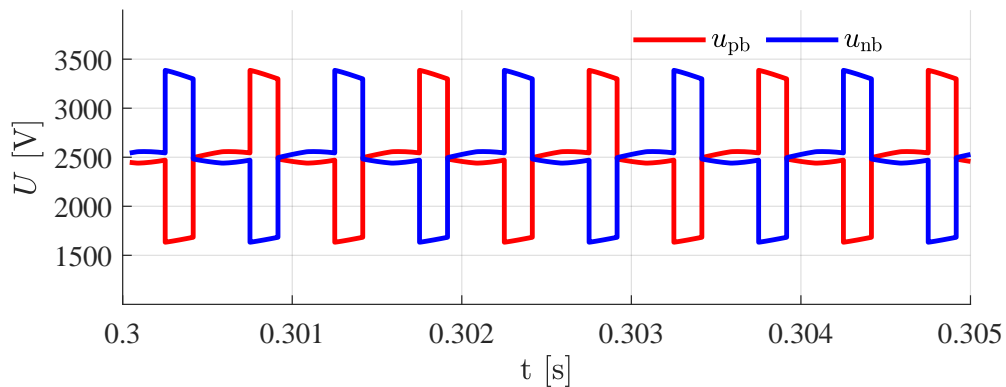


Figure 4.21: Simulation demonstrator – Resulting arm voltage in phase B

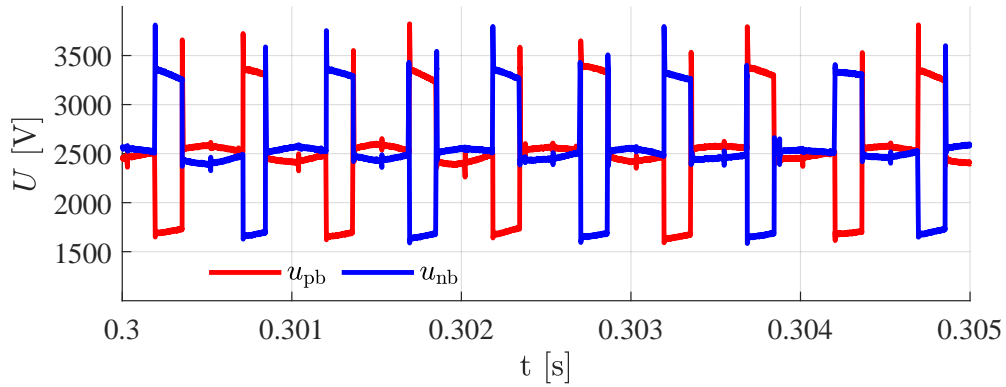


Figure 4.22: Hardware demonstrator – Resulting arm voltage in phase B

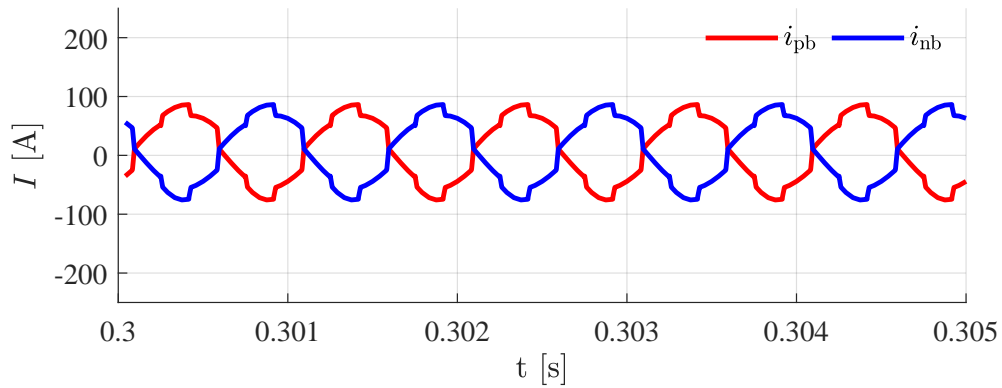


Figure 4.23: Simulation demonstrator – Resulting arm current in phase B

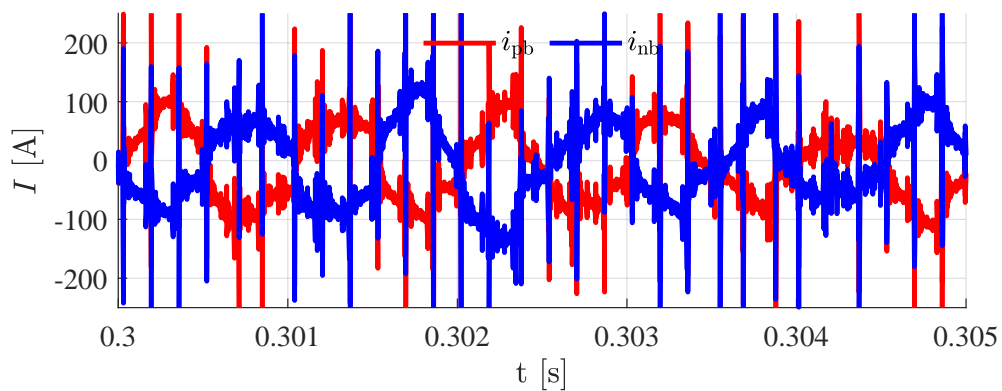


Figure 4.24: Hardware demonstrator – Resulting arm current in phase B

Furthermore, both the input and circulating currents are illustrated in Figure

4.25. By employing BM and constraining the number of always-inserted submodules per phase during operation, the circulating currents are naturally low. Without considering any additional energy controller, this results in non-significant ripple on the MVDC side.

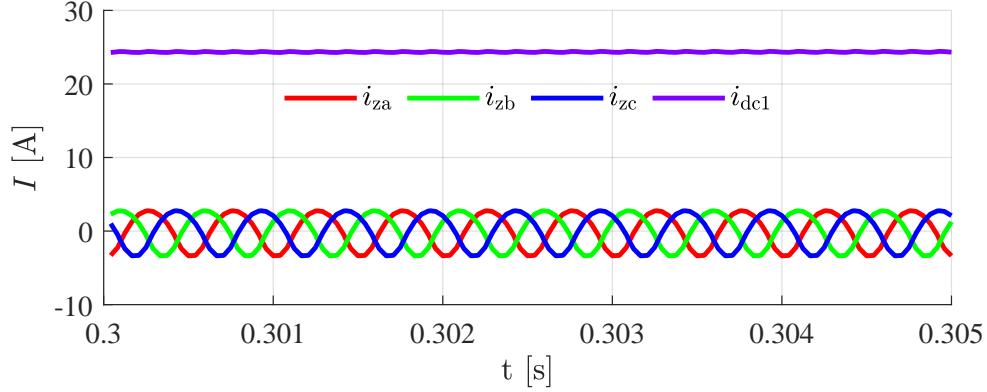


Figure 4.25: Simulation demonstrator – Resulting circulating and input currents

To validate the controller's performance, a conventional PI controller (1-DOF controller and for this section named as linear controller (LC)), designed for the maximum power transfer operating range, is compared with the proposed adaptive controller (AC). The LC was configured to achieve a critically damped step response with a settling time of 50 ms. Due to the MSC's non-linear behavior, the performance of the LC is achieved on a trial-and-error basis. For other operation points, only a stable response was taken into consideration. Similar to the previous chapter, the proposed AC takes into account non-linear behavior. Therefore, this comparison aims to demonstrate the AC's ability to effectively decouple reference tracking from disturbance rejection, highlighting its superior adaptability and dynamic performance.

As most operation relies on maintaining U_{dc2} constant regardless the demanded load, the disturbance rejection capability of both controllers is compared in Figure 4.26 for several load levels. Initially, the MSC supplies a current of 50 A. At $t = 0.8$ s, the current demand steps up to 150 A, followed by a further increase to its rated value of 400 A after 100 ms. Subsequently, the current demand is decreased in reverse order. The proposed adaptive structure results in a smaller voltage change at the desired settling time without overshoot, when compared with the LC option. From Figure 4.27, one notices the chosen load currents lead to different operation modes. The adaptive term is capable to adjust to the converter operation point and provide a uniform disturbance rejection response.

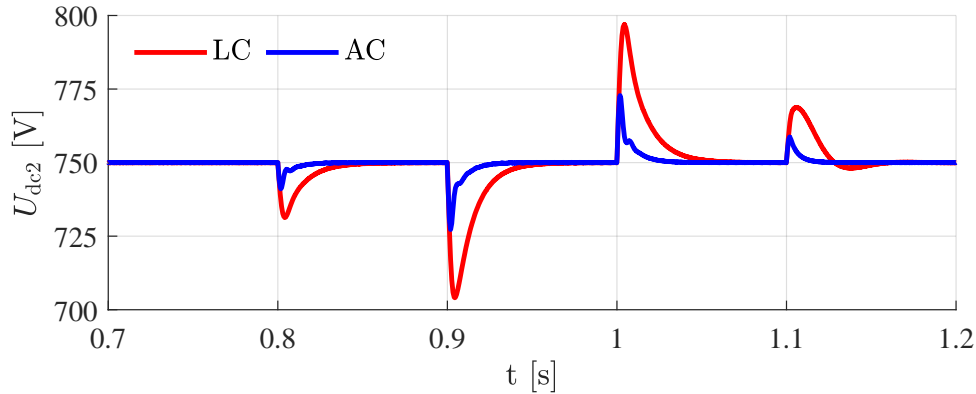


Figure 4.26: Load step change – voltage response

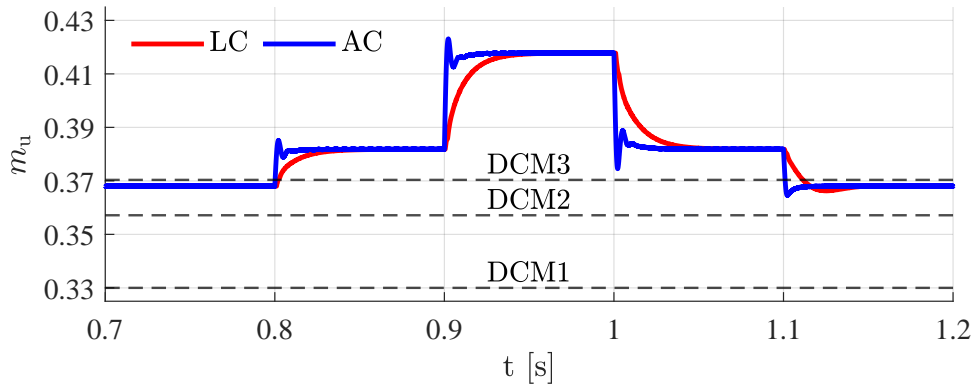


Figure 4.27: Load step change – modulation index response

Subsequently, the step response to an output voltage reference change for both controllers is shown in Figure 4.28. First, a current demand of 50 A. Opposite to LC, the proposed solution provides the desired critically damped response with the intended transient settling time. Notice, in Figure 4.29 that the reference change forces the use of three different operation modes. Consequently, using the LC leads to an undesired overshoot. Focusing on $t = 1.8$ s, where a lower voltage reference is requested, the current is quickly reduced to a minimum, allowing the output capacitor to smoothly discharge.

As expected, for a higher load demand (250 A), there is almost no difference between both controllers. This test is illustrated in Figure 4.30, which reflects the fact that during this voltage variation, the operation remains within a single conduction mode, as shown in Figure 4.31.

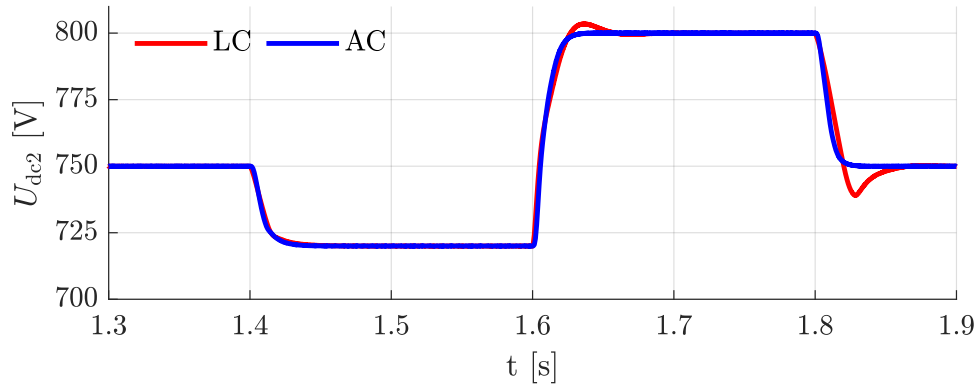


Figure 4.28: Reference change at low load – voltage response

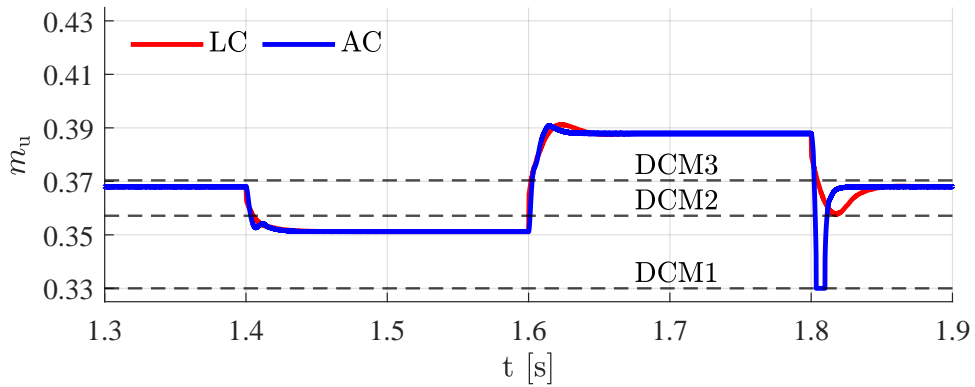


Figure 4.29: Reference change at low load – modulation index response

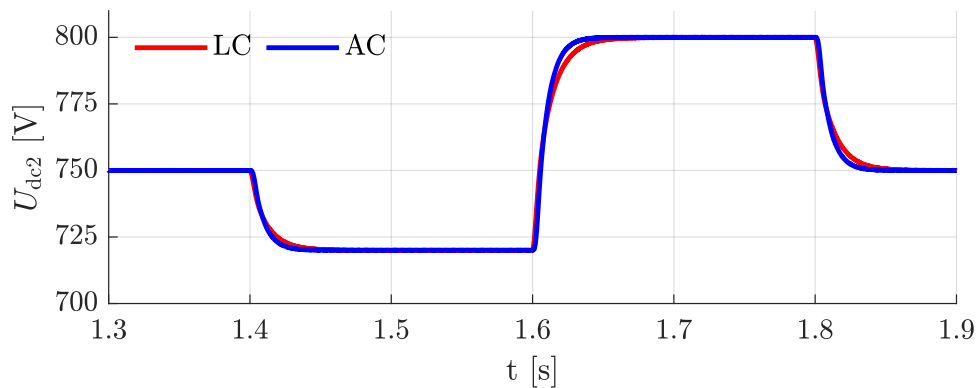


Figure 4.30: Reference change at high load – voltage response

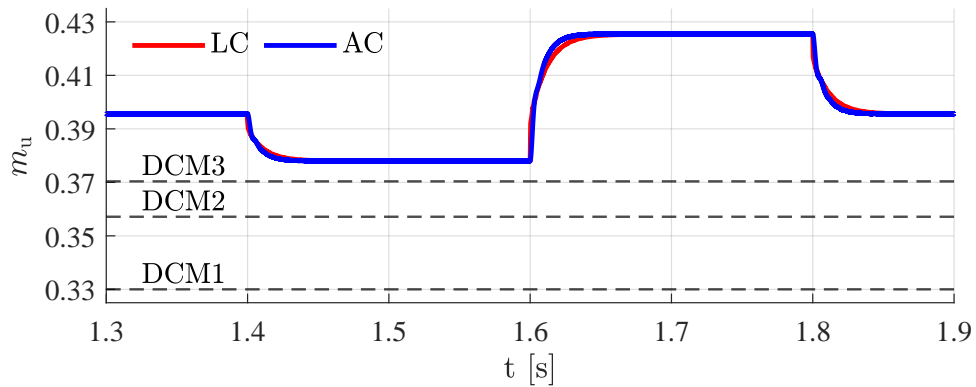


Figure 4.31: Reference change at high load – modulation index response

To conclude, adopting the proposed adaptive control structure not only enhances the overall control performance but also significantly simplifies the design process for achieving tangible performance targets. Interestingly, this structure resembles the feedback linearization approach presented in the previous chapter. However, since the MSC is a switched system, classical feedback linearization theory does not apply. Nevertheless, the obtained results demonstrate that the proposed method achieves a comparable level of performance.

5 Hardware Setups

During this thesis, several types of practical implementations were carried out. This chapter provides an overview on the power converters and control platforms developed and used to obtain the results of previous chapters.

5.1 Low-power prototype

The MMC prototype consists of six identical arms, each comprising six submodules, resulting in a total of 36 SM. The prototype currently rated and validated for 1 kW operation. However its design allows for up to 10 SM per arm and supports bidirectional power flow. A visualization of MMC prototype operating as inverter with resistive loads connected to its output terminals is given in Figure 5.1.

Each SM is rated for 100 V and can be configured either as a HB-SM or a FB-SM, where a Local Field Programmable Gate Array (LFPGA) is responsible to monitor the capacitor voltage and safely provide the required gate signals. The topology is modular, so the the hardware in Figure 5.2 is designed with a flexible mindset:

- Compatible semiconductors with TO-247 package, enabling the use of Insulated-Gate Bipolar Transistor (IGBT)s and MOSFETs. Additionally, Silicon, SiC and GaN Mosfets are currently offered in this package.
- Gate driver boards are easily replaceable for the target semiconductors, without redesigning the the entire SM.
- The same idea applies for the LFPGA, which is currently a low-cost, low-performance one.
- The total submodule capacitance can be adjusted to several combinations of electrolytic- and/or film-based technologies
- For future applications, additional temperature and current sensors where accounted in the design
- Auxiliary supply accepts a wide range of voltages (9 V – 30 V) and rated

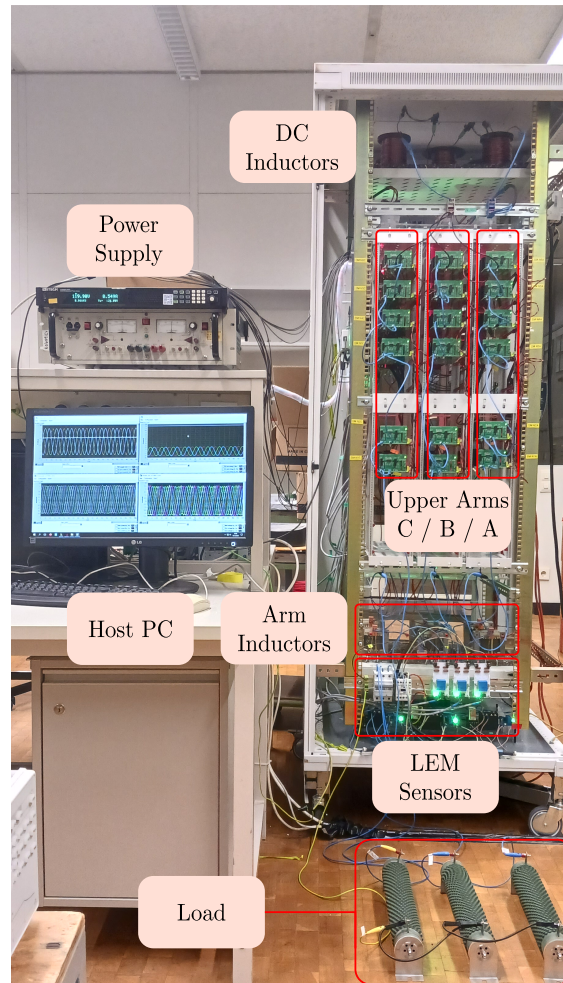


Figure 5.1: MMC 1 kW prototype

power of 25 W

The LFPGAs exchange information with a CFPGA, given in Figure 5.3. The CFPGA (Artix-7) provides significantly higher performance compared to the LFPGAs (Spartan-6). This performance advantage is essential for executing the following tasks:

- Data acquisition – Measurement of all SM voltages, arm currents, DC- and AC-side voltages. Additionally, low-pass filters are deployed for signal reliability.
- Actuator – Arm voltage modulation using a level-shifted PWM and sorting algorithm, described in Figure 2.12.
- Communication interface – Through a target-improved Universal Asynchronous Receive Transmit (UART) communication, the central controller

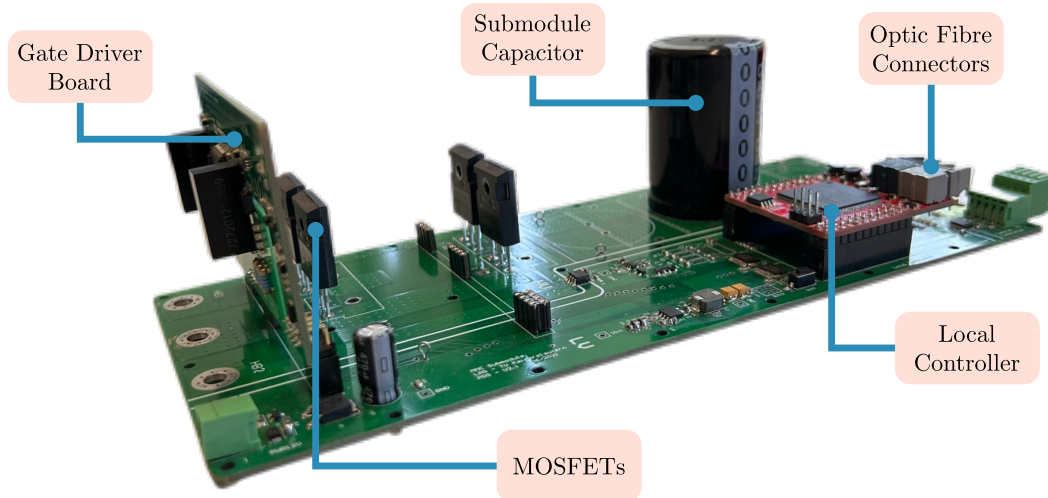


Figure 5.2: Prototype half- and full-bridge submodule

exchanges commands and measured data with the master controller and all submodules.

- Safety – In addition to fault detection, in the central controller, security-check routines to safely enable and disable the MMC operation are executed

To achieve this, a modular hardware interface was designed, where a base board currently interfaces six optical fiber boards and four Analog-to-Digital Converter (ADC) boards and the central controller board. For improved wiring efficiency, the boards can be placed in any of the available slots. Hence, the current design provides 48 independent communication channels and 16 measurement channels. For compatibility with the demonstrator hardware inserted in a MV environment, the communication occurs via optical fiber receivers and transceivers. The same applies for the measurements obtained with voltage and current transducers, where isolated $\Sigma\Delta$ -ADC are used. Each ADC board can measure up to eight transducers.

To achieve this, a modular hardware interface was developed, in which a base board connects to six optical fiber boards and four ADC boards. The fiber optic channels facilitate signal exchange with the CFPGA and LFPGAs. For improved wiring flexibility, the boards can be inserted into any of the available slots. The current implementation supports 48 independent communication channels and 16 measurement channels. To ensure compatibility with the Demonstrator hardware operating in a medium-voltage environment, communication is handled via optical fiber receivers and transceivers. A similar approach is applied to voltage and current measurements, which are acquired using isolated $\Sigma\Delta$ ADC devices. Each ADC board can interface with up to eight current/voltage transducers.

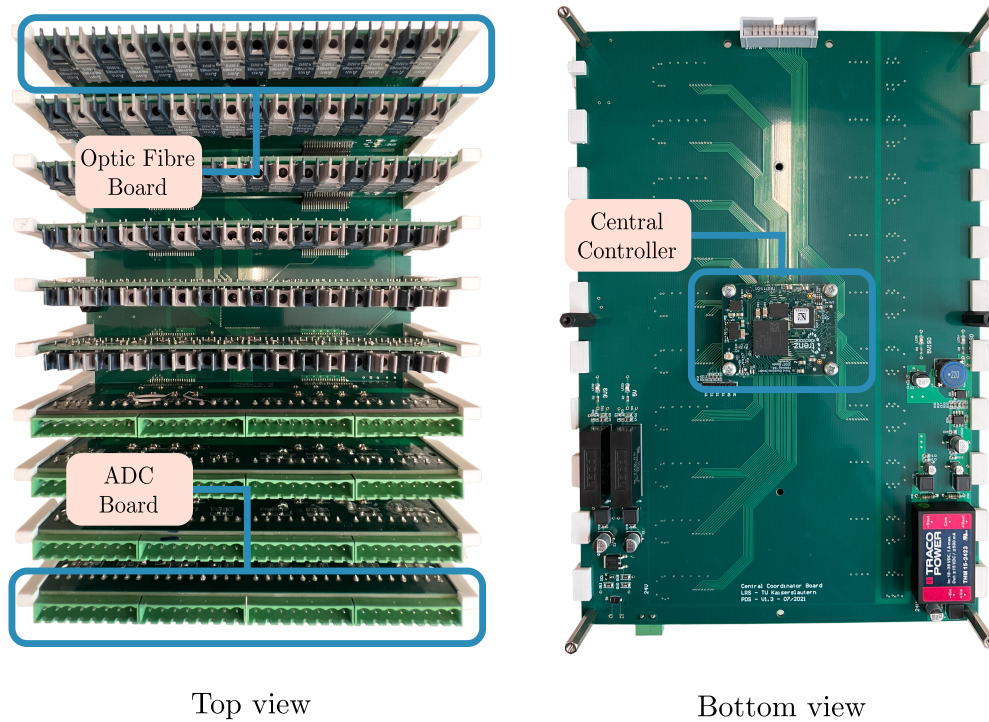


Figure 5.3: Central FPGA controller board

Lastly, the master controller is deployed in a cost-effective SoC development board, named PYNQ-Z2, consists of the combination of two ARM Cortex-A9 CPUs (Processing System (PS)) and a Artix-7 FPGA (Programmable Logic (PL)). Additionally, an optical fiber interface was developed to communicate with the central controller, as shown in Figure 5.4. A target-specific UART communication enables the delivery of relevant data to the master controller for control algorithm execution. Upon completion, the calculated arm modulation indexes are transmitted back. Furthermore, the communication between SoC and CFPGA is established on the PL-side due to the parallel nature of the programmable logic. In this implementation, the chosen communication channels is provided in Table 5.1.

The control algorithm is implemented and executed on the PS, offering the implementation of embedded C-code on the processor. It also provides a user interface to change reference values and to plot signals/variables on the host PC via USB. To conclude, the established prototype aims for a decentralized and modular system architecture. The hardware of a MMC interconnects several complex subsystems. Hence, future different requirements do not lead to an entire hardware redesign. A block diagram of the system architecture is given in Figure 5.5 and the MMC prototype circuit parameters is provided in Table 5.2. Further details

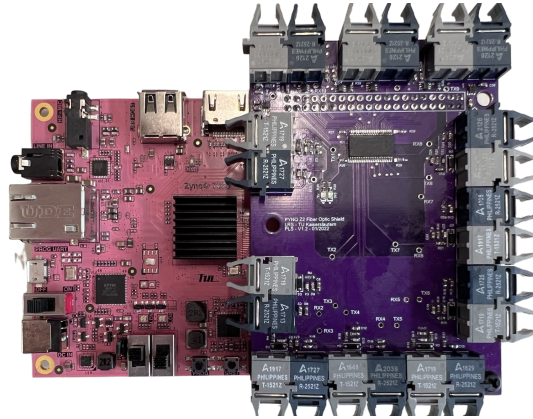


Figure 5.4: Master controller

Table 5.1: Communication channels between Master and CFPGA

Channel	Signals	
	TX	RX
1	$U_{cp}^{\Sigma}, U_{cn}^{\Sigma}$	m_p, m_n
2	I_p, I_n	none
3	U_g, I_g	none
4	U_{dc}, I_{dc}	none
5	Ready	Reset, Error
6	Error type	min/max values

are found in works developed in [182, 195]

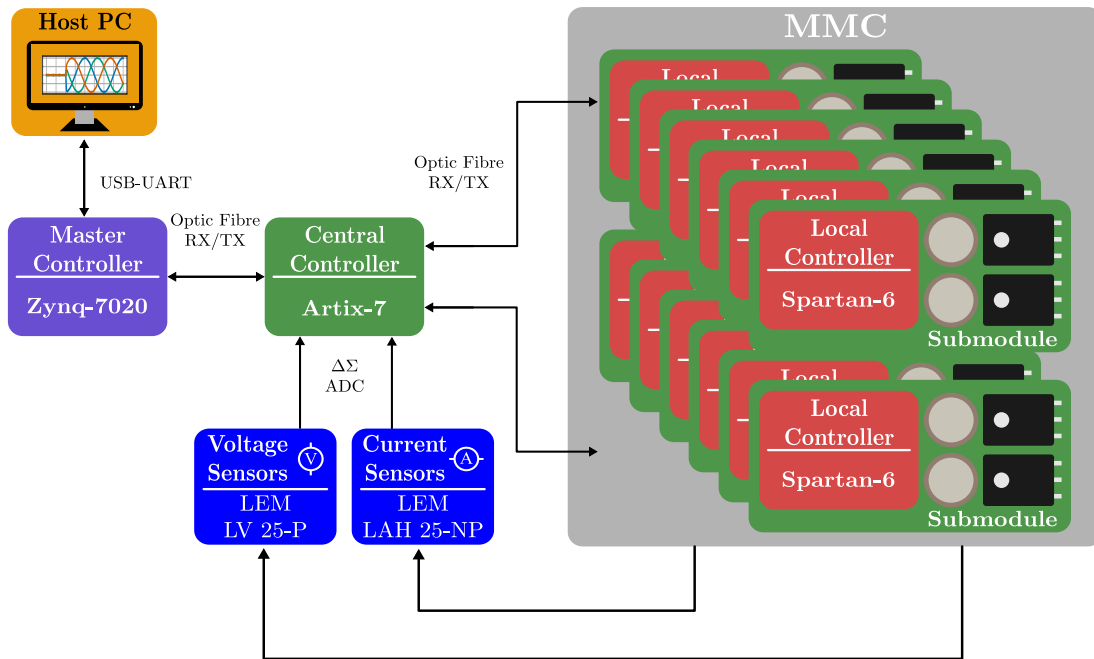


Figure 5.5: Block diagram of prototype's system architecture

5.2 Open Processor-in-the-Loop (OPiL)

Making use of the same line of thinking, any changes in the control algorithm are now only focused on the SoC development board. Zooming in its structure, the allocation of available resources for the designed functions is provided in Figure 5.6. As described earlier, functions were assigned based on convenience and available resources. However, as systems evolve and control algorithms become more complex, alternative resource allocation strategies may be required. As highlighted in [196], the ability to generate binary files alone does not guarantee successful deployment—posing a risk to the developed hardware.

To mitigate this risk, low-cost testing methods can be employed. One such method is PiL testing, where the control algorithm is deployed on the embedded target and evaluated in a closed-loop simulation. In this setup, both the plant measurements and actuator signals are simulated using simulation platforms as PLECS and Matlab/Simulink. Since real-time constraints are not enforced during PiL test, the implementation can be iteratively refined in closed-loop to meet acceptable execution performance. PiL also allows safe and efficient experimentation with different implementation strategies, compiler configurations, and memory execution options (e.g., from flash or RAM), all while maintaining closed-loop validation of the controller.

Table 5.2: MMC prototype - circuit parameter of low voltage MMC

Symbol	Description	Value
U_{dc}	DC grid voltage	120 V
L_d	DC interface inductance	750 μ H
L_d	DC interface resistance	245 m Ω
R_g	AC phase load resistor	10 Ω
L_{arm}	Arm inductance	3.19 mH
R_{arm}	Arm resistance	47 m Ω
C_{sm}	SM capacitor	4.5 mF
N_{sm}	Number of SM per arm	6
U_{Csm}	Average SM voltage	20 V
f_{smp}	Sampling frequency	6 kHz
f_{car}	PWM carrier frequency	6 kHz
f_{sw}	SM switching frequency	1 kHz

However, to the best of the author's knowledge, such PiL configurations are typically restricted to authorized vendors in cooperation with specific simulation tool providers. As an alternative, an open-source framework OPiL containing pre-defined functions in C was developed in [197] to manage the data flow between simulation and controller. These blocks are made modular, so that it can easily support different simulation software and embedded controllers. As a result, the control algorithm deployed in the PYNQ-Z2 development board could be tested against the MMC model developed in PLECS. A general representation of the OPiL concept is given in Figure 5.7. Further details and resources are given in [198].

5.3 High-power demonstrator

A representation of 300 kW demonstrator, developed during the GridCON project is given in Figure 5.8. The circuit parameters are given in Table 5.3. Opposite to the prototype, the MSC includes an active liquid-cooling system and the overall structure is managed to place in a standard server cabinet. Therefore, after

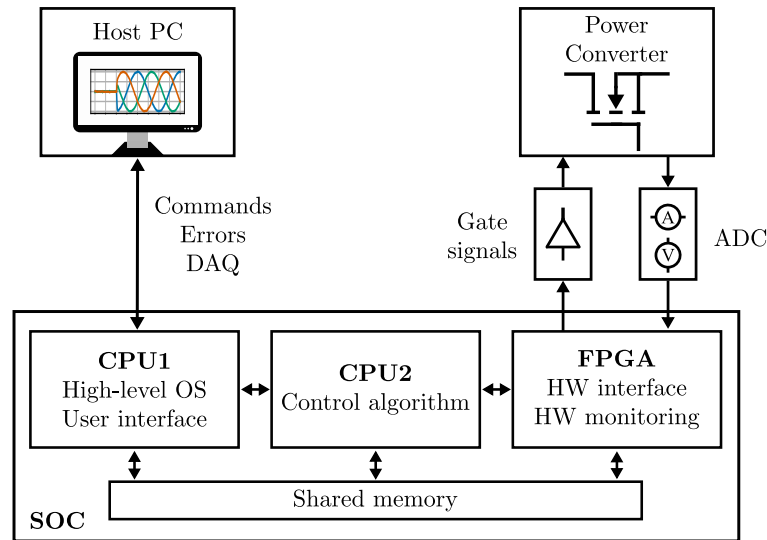


Figure 5.6: Example of control system implementation in a System-On-Chip

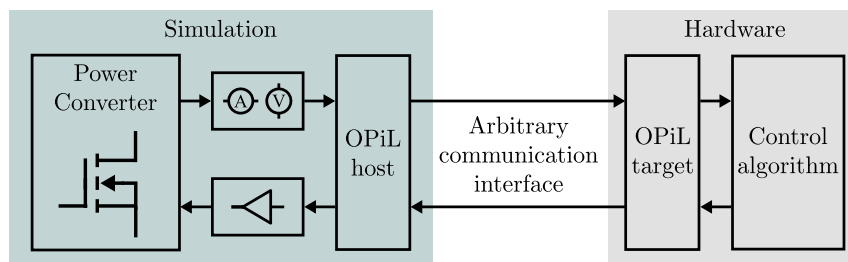


Figure 5.7: Concept of Open Processor-in-the-Loop (OPiL)

a careful component placement without compromising safety limits, a 40% decrease in the converter size as compared to its predecessor setup was achieved [187, 193]. The structure of the SMs replicates that of the prototype, comprising three separate boards, as illustrated in Figure 5.9. The integrated cooling system ensures safe operation of both the semiconductor module and the film capacitors, which are subjected to high current levels. However, the current design is restricted to a half-bridge configuration in order to preserve the high power density within the MSC. Furthermore, the system architecture closely resembles that of the prototype, up to the point where the master controller is replaced by a dSPACE system, as externally dictated by the project requirements. The use of dSPACE enabled rapid prototyping and easy development of a user interface. A setup representation is given in Figure 5.10.



Figure 5.8: Mobile Side Converter – 300 kW Demonstrator

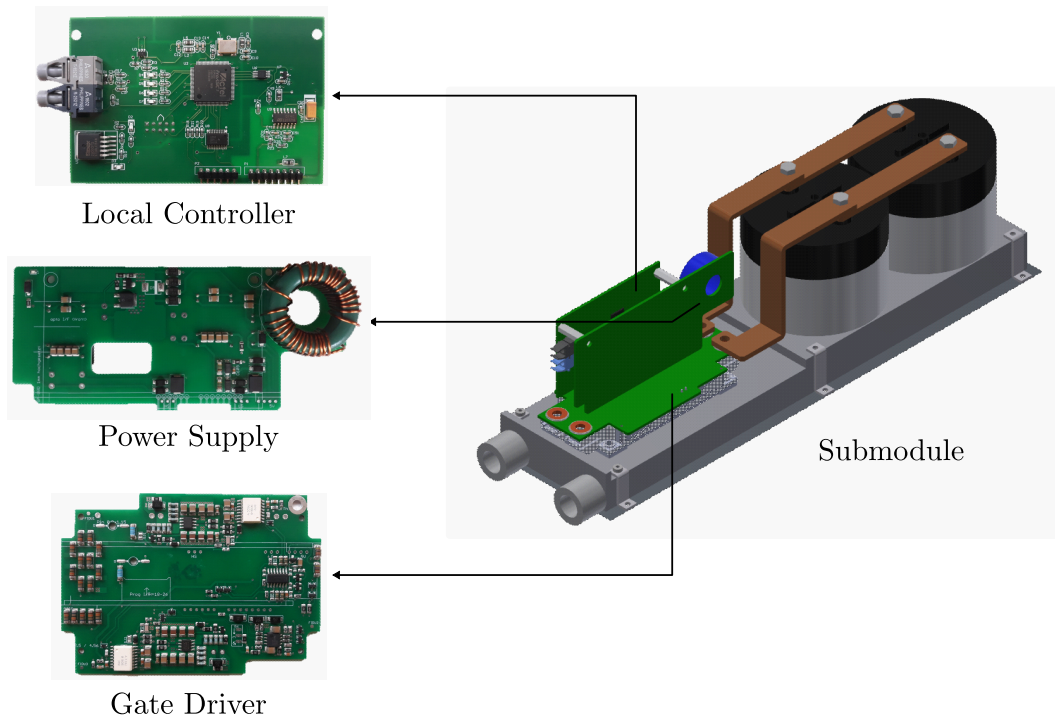


Figure 5.9: Demonstrator half-bridge submodule



Figure 5.10: Control platform – dSPACE , central FPGA and user interface

Table 5.3: Circuit parameter of medium voltage MSC Demonstrator

Symbol	Description	Value
U_{dc1}	DC grid voltage	5600 V
U_{dc2}	Machine voltage	750 V
C_{dc2}	Output capacitor	12.24 mF
L_{arm}	Arm inductance	0.2 mH
R_{arm}	Arm resistance	10 m Ω
C_{sm}	SM capacitor	0.88 mF
N_{sm}	Number of SM per arm	5
N_{ins}	Number of inserted SM per Phase	8
U_{Csm}	Average SM voltage	700 V
f_{smp}	Sampling frequency	6 kHz
f_{car}	PWM carrier frequency	1 kHz
f_{sw}	SM switching frequency	1 kHz

6 Conclusion

This thesis has explored the topological structure of the Modular Multilevel Converter, with focus on its modularity and flexible energy storage capabilities. The research conducted, introduced and analyzed two unexplored features of the MMC, enhanced by the control strategies developed in the course this investigation.

6.1 Summary

From the data collected, an increasing population associated with economic growth in underdevelopment countries will demand more energy production. With the current energy mix consumption, further global warming is only avoidable through urgent large-scale electrification based on renewable energy sources and storage systems. Given that these technologies are inherently DC in nature, a strong case is made for the transition from traditional AC-based electrical grids to DC or hybrid AC/DC grid architectures. This transition is made feasible by advancements in power electronics and converter design, where their fundamental principles were outlined for basic understanding of the subsequent chapters. For transmission and distribution networks, only multilevel power converter topologies can cope with their voltage requirements. Among them, the MMC emerges as the most flexible, cost-effective and promising solution.

The MMC topology has been analyzed by deconstructing it into its fundamental building blocks, with particular emphasis on its flexible energy storage capabilities. A comprehensive circuit analysis of the topology was conducted, serving as the foundation for deriving both linear and nonlinear state-space models. Insights in available modulation techniques and intra-arm balancing methodologies were provided. Both switching and average models were described and compared to prove the suitability of the last. At the cost of increased switching frequency for lower number of available submodules, the average model effectively represents the fundamental behavior of the topology, thereby serving as a reliable basis for control design.

Afterwards, the concept of power decoupling between the AC and DC grids is introduced. By exploiting the distributed energy storage capability of the MMC,

distinct transient responses to a common power reference change can be realized on the AC and DC sides. In this way, the converter can independently regulate the power exchange with both networks while simultaneously supporting the stabilization of the AC and DC grid dynamics. Compared to other converter topologies, the MMC uniquely enables independent and simultaneous control of the power exchanged with the source and sink networks. Hence the MMC should be considered when interfacing grid from different nature, specially when connected with weak networks, where faster transient responses may risk operation at the weaker side. This capability is enhanced by the installed capacitance and developed control algorithm. The Input-Output Feedback Linearization technique was used to cancel the inner-loop non-linear relations. Hence, to obtain linear and decoupled control of the DC-,AC- and circulating currents. In cascaded structure, these are responsible to drive the average energy stored in the arm capacitors. Such technique is susceptible to parameter uncertainties, which may jeopardize the control action in a practical setup. To counteract, an extended disturbance observer was developed. Afterwards a 2-DOF controller has been designed to control the arm energies and guarantee decoupled disturbance and reference change dynamics. The controller performance was validated in a laboratory prototype, built during the course of this thesis. Additionally, to address hardware limitations, a long-horizon Model Predictive Controller was investigated as an outer-loop control strategy. The results indicate that it achieves good performance while respecting constraints on the maximum instantaneous power exchanged with the grid and the stored energy. The last controller was tested in a Processor-in-the-Loop environment to access its feasibility under different prediction and constrained horizons.

Additionally, the development of a Mobile Side Converter (MSC) specifically designed for heavy-duty agricultural electrification is presented. In this challenging application, where electrification is typically difficult, a MVDC microgrid supplies power to multiple agricultural machines, significantly improving overall system efficiency. The MSC is intended for direct integration into each machine and utilizes a MMC architecture to step down the MVDC to the LVDC levels required by onboard subsystems. Unlike conventional approaches, the converter achieves a high voltage step-down ratio without the use of a transformer by increasing the number of permanently inserted submodules—trading off the number of available voltage levels, overall to enhance power density. Despite the highly non-linear nature of the resulting circuit, its various operational modes are comprehensively analyzed and experimentally validated using a 300 kW demonstrator. Furthermore, a reduced-order model is developed to support the design of an adaptive controller capable of delivering distinct and robust transient responses to both disturbances and reference changes. Compared to traditional solutions, this controller demonstrates significantly improved transient performance and adaptability, making it particularly well-suited for handling the dynamic and variable load

conditions inherent in agricultural applications.

6.2 Future Work

To fully realize the potential of the proposed capabilities, future research should address the limitations identified in this thesis. Several important and unresolved questions have emerged throughout the investigation, offering clear directions for continued exploration. For instance, this work highlights a strong motivation to achieve a predetermined transient response; however, the presence of mixed-frequency components within the circulating currents poses a significant challenge, particularly during reference tracking, making it difficult to meet the desired dynamic performance.

The concept of power decoupling could be further extended to other functionalities of interconnecting power converters, especially under faulty or unbalanced conditions. Furthermore, the stabilization of the DC grid under long cable configurations deserves dedicated investigation, as cable-induced resonances and propagation effects may introduce poorly damped dynamics that challenge both the control design and the achievable power decoupling performance. Such scenarios introduce additional mixed-frequency components on both the DC and AC sides of the grid, potentially compromising the effectiveness of the feedback linearization strategy and the robustness ensured by the designed disturbance observer. Advancing research in this direction could also contribute to improve the performance of the designed MPC strategy. Despite the controller's strong performance, minor constraint violations in certain energy components have been observed, likely due to mismatches in the closed-loop model of the circulating current.

Moreover, exploring alternative solvers for practical implementation of long-horizon MPC is a promising direction for evaluating the controller's feasibility in real-world conditions. Deployment on a more capable embedded platform may also offer improvements in performance and scalability.

Regarding the MSC, the practical hardware implementation of the proposed adaptive controller represents a key next step, especially given the encouraging simulation results. Additionally, integrating power decoupling principles into MSC operation presents an exciting opportunity, although this will first require the development of a dedicated energy controller for the converter architecture presented in this work.

A Auxiliary Math

A.1 Reference frames

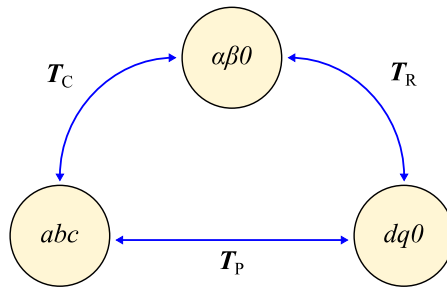


Figure A.1: Relationships between the Park and Clarke transformations

$$\mathbf{T}_C = \begin{bmatrix} \frac{2}{3} & -\frac{1}{3} & -\frac{1}{3} \\ 0 & \frac{\sqrt{3}}{3} & -\frac{\sqrt{3}}{3} \end{bmatrix} \quad (\text{A.1})$$

$$\mathbf{T}_{iC} = \begin{bmatrix} 1 & 0 \\ -\frac{1}{2} & \frac{\sqrt{3}}{2} \\ -\frac{1}{2} & -\frac{\sqrt{3}}{2} \end{bmatrix} \quad (\text{A.2})$$

$$\mathbf{T}_{C0} = \begin{bmatrix} \frac{2}{3} & -\frac{1}{3} & -\frac{1}{3} \\ 0 & \frac{\sqrt{3}}{3} & -\frac{\sqrt{3}}{3} \\ \frac{1}{3} & \frac{1}{3} & \frac{1}{3} \end{bmatrix} \quad (\text{A.3})$$

$$\mathbf{T}_{iC0} = \begin{bmatrix} 1 & 0 & 1 \\ -\frac{1}{2} & \frac{\sqrt{3}}{2} & 1 \\ -\frac{1}{2} & -\frac{\sqrt{3}}{2} & 1 \end{bmatrix} \quad (\text{A.4})$$

$$\mathbf{T}_{R,n+} = \begin{bmatrix} \cos(n\theta) & \sin(n\theta) \\ -\sin(n\theta) & \cos(n\theta) \end{bmatrix} \quad (\text{A.5})$$

$$\mathbf{T}_{R,n-} = \mathbf{T}_{R,n+}^{-1} = \begin{bmatrix} \cos(n\theta) & -\sin(n\theta) \\ \sin(n\theta) & \cos(n\theta) \end{bmatrix} \quad (\text{A.6})$$

$$\mathbf{T}_{R0,n+} = \begin{bmatrix} \cos(n\theta) & \sin(n\theta) & 0 \\ -\sin(n\theta) & \cos(n\theta) & 0 \\ 0 & 0 & 1 \end{bmatrix} \quad (\text{A.7})$$

$$\mathbf{T}_{R0,n-} = \mathbf{T}_{R0,n+}^{-1} = \begin{bmatrix} \cos(n\theta) & -\sin(n\theta) & 0 \\ \sin(n\theta) & \cos(n\theta) & 0 \\ 0 & 0 & 1 \end{bmatrix} \quad (\text{A.8})$$

$$\mathbf{T}_P = \frac{2}{3} \begin{bmatrix} \cos(\theta) & \cos(\theta - \frac{2\pi}{3}) & \cos(\theta + \frac{2\pi}{3}) \\ -\sin(\theta) & -\sin(\theta - \frac{2\pi}{3}) & -\sin(\theta + \frac{2\pi}{3}) \end{bmatrix} \quad (\text{A.9})$$

$$\mathbf{T}_{iP} = \begin{bmatrix} \cos(\theta) & -\sin(\theta) \\ \cos(\theta - \frac{2\pi}{3}) & -\sin(\theta - \frac{2\pi}{3}) \\ \cos(\theta + \frac{2\pi}{3}) & -\sin(\theta + \frac{2\pi}{3}) \end{bmatrix} \quad (\text{A.10})$$

$$\mathbf{T}_{P0} = \frac{2}{3} \begin{bmatrix} \cos(\theta) & \cos(\theta - \frac{2\pi}{3}) & \cos(\theta + \frac{2\pi}{3}) \\ -\sin(\theta) & -\sin(\theta - \frac{2\pi}{3}) & -\sin(\theta + \frac{2\pi}{3}) \\ \frac{1}{2} & \frac{1}{2} & \frac{1}{2} \end{bmatrix} \quad (\text{A.11})$$

$$\mathbf{T}_{iP0} = \begin{bmatrix} \cos(\theta) & -\sin(\theta) & 1 \\ \cos(\theta - \frac{2\pi}{3}) & -\sin(\theta - \frac{2\pi}{3}) & 1 \\ \cos(\theta + \frac{2\pi}{3}) & -\sin(\theta + \frac{2\pi}{3}) & 1 \end{bmatrix} \quad (\text{A.12})$$

A.2 Auxiliary transformations

In this subsection, the auxiliary transformations and vectors are listed as intermediate steps to obtain the non-linear model in subsection 2.3.2.

$$\mathbf{T}_{\text{gzd,pn}} = \begin{bmatrix} \frac{1}{2} & 0 & 0 & 1 & 0 & 0 & \frac{1}{3} \\ 0 & \frac{1}{2} & 0 & 0 & 1 & 0 & \frac{1}{3} \\ 0 & 0 & \frac{1}{2} & 0 & 0 & 1 & \frac{1}{3} \\ -\frac{1}{2} & 0 & 0 & 1 & 0 & 0 & \frac{1}{3} \\ 0 & -\frac{1}{2} & 0 & 0 & 1 & 0 & \frac{1}{3} \\ 0 & 0 & -\frac{1}{2} & 0 & 0 & 1 & \frac{1}{3} \end{bmatrix} \quad (\text{A.13})$$

$$\mathbf{T}_{\text{iC,xi}} = \begin{bmatrix} 1 & 0 & 1 & 0 & 0 & 0 \\ -\frac{1}{2} & \frac{\sqrt{3}}{2} & 1 & 0 & 0 & 0 \\ -\frac{1}{2} & -\frac{\sqrt{3}}{2} & 1 & 0 & 0 & 0 \\ 0 & 0 & 0 & 1 & 0 & 0 \\ 0 & 0 & 0 & -\frac{1}{2} & \frac{\sqrt{3}}{2} & 0 \\ 0 & 0 & 0 & -\frac{1}{2} & -\frac{\sqrt{3}}{2} & 0 \\ 0 & 0 & 0 & 0 & 0 & 1 \end{bmatrix} \quad (\text{A.14})$$

$$\mathbf{T}_{\text{gzd,pn}} \cdot \mathbf{T}_{\text{iC,xi}} = \mathbf{T}_{\text{xi,pn0}} = \begin{bmatrix} \frac{1}{2} & 0 & \frac{1}{2} & 1 & 0 & \frac{1}{3} \\ -\frac{1}{4} & \frac{\sqrt{3}}{4} & \frac{1}{2} & -\frac{1}{2} & \frac{\sqrt{3}}{2} & \frac{1}{3} \\ -\frac{1}{4} & -\frac{\sqrt{3}}{4} & \frac{1}{2} & -\frac{1}{2} & -\frac{\sqrt{3}}{2} & \frac{1}{3} \\ -\frac{1}{2} & 0 & -\frac{1}{2} & 1 & 0 & \frac{1}{3} \\ \frac{1}{4} & -\frac{\sqrt{3}}{4} & -\frac{1}{2} & -\frac{1}{2} & \frac{\sqrt{3}}{2} & \frac{1}{3} \\ \frac{1}{4} & \frac{\sqrt{3}}{4} & -\frac{1}{2} & -\frac{1}{2} & -\frac{\sqrt{3}}{2} & \frac{1}{3} \end{bmatrix} \quad (\text{A.15})$$

$$\mathbf{T}_{\text{xi,pn}} = \begin{bmatrix} \frac{1}{2} & 0 & 1 & 0 & \frac{1}{3} \\ -\frac{1}{4} & \frac{\sqrt{3}}{4} & -\frac{1}{2} & \frac{\sqrt{3}}{2} & \frac{1}{3} \\ -\frac{1}{4} & -\frac{\sqrt{3}}{4} & -\frac{1}{2} & -\frac{\sqrt{3}}{2} & \frac{1}{3} \\ -\frac{1}{2} & 0 & 1 & 0 & \frac{1}{3} \\ \frac{1}{4} & -\frac{\sqrt{3}}{4} & -\frac{1}{2} & \frac{\sqrt{3}}{2} & \frac{1}{3} \\ \frac{1}{4} & \frac{\sqrt{3}}{4} & -\frac{1}{2} & -\frac{\sqrt{3}}{2} & \frac{1}{3} \end{bmatrix} \quad (\text{A.16})$$

$$\mathbf{T}_{C,ui} = \begin{bmatrix} \frac{2}{3} & -\frac{1}{3} & -\frac{1}{3} & 0 & 0 & 0 \\ 0 & \frac{\sqrt{3}}{3} & -\frac{\sqrt{3}}{3} & 0 & 0 & 0 \\ 0 & 0 & 0 & \frac{2}{3} & -\frac{1}{3} & -\frac{1}{3} \\ 0 & 0 & 0 & 0 & \frac{\sqrt{3}}{3} & -\frac{\sqrt{3}}{3} \\ \frac{1}{3} & \frac{1}{3} & \frac{1}{3} & \frac{1}{3} & \frac{1}{3} & \frac{1}{3} \end{bmatrix} \quad (\text{A.17})$$

$$\mathbf{T}_{iC,ui} = \begin{bmatrix} 1 & 0 & 0 & 0 & \frac{1}{2} \\ -\frac{1}{2} & \frac{\sqrt{3}}{2} & 0 & 0 & \frac{1}{2} \\ -\frac{1}{2} & -\frac{\sqrt{3}}{2} & 0 & 0 & \frac{1}{2} \\ 0 & 0 & 1 & 0 & \frac{1}{2} \\ 0 & 0 & -\frac{1}{2} & \frac{\sqrt{3}}{2} & \frac{1}{2} \\ 0 & 0 & -\frac{1}{2} & -\frac{\sqrt{3}}{2} & \frac{1}{2} \end{bmatrix} \quad (\text{A.18})$$

$$\mathbf{T}_{\Sigma\Delta} = \begin{bmatrix} \frac{2}{3} & -\frac{1}{3} & -\frac{1}{3} & \frac{2}{3} & -\frac{1}{3} & -\frac{1}{3} \\ 0 & \frac{\sqrt{3}}{3} & -\frac{\sqrt{3}}{3} & 0 & \frac{\sqrt{3}}{3} & -\frac{\sqrt{3}}{3} \\ \frac{1}{3} & \frac{1}{3} & \frac{1}{3} & \frac{1}{3} & \frac{1}{3} & \frac{1}{3} \\ \frac{2}{3} & -\frac{1}{3} & -\frac{1}{3} & -\frac{2}{3} & \frac{1}{3} & \frac{1}{3} \\ 0 & \frac{\sqrt{3}}{3} & -\frac{\sqrt{3}}{3} & 0 & -\frac{\sqrt{3}}{3} & \frac{\sqrt{3}}{3} \\ \frac{1}{3} & \frac{1}{3} & \frac{1}{3} & -\frac{1}{3} & -\frac{1}{3} & -\frac{1}{3} \end{bmatrix} \quad (\text{A.19})$$

A.3 Trigonometry

$$A_1 \cos(\omega_1 t) \cdot A_2 \cos(\omega_2 t) = \frac{A_1 A_2}{2} \cos((\omega_1 + \omega_2)t) + \frac{A_1 A_2}{2} \cos((\omega_1 - \omega_2)t). \quad (\text{A.20})$$

$$\int \cos(nt) dt = \frac{\sin(nt)}{n} + C \quad (\text{A.21})$$

B Arm Power Flow

Building on the stability analysis of the internal dynamics in 3.2.2, this section presents the derivation of the Arm power flow in the MMC as a foundation for further examination of the energy states. Following the relations in (2.16) and (3.22), yields,

$$\begin{aligned}
P_{pa} = & \frac{U_{dc}i_{dc}}{6} + \frac{U_{dc}i_{g\alpha}}{4} - \frac{U_{g\alpha}i_{dc}}{3} - \frac{U_{g\alpha}i_{g\alpha}}{2} \\
& + \frac{U_{dc}i_{z\alpha}}{2} - U_{g\alpha}i_{z\alpha} - \frac{R_{dc}i_{dc}^2}{6} - \frac{R_{ac}i_{g\alpha}^2}{2} - \frac{R_zi_{z\alpha}^2}{2} \\
& - \frac{R_{ac}i_{dc}i_{g\alpha}}{3} - \frac{R_{dc}i_{dc}i_{g\alpha}}{4} - \frac{R_{dc}i_{dc}i_{z\alpha}}{2} \\
& - R_{ac}i_{g\alpha}i_{z\alpha} - \frac{R_zi_{dc}i_{z\alpha}}{6} - \frac{R_zi_{g\alpha}i_{z\alpha}}{4}
\end{aligned} \tag{B.1}$$

$$\begin{aligned}
P_{pb} = & \frac{U_{dc}i_{dc}}{6} - \frac{U_{dc}i_{g\alpha}}{8} + \frac{U_{g\alpha}i_{dc}}{6} - \frac{3U_{g\beta}i_{g\beta}}{8} - \frac{U_{g\alpha}i_{g\alpha}}{8} \\
& - \frac{U_{dc}i_{z\alpha}}{4} - \frac{3U_{g\beta}i_{z\beta}}{4} - \frac{U_{g\alpha}i_{z\alpha}}{4} - \frac{R_{dc}i_{dc}^2}{6} \\
& - \frac{3R_{ac}i_{g\beta}^2}{8} - \frac{R_{ac}i_{g\alpha}^2}{8} - \frac{3R_zi_{z\beta}^2}{8} - \frac{R_zi_{z\alpha}^2}{8} \\
& + \frac{\sqrt{3}U_{dc}i_{g\beta}}{8} - \frac{\sqrt{3}U_{g\beta}i_{dc}}{6} + \frac{\sqrt{3}U_{g\beta}i_{g\alpha}}{8} + \frac{\sqrt{3}U_{g\alpha}i_{g\beta}}{8} \\
& + \frac{\sqrt{3}U_{dc}i_{z\beta}}{4} + \frac{\sqrt{3}U_{g\beta}i_{z\alpha}}{4} + \frac{\sqrt{3}U_{g\alpha}i_{z\beta}}{4} \\
& + \frac{R_{ac}i_{dc}i_{g\alpha}}{6} + \frac{R_{dc}i_{dc}i_{g\alpha}}{8} + \frac{R_{dc}i_{dc}i_{z\alpha}}{4} \\
& - \frac{3R_{ac}i_{g\beta}i_{z\beta}}{4} - \frac{R_{ac}i_{g\alpha}i_{z\alpha}}{4} + \frac{R_zi_{dc}i_{z\alpha}}{12} \\
& - \frac{3R_zi_{g\beta}i_{z\beta}}{16} - \frac{R_zi_{g\alpha}i_{z\alpha}}{16} - \frac{\sqrt{3}R_{ac}i_{dc}i_{g\beta}}{6} \\
& - \frac{\sqrt{3}R_{dc}i_{dc}i_{g\beta}}{8} + \frac{\sqrt{3}R_{ac}i_{g\beta}i_{g\alpha}}{4} - \frac{\sqrt{3}R_{dc}i_{dc}i_{z\beta}}{4} \\
& + \frac{\sqrt{3}R_{ac}i_{g\beta}i_{z\alpha}}{4} + \frac{\sqrt{3}R_{ac}i_{g\alpha}i_{z\beta}}{4} - \frac{\sqrt{3}R_zi_{dc}i_{z\beta}}{12}
\end{aligned}$$

$$+ \frac{\sqrt{3}R_z i_{g\beta} i_{z\alpha}}{16} + \frac{\sqrt{3}R_z i_{g\alpha} i_{z\beta}}{16} + \frac{\sqrt{3}R_z i_{z\beta} i_{z\alpha}}{4} \quad (\text{B.2})$$

$$\begin{aligned} P_{pc} = & \frac{U_{dc} i_{dc}}{6} - \frac{U_{dc} i_{g\alpha}}{8} + \frac{U_{g\alpha} i_{dc}}{6} - \frac{3U_{g\beta} i_{g\beta}}{8} - \frac{U_{g\alpha} i_{g\alpha}}{8} \\ & - \frac{U_{dc} i_{z\alpha}}{4} - \frac{3U_{g\beta} i_{z\beta}}{4} - \frac{U_{g\alpha} i_{z\alpha}}{4} - \frac{R_{dc} i_{dc}^2}{6} \\ & - \frac{3R_{ac} i_{g\beta}^2}{8} - \frac{R_{ac} i_{g\alpha}^2}{8} - \frac{3R_z i_{z\beta}^2}{8} - \frac{R_z i_{z\alpha}^2}{8} \\ & - \frac{\sqrt{3}U_{dc} i_{g\beta}}{8} + \frac{\sqrt{3}U_{g\beta} i_{dc}}{6} - \frac{\sqrt{3}U_{g\beta} i_{g\alpha}}{8} - \frac{\sqrt{3}U_{g\alpha} i_{g\beta}}{8} \\ & - \frac{\sqrt{3}U_{dc} i_{z\beta}}{4} - \frac{\sqrt{3}U_{g\beta} i_{z\alpha}}{4} - \frac{\sqrt{3}U_{g\alpha} i_{z\beta}}{4} \\ & + \frac{R_{ac} i_{dc} i_{g\alpha}}{6} + \frac{R_{dc} i_{dc} i_{g\alpha}}{8} + \frac{R_{dc} i_{dc} i_{z\alpha}}{4} \\ & - \frac{3R_{ac} i_{g\beta} i_{z\beta}}{4} - \frac{R_{ac} i_{g\alpha} i_{z\alpha}}{4} + \frac{R_z i_{dc} i_{z\alpha}}{12} \\ & - \frac{3R_z i_{g\beta} i_{z\beta}}{16} - \frac{R_z i_{g\alpha} i_{z\alpha}}{16} + \frac{\sqrt{3}R_{ac} i_{dc} i_{g\beta}}{6} \\ & + \frac{\sqrt{3}R_{dc} i_{dc} i_{g\beta}}{8} - \frac{\sqrt{3}R_{ac} i_{g\beta} i_{g\alpha}}{4} + \frac{\sqrt{3}R_{dc} i_{dc} i_{z\beta}}{4} \\ & - \frac{\sqrt{3}R_{ac} i_{g\beta} i_{z\alpha}}{4} - \frac{\sqrt{3}R_{ac} i_{g\alpha} i_{z\beta}}{4} + \frac{\sqrt{3}R_z i_{dc} i_{z\beta}}{12} \\ & - \frac{\sqrt{3}R_z i_{g\beta} i_{z\alpha}}{16} - \frac{\sqrt{3}R_z i_{g\alpha} i_{z\beta}}{16} - \frac{\sqrt{3}R_z i_{z\beta} i_{z\alpha}}{4} \end{aligned} \quad (\text{B.3})$$

$$\begin{aligned} P_{na} = & \frac{U_{dc} i_{dc}}{6} - \frac{U_{dc} i_{g\alpha}}{4} + \frac{U_{g\alpha} i_{dc}}{3} - \frac{U_{g\alpha} i_{g\alpha}}{2} + \frac{U_{dc} i_{z\alpha}}{2} \\ & + U_{g\alpha} i_{z\alpha} - \frac{R_{dc} i_{dc}^2}{6} - \frac{R_{ac} i_{g\alpha}^2}{2} - \frac{R_z i_{z\alpha}^2}{2} \\ & + \frac{R_{ac} i_{dc} i_{g\alpha}}{3} + \frac{R_{dc} i_{dc} i_{g\alpha}}{4} - \frac{R_{dc} i_{dc} i_{z\alpha}}{2} \\ & + R_{ac} i_{g\alpha} i_{z\alpha} - \frac{R_z i_{dc} i_{z\alpha}}{6} + \frac{R_z i_{g\alpha} i_{z\alpha}}{4} \end{aligned} \quad (\text{B.4})$$

$$\begin{aligned} P_{nb} = & \frac{U_{dc} i_{dc}}{6} + \frac{U_{dc} i_{g\alpha}}{8} - \frac{U_{g\alpha} i_{dc}}{6} - \frac{3U_{g\beta} i_{g\beta}}{8} - \frac{U_{g\alpha} i_{g\alpha}}{8} \\ & - \frac{U_{dc} i_{z\alpha}}{4} + \frac{3U_{g\beta} i_{z\beta}}{4} + \frac{U_{g\alpha} i_{z\alpha}}{4} - \frac{R_{dc} i_{dc}^2}{6} \\ & - \frac{3R_{ac} i_{g\beta}^2}{8} - \frac{R_{ac} i_{g\alpha}^2}{8} - \frac{3R_z i_{z\beta}^2}{8} - \frac{R_z i_{z\alpha}^2}{8} \end{aligned}$$

$$\begin{aligned}
& -\frac{\sqrt{3}U_{dc}i_{g\beta}}{8} + \frac{\sqrt{3}U_{g\beta}i_{dc}}{6} + \frac{\sqrt{3}U_{g\beta}i_{g\alpha}}{8} + \frac{\sqrt{3}U_{g\alpha}i_{g\beta}}{8} \\
& + \frac{\sqrt{3}U_{dc}i_{z\beta}}{4} - \frac{\sqrt{3}U_{g\beta}i_{z\alpha}}{4} - \frac{\sqrt{3}U_{g\alpha}i_{z\beta}}{4} \\
& - \frac{R_{ac}i_{dc}i_{g\alpha}}{6} - \frac{R_{dc}i_{dc}i_{g\alpha}}{8} + \frac{R_{dc}i_{dc}i_{z\alpha}}{4} \\
& + \frac{3R_{ac}i_{g\beta}i_{z\beta}}{4} + \frac{R_{ac}i_{g\alpha}i_{z\alpha}}{4} + \frac{R_zi_{dc}i_{z\alpha}}{12} \\
& + \frac{3R_zi_{g\beta}i_{z\beta}}{16} + \frac{R_zi_{g\alpha}i_{z\alpha}}{16} + \frac{\sqrt{3}R_{ac}i_{dc}i_{g\beta}}{6} \\
& + \frac{\sqrt{3}R_{dc}i_{dc}i_{g\beta}}{8} + \frac{\sqrt{3}R_{ac}i_{g\beta}i_{g\alpha}}{4} - \frac{\sqrt{3}R_{dc}i_{dc}i_{z\beta}}{4} \\
& - \frac{\sqrt{3}R_{ac}i_{g\beta}i_{z\alpha}}{4} - \frac{\sqrt{3}R_{ac}i_{g\alpha}i_{z\beta}}{4} - \frac{\sqrt{3}R_zi_{dc}i_{z\beta}}{12} \\
& - \frac{\sqrt{3}R_zi_{g\beta}i_{z\alpha}}{16} - \frac{\sqrt{3}R_zi_{g\alpha}i_{z\beta}}{16} + \frac{\sqrt{3}R_zi_{z\beta}i_{z\alpha}}{4}
\end{aligned} \tag{B.5}$$

$$\begin{aligned}
P_{nc} = & \frac{U_{dc}i_{dc}}{6} + \frac{U_{dc}i_{g\alpha}}{8} - \frac{U_{g\alpha}i_{dc}}{6} - \frac{3U_{g\beta}i_{g\beta}}{8} - \frac{U_{g\alpha}i_{g\alpha}}{8} \\
& - \frac{U_{dc}i_{z\alpha}}{4} + \frac{3U_{g\beta}i_{z\beta}}{4} + \frac{U_{g\alpha}i_{z\alpha}}{4} - \frac{R_{dc}i_{dc}^2}{6} \\
& - \frac{3R_{ac}i_{g\beta}^2}{8} - \frac{R_{ac}i_{g\alpha}^2}{8} - \frac{3R_zi_{z\beta}^2}{8} - \frac{R_zi_{z\alpha}^2}{8} \\
& + \frac{\sqrt{3}U_{dc}i_{g\beta}}{8} - \frac{\sqrt{3}U_{g\beta}i_{dc}}{6} - \frac{\sqrt{3}U_{g\beta}i_{g\alpha}}{8} - \frac{\sqrt{3}U_{g\alpha}i_{g\beta}}{8} \\
& - \frac{\sqrt{3}U_{dc}i_{z\beta}}{4} + \frac{\sqrt{3}U_{g\beta}i_{z\alpha}}{4} + \frac{\sqrt{3}U_{g\alpha}i_{z\beta}}{4} \\
& - \frac{R_{ac}i_{dc}i_{g\alpha}}{6} - \frac{R_{dc}i_{dc}i_{g\alpha}}{8} + \frac{R_{dc}i_{dc}i_{z\alpha}}{4} \\
& + \frac{3R_{ac}i_{g\beta}i_{z\beta}}{4} + \frac{R_{ac}i_{g\alpha}i_{z\alpha}}{4} + \frac{R_zi_{dc}i_{z\alpha}}{12} \\
& + \frac{3R_zi_{g\beta}i_{z\beta}}{16} + \frac{R_zi_{g\alpha}i_{z\alpha}}{16} - \frac{\sqrt{3}R_{ac}i_{dc}i_{g\beta}}{6} \\
& - \frac{\sqrt{3}R_{dc}i_{dc}i_{g\beta}}{8} - \frac{\sqrt{3}R_{ac}i_{g\beta}i_{g\alpha}}{4} + \frac{\sqrt{3}R_{dc}i_{dc}i_{z\beta}}{4} \\
& + \frac{\sqrt{3}R_{ac}i_{g\beta}i_{z\alpha}}{4} + \frac{\sqrt{3}R_{ac}i_{g\alpha}i_{z\beta}}{4} + \frac{\sqrt{3}R_zi_{dc}i_{z\beta}}{12} \\
& + \frac{\sqrt{3}R_zi_{g\beta}i_{z\alpha}}{16} + \frac{\sqrt{3}R_zi_{g\alpha}i_{z\beta}}{16} - \frac{\sqrt{3}R_zi_{z\beta}i_{z\alpha}}{4}
\end{aligned} \tag{B.6}$$

Alternatively, consider the total energy per phase and the energy difference between the upper and lower arms. In steady-state operation, it is desirable to

maintain equal energy in each phase while ensuring zero difference between the upper and lower arms. This approach also simplifies the previous derivation.

$$\begin{aligned}
P_{\Sigma a} &= P_{pa} + P_{na} \\
&= \frac{U_{dc} i_{dc}}{3} - U_{g\alpha} i_{g\alpha} + U_{dc} i_{z\alpha} \\
&\quad - \frac{R_{dc} i_{dc}^2}{3} - R_{ac} i_{g\alpha}^2 - R_z i_{z\alpha}^2 \\
&\quad - R_{dc} i_{dc} i_{z\alpha} - \frac{R_z i_{dc} i_{z\alpha}}{3}
\end{aligned} \tag{B.7}$$

$$\begin{aligned}
P_{\Delta a} &= P_{pa} - P_{na} \\
&= \frac{U_{dc} i_{g\alpha}}{2} - \frac{2U_{g\alpha} i_{dc}}{3} - 2U_{g\alpha} i_{z\alpha} \\
&\quad - \frac{2R_{ac} i_{dc} i_{g\alpha}}{3} - \frac{R_{dc} i_{dc} i_{g\alpha}}{2} \\
&\quad - 2R_{ac} i_{g\alpha} i_{z\alpha} - \frac{R_z i_{g\alpha} i_{z\alpha}}{2}
\end{aligned} \tag{B.8}$$

$$\begin{aligned}
P_{\Sigma b} &= P_{pb} + P_{nb} \\
&= \frac{U_{dc} i_{dc}}{3} - \frac{3U_{g\beta} i_{g\beta}}{4} - \frac{U_{g\alpha} i_{g\alpha}}{4} - \frac{U_{dc} i_{z\alpha}}{2} \\
&\quad - \frac{R_{dc} i_{dc}^2}{3} - \frac{3R_{ac} i_{g\beta}^2}{4} - \frac{R_{ac} i_{g\alpha}^2}{4} - \frac{3R_z i_{z\beta}^2}{4} - \frac{R_z i_{z\alpha}^2}{4} \\
&\quad + \frac{\sqrt{3}U_{g\beta} i_{g\alpha}}{4} + \frac{\sqrt{3}U_{g\alpha} i_{g\beta}}{4} + \frac{\sqrt{3}U_{dc} i_{z\beta}}{2} + \frac{R_{dc} i_{dc} i_{z\alpha}}{2} + \frac{R_z i_{dc} i_{z\alpha}}{6} \\
&\quad + \frac{\sqrt{3}R_{ac} i_{g\beta} i_{g\alpha}}{2} - \frac{\sqrt{3}R_{dc} i_{dc} i_{z\beta}}{2} - \frac{\sqrt{3}R_z i_{dc} i_{z\beta}}{6} + \frac{\sqrt{3}R_z i_{z\beta} i_{z\alpha}}{2}
\end{aligned} \tag{B.9}$$

$$\begin{aligned}
P_{\Delta b} &= P_{pb} - P_{nb} \\
&= \frac{U_{g\alpha} i_{dc}}{3} - \frac{U_{dc} i_{g\alpha}}{4} - \frac{3U_{g\beta} i_{z\beta}}{2} - \frac{U_{g\alpha} i_{z\alpha}}{2} + \frac{\sqrt{3}U_{dc} i_{g\beta}}{4} - \frac{\sqrt{3}U_{g\beta} i_{dc}}{3} \\
&\quad + \frac{\sqrt{3}U_{g\beta} i_{z\alpha}}{2} + \frac{\sqrt{3}U_{g\alpha} i_{z\beta}}{2} + \frac{R_{ac} i_{dc} i_{g\alpha}}{3} + \frac{R_{dc} i_{dc} i_{g\alpha}}{4} - \frac{3R_{ac} i_{g\beta} i_{z\beta}}{2} \\
&\quad - \frac{R_{ac} i_{g\alpha} i_{z\alpha}}{2} - \frac{3R_z i_{g\beta} i_{z\beta}}{8} - \frac{R_z i_{g\alpha} i_{z\alpha}}{8} - \frac{\sqrt{3}R_{ac} i_{dc} i_{g\beta}}{3} - \frac{\sqrt{3}R_{dc} i_{dc} i_{g\beta}}{4} \\
&\quad + \frac{\sqrt{3}R_{ac} i_{g\beta} i_{z\alpha}}{2} + \frac{\sqrt{3}R_{ac} i_{g\alpha} i_{z\beta}}{2} + \frac{\sqrt{3}R_z i_{g\beta} i_{z\alpha}}{8} + \frac{\sqrt{3}R_z i_{g\alpha} i_{z\beta}}{8}
\end{aligned} \tag{B.10}$$

$$P_{\Sigma c} = P_{pc} + P_{nc}$$

$$\begin{aligned}
&= \frac{U_{dc} i_{dc}}{3} - \frac{3U_{g\beta} i_{g\beta}}{4} - \frac{U_{g\alpha} i_{g\alpha}}{4} - \frac{U_{dc} i_{z\alpha}}{2} \\
&\quad - \frac{R_{dc} i_{dc}^2}{3} - \frac{3R_{ac} i_{g\beta}^2}{4} - \frac{R_{ac} i_{g\alpha}^2}{4} - \frac{3R_z i_{z\beta}^2}{4} - \frac{R_z i_{z\alpha}^2}{4} \\
&\quad - \frac{\sqrt{3}U_{g\beta} i_{g\alpha}}{4} - \frac{\sqrt{3}U_{g\alpha} i_{g\beta}}{4} - \frac{\sqrt{3}U_{dc} i_{z\beta}}{2} + \frac{R_{dc} i_{dc} i_{z\alpha}}{2} + \frac{R_z i_{dc} i_{z\alpha}}{6} \\
&\quad - \frac{\sqrt{3}R_{ac} i_{g\beta} i_{g\alpha}}{2} + \frac{\sqrt{3}R_{dc} i_{dc} i_{z\beta}}{2} + \frac{\sqrt{3}R_z i_{dc} i_{z\beta}}{6} - \frac{\sqrt{3}R_z i_{z\beta} i_{z\alpha}}{2} \quad (B.11)
\end{aligned}$$

$$\begin{aligned}
P_{\Delta c} &= P_{pc} - P_{nc} \\
&= \frac{U_{g\alpha} i_{dc}}{3} - \frac{U_{dc} i_{g\alpha}}{4} - \frac{3U_{g\beta} i_{z\beta}}{2} - \frac{U_{g\alpha} i_{z\alpha}}{2} - \frac{\sqrt{3}U_{dc} i_{g\beta}}{4} + \frac{\sqrt{3}U_{g\beta} i_{dc}}{3} \\
&\quad - \frac{\sqrt{3}U_{g\beta} i_{z\alpha}}{2} - \frac{\sqrt{3}U_{g\alpha} i_{z\beta}}{2} + \frac{R_{ac} i_{dc} i_{g\alpha}}{3} + \frac{R_{dc} i_{dc} i_{g\alpha}}{4} \\
&\quad - \frac{3R_{ac} i_{g\beta} i_{z\beta}}{2} - \frac{R_{ac} i_{g\alpha} i_{z\alpha}}{2} - \frac{3R_z i_{g\beta} i_{z\beta}}{8} - \frac{R_z i_{g\alpha} i_{z\alpha}}{8} \\
&\quad + \frac{\sqrt{3}R_{ac} i_{dc} i_{g\beta}}{3} + \frac{\sqrt{3}R_{dc} i_{dc} i_{g\beta}}{4} - \frac{\sqrt{3}R_{ac} i_{g\beta} i_{z\alpha}}{2} - \frac{\sqrt{3}R_{ac} i_{g\alpha} i_{z\beta}}{2} \\
&\quad - \frac{\sqrt{3}R_z i_{g\beta} i_{z\alpha}}{8} - \frac{\sqrt{3}R_z i_{g\alpha} i_{z\beta}}{8} \quad (B.12)
\end{aligned}$$

The number of terms is further reduced, when the $\alpha\beta 0$ reference frame is considered.

$$\begin{bmatrix} P_{\Sigma\alpha} \\ P_{\Sigma\beta} \\ P_{\Sigma 0} \end{bmatrix} = \mathbf{T}_{C0} \cdot \begin{bmatrix} P_{pa} + P_{na} \\ P_{pb} + P_{nb} \\ P_{pc} + P_{nc} \end{bmatrix} \quad (B.13)$$

$$\begin{bmatrix} P_{\Delta\alpha} \\ P_{\Delta\beta} \\ P_{\Delta 0} \end{bmatrix} = \mathbf{T}_{C0} \cdot \begin{bmatrix} P_{pa} - P_{na} \\ P_{pb} - P_{nb} \\ P_{pc} - P_{nc} \end{bmatrix} \quad (B.14)$$

By extension of the previous system, the following relations are obtained,

$$\begin{aligned}
P_{\Sigma\alpha} &= \frac{U_{g\beta} i_{g\beta}}{2} - \frac{U_{g\alpha} i_{g\alpha}}{2} + U_{dc} i_{z\alpha} \\
&\quad + \frac{R_{ac} i_{g\beta}^2}{2} - \frac{R_{ac} i_{g\alpha}^2}{2} + \frac{R_z i_{z\beta}^2}{2} - \frac{R_z i_{z\alpha}^2}{2} - R_{dc} i_{dc} i_{z\alpha} - \frac{R_z i_{dc} i_{z\alpha}}{3} \quad (B.15)
\end{aligned}$$

$$\begin{aligned}
P_{\Sigma\beta} &= \frac{U_{g\beta} i_{g\alpha}}{2} + \frac{U_{g\alpha} i_{g\beta}}{2} + U_{dc} i_{z\beta} \\
&\quad + R_{ac} i_{g\beta} i_{g\alpha} - R_{dc} i_{dc} i_{z\beta} - \frac{R_z i_{dc} i_{z\beta}}{3} + R_z i_{z\beta} i_{z\alpha} \quad (B.16)
\end{aligned}$$

$$P_{\Sigma 0} = \frac{U_{dc} i_{dc}}{3} - \frac{U_{g\alpha} i_{g\alpha}}{2} - \frac{U_{g\beta} i_{g\beta}}{2} - \frac{R_{dc} i_{dc}^2}{3} - \frac{R_{ac} i_{g\beta}^2}{2} - \frac{R_{ac} i_{g\alpha}^2}{2} - \frac{R_z i_{z\beta}^2}{2} - \frac{R_z i_{z\alpha}^2}{2} \quad (\text{B.17})$$

$$P_{\Delta\alpha} = \frac{U_{dc} i_{g\alpha}}{2} - \frac{2U_{g\alpha} i_{dc}}{3} + U_{g\beta} i_{z\beta} - U_{g\alpha} i_{z\alpha} - \frac{2R_{ac} i_{dc} i_{g\alpha}}{3} - \frac{R_{dc} i_{dc} i_{g\alpha}}{2} + R_{ac} i_{g\beta} i_{z\beta} - R_{ac} i_{g\alpha} i_{z\alpha} + \frac{R_z i_{g\beta} i_{z\beta}}{4} - \frac{R_z i_{g\alpha} i_{z\alpha}}{4} \quad (\text{B.18})$$

$$P_{\Delta\beta} = \frac{U_{dc} i_{g\beta}}{2} - \frac{2U_{g\beta} i_{dc}}{3} + U_{g\beta} i_{z\alpha} + U_{g\alpha} i_{z\beta} - \frac{2R_{ac} i_{dc} i_{g\beta}}{3} - \frac{R_{dc} i_{dc} i_{g\beta}}{2} + R_{ac} i_{g\beta} i_{z\alpha} + R_{ac} i_{g\alpha} i_{z\beta} + \frac{R_z i_{g\beta} i_{z\alpha}}{4} + \frac{R_z i_{g\alpha} i_{z\beta}}{4} \quad (\text{B.19})$$

$$P_{\Delta 0} = -U_{g\beta} i_{z\beta} - U_{g\alpha} i_{z\alpha} - R_{ac} i_{g\beta} i_{z\beta} - R_{ac} i_{g\alpha} i_{z\alpha} - \frac{R_z i_{g\beta} i_{z\beta}}{4} - \frac{R_z i_{g\alpha} i_{z\alpha}}{4} \quad (\text{B.20})$$

C Discretization

The controllers in this thesis are mostly presented in the continuous-time domain. However in practice, a discretization is necessary for practical implementation. This section describes the discretization methods used.

C.1 Transfer functions

Continuous transfer functions must be discretized in to the z domain. For this, the Tustin method (also bilinear transform) is used, yielding

$$s = \frac{2}{T_s} \frac{1 - z^{-1}}{1 + z^{-1}} \quad (\text{C.1})$$

where T_s is the sampling time. However, for resonant controllers and notch filters, the precise transformation of pole locations is crucial. If not done correctly, the target frequency may shift during the discretization process. To better conserve the desired frequency in discrete time domain, the Tustin transform from (C.1) is extended using a technique known as prewarping , yielding

$$s = \frac{\omega_{PW}}{\tan\left(\frac{\omega_{PW} T_s}{2}\right)} \frac{1 - z^{-1}}{1 + z^{-1}} \quad (\text{C.2})$$

where ω_{PW} as the pre-warping frequency [157].

C.2 State-space representations

For systems represented as state-space models, the Zero-Order-Hold (ZOH) discretization method is utilized. Consider the solution of a continuous state-space model

$$\dot{x}(t) = Ax(t) + Bu(t), \quad y(t) = Cx(t) \quad (\text{C.3})$$

is given by

$$x(t) = e^{At}x(0) + \int_0^t e^{A(t-\tau)}Bu(\tau)d\tau \quad (\text{C.4})$$

Assuming that the input $u(t)$ is sampled using a ZOH and between two consecutive samples the input remains constant, i.e. $u(t) \implies u(kT)$ for $kT \leq t \leq (k+1)T$, the solution of the states differential equation for two consecutive samples results in

$$x(k+1) = e^{AT}x(k) + \int_0^T e^{As}dsBu(k) \quad (\text{C.5})$$

For simplicity, $T = T_s$. The discretized state-space model is determined as

$$x(k+1) = A_dx(k) + B_du(k), \quad y(k) = C_dx(k) \quad (\text{C.6})$$

where

$$A_d = e^{AT} \quad (\text{C.7})$$

$$B_d = \int_0^T e^{As}dsB = A^{-1}(e^{AT} - I)B \quad (\text{C.8})$$

$$C_d = C \quad (\text{C.9})$$

as the discrete system matrices.

For the EDOB the system includes an observer matrix, which is treated as an input matrix for the discretization process. According to (3.52), the state-space model of the EDOB is given by

$$\dot{\hat{\mathbf{x}}}_m = \mathbf{A}_m\hat{\mathbf{x}}_m + \mathbf{B}_m\gamma_m + \mathbf{L}_m(y_m - \hat{y}_m), \quad (\text{C.10})$$

$$\hat{y}_m = \mathbf{C}_m\hat{\mathbf{x}}_m \quad (\text{C.11})$$

where $\hat{\mathbf{x}}_m = (\hat{x}_{i,m} \quad \hat{\rho}_m)^T$. Inserting (C.11) into (C.10) outputs

$$\begin{aligned} \dot{\hat{\mathbf{x}}}_m &= \mathbf{A}_m\hat{\mathbf{x}}_m + \mathbf{B}_m\gamma_m + \mathbf{L}_m(y_m - \mathbf{C}_m\hat{\mathbf{x}}_m) \\ &= (\mathbf{A}_m - \mathbf{L}_m\mathbf{C}_m)\hat{\mathbf{x}}_m + \mathbf{B}_m\gamma_m + \mathbf{L}_my_m \\ &= \bar{\mathbf{A}}_m\hat{\mathbf{x}}_m + \mathbf{B}_m\gamma_m + \mathbf{L}_my_m \end{aligned} \quad (\text{C.12})$$

The solution of (C.12) results in

$$\hat{\mathbf{x}}_m = e^{\bar{\mathbf{A}}_m t} \hat{\mathbf{x}}_m(0) + \int_0^t e^{\bar{\mathbf{A}}_m(t-\tau)} \mathbf{B}_m \gamma_m(\tau) d\tau + \int_0^t e^{\bar{\mathbf{A}}_m(t-\tau)} \mathbf{L}_m y_m(\tau) d\tau \quad (\text{C.13})$$

Assuming that the input γ_m and the system output y_m are sampled with a ZOH, i.e. $\gamma_m \implies \gamma_m(kT)$ and $y_m(t) \implies y_m(kT)$ for $kT \leq t \leq (k+1)T$, the solution in (C.13) leads to

$$\hat{\mathbf{x}}_m(k+1) = e^{\bar{\mathbf{A}}_m T} \hat{\mathbf{x}}_m(k) + \int_0^T e^{\bar{\mathbf{A}}_m s} ds \mathbf{B}_m \gamma_m(k) + \int_0^T e^{\bar{\mathbf{A}}_m s} ds \mathbf{L}_m y_m(k) \quad (\text{C.14})$$

From (C.14), the discrete EDOB is derived as

$$\hat{\mathbf{x}}_m(k+1) = \bar{\mathbf{A}}_{m,d} \hat{\mathbf{x}}_m(k) + \mathbf{B}_{m,d} \gamma_m(k) + \mathbf{L}_{m,d} y_m(k) \quad (\text{C.15})$$

where

$$\bar{\mathbf{A}}_{m,d} = e^{\bar{\mathbf{A}}_m T} \quad (\text{C.16})$$

$$\mathbf{B}_{m,d} = \int_0^T e^{\bar{\mathbf{A}}_m s} ds \mathbf{B}_m = \bar{\mathbf{A}}_m^{-1} \left(e^{\bar{\mathbf{A}}_m T} - \mathbf{I} \right) \mathbf{B}_m \quad (\text{C.17})$$

$$\mathbf{L}_{m,d} = \int_0^T e^{\bar{\mathbf{A}}_m s} ds \mathbf{L}_m = \bar{\mathbf{A}}_m^{-1} \left(e^{\bar{\mathbf{A}}_m T} - \mathbf{I} \right) \mathbf{L}_m \quad (\text{C.18})$$

D Remaining MSC Operation Ratios

In this appendix, the boundary conditions and current equations of the ratios 1, 2 and 4 are summarized. Same as stated in Section 4.3, the current equations are only described for the phase current a . Due to the odd symmetry of the phase currents, its sufficient to describe the current slopes in the range from $[0, \pi]$. Furthermore, the derivation of the boundary conditions follows the calculation presented in Section 4.3.

D.1 Ratio 1

Table D.1: Boundary conditions for Ratio 1

Mode	Boundary conditions
DCM1	$0 \leq m_u < \frac{U_{dc2}}{3U_{sm}}$
DCM2	$\frac{U_{dc2}}{3U_{sm}} \leq m_u < \frac{U_{dc2}}{2U_{sm}-U_{dc2}}$
DCM3	$\frac{U_{dc2}}{2U_{sm}-U_{dc2}} \leq m_u < \frac{2U_{dc2}}{3U_{sm}}$
CCM1	$\frac{2U_{dc2}}{3U_{sm}} \leq m_u < \frac{1}{3}$
CCM2	$\frac{1}{3} \leq m_u < \frac{2(U_{sm}-U_{dc2})}{3U_{sm}}$
CCM3	$\frac{2(U_{sm}-U_{dc2})}{3U_{sm}} \leq m_u < \frac{2}{3}$
CCM4	$\frac{2}{3} \leq m_u < \frac{2U_{sm}+U_{dc2}}{3U_{sm}}$
CCM5	$\frac{2U_{sm}+U_{dc2}}{3U_{sm}} \leq m_u \leq 1$

Table D.2: Current equations for i_{sa} in DCM1

Interval	Current equations for phase a : $i_{sa}(\varphi)$
1	$i_1 - i_0 = 0$
2	$i_2 - i_1 = \frac{U_{sm} - U_{dc2}}{3\omega L} m_u \pi$
3	$i_3 - i_2 = -\frac{U_{dc2}}{3\omega L} \varphi$
4	$i_4 - i_3 = 0$
5	$i_5 - i_4 = \frac{2U_{sm} - 2U_{dc2}}{3\omega L} m_u \pi$
6	$i_6 - i_5 = -\frac{2U_{dc2}}{3\omega L} \varphi$
7	$i_7 - i_6 = 0$
8	$i_8 - i_7 = \frac{U_{sm} - U_{dc2}}{3\omega L} m_u \pi$
9	$i_9 - i_8 = -\frac{U_{dc2}}{3\omega L} \varphi$
10	$i_0 - i_9 = 0$

D.1.1 DCM1

$$i_0 = i_1 = i_3 = i_4 = i_6 = i_7 = i_9 = 0 \quad (D.1)$$

$$\varphi = m_u \pi \frac{U_{sm} - U_{dc2}}{U_{dc2}} \quad (D.2)$$

D.1.2 DCM2

Table D.3: Current equations for i_{sa} in DCM2

Interval	Current equations for phase a : $i_{sa}(\varphi)$
1	$i_1 - i_0 = \frac{U_{dc2}}{2\omega L} \left(\frac{\pi}{6} - \frac{m_u \pi}{2} \right)$
2	$i_2 - i_1 = \frac{U_{sm} + U_{dc2}}{3\omega L} \varphi_1$
3	$i_3 - i_2 = \frac{U_{sm} - U_{dc2}}{3\omega L} (m_u \pi - \varphi_1)$
4	$i_4 - i_3 = -\frac{U_{dc2}}{3\omega L} \varphi_2$
5	$i_5 - i_4 = 0$
6	$i_6 - i_5 = \frac{2U_{sm} - U_{dc2}}{3\omega L} \varphi_1$
7	$i_7 - i_6 = \frac{2U_{sm} - 2U_{dc2}}{3\omega L} (m_u \pi - \varphi_1)$
8	$i_8 - i_7 = -\frac{2U_{dc2}}{3\omega L} \varphi_2$
9	$i_9 - i_8 = -\frac{U_{dc2}}{2\omega L} \left(\frac{\pi}{3} - m_u \pi - \varphi_2 \right)$
10	$i_{10} - i_9 = \frac{U_{sm} - 2U_{dc2}}{3\omega L} \varphi_1$
11	$i_{11} - i_{10} = \frac{U_{sm} - U_{dc2}}{3\omega L} (m_u \pi - \varphi_1)$
12	$i_{12} - i_{11} = -\frac{U_{dc2}}{3\omega L} \varphi_2$
13	$-i_0 - i_{12} = -\frac{U_{dc2}}{2\omega L} \left(\frac{\pi}{6} - \frac{m_u \pi}{2} \right)$

$$i_2 = i_4 = i_5 = 0 \quad (D.3)$$

$$\varphi_1 = \pi \frac{3m_u U_{sm} - U_{dc2}}{U_{sm} + U_{dc2}} \quad (D.4)$$

$$\varphi_2 = \frac{U_{sm} - U_{dc2}}{U_{dc2}} (m_u \pi - \varphi_1) \quad (D.5)$$

D.1.3 DCM3

Table D.4: Current equations for i_{sa} in DCM3

Interval	Current equations for phase a : $i_{sa}(\varphi)$
1	$i_1 - i_0 = \frac{U_{dc2}}{2\omega L} \left(\frac{\pi}{6} - \frac{m_u \pi}{2} \right)$
2	$i_2 - i_1 = \frac{U_{sm} + U_{dc2}}{3\omega L} m_u \pi$
3	$i_3 - i_2 = \frac{U_{dc2}}{3\omega L} \varphi$
4	$i_4 - i_3 = 0$
5	$i_5 - i_4 = \frac{2U_{sm} - U_{dc2}}{3\omega L} m_u \pi$
6	$i_6 - i_5 = -\frac{U_{dc2}}{3\omega L} \varphi$
7	$i_7 - i_6 = -\frac{U_{dc2}}{2\omega L} \left(\frac{\pi}{3} - m_u \pi - \varphi \right)$
8	$i_8 - i_7 = \frac{U_{sm} - 2U_{dc2}}{3\omega L} m_u \pi$
9	$i_9 - i_8 = -\frac{2U_{dc2}}{3\omega L} \varphi$
10	$-i_0 - i_9 = -\frac{U_{dc2}}{2\omega L} \left(\frac{\pi}{6} - \frac{m_u \pi}{2} \right)$

$$i_3 = i_4 = 0 \quad (D.6)$$

$$\varphi = \pi \frac{(2U_{sm} - U_{dc2})m_u - U_{dc2}}{U_{dc2}} \quad (D.7)$$

D.1.4 CCM1

Table D.5: Current equations for i_{sa} in CCM1

Interval	Current equations for phase a : $i_{sa}(\varphi)$
1	$i_1 - i_0 = \frac{2U_{dc2}}{3\omega L} \left(\frac{\pi}{6} - \frac{m_u \pi}{2} \right)$
2	$i_2 - i_1 = \frac{U_{sm} + 2U_{dc2}}{3\omega L} \varphi$
3	$i_3 - i_2 = \frac{U_{sm} + U_{dc2}}{3\omega L} (m_u \pi - \varphi)$
4	$i_4 - i_3 = \frac{U_{dc2}}{3\omega L} \left(\frac{\pi}{3} - m_u \pi \right)$
5	$i_5 - i_4 = \frac{2U_{sm} + U_{dc2}}{3\omega L} \varphi$
6	$i_6 - i_5 = \frac{2U_{sm} - U_{dc2}}{3\omega L} (m_u \pi - \varphi)$
7	$i_7 - i_6 = -\frac{U_{dc2}}{3\omega L} \left(\frac{\pi}{3} - m_u \pi \right)$
8	$i_8 - i_7 = \frac{U_{sm} - U_{dc2}}{3\omega L} \varphi$
9	$i_9 - i_8 = \frac{U_{sm} - 2U_{dc2}}{3\omega L} (m_u \pi - \varphi)$
10	$-i_0 - i_9 = -\frac{2U_{dc2}}{3\omega L} \left(\frac{\pi}{6} - \frac{m_u \pi}{2} \right)$

$$i_5 = 0 \tag{D.8}$$

$$\varphi = \pi \frac{3m_u U_{sm} - 2U_{dc2}}{6U_{sm}} \tag{D.9}$$

D.1.5 CCM2

Table D.6: Current equations for i_{sa} in CCM2

Interval	Current equations for phase a : $i_{sa}(\varphi)$
1	$i_1 - i_0 = \frac{2U_{dc2}}{3\omega L} \left(\frac{m_u\pi}{2} - \frac{\pi}{6} \right)$
2	$i_2 - i_1 = \frac{U_{sm} + 2U_{dc2}}{3\omega L} \varphi$
3	$i_3 - i_2 = \frac{U_{sm} + U_{dc2}}{3\omega L} \left(\frac{2\pi}{3} - m_u\pi - \varphi \right)$
4	$i_4 - i_3 = \frac{3U_{sm} + U_{dc2}}{3\omega L} \left(m_u\pi - \frac{\pi}{3} \right)$
5	$i_5 - i_4 = \frac{2U_{sm} + U_{dc2}}{3\omega L} \varphi$
6	$i_6 - i_5 = \frac{2U_{sm} - U_{dc2}}{3\omega L} \left(\frac{2\pi}{3} - m_u\pi - \varphi \right)$
7	$i_7 - i_6 = \frac{3U_{sm} - U_{dc2}}{3\omega L} \left(m_u\pi - \frac{\pi}{3} \right)$
8	$i_8 - i_7 = \frac{U_{sm} - U_{dc2}}{3\omega L} \varphi$
9	$i_9 - i_8 = \frac{U_{sm} - 2U_{dc2}}{3\omega L} \left(\frac{2\pi}{3} - m_u\pi - \varphi \right)$
10	$-i_0 - i_9 = -\frac{2U_{dc2}}{3\omega L} \left(\frac{\pi}{6} - \frac{m_u\pi}{2} \right)$

$$i_5 = 0 \quad (D.10)$$

$$\varphi = \pi \frac{2U_{sm} - 3m_u U_{sm} - 2U_{dc2}}{6U_{sm}} \quad (D.11)$$

D.1.6 CCM3

Table D.7: Current equations for i_{sa} in CCM3

Interval	Current equations for phase a : $i_{sa}(\varphi)$
1	$i_1 - i_0 = \frac{2U_{dc2}}{3\omega L} \left(\frac{\pi}{6} - \frac{m_u \pi}{2} + \varphi \right)$
2	$i_2 - i_1 = \frac{U_{dc2}}{3\omega L} \left(m_u \pi - \frac{\pi}{3} - \varphi \right)$
3	$i_3 - i_2 = \frac{U_{sm} + U_{dc2}}{3\omega L} \left(\frac{2\pi}{3} - m_u \pi \right)$
4	$i_4 - i_3 = \frac{3U_{sm} + U_{dc2}}{3\omega L} \varphi$
5	$i_5 - i_4 = \frac{3U_{sm} - U_{dc2}}{3\omega L} \left(m_u \pi - \frac{\pi}{3} - \varphi \right)$
6	$i_6 - i_5 = \frac{2U_{sm} - U_{dc2}}{3\omega L} \left(\frac{2\pi}{3} - m_u \pi \right)$
7	$i_7 - i_6 = \frac{3U_{sm} - U_{dc2}}{3\omega L} \varphi$
8	$i_8 - i_7 = \frac{3U_{sm} - 2U_{dc2}}{3\omega L} \left(m_u \pi - \frac{\pi}{3} - \varphi \right)$
9	$i_9 - i_8 = \frac{U_{sm} - 2U_{dc2}}{3\omega L} \left(\frac{2\pi}{3} - m_u \pi \right)$
10	$-i_0 - i_9 = -\frac{2U_{dc2}}{3\omega L} \left(\frac{\pi}{6} - \frac{m_u \pi}{2} + \varphi \right)$

$$i_4 = 0 \tag{D.12}$$

$$\varphi = \pi \frac{6m_u U_{sm} - U_{sm} - 2U_{dc2}}{9U_{sm}} \tag{D.13}$$

D.1.7 CCM4

Table D.8: Current equations for i_{sa} in CCM4

Interval	Current equations for phase a : $i_{sa}(\varphi)$
1	$i_1 - i_0 = \frac{2U_{dc2}}{3\omega L}(\varphi + \frac{m_u\pi}{2} - \frac{\pi}{2})$
2	$i_2 - i_1 = \frac{U_{dc2}}{3\omega L}(\pi - m_u\pi - \varphi)$
3	$i_3 - i_2 = \frac{2U_{sm}+U_{dc2}}{3\omega L}(m_u\pi - \frac{2\pi}{3})$
4	$i_4 - i_3 = \frac{3U_{sm}+U_{dc2}}{3\omega L}\varphi$
5	$i_5 - i_4 = \frac{3U_{sm}-U_{dc2}}{3\omega L}(\pi - m_u\pi - \varphi)$
6	$i_6 - i_5 = \frac{4U_{sm}-U_{dc2}}{3\omega L}(m_u\pi - \frac{2\pi}{3})$
7	$i_7 - i_6 = \frac{3U_{sm}-U_{dc2}}{3\omega L}\varphi$
8	$i_8 - i_7 = \frac{3U_{sm}-2U_{dc2}}{3\omega L}(\pi - m_u\pi - \varphi)$
9	$i_9 - i_8 = \frac{2U_{sm}-2U_{dc2}}{3\omega L}(m_u\pi - \frac{2\pi}{3})$
10	$-i_0 - i_9 = -\frac{2U_{dc2}}{3\omega L}(\varphi + \frac{m_u\pi}{2} - \frac{\pi}{2})$

$$i_4 = 0 \tag{D.14}$$

$$\varphi = \pi \frac{5U_{sm} - 3m_u U_{sm} - 2U_{dc2}}{9U_{sm}} \tag{D.15}$$

D.1.8 CCM5

Table D.9: Current equations for i_{sa} in CCM5

Interval	Current equations for phase a : $i_{sa}(\varphi)$
1	$i_1 - i_0 = \frac{2U_{dc2}}{3\omega L} \left(\frac{\pi}{2} - \frac{m_u \pi}{2} \right)$
2	$i_2 - i_1 = \frac{2U_{sm} + 2U_{dc2}}{3\omega L} \varphi$
3	$i_3 - i_2 = \frac{2U_{sm} + U_{dc2}}{3\omega L} \left(m_u \pi - \frac{2\pi}{3} - \varphi \right)$
4	$i_4 - i_3 = \frac{3U_{sm} + U_{dc2}}{3\omega L} \left(\pi - m_u \pi \right)$
5	$i_5 - i_4 = \frac{4U_{sm} + U_{dc2}}{3\omega L} \varphi$
6	$i_6 - i_5 = \frac{4U_{sm} - U_{dc2}}{3\omega L} \left(m_u \pi - \frac{2\pi}{3} - \varphi \right)$
7	$i_7 - i_6 = \frac{3U_{sm} - U_{dc2}}{3\omega L} \left(\pi - m_u \pi \right)$
8	$i_8 - i_7 = \frac{2U_{sm} - U_{dc2}}{3\omega L} \varphi$
9	$i_9 - i_8 = \frac{2U_{sm} - 2U_{dc2}}{3\omega L} \left(m_u \pi - \frac{2\pi}{3} - \varphi \right)$
10	$-i_0 - i_9 = -\frac{2U_{dc2}}{3\omega L} \left(\frac{\pi}{2} - \frac{m_u \pi}{2} \right)$

$$i_5 = 0 \tag{D.16}$$

$$\varphi = \pi \frac{3m_u U_{sm} - 2U_{sm} - U_{dc2}}{6U_{sm}} \tag{D.17}$$

D.2 Ratio 2

Table D.10: Boundary conditions for Ratio 2

Mode	Boundary conditions
DCM1	$0 \leq m_u < \frac{U_{dc2}}{3U_{sm}}$
CCM1	$\frac{2U_{dc2}}{3U_{sm}} \leq m_u < \frac{1}{3}$
CCM2	$\frac{1}{3} \leq m_u < \frac{(U_{sm}+U_{dc2})}{6U_{sm}}$
CCM3	$\frac{(U_{sm}+U_{dc2})}{6U_{sm}} \leq m_u < \frac{2}{3}$
CCM4	$\frac{2}{3} \leq m_u < \frac{2U_{sm}+U_{dc2}}{3U_{sm}}$
CCM5	$\frac{2U_{sm}+U_{dc2}}{3U_{sm}} \leq m_u \leq 1$

D.2.1 DCM1

Table D.11: Current equations for i_{sa} in DCM1

Interval	Current equations for phase a : $i_{sa}(\varphi)$
1	$i_1 - i_0 = 0$
2	$i_2 - i_1 = \frac{U_{sm} - U_{dc2}}{3\omega L} m_u \pi$
3	$i_3 - i_2 = -\frac{U_{dc2}}{3\omega L} \varphi$
4	$i_4 - i_3 = 0$
5	$i_5 - i_4 = \frac{2U_{sm} - 2U_{dc2}}{3\omega L} m_u \pi$
6	$i_6 - i_5 = -\frac{2U_{dc2}}{3\omega L} \varphi$
7	$i_7 - i_6 = 0$
8	$i_8 - i_7 = \frac{U_{sm} - U_{dc2}}{3\omega L} m_u \pi$
9	$i_9 - i_8 = -\frac{U_{dc2}}{3\omega L} \varphi$
10	$i_0 - i_9 = 0$

$$i_0 = i_1 = i_3 = i_4 = i_6 = i_7 = i_9 = 0 \quad (\text{D.18})$$

$$\varphi = m_u \pi \frac{U_{sm} - U_{dc2}}{U_{dc2}} \quad (\text{D.19})$$

D.2.2 CCM1

Table D.12: Current equations for i_{sa} in CCM1

Interval	Current equations for phase a : $i_{sa}(\varphi)$
1	$i_1 - i_0 = \frac{U_{dc2}}{3\omega L} \left(\frac{\pi}{6} - \frac{m_u \pi}{2} \right)$
2	$i_2 - i_1 = \frac{U_{sm} + U_{dc2}}{3\omega L} \varphi$
3	$i_3 - i_2 = \frac{U_{sm} - U_{dc2}}{3\omega L} (m_u \pi - \varphi)$
4	$i_4 - i_3 = -\frac{U_{dc2}}{3\omega L} \left(\frac{\pi}{3} - \frac{m_u \pi}{2} \right)$
5	$i_5 - i_4 = \frac{2U_{sm} - U_{dc2}}{3\omega L} \varphi$
6	$i_6 - i_5 = \frac{2U_{sm} - 2U_{dc2}}{3\omega L} (m_u \pi - \varphi)$
7	$i_7 - i_6 = -\frac{2U_{dc2}}{3\omega L} \left(\frac{\pi}{3} - \frac{m_u \pi}{2} \right)$
8	$i_8 - i_7 = \frac{U_{sm} - 2U_{dc2}}{3\omega L} \varphi$
9	$i_9 - i_8 = \frac{U_{sm} - U_{dc2}}{3\omega L} (m_u \pi - \varphi)$
10	$-i_0 - i_9 = -\frac{U_{dc2}}{3\omega L} \left(\frac{\pi}{6} - \frac{m_u \pi}{2} \right)$

$$i_2 = 0 \tag{D.20}$$

$$\varphi = \pi \frac{6m_u U_{sm} - 2U_{dc2}}{3U_{sm}} \tag{D.21}$$

D.2.3 CCM2

Table D.13: Current equations for i_{sa} in CCM2

Interval	Current equations for phase a : $i_{sa}(\varphi)$
1	$i_1 - i_0 = \frac{U_{dc2}}{3\omega L} \left(\frac{m_u \pi}{2} - \frac{\pi}{6} \right)$
2	$i_2 - i_1 = \frac{U_{sm} + U_{dc2}}{3\omega L} \varphi$
3	$i_3 - i_2 = \frac{U_{sm} - U_{dc2}}{3\omega L} \left(\frac{2\pi}{3} - m_u \pi - \varphi \right)$
4	$i_4 - i_3 = \frac{3U_{sm} - U_{dc2}}{3\omega L} \left(m_u \pi - \frac{\pi}{3} \right)$
5	$i_5 - i_4 = \frac{2U_{sm} - U_{dc2}}{3\omega L} \varphi$
6	$i_6 - i_5 = \frac{2U_{sm} - 2U_{dc2}}{3\omega L} \left(\frac{2\pi}{3} - m_u \pi - \varphi \right)$
7	$i_7 - i_6 = \frac{3U_{sm} - 2U_{dc2}}{3\omega L} \left(m_u \pi - \frac{\pi}{3} \right)$
8	$i_8 - i_7 = \frac{U_{sm} - 2U_{dc2}}{3\omega L} \varphi$
9	$i_9 - i_8 = \frac{U_{sm} - U_{dc2}}{3\omega L} \left(\frac{2\pi}{3} - m_u \pi - \varphi \right)$
10	$-i_0 - i_9 = -\frac{U_{dc2}}{3\omega L} \left(\frac{m\pi}{2} - \frac{\pi}{6} \right)$

$$i_2 = 0 \tag{D.22}$$

$$\varphi = \pi \frac{3m_u U_{sm} + U_{sm} - 2U_{dc2}}{3U_{sm}} \tag{D.23}$$

D.2.4 CCM3

Table D.14: Current equations for i_{sa} in CCM3

Interval	Current equations for phase a : $i_{sa}(\varphi)$
1	$i_1 - i_0 = \frac{2U_{dc2}}{3\omega L} \left(\frac{\pi}{6} - \frac{m_u \pi}{2} + \varphi \right)$
2	$i_2 - i_1 = \frac{U_{dc2}}{3\omega L} (m_u \pi - \frac{\pi}{3} - \varphi)$
3	$i_3 - i_2 = \frac{U_{sm} + U_{dc2}}{3\omega L} \left(\frac{2\pi}{3} - m_u \pi \right)$
4	$i_4 - i_3 = \frac{3U_{sm} + U_{dc2}}{3\omega L} \varphi$
5	$i_5 - i_4 = \frac{3U_{sm} - U_{dc2}}{3\omega L} (m_u \pi - \frac{\pi}{3} - \varphi)$
6	$i_6 - i_5 = \frac{2U_{sm} - U_{dc2}}{3\omega L} \left(\frac{2\pi}{3} - m_u \pi \right)$
7	$i_7 - i_6 = \frac{3U_{sm} - U_{dc2}}{3\omega L} \varphi$
8	$i_8 - i_7 = \frac{3U_{sm} - 2U_{dc2}}{3\omega L} (m_u \pi - \frac{\pi}{3} - \varphi)$
9	$i_9 - i_8 = \frac{U_{sm} - 2U_{dc2}}{3\omega L} \left(\frac{2\pi}{3} - m_u \pi \right)$
10	$-i_0 - i_9 = -\frac{2U_{dc2}}{3\omega L} \left(\frac{\pi}{6} - \frac{m_u \pi}{2} + \varphi \right)$

$$i_4 = 0 \tag{D.24}$$

$$\varphi = \pi \frac{6m_u U_{sm} - U_{sm} - 2U_{dc2}}{9U_{sm}} \tag{D.25}$$

D.2.5 CCM4

Table D.15: Current equations for i_{sa} in CCM4

Interval	Current equations for phase a : $i_{sa}(\varphi)$
1	$i_1 - i_0 = \frac{2U_{dc2}}{3\omega L}(\varphi + \frac{m_u\pi}{2} - \frac{\pi}{2})$
2	$i_2 - i_1 = \frac{U_{dc2}}{3\omega L}(\pi - m_u\pi - \varphi)$
3	$i_3 - i_2 = \frac{2U_{sm}+U_{dc2}}{3\omega L}(m_u\pi - \frac{2\pi}{3})$
4	$i_4 - i_3 = \frac{3U_{sm}+U_{dc2}}{3\omega L}\varphi$
5	$i_5 - i_4 = \frac{3U_{sm}-U_{dc2}}{3\omega L}(\pi - m_u\pi - \varphi)$
6	$i_6 - i_5 = \frac{4U_{sm}-U_{dc2}}{3\omega L}(m_u\pi - \frac{2\pi}{3})$
7	$i_7 - i_6 = \frac{3U_{sm}-U_{dc2}}{3\omega L}\varphi$
8	$i_8 - i_7 = \frac{3U_{sm}-2U_{dc2}}{3\omega L}(\pi - m_u\pi - \varphi)$
9	$i_9 - i_8 = \frac{2U_{sm}-2U_{dc2}}{3\omega L}(m_u\pi - \frac{2\pi}{3})$
10	$-i_0 - i_9 = -\frac{2U_{dc2}}{3\omega L}(\varphi + \frac{m_u\pi}{2} - \frac{\pi}{2})$

$$i_4 = 0 \tag{D.26}$$

$$\varphi = \pi \frac{5U_{sm} - 3m_u U_{sm} - 2U_{dc2}}{9U_{sm}} \tag{D.27}$$

D.2.6 CCM5

Table D.16: Current equations for i_{sa} in CCM5

Interval	Current equations for phase a : $i_{sa}(\varphi)$
1	$i_1 - i_0 = \frac{2U_{dc2}}{3\omega L} \left(\frac{\pi}{2} - \frac{m_u \pi}{2} \right)$
2	$i_2 - i_1 = \frac{2U_{sm} + 2U_{dc2}}{3\omega L} \varphi$
3	$i_3 - i_2 = \frac{2U_{sm} + U_{dc2}}{3\omega L} \left(m_u \pi - \frac{2\pi}{3} - \varphi \right)$
4	$i_4 - i_3 = \frac{3U_{sm} + U_{dc2}}{3\omega L} (\pi - m_u \pi)$
5	$i_5 - i_4 = \frac{4U_{sm} + U_{dc2}}{3\omega L} \varphi$
6	$i_6 - i_5 = \frac{4U_{sm} - U_{dc2}}{3\omega L} \left(m_u \pi - \frac{2\pi}{3} - \varphi \right)$
7	$i_7 - i_6 = \frac{3U_{sm} - U_{dc2}}{3\omega L} (\pi - m_u \pi)$
8	$i_8 - i_7 = \frac{2U_{sm} - U_{dc2}}{3\omega L} \varphi$
9	$i_9 - i_8 = \frac{2U_{sm} - 2U_{dc2}}{3\omega L} \left(m_u \pi - \frac{2\pi}{3} - \varphi \right)$
10	$-i_0 - i_9 = -\frac{2U_{dc2}}{3\omega L} \left(\frac{\pi}{2} - \frac{m_u \pi}{2} \right)$

$$i_5 = 0 \tag{D.28}$$

$$\varphi = \pi \frac{3m_u U_{sm} - 2U_{sm} - U_{dc2}}{6U_{sm}} \tag{D.29}$$

D.3 Ratio 4

The modes for ratio 4 are not completely described, due to the fact that the MSC operating point is in ratio 3 and reaches ratio 1, 2 and 3. Currently, the mode DCM3 is not described.

Table D.17: Boundary conditions for Ratio 4

Mode	Boundary conditions
DCM1	$\frac{1}{3} \leq m_u < \frac{U_{dc2}}{3U_{sm}}$
DCM2	$\frac{U_{dc2}}{3U_{sm}} \leq m_u < \frac{2}{3}$
DCM3	$\frac{2}{3} \leq m_u < \frac{2U_{dc2}-U_{sm}}{3U_{sm}}$
CCM1	$\frac{2U_{dc2}-U_{sm}}{3U_{sm}} \leq m_u < 1$

D.3.1 DCM1

Table D.18: Current equations for $i_{sa}(\varphi)$ in DCM1

Interval	Current equations for phase a : i_{sa}
1	$i_1 - i_0 = 0 \left(\frac{\pi}{2} - \frac{m_u \pi}{2} \right)$
2	$i_2 - i_1 = \frac{2U_{sm}-U_{dc2}}{2\omega L} \left(m_u \pi - \frac{\pi}{3} \right)$
3	$i_3 - i_2 = \frac{U_{sm}-U_{dc2}}{2\omega L} \varphi$
4	$i_4 - i_3 = 0 \left(\frac{2\pi}{3} - m_u \pi - \varphi \right)$
5	$i_5 - i_4 = \frac{2U_{sm}-U_{dc2}}{2\omega L} \left(m_u \pi - \frac{\pi}{3} \right)$
6	$i_6 - i_5 = \frac{U_{sm}-U_{dc2}}{2\omega L} \varphi$
7	$i_0 - i_6 = 0 \left(\frac{\pi}{2} - \frac{m_u \pi}{2} \right)$

$$i_0 = i_1 = i_3 = i_4 = i_6 = i_7 = 0 \quad (\text{D.30})$$

$$\varphi = \pi \frac{U_{\text{dc}2} - 2U_{\text{sm}}}{U_{\text{sm}} - U_{\text{dc}2}} \frac{3m_u - 1}{3} \quad (\text{D.31})$$

D.3.2 DCM2

Table D.19: Current equations for i_{sa} in DCM2

Interval	Current equations for phase a : $i_{\text{sa}}(\varphi)$
1	$i_1 - i_0 = 0 \frac{\pi}{2} (1 - m_u)$
2	$i_2 - i_1 = \frac{3U_{\text{sm}} - U_{\text{dc}2}}{3\omega L} \varphi$
3	$i_3 - i_2 = \frac{2U_{\text{sm}} - U_{\text{dc}2}}{2\omega L} (m_u \pi - \frac{\pi}{3} - \varphi)$
4	$i_4 - i_3 = \frac{U_{\text{sm}} - U_{\text{dc}2}}{2\omega L} (\frac{2\pi}{3} - m_u \pi)$
5	$i_5 - i_4 = \frac{3U_{\text{sm}} - 2U_{\text{dc}2}}{3\omega L} \varphi$
6	$i_6 - i_5 = \frac{2U_{\text{sm}} - U_{\text{dc}2}}{2\omega L} (m_u \pi - \frac{\pi}{3} - \varphi)$
7	$i_7 - i_6 = \frac{U_{\text{sm}} - U_{\text{dc}2}}{2\omega L} (\frac{2\pi}{3} - m_u \pi)$
8	$i_8 - i_7 = -\frac{U_{\text{dc}2}}{3\omega L} \varphi$
9	$i_0 - i_8 = 0 (\frac{m_u \pi}{2} - \frac{\pi}{6} - \varphi_2)$

D.3.3 CCM1

$$i_0 = i_1 = i_8 = i_9 = 0 \quad (\text{D.32})$$

$$\varphi = \pi \frac{3m_u U_{\text{sm}} + U_{\text{sm}} - 2U_{\text{dc}2}}{6U_{\text{sm}}} \quad (\text{D.33})$$

Table D.20: Current equations for i_{sa} in CCM3

Interval	Current equations for phase a : i_{sa}
1	$i_1 - i_0 = \frac{U_{dc2}}{3\omega L} \left(\frac{\pi}{2} - \frac{m_u \pi}{2} \right)$
2	$i_2 - i_1 = \frac{2U_{sm} + U_{dc2}}{3\omega L} \varphi$
3	$i_3 - i_2 = \frac{2U_{sm} - U_{dc2}}{3\omega L} \left(m_u \pi - \frac{2\pi}{3} - \varphi \right)$
4	$i_4 - i_3 = \frac{3U_{sm} - U_{dc2}}{3\omega L} (\pi - m_u \pi)$
5	$i_5 - i_4 = \frac{4U_{sm} - U_{dc2}}{3\omega L} \varphi$
6	$i_6 - i_5 = \frac{4U_{sm} - 2U_{dc2}}{3\omega L} \left(m_u \pi - \frac{2\pi}{3} - \varphi \right)$
7	$i_7 - i_6 = \frac{3U_{sm} - 2U_{dc2}}{3\omega L} (\pi - m_u \pi)$
8	$i_8 - i_7 = \frac{2U_{sm} - 2U_{dc2}}{3\omega L} \varphi$
9	$i_9 - i_8 = \frac{2U_{sm} - U_{dc2}}{3\omega L} \left(m_u \pi - \frac{2\pi}{3} - \varphi \right)$
10	$-i_0 - i_9 = -\frac{U_{dc2}}{3\omega L} \left(\frac{\pi}{2} - \frac{m_u \pi}{2} \right)$

Bibliography

- [1] United Nations. *Transforming Our World: The 2030 Agenda for Sustainable Development*. 2015. URL: <https://sdgs.un.org/2030agenda>.
- [2] Max Roser and Hannah Ritchie. “Two Centuries of Rapid Global Population Growth Will Come to an End”. In: *Our World in Data* (2023). URL: <https://ourworldindata.org/world-population-growth-past-future>.
- [3] United Nations Department of Economic and Population Division Social Affairs. *World Population Prospects 2024: Key Messages*. 2023. URL: https://population.un.org/wpp/Publications/Files/WPP2024_Key-Messages.pdf.
- [4] Hannah Ritchie and Pablo Rosado. “Electricity Mix”. In: *Our World in Data* (2024). URL: <https://ourworldindata.org/electricity-mix>.
- [5] Vaclav Smil. *Energy and Civilization: A History*. MIT Press, 2017.
- [6] Spencer R. Weart. *The Discovery of Global Warming: Revised and Expanded Edition*. Harvard University Press, 2008.
- [7] Hannah Ritchie, Pablo Rosado, and Veronika Samborska. “Climate Change”. In: *Our World in Data* (2024). URL: <https://ourworldindata.org/climate-change>.
- [8] Intergovernmental Panel on Climate Change. *Climate Change 2023: Synthesis Report*. Intergovernmental Panel on Climate Change, 2023. URL: <https://www.ipcc.ch/report/ar6/wg1/#Synthesis-Report>.
- [9] European Commission and Directorate-General for Climate Action. *Going Climate-Neutral by 2050: A Strategic Long-Term Vision for a Prosperous, Modern, Competitive, and Climate-Neutral EU Economy*. Publications Office, 2019. DOI: [doi/10.2834/02074](https://doi.org/10.2834/02074).
- [10] Climate Watch. *Historical Emissions Data*. 2024. URL: <https://www.climatewatchdata.org/data-explorer/historical-emissions>.
- [11] International Renewable Energy Agency (IRENA). *Decarbonising hard-to-abate sectors with renewables: Perspectives for the G7*. 2024. URL: https://www.irena.org/-/media/Files/IRENA/Agency/Publication/2024/Apr/IRENA_G7_Decarbonising_hard_to_abate_sectors_2024.pdf.

-
- [12] Energy Institute. *Statistical Review of World Energy 2024*. 2024. URL: <https://www.energyinst.org/statistical-review>.
- [13] DNV Group. *Energy Transition Outlook 2024: A Global and Regional Forecast to 2050*. DNV, 2024.
- [14] AFRY. *The Fossil Detox Report*. 2024. URL: <https://afry.com/en/fossil-detox-report>.
- [15] International Energy Agency. *Energy Efficiency 2024*. International Energy Agency, Nov. 2024. URL: <https://www.iea.org/reports/energy-efficiency-2024>.
- [16] Bruce N. Stram. “Key challenges to expanding renewable energy”. In: *Energy Policy* 96 (2016), pp. 728–734. ISSN: 0301-4215. DOI: 10.1016/j.enpol.2016.05.034.
- [17] Max Wei, Colin A. McMillan, and Stephane de la Rue du Can. “Electrification of Industry: Potential, Challenges and Outlook”. In: *Current Sustainable/Renewable Energy Reports* 6 (2019), pp. 140–148. DOI: 10.1007/s40518-019-00136-1.
- [18] European Union. *Energy Storage - Underpinning a Decarbonised and Secure EU Energy System*. 2023.
- [19] Oliver Schmidt and Iain Staffell. *Monetizing Energy Storage: A Toolkit to Assess Future Cost and Value*. Oxford: Oxford University Press, 2024. ISBN: 978-0192845375.
- [20] MIT Energy Initiative. *The Future of Solar Energy*. 2015. URL: <https://energy.mit.edu/wp-content/uploads/2015/05/MITEI-The-Future-of-Solar-Energy.pdf>.
- [21] Victor von Loessl. “Smart meter-related data privacy concerns and dynamic electricity tariffs: Evidence from a stated choice experiment”. In: *Energy Policy* 180 (2023), p. 113645. ISSN: 0301-4215. DOI: 10.1016/j.enpol.2023.113645. URL: <https://doi.org/10.1016/j.enpol.2023.113645>.
- [22] TenneT. *TenneT’s Position on Large Battery Energy Storage Systems (BESS)*. 2024. URL: <https://www.tennet.eu/battery-energy-storage-systems-bess>.
- [23] R. Ranjith Kumar et al. “Advances in Batteries, Battery Modeling, Battery Management System, Battery Thermal Management, SOC, SOH, and Charge/Discharge Characteristics in EV Applications”. In: *IEEE Access* 11 (2023), pp. 105761–105809. DOI: 10.1109/ACCESS.2023.3318121.

- [24] Maria C. Argyrou, Paul Christodoulides, and Soteris A. Kalogirou. “Energy storage for electricity generation and related processes: Technologies appraisal and grid scale applications”. In: *Renewable and Sustainable Energy Reviews* 94 (2018), pp. 804–821. ISSN: 1364-0321. DOI: 10.1016/j.rser.2018.06.044.
- [25] Rik W. De Doncker. *Power Electronics: Fundamentals, Topologies, Analysis*. 5th. Aachen, Germany: Institute for Power Electronics and Electrical Drives (ISEA), RWTH Aachen University, 2014.
- [26] Institute of Electrical and Electronics Engineers (IEEE). *IEEE Standard for Interconnection and Interoperability of Distributed Energy Resources with Associated Electric Power Systems Interfaces*. IEEE, 2020. DOI: 10.1109/IEEESTD.2020.9243443.
- [27] *Requirements for Generating Plants to be Connected in Parallel with Distribution Networks — Part 1: Connection to a LV Distribution Network*. CENELEC, 2019.
- [28] Jing Yuan et al. “An overview of photovoltaic microinverters: Topology, efficiency, and reliability”. In: *2019 IEEE 13th International Conference on Compatibility, Power Electronics and Power Engineering (CPE-POWERENG)*. IEEE, 2019, pp. 1–6.
- [29] Murat Yilmaz and Philip T. Krein. “Review of Battery Charger Topologies, Charging Power Levels, and Infrastructure for Plug-In Electric and Hybrid Vehicles”. In: *IEEE Transactions on Power Electronics* 28.5 (2013), pp. 2151–2169. DOI: 10.1109/TPEL.2012.2212917.
- [30] N. Femia et al. “Optimization of perturb and observe maximum power point tracking method”. In: *IEEE Transactions on Power Electronics* 20.4 (2005), pp. 963–973. DOI: 10.1109/TPEL.2005.850975.
- [31] SMA Solar Technology AG. *Sunny Tripower 8.0 / 10.0 Datasheet*. <https://files.sma.de/downloads/STP8-10-3AV-40-DS-en-40.pdf>. Version 4.0.
- [32] Sheldon S. Williamson, Akshay K. Rathore, and Fariborz Musavi. “Industrial Electronics for Electric Transportation: Current State-of-the-Art and Future Challenges”. In: *IEEE Transactions on Industrial Electronics* 62.5 (2015), pp. 3021–3032. DOI: 10.1109/TIE.2015.2409052.
- [33] Chuanhong Zhao, Simon D. Round, and Johann W. Kolar. “An Isolated Three-Port Bidirectional DC-DC Converter With Decoupled Power Flow Management”. In: *IEEE Transactions on Power Electronics* 23.5 (2008), pp. 2443–2453. DOI: 10.1109/TPEL.2008.2002056.

- [34] Amit Kumar Bhattacharjee, Nasser Kutkut, and Issa Batarseh. “Review of Multiport Converters for Solar and Energy Storage Integration”. In: *IEEE Transactions on Power Electronics* 34.2 (2019), pp. 1431–1445. DOI: 10.1109/TPEL.2018.2830788.
- [35] Shigenori Inoue and Hirofumi Akagi. “A Bidirectional DC–DC Converter for an Energy Storage System With Galvanic Isolation”. In: *IEEE Transactions on Power Electronics* 22.6 (2007), pp. 2299–2306. DOI: 10.1109/TPEL.2007.909248.
- [36] Neyyala Raju, N. Murali Mohan, and Vijay Kumar. “A Review of Extended Voltage Range DC-DC Converter Topologies”. In: *Intelligent Computing and Optimization*. Vol. 569. Lecture Notes in Networks and Systems. Springer, 2023, pp. 770–780. DOI: 10.1007/978-3-031-19958-5_73. URL: https://link.springer.com/chapter/10.1007/978-3-031-19958-5_73.
- [37] Texas Instruments. *Benefits of Galvanic Isolation in High Voltage Power Systems*. White Paper. 2023. URL: <https://www.ti.com/lit/wp/slyy204c/slyy204c.pdf>.
- [38] R.W.A.A. De Doncker, D.M. Divan, and M.H. Kheraluwala. “A three-phase soft-switched high-power-density DC/DC converter for high-power applications”. In: *IEEE Transactions on Industry Applications* 27.1 (1991), pp. 63–73. DOI: 10.1109/28.67533.
- [39] P.W. Wheeler et al. “Matrix converters: a technology review”. In: *IEEE Transactions on Industrial Electronics* 49.2 (2002), pp. 276–288. DOI: 10.1109/41.993260.
- [40] Lee Empringham et al. “Technological Issues and Industrial Application of Matrix Converters: A Review”. In: *IEEE Transactions on Industrial Electronics* 60.10 (2013), pp. 4260–4271. DOI: 10.1109/TIE.2012.2216231.
- [41] Alexandre Bento et al. “On the Potential Contributions of Matrix Converters for the Future Grid Operation, Sustainable Transportation and Electrical Drives Innovation”. In: *Applied Sciences* 11.10 (2021). ISSN: 2076-3417. DOI: 10.3390/app11104597. URL: <https://www.mdpi.com/2076-3417/11/10/4597>.
- [42] Morten Rahr Nielsen et al. “High-Power Electronic Applications Enabled by Medium Voltage Silicon-Carbide Technology: An Overview”. In: *IEEE Transactions on Power Electronics* 40.1 (2025), pp. 987–1011. DOI: 10.1109/TPEL.2024.3442483.
- [43] Philipp Joebges. “Distributed Real-Time Simulation of Modular Bidirectional DC-DC Converters: For Control System Development”. PhD thesis. RWTH Aachen University, 2019. URL: <https://publications.rwth-aachen.de/record/834674>.

- [44] R. W. De Doncker. “The War of Currents: How DC Technology Lost the Battle 150 Years Ago, but May Win the War in a Liberalized Energy Market”. In: *Electric Energy T&D Magazine Quarterly* 2020.3 (2020), pp. 28–33.
- [45] Council of European Energy Regulators (CEER). *2nd CEER Report on Power Losses*. Accessed November 29, 2024. 2020. URL: <https://www.ceer.eu/publication/2nd-ceer-report-on-power-losses>.
- [46] Jackson John Justo et al. “AC-microgrids versus DC-microgrids with distributed energy resources: A review”. In: *Renewable and Sustainable Energy Reviews* 24 (2013), pp. 387–405. ISSN: 1364-0321. DOI: <https://doi.org/10.1016/j.rser.2013.03.067>. URL: <https://www.sciencedirect.com/science/article/pii/S1364032113002268>.
- [47] Maria Fotopoulou et al. “State of the Art of Low and Medium Voltage Direct Current (DC) Microgrids”. In: *Energies* 14.18 (2021). ISSN: 1996-1073. DOI: [10.3390/en14185595](https://doi.org/10.3390/en14185595). URL: <https://www.mdpi.com/1996-1073/14/18/5595>.
- [48] Nadir Idir, Yannick Weens, and Jean-Jacques Franchaud. “Skin effect and dielectric loss models of power cables”. In: *IEEE Transactions on Dielectrics and Electrical Insulation* 16.1 (2009), pp. 147–154. DOI: [10.1109/TDEI.2009.4784562](https://doi.org/10.1109/TDEI.2009.4784562).
- [49] ABB. *HVDC Light and SVC: Enabling the Power Transmission of the Future*. Tech. rep. ABB. URL: <https://new.abb.com/docs/default-source/ewea-doc/hvdc-light-and-svc.pdf>.
- [50] Siemens Energy. *HVDC PLUS: Advanced Technology for Power Transmission*. Tech. rep. Siemens Energy, 2022. URL: https://p3.aprimocdn.net/siemensenergy/06d5dc32-1572-4874-bdc0-b0810130c24c/2022-03-11-HVDC-PLUS-pdf_Original%20file.pdf.
- [51] Jesper Larsson. *Transmission Systems for Grid Connection of Offshore Wind Farms: HVAC vs HVDC Breaking Point*. 2021.
- [52] Andrei Stan, Sorina Costinaş, and Georgiana Ion. “Overview and Assessment of HVDC Current Applications and Future Trends”. In: *Energies* 15.3 (2022). ISSN: 1996-1073. DOI: [10.3390/en15031193](https://doi.org/10.3390/en15031193). URL: <https://www.mdpi.com/1996-1073/15/3/1193>.
- [53] Abdulrahman Alassi et al. “HVDC Transmission: Technology Review, Market Trends and Future Outlook”. In: *Renewable and Sustainable Energy Reviews* 112 (2019), pp. 530–554. ISSN: 1364-0321. DOI: <https://doi.org/10.1016/j.rser.2019.04.062>. URL: <https://www.sciencedirect.com/science/article/pii/S1364032119302837>.

-
- [54] Santiago Sanchez et al. “Dynamics and Stability of Meshed Multiterminal HVDC Networks”. In: *IEEE Transactions on Power Systems* 34.3 (2019), pp. 1824–1833. DOI: 10.1109/TPWRS.2018.2889516.
- [55] Oriol Gomis-Bellmunt et al. “Flexible Converters for Meshed HVDC Grids: From Flexible AC Transmission Systems (FACTS) to Flexible DC Grids”. In: *IEEE Transactions on Power Delivery* 35.1 (2020), pp. 2–15. DOI: 10.1109/TPWRD.2019.2939588.
- [56] Mike Barnes et al. “HVDC Circuit Breakers—A Review”. In: *IEEE Access* 8 (2020), pp. 211829–211848. DOI: 10.1109/ACCESS.2020.3039921.
- [57] Mashood Nasir et al. “Solar PV-Based Scalable DC Microgrid for Rural Electrification in Developing Regions”. In: *IEEE Transactions on Sustainable Energy* 9.1 (2018), pp. 390–399. DOI: 10.1109/TSTE.2017.2736160.
- [58] J. Brombach et al. “Optimized cabin power supply with a +/- 270 V DC grid on a modern aircraft”. In: *2011 7th International Conference-Workshop Compatibility and Power Electronics (CPE)*. 2011, pp. 425–428. DOI: 10.1109/CPE.2011.5942274.
- [59] Mohammad Yaqoob et al. “A Comprehensive Review on Small Satellite Microgrids”. In: *IEEE Transactions on Power Electronics* 37.10 (2022), pp. 12741–12762. DOI: 10.1109/TPEL.2022.3175093.
- [60] Kyunghwa Kim et al. “DC-grid system for ships: a study of benefits and technical considerations”. In: *Journal of International Maritime Safety, Environmental Affairs, and Shipping* 2.1 (2018), pp. 1–12.
- [61] Bernd Wunder et al. “Energy efficient DC-grids for commercial buildings”. In: *2014 IEEE 36th International Telecommunications Energy Conference (INTELEC)*. 2014, pp. 1–8. DOI: 10.1109/INTLEC.2014.6972215.
- [62] Johann Austermann and Hartwig Stammberger. *DC-INDUSTRIE2 System Concept*. Open DC Alliance (ODCA). Feb. 2024.
- [63] Enrique Rodriguez-Diaz, Juan C. Vasquez, and Josep M. Guerrero. “Potential energy savings by using direct current for residential applications: A Danish household study case”. In: *2017 IEEE Second International Conference on DC Microgrids (ICDCM)*. 2017, pp. 547–552. DOI: 10.1109/ICDCM.2017.8001100.
- [64] Mohsen Ghaffarpour Jahromi et al. “Powering Mobile Mining Machines: DC Versus AC Power”. In: *IEEE Industry Applications Magazine* 22.5 (2016), pp. 63–72. DOI: 10.1109/MIAS.2015.2459082.

- [65] Arne Hinz, Marco Stieneker, and Rik W. De Doncker. “Impact and opportunities of medium-voltage DC grids in urban railway systems”. In: *2016 18th European Conference on Power Electronics and Applications (EPE'16 ECCE Europe)*. 2016, pp. 1–10. DOI: 10.1109/EPE.2016.7695410.
- [66] CIGRE Electra. *Medium Voltage Direct Current (MVDC) Grid Feasibility Study*. 2020. URL: <https://electra.cigre.org/309-april-2020/technical-brochures/medium-voltage-direct-current-mvdc-grid-feasibility-study.html>.
- [67] *HyperRide - Hybrid Provision of Energy based on Reliability and Resiliency by Integration of Dc Equipment*. 2024. URL: <https://hyperride.eu/>.
- [68] *TIGON - Towards Intelligent DC-based hybrid Grids Optimizing the network performance*. 2024. URL: <http://tigon-project.eu/>.
- [69] *ENSURE - Neue EnergieNetzStruktURen für die Energiewende*. 2025. URL: <https://www.kopernikus-projekte.de/en/projects/ensure>.
- [70] *FEN (Flexible Elektrische Netze) Research Campus Aachen*. 2024. URL: <https://www.fenaachen.net/>.
- [71] Oriol Gomis-Bellmunt et al. “Principles of Operation of Grids of DC and AC Subgrids Interconnected by Power Converters”. In: *IEEE Transactions on Power Delivery* 36.2 (2021), pp. 1107–1117. DOI: 10.1109/TPWRD.2020.3002269.
- [72] *Technical Connection Rules for Medium-Voltage (VDE-AR-N 4110)*. Available from: <https://www.vde.com/en>. VDE (Association for Electrical, Electronic and Information Technologies). Berlin, Germany, 2018.
- [73] Infineon Technologies AG. *FZ750R65KE3 IGBT Module Datasheet*. 2018. URL: https://www.infineon.com/dgdl/Infineon-FZ750R65KE3-DataSheet-v01_10-EN.pdf.
- [74] Tobias Nieckula Ubostad and Dimosthenis Peftitsis. “Design Considerations for Series-Connected SiC MOSFETs Operating at 100 kV/ μ s”. In: *2023 IEEE Applied Power Electronics Conference and Exposition (APEC)*. 2023, pp. 217–224. DOI: 10.1109/APEC43580.2023.10131240.
- [75] Morten Rahr Nielsen et al. “Comparison of Two Third-Generation 10 kV SiC MOSFET Die’s Switching Performance on a System Level”. In: *2024 IEEE 10th International Power Electronics and Motion Control Conference (IPEMC2024-ECCE Asia)*. 2024, pp. 1250–1255. DOI: 10.1109/IPEMC-ECCEAsia60879.2024.10567349.

- [76] Ibrahim Alhurayyis, Ahmad Elkhateb, and John Morrow. “Isolated and Nonisolated DC-to-DC Converters for Medium-Voltage DC Networks: A Review”. In: *IEEE Journal of Emerging and Selected Topics in Power Electronics* 9.6 (2021), pp. 7486–7500. DOI: 10.1109/JESTPE.2020.3028057.
- [77] Abel Antonio-Ferreira, Carlos Collados-Rodriguez, and Oriol Gomis-Bellmunt. “Modulation techniques applied to medium voltage modular multilevel converters for renewable energy integration: A review”. In: *Electric Power Systems Research* 155 (2018), pp. 21–39.
- [78] Pedro dos Santos, Mateo Vazquez, and Steven Liu. “Flexible and General Strategy of Space Vector Modulation for Multilevel Converters”. In: *PCIM Asia 2020; International Exhibition and Conference for Power Electronics, Intelligent Motion, Renewable Energy and Energy Management*. 2020, pp. 1–7.
- [79] Jonas Weires, Pedro Leal dos Santos, and Steven Liu. “Optimized Pulse Pattern with Half-wave Symmetry for 5-Level Converter”. In: *2022 24th European Conference on Power Electronics and Applications (EPE’22 ECCE Europe)*. 2022, pp. 1–10.
- [80] Jon Azurza Anderson et al. “Three Levels Are Not Enough: Scaling Laws for Multilevel Converters in AC/DC Applications”. In: *IEEE Transactions on Power Electronics* 36.4 (2021), pp. 3967–3986. DOI: 10.1109/TPEL.2020.3018857.
- [81] Gwendolin Rohner et al. “Hardware-Based Comparative Analysis of Multilevel Inverter Topologies for Integrated Motor Drives Considering Overload Operation”. In: *IEEE Open Journal of Power Electronics* 4 (2023), pp. 934–944. DOI: 10.1109/OJPEL.2023.3327423.
- [82] J. Rodriguez, Jih-Sheng Lai, and Fang Zheng Peng. “Multilevel inverters: a survey of topologies, controls, and applications”. In: *IEEE Transactions on Industrial Electronics* 49.4 (2002), pp. 724–738. DOI: 10.1109/TIE.2002.801052.
- [83] Shoaib Munawar et al. “Multilevel Inverters Design, Topologies, and Applications: Research Issues, Current, and Future Directions”. In: *IEEE Access* 12 (2024), pp. 149320–149350. DOI: 10.1109/ACCESS.2024.3472752.
- [84] Luis AM Barros, António P Martins, and José Gabriel Pinto. “A comprehensive review on modular multilevel converters, submodule topologies, and modulation techniques”. In: *Energies* 15.3 (2022), p. 1078.
- [85] Fabian Gebhardt, Hauke Vach, and Friedrich W Fuchs. “Comparison of transformerless multilevel topologies for photovoltaic application concerning efficiency, leakage current and mechanical volume”. In: *PCIM Europe Conference Proceedings*. 2012, pp. 1116–1123.

- [86] Raghbendra Tiwari, Roy Nilsen, and Arne Nysveen. “Evaluation and Comparison between Multilevel Converters for Variable Speed Operation of Pumped Storage Power Plants with Full-size Converters”. In: *2021 IEEE Industry Applications Society Annual Meeting (IAS)*. 2021, pp. 1–8. DOI: 10.1109/IAS48185.2021.9677283.
- [87] A. Lesnicar and R. Marquardt. “An innovative modular multilevel converter topology suitable for a wide power range”. In: *2003 IEEE Bologna Power Tech Conference Proceedings*, vol. 3. 2003, 6 pp. Vol.3-. DOI: 10.1109/PTC.2003.1304403.
- [88] Jingyang Fang et al. “A Review of Multilevel Converters With Parallel Connectivity”. In: *IEEE Transactions on Power Electronics* 36.11 (2021), pp. 12468–12489. DOI: 10.1109/TPEL.2021.3075211.
- [89] Yumeng Tian et al. “Review, Classification and Loss Comparison of Modular Multilevel Converter Submodules for HVDC Applications”. In: *Energies* 15.6 (2022). ISSN: 1996-1073. DOI: 10.3390/en15061985. URL: <https://www.mdpi.com/1996-1073/15/6/1985>.
- [90] Marcin Zygmanski, Bogusław Grzesik, and Radosław Nalepa. “Capacitance and inductance selection of the modular multilevel converter”. In: *2013 15th European Conference on Power Electronics and Applications (EPE)*. 2013, pp. 1–10. DOI: 10.1109/EPE.2013.6634446.
- [91] SuperGrid Institute. “Methodology for Defining Arm Inductance Range in Modular Multilevel Converters for HVDC Applications”. In: (Sept. 2024). URL: <https://www.supergrid-institute.com/2024/09/26/arm-inductance-range-modular-multilevel-converters-hvdc/>.
- [92] Aditya Shekhar et al. “Number of Levels, Arm Inductance and Modulation Trade-offs for High Power Medium Voltage Grid-Connected Modular Multilevel Converters”. In: *2019 10th International Conference on Power Electronics and ECCE Asia (ICPE 2019 - ECCE Asia)*. 2019, pp. 1–8. DOI: 10.23919/ICPE2019-ECCEAsia42246.2019.8797231.
- [93] A. Hillers and J. Biela. “Optimal design of the modular multilevel converter for an energy storage system based on split batteries”. In: *2013 15th European Conference on Power Electronics and Applications (EPE)*. 2013, pp. 1–11. DOI: 10.1109/EPE.2013.6634660.
- [94] Yang Wang et al. “Design and Optimization of the Arm Inductor for Modular Multilevel Converter”. In: *2022 International Symposium on Power Electronics, Electrical Drives, Automation and Motion (SPEEDAM)*. 2022, pp. 354–359. DOI: 10.1109/SPEEDAM53979.2022.9842277.

- [95] Antonios Antonopoulos, Lennart Angquist, and Hans-Peter Nee. “On dynamics and voltage control of the Modular Multilevel Converter”. In: *2009 13th European Conference on Power Electronics and Applications*. 2009, pp. 1–10.
- [96] Marcin Zygmanski et al. “Selected aspects of Modular Multilevel Converter operation”. In: *Bulletin of the Polish Academy of Sciences, Technical Sciences* 62 (June 2014), pp. 2014–38. DOI: 10.2478/bpasts-2014-0038.
- [97] Salman Saeed Khan and Elisabetta Tedeschi. “Modeling of MMC for Fast and Accurate Simulation of Electromagnetic Transients: A Review”. In: *Energies* 10.8 (2017). ISSN: 1996-1073. DOI: 10.3390/en10081161. URL: <https://www.mdpi.com/1996-1073/10/8/1161>.
- [98] Kalle Ilves et al. “On Energy Storage Requirements in Modular Multilevel Converters”. In: *IEEE Transactions on Power Electronics* 29.1 (2014), pp. 77–88. DOI: 10.1109/TPEL.2013.2254129.
- [99] L.M. Redondo et al. “High-voltage high-frequency Marx-bank type pulse generator using integrated power semiconductor half-bridges”. In: *2005 European Conference on Power Electronics and Applications*. 2005, 8 pp.–P.8. DOI: 10.1109/EPE.2005.219301.
- [100] Shuren Wang et al. “Analysis and Assessment of Modular Multilevel Converter Internal Control Schemes”. In: *IEEE Journal of Emerging and Selected Topics in Power Electronics* 8.1 (2020), pp. 697–719. DOI: 10.1109/JESTPE.2019.2899794.
- [101] Apparao Dekka et al. “Evolution of Topologies, Modeling, Control Schemes, and Applications of Modular Multilevel Converters”. In: *IEEE Journal of Emerging and Selected Topics in Power Electronics* 5.4 (2017), pp. 1631–1656. DOI: 10.1109/JESTPE.2017.2742938.
- [102] Colm J. O’Rourke et al. “A Geometric Interpretation of Reference Frames and Transformations: dq0, Clarke, and Park”. In: *IEEE Transactions on Energy Conversion* 34.4 (2019), pp. 2070–2083. DOI: 10.1109/TEC.2019.2941175.
- [103] Stefan Milovanovic. “MMC-based conversion for MVDC applications”. PhD thesis. Lausanne, EPFL, 2020. DOI: 10.5075/epfl-thesis-8613. URL: <https://infoscience.epfl.ch/handle/20.500.14299/168306>.
- [104] Simon Fuchs. “MMCs Made Compact and Fast - Towards Modular Multilevel Converters with Minimized Module Capacitors and Fast Transient Operation Utilizing Advanced Control Methods”. PhD thesis. ETH Zurich, 2022. URL: <https://www.research-collection.ethz.ch/handle/20.500.11850/558253>.

- [105] P. Münch. *Konzeption und Entwurf integrierter Regelungen für Modulare Multilevel Umrichter*. Forschungsberichte Aus Dem Lehrstuhl Für Regelungssysteme Series. Logos-Verlag, 2011. ISBN: 9783832529031.
- [106] Gene F Franklin et al. *Feedback control of dynamic systems*. Vol. 4. Prentice hall Upper Saddle River, 2002.
- [107] H.K. Khalil. *Nonlinear Systems*. Pearson Education. Prentice Hall, 2014. ISBN: 9780130673893.
- [108] A. Isidori. *Nonlinear Control Systems*. Communications and Control Engineering. Springer London, 1995. ISBN: 9783540199168.
- [109] Lennart Angquist et al. “Open-Loop Control of Modular Multilevel Converters Using Estimation of Stored Energy”. In: *IEEE Transactions on Industry Applications* 47.6 (2011), pp. 2516–2524. DOI: 10.1109/TIA.2011.2168593.
- [110] Simon Fuchs, Simon Beck, and Jürgen Biela. “Analysis and Reduction of the Output Voltage Error of PWM for Modular Multilevel Converters”. In: *IEEE Transactions on Industrial Electronics* 66.3 (2019), pp. 2291–2301. DOI: 10.1109/TIE.2018.2844821.
- [111] Makoto Hagiwara and Hirofumi Akagi. “Control and Experiment of Pulsewidth-Modulated Modular Multilevel Converters”. In: *IEEE Transactions on Power Electronics* 24.7 (2009), pp. 1737–1746. DOI: 10.1109/TPEL.2009.2014236.
- [112] Mattia Ricco et al. “FPGA-Based Implementation of MMC Control Based on Sorting Networks”. In: *Energies* 11.9 (2018). ISSN: 1996-1073. DOI: 10.3390/en11092394. URL: <https://www.mdpi.com/1996-1073/11/9/2394>.
- [113] Theodor Heath et al. “Capacitor balancing controller voltage sorting statistics in modular multilevel converters”. In: *2017 IEEE Southern Power Electronics Conference (SPEC)*. 2017, pp. 1–8. DOI: 10.1109/SPEC.2017.8333550.
- [114] Qingbo Xi, Yizhi Tian, and Yanfang Fan. “Capacitor Voltage Balancing Control of MMC Sub-Module Based on Neural Network Prediction”. In: *Electronics* 13.4 (2024). ISSN: 2079-9292. DOI: 10.3390/electronics13040795. URL: <https://www.mdpi.com/2079-9292/13/4/795>.
- [115] Safia Babikir Bashir and Abdul Rahiman Beig. “An improved voltage balancing algorithm for grid connected MMC for medium voltage energy conversion”. In: *International Journal of Electrical Power & Energy Systems* 95 (2018), pp. 550–560.

- [116] Andrés Mora et al. “Model-Predictive-Control-Based Capacitor Voltage Balancing Strategies for Modular Multilevel Converters”. In: *IEEE Transactions on Industrial Electronics* 66.3 (2019), pp. 2432–2443. DOI: 10.1109/TIE.2018.2844842.
- [117] Jiapeng Yin et al. “Direct Pulsewidth Modulation Technique for Modular Multilevel Converters Based on Full-Bridge Submodules”. In: *IEEE Transactions on Power Electronics* 40.1 (2025), pp. 1085–1098. DOI: 10.1109/TPEL.2024.3459052.
- [118] Rosheila Darus et al. “A Modified Voltage Balancing Algorithm for the Modular Multilevel Converter: Evaluation for Staircase and Phase-Disposition PWM”. In: *IEEE Transactions on Power Electronics* 30.8 (2015), pp. 4119–4127. DOI: 10.1109/TPEL.2014.2359005.
- [119] Antonios Antonopoulos, Lennart Angquist, and Hans-Peter Nee. “On dynamics and voltage control of the Modular Multilevel Converter”. In: *2009 13th European Conference on Power Electronics and Applications*. 2009, pp. 1–10.
- [120] Plexim GmbH. *PLECS*. Version 4.8.4. Simulation software for power electronics and electrical systems. URL: <https://www.plexim.com>.
- [121] Minyuan Guan, Zheng Xu, and Hairong Chen. “Control and modulation strategies for modular multilevel converter based HVDC system”. In: *IECON 2011 - 37th Annual Conference of the IEEE Industrial Electronics Society*. 2011, pp. 849–854. DOI: 10.1109/IECON.2011.6119421.
- [122] Gum Tae Son et al. “Design and Control of a Modular Multilevel HVDC Converter With Redundant Power Modules for Noninterruptible Energy Transfer”. In: *IEEE Transactions on Power Delivery* 27.3 (2012), pp. 1611–1619. DOI: 10.1109/TPWRD.2012.2190530.
- [123] Prafullachandra M. Meshram and Vijay B. Borghate. “A Simplified Nearest Level Control (NLC) Voltage Balancing Method for Modular Multilevel Converter (MMC)”. In: *IEEE Transactions on Power Electronics* 30.1 (2015), pp. 450–462. DOI: 10.1109/TPEL.2014.2317705.
- [124] Alinaghi Marzoughi et al. “Analysis of capacitor voltage ripple minimization in modular multilevel converter based on average model”. In: *2015 IEEE 16th Workshop on Control and Modeling for Power Electronics (COMPEL)*. 2015, pp. 1–7. DOI: 10.1109/COMPEL.2015.7236451.
- [125] H.W. van der Broeck, H.-C. Skudelny, and G.V. Stanke. “Analysis and realization of a pulsewidth modulator based on voltage space vectors”. In: *IEEE Transactions on Industry Applications* 24.1 (1988), pp. 142–150. DOI: 10.1109/28.87265.

- [126] Soham Dutta, Minghui Lu, and Brian Johnson. “Decentralized PWM Interleaving for Ripple Minimization in both Symmetric and Asymmetric Parallel-connected DC-DC Converters”. In: *2021 IEEE Energy Conversion Congress and Exposition (ECCE)*. 2021, pp. 2894–2901. DOI: 10.1109/ECCE47101.2021.9595611.
- [127] Andres E. Leon and Santiago J. Amodeo. “Energy Balancing Improvement of Modular Multilevel Converters Under Unbalanced Grid Conditions”. In: *IEEE Transactions on Power Electronics* 32.8 (2017), pp. 6628–6637. DOI: 10.1109/TPEL.2016.2621000.
- [128] Jinke Li et al. “Operation and Control Methods of Modular Multilevel Converters in Unbalanced AC Grids: A Review”. In: *IEEE Journal of Emerging and Selected Topics in Power Electronics* 7.2 (2019), pp. 1258–1271. DOI: 10.1109/JESTPE.2018.2856505.
- [129] Joan Rocabert et al. “Control of Power Converters in AC Microgrids”. In: *IEEE Transactions on Power Electronics* 27.11 (2012), pp. 4734–4749. DOI: 10.1109/TPEL.2012.2199334.
- [130] J. Li et al. “Operation and Control Methods of Modular Multilevel Converters in Unbalanced AC Grids: A Review”. In: *IEEE J. Emerg. Sel. Top. Power Electron.* 7.2 (2019), pp. 1258–1271. DOI: 10.1109/JESTPE.2018.2856505.
- [131] Andres E. Leon and Santiago J. Amodeo. “Energy Balancing Improvement of Modular Multilevel Converters Under Unbalanced Grid Conditions”. In: *IEEE Trans. Power Electron.* 32.8 (2017), pp. 6628–6637. DOI: 10.1109/TPEL.2016.2621000.
- [132] António-Ferreira et al. “Modulation techniques applied to medium voltage modular multilevel converters for renewable energy integration: A review”. In: *Electric Power Systems Research* 155 (2018), pp. 21–39. ISSN: 0378-7796. DOI: <https://doi.org/10.1016/j.epsr.2017.08.015>.
- [133] Philipp Münch, Steven Liu, and Mike Dommaschk. “Modeling and current control of modular multilevel converters considering actuator and sensor delays”. In: *35th IECON*. 2009, pp. 1633–1638. DOI: 10.1109/IECON.2009.5414756.
- [134] Tobias Geyer. *Model Predictive Control of Industrial Power Electronics*. John Wiley & Sons, 2016.
- [135] Simon Fuchs, Min Jeong, and Jürgen Biela. “Long Horizon, Quadratic Programming Based Model Predictive Control (MPC) for Grid Connected Modular Multilevel Converters (MMC)”. In: *45th IECON*. 2019, pp. 1805–1812. DOI: 10.1109/IECON.2019.8927493.

- [136] Na Chai et al. “Three-Phase Model-Based Predictive Control Methods With Reduced Calculation Burden for Modular Multilevel Converters”. In: *IEEE J. Emerg. Sel. Top. Power Electron.* 10.6 (2022), pp. 7037–7048. DOI: 10.1109/JESTPE.2022.3170503.
- [137] Min Jeong, Simon Fuchs, and Jürgen Biela. “High Performance LQR Control of Modular Multilevel Converters with Simple Control Structure and Implementation”. In: *2020 EPE ECCE Europe*. 2020, P.1–P.10. DOI: 10.23919/EPE20ECCEurope43536.2020.9215617.
- [138] Guacira Costa de Oliveira et al. “Bilinear Quadratic Feedback Control of Modular Multilevel Converters”. In: *Energies* 16.18 (2023). ISSN: 1996-1073. DOI: 10.3390/en16186713. URL: <https://www.mdpi.com/1996-1073/16/18/6713>.
- [139] Philipp Münch et al. “Integrated current control, energy control and energy balancing of Modular Multilevel Converters”. In: *36th IECON*. 2010, pp. 150–155. DOI: 10.1109/IECON.2010.5675185.
- [140] Shunfeng Yang, Peng Wang, and Yi Tang. “Feedback Linearization-Based Current Control Strategy for Modular Multilevel Converters”. In: *IEEE Trans. Power Electron.* 33.1 (2018), pp. 161–174. DOI: 10.1109/TPEL.2017.2662062.
- [141] Zou et al. “Phase-Unsynchronized Power Decoupling Control of MMC Based on Feedback Linearization”. In: *IEEE Trans. Power Electron.* 37.3 (2022), pp. 2946–2958. DOI: 10.1109/TPEL.2021.3119527.
- [142] Lu, X. et al. “Feedback Linearization Control for MMC Considering Capacitor Voltage Harmonics”. In: *PSGEC*. 2021, pp. 112–117. DOI: 10.1109/PSGEC51302.2021.9542222.
- [143] A. Dekka et al. “Model Predictive Control of High-Power Modular Multilevel Converters—An Overview”. In: *IEEE J. Emerg. Sel. Top. Power Electron.* 7.1 (2019), pp. 168–183. DOI: 10.1109/JESTPE.2018.2880137.
- [144] Silpa Baburajan et al. “Design of Common DC-Link Capacitor in Multiple-Drive System Based on Reduced DC-Link Current Harmonics Modulation”. In: *IEEE Transactions on Power Electronics* 37.8 (2022), pp. 9703–9717. DOI: 10.1109/TPEL.2022.3143545.
- [145] Gilbert Bergna-Diaz et al. “Optimal Shaping of the MMC Circulating Currents for Preventing AC-Side Power Oscillations From Propagating Into HVdc Grids”. In: *IEEE Journal of Emerging and Selected Topics in Power Electronics* 7.2 (2019), pp. 1015–1030. DOI: 10.1109/JESTPE.2019.2894677.

- [146] Rayane Mourouvin et al. “AC/DC Dynamic Interactions of MMC-HVDC in Grid-Forming for Wind-Farm Integration in AC Systems”. In: *2020 22nd European Conference on Power Electronics and Applications (EPE'20 ECCE Europe)*. 2020, P.1–P.9. DOI: 10.23919/EPE20ECCEEurope43536.2020.9215668.
- [147] Abel A. Taffese, Elisabetta Tedeschi, and Erik de Jong. “A control scheme for utilizing energy storage of the modular multilevel converter for power oscillation damping”. In: *2017 IEEE 18th Workshop on Control and Modeling for Power Electronics (COMPEL)*. 2017, pp. 1–8. DOI: 10.1109/COMPEL.2017.8013415.
- [148] Yonggang Zhang et al. “Small-Signal AC-DC Coupling Analysis of Grid-Following and Grid-Forming MMCs”. In: *2024 IEEE Power & Energy Society General Meeting (PESGM)*. 2024, pp. 1–5. DOI: 10.1109/PESGM51994.2024.10689133.
- [149] Enric Sánchez-Sánchez, Eduardo Prieto-Araujo, and Oriol Gomis-Bellmunt. “The Role of the Internal Energy in MMCs Operating in Grid-Forming Mode”. In: *IEEE Journal of Emerging and Selected Topics in Power Electronics* 8.2 (2020), pp. 949–962. DOI: 10.1109/JESTPE.2019.2961774.
- [150] Marija Jankovic et al. “Arm-Balancing Control and Experimental Validation of a Grid-Connected MMC With Pulsed DC Load”. In: *IEEE Transactions on Industrial Electronics* 64.12 (2017), pp. 9180–9190. DOI: 10.1109/TIE.2017.2711516.
- [151] Hendrik Fehr and Albrecht Gensior. “MMC Stationary Operating Regimes in Case of Periodic Power Demand on the DC Side”. In: *IEEE Transactions on Power Electronics* 37.7 (2022), pp. 7640–7651. DOI: 10.1109/TPEL.2022.3143318.
- [152] Nguyen Hoang Viet, Pham Hong Duong, and Nguyen Tien Duc. “Feedback Linearization Control and Current Control Mode for Boost Converter”. In: *2024 16th International Conference on Electronics, Computers and Artificial Intelligence (ECAI)*. 2024, pp. 1–6. DOI: 10.1109/ECAI61503.2024.10607550.
- [153] Costas Kravaris and Masoud Soroush. “Synthesis of multivariable nonlinear controllers by input/output linearization”. In: *AICHE Journal* 36.2 (1990), pp. 249–264. DOI: <https://doi.org/10.1002/aic.690360211>.
- [154] Prof. Dr.-Ing Steven Liu. “Vorlesung Lineare Regelungen (Regelungstechnik 1)”. In: Lehrstuhl für Regelungssysteme. 2024. Chap. 3.
- [155] Alon Kuperman. “Proportional-Resonant Current Controllers Design Based on Desired Transient Performance”. In: *IEEE Transactions on Power Electronics* 30.10 (2015), pp. 5341–5345. DOI: 10.1109/TPEL.2015.2408053.

- [156] Vinícius F. Montagner and Samuel P. Ribas. “State feedback control for tracking sinusoidal references with rejection of disturbances applied to UPS systems”. In: *2009 35th Annual Conference of IEEE Industrial Electronics*. 2009, pp. 1764–1769. DOI: 10.1109/IECON.2009.5414814.
- [157] Alejandro Yepes. “Digital Resonant Current Controllers for Voltage Source Converters”. PhD thesis. Dec. 2011.
- [158] Sizhan Zhou et al. “DQ Current Control of Voltage Source Converters With a Decoupling Method Based on Preprocessed Reference Current Feed-forward”. In: *IEEE Transactions on Power Electronics* 32.11 (2017), pp. 8904–8921. DOI: 10.1109/TPEL.2017.2651139.
- [159] Zunaib Ali et al. “Three-phase phase-locked loop synchronization algorithms for grid-connected renewable energy systems: A review”. In: *Renewable and Sustainable Energy Reviews* 90 (2018), pp. 434–452. ISSN: 1364-0321. DOI: <https://doi.org/10.1016/j.rser.2018.03.086>. URL: <https://www.sciencedirect.com/science/article/pii/S1364032118301813>.
- [160] F. Briz, M.W. Degner, and R.D. Lorenz. “Analysis and design of current regulators using complex vectors”. In: *IEEE Transactions on Industry Applications* 36.3 (2000), pp. 817–825. DOI: 10.1109/28.845057.
- [161] Philipp Muench, Steven Liu, and Günter Ebner. “Multivariable current control of Modular Multilevel Converters with disturbance rejection and harmonics compensation”. In: *2010 IEEE International Conference on Control Applications*. 2010, pp. 196–201. DOI: 10.1109/CCA.2010.5611205.
- [162] Shihua Li et al. *Disturbance observer-based control: methods and applications*. CRC press, 2014.
- [163] Ngansom Emeric Claudel. “Improving Robustness of Feedback Linearization Controller for Multi Modular Converter”. Master Thesis. Kaiserslautern, Germany: University of Kaiserslautern-Landau (RPTU), Feb. 2024.
- [164] Jun Yang, Wen-Hua Chen, and Shihua Li. “Autopilot design of bank-to-turn missiles using state-space disturbance observers”. In: *UKACC International Conference on Control 2010*. 2010, pp. 1–6. DOI: 10.1049/ic.2010.0454.
- [165] Di Shi, Zhong Wu, and Wusheng Chou. “Super-Twisting Extended State Observer and Sliding Mode Controller for Quadrotor UAV Attitude System in Presence of Wind Gust and Actuator Faults”. In: *Electronics* 7.8 (2018). ISSN: 2079-9292. DOI: 10.3390/electronics7080128. URL: <https://www.mdpi.com/2079-9292/7/8/128>.
- [166] Hirofumi Akagi, Edson Hirokazu Watanabe, and Mauricio Aredes. *The Instantaneous Power Theory*. 2017, pp. 37–109. DOI: 10.1002/9781119307181.ch3.

- [167] Philipp Münch. “Konzeption und Entwurf integrierter Regelungen für Modulare Multilevel Umrichter”. German. PhD thesis. TU Kaiserslautern, 2010.
- [168] Johannes Kolb. “Optimale Betriebsführung des Modularen Multilevel-Umrichters als Antriebsumrichter für Drehstrommaschinen”. German. PhD thesis. 2014. 310 pp. ISBN: 978-3-7315-0183-1. DOI: 10.5445/KSP/1000039063.
- [169] Prof. Dr.-Ing Steven Liu. “Vorlesung Lineare Regelungen (Regelungstechnik 1)”. In: Lehrstuhl für Regelungssysteme. 2024. Chap. 6.
- [170] Vicente Balaguer et al. “Enhanced 2-DOF PID Controller Tuning Based on an Uncertainty and Disturbance Estimator With Experimental Validation”. In: *IEEE Access* 9 (2021). DOI: 10.1109/ACCESS.2021.3095057.
- [171] Emil Grosswald. *Bessel polynomials*. Vol. 698. Springer, 2006.
- [172] I. M. Filanovsky. “Polynomial Filters with Controllable Overshoot In Their Step Transient Responses”. In: *2021 IEEE International Midwest Symposium on Circuits and Systems (MWSCAS)*. 2021, pp. 382–385. DOI: 10.1109/MWSCAS47672.2021.9531729.
- [173] Prof. Dr.-Ing. Daniel Görges. “Lecture Notes on Model Predictive Control”. In: Lehrstuhl für Elektromöblität. 2024. Chap. 5.
- [174] Liuping Wang. *Model Predictive Control System Design and Implementation Using MATLAB*. London: Springer, 2009. ISBN: 978-1-84882-331-0. DOI: 10.1007/978-1-84882-331-0.
- [175] Mohammed Alhajeri and Masoud Soroush. “Tuning Guidelines for Model-Predictive Control”. In: *Industrial & Engineering Chemistry Research* 59.10 (2020), pp. 4177–4191. DOI: 10.1021/acs.iecr.9b05931.
- [176] Mengjia Zhu, Alberto Bemporad, and Dario Piga. “Preference-based MPC calibration”. In: *2021 European Control Conference (ECC)*. 2021, pp. 638–645. DOI: 10.23919/ECC54610.2021.9654900.
- [177] Tobias Geyer. “Algebraic Tuning Guidelines for Model Predictive Torque and Flux Control”. In: *IEEE Transactions on Industry Applications* 54.5 (2018), pp. 4464–4475. DOI: 10.1109/TIA.2018.2835375.
- [178] Andre Shigueo Yamashita, Antônio Carlos Zanin, and Darci Odloak. “Tuning of model predictive control with multi-objective optimization”. In: *Brazilian Journal of Chemical Engineering* 33.2 (2016), pp. 333–346.
- [179] Clifford Hildreth. “A quadratic programming procedure”. In: *Naval research logistics quarterly* 4.1 (1957), pp. 79–85.
- [180] Marco Guerreiro, Pedro Dos Santos, and Steven Liu. “On the design of a model predictive controller for a DC-DC buck converter”. In: *2023 25th European Conference on Power Electronics and Applications (EPE'23 ECCE Europe)*. 2023, pp. 1–8. DOI: 10.23919/EPE23ECCEurope58414.2023.10264352.

- [181] Marco Guerreiro. *PyCTL: Hildreth Quadratic Programming Solver for Embedded Digital Control*. <https://github.com/mtg Guerreiro/pyctl>. 2024.
- [182] Marcel Wingert. “Improvement and Validation of a Control Platform for a Modular Multilevel Converter”. Master’s Thesis. Rheinland-Pfälzische Technische Universität Kaiserslautern-Landau, Feb. 2025.
- [183] Robert Finger et al. “Precision farming at the nexus of agricultural production and the environment”. In: *Annual Review of Resource Economics* 11.1 (2019), pp. 313–335.
- [184] Tim Nagel et al. “Design of MVDC Power Transmission for a Grid Connected Agricultural Machine”. In: *2016 IEEE Vehicle Power and Propulsion Conference (VPPC)*. 2016, pp. 1–6. DOI: 10.1109/VPPC.2016.7791661.
- [185] M Stöhr and B Hackenberg. “Enhancing synergy effects between the electrification of agricultural machines and renewable energy deployment with semi-stationary energy storage in rural grids”. In: *Energy Procedia* 155 (2018), pp. 179–187.
- [186] *GridCon Project - Research for Future Grid Converters*. URL: <https://www.gridcon-project.de/>.
- [187] Hafiz Kashif Iqbal et al. “Volume Optimization of a 300kW MMC based DC-DC Converter for a DC Grid Connected Agricultural Machine”. In: *PCIM Asia 2021; International Exhibition and Conference for Power Electronics, Intelligent Motion, Renewable Energy and Energy Management*. 2021, pp. 1–6.
- [188] Luis Camurca et al. “Future MVDC Applications Using Modular Multilevel Converter”. In: *2020 6th IEEE International Energy Conference (ENERGYCon)*. 2020, pp. 1024–1029. DOI: 10.1109/ENERGYCon48941.2020.9236465.
- [189] Christian Sommer et al. “Analytical investigation of the three-phase single active bridge for offshore applications”. In: *2016 18th European Conference on Power Electronics and Applications (EPE’16 ECCE Europe)*. 2016, pp. 1–10. DOI: 10.1109/EPE.2016.7695590.
- [190] Yu Sang et al. “Analysis and Control of a Parallel DC Collection System for Wind Turbines with Single Active Bridge Converters”. In: *2018 IEEE Energy Conversion Congress and Exposition (ECCE)*. 2018, pp. 1005–1012. DOI: 10.1109/ECCE.2018.8557370.
- [191] G.D. Marques. “A simple and accurate system simulation of three-phase diode rectifiers”. In: *IECON ’98. Proceedings of the 24th Annual Conference of the IEEE Industrial Electronics Society (Cat. No.98CH36200)*. Vol. 1. 1998, 416–421 vol.1. DOI: 10.1109/IECON.1998.724276.

-
- [192] Yu Sang, Adrià Junyent-Ferré, and Tim C. Green. “Operational Principles of Three-Phase Single Active Bridge DC/DC Converters Under Duty Cycle Control”. In: *IEEE Transactions on Power Electronics* 35.8 (2020), pp. 8737–8750. DOI: 10.1109/TPEL.2020.2964901.
- [193] Jawad Ismail et al. “Experimental evaluation of a high power medium voltage converter for a DC grid connected agricultural machine”. In: *PCIM Europe digital days 2020; International Exhibition and Conference for Power Electronics, Intelligent Motion, Renewable Energy and Energy Management*. VDE. 2020, pp. 1–7.
- [194] Robert W Erickson and Dragan Maksimovic. *Fundamentals of power electronics*. Springer Science & Business Media, 2007.
- [195] Shrikant Kharade. “Development and Realization of a Control Platform for a Modular Multilevel Converter”. Master’s Thesis. Technische Universität Kaiserslautern, Aug. 2022.
- [196] Alexandra Löckel. “Development of a Gridforming Control for Modular Multilevel Converters”. Master’s Thesis. Technische Universität Kaiserslautern, Apr. 2022.
- [197] Marco Guerreiro et al. “An Open Processor-in-the-Loop Framework for Power Converter Control”. In: *IECON 2023- 49th Annual Conference of the IEEE Industrial Electronics Society*. 2023, pp. 1–6. DOI: 10.1109/IECON51785.2023.10312423.
- [198] Marco Guerreiro. *OPIL - Open Processor-in-the-Loop Framework*. <https://gitlab.rhrk.uni-kl.de/lrs/opil>. 2025.

Zusammenfassung

Diese Dissertation untersucht die topologische Struktur des Modularen Multilevel-Umrichters (MMC) mit besonderem Fokus auf dessen Modularität und flexiblen Energiespeicherfähigkeiten. Im Rahmen dieser Arbeit wurden zwei bislang unerforschte Eigenschaften des MMC eingeführt und analysiert, die durch die im Verlauf der Forschung entwickelten Regelungsstrategien gezielt erschlossen werden konnten.

Die gesammelten Daten deuten darauf hin, dass das globale Bevölkerungswachstum – insbesondere in wirtschaftlich aufstrebenden Ländern – mit einem stark steigenden Energiebedarf einhergeht. Bei Beibehaltung des derzeitigen Energiemixes ist eine weitere globale Erwärmung nur durch eine zügige, breit angelegte Elektrifizierung auf Basis erneuerbarer Energiequellen und Energiespeichersysteme abzuwenden. Da diese Technologien im Kern auf Gleichstrom (DC) beruhen, spricht vieles für einen Übergang von traditionellen Wechselstrom- (AC)-Netzen hin zu Gleichstrom- oder hybriden AC/DC-Netzarchitekturen. Diese Umstellung wird durch Fortschritte in der Leistungselektronik und der Entwicklung moderner Umrichterkonzepte ermöglicht, deren grundlegende Prinzipien im Rahmen dieser Arbeit für ein besseres Verständnis in den Folgekapiteln dargestellt wurden. Für Übertragungs- und Verteilnetze können nur mehrstufige Umrichtertopologien den gestiegenen Spannungsanforderungen gerecht werden. Unter diesen gilt der MMC als die flexibelste, kosteneffizienteste und vielversprechendste Lösung.

Die MMC-Topologie wurde durch Zerlegung in ihre grundlegenden Bausteine analysiert, wobei ein besonderer Schwerpunkt auf die flexiblen Energiespeicherfähigkeiten gelegt wurde. Eine umfassende Schaltungsanalyse diente als Grundlage für die Herleitung linearer und nichtlinearer Zustandsraummodelle. Verschiedene Modulationsverfahren und Balanciermethoden innerhalb eines Arms wurden vorgestellt. Sowohl Schalt- als auch gemittelte Modelle wurden beschrieben und miteinander verglichen, um die Eignung des gemittelten Modells zu belegen. Letzteres bildet das dynamische Verhalten der Topologie mit hinreichender Genauigkeit ab, insbesondere bei erhöhter Schaltfrequenz und reduzierter Anzahl verfügbarer Submodule, und dient daher als solide Grundlage für die Regelungsauslegung.

Im Anschluss wurde das Konzept der Leistungsentkopplung zwischen AC- und DC-Netzen vorgestellt. Durch gezielte Nutzung der Energiespeicherfähigkeit des

MMC lassen sich auf beiden Netzseiten unterschiedliche transiente Reaktionen auf eine gemeinsame Leistungsreferenz erzielen. Im Vergleich zu anderen Umrichter-topologien ist der MMC einzigartig in der Lage, die Energieflüsse zu Quelle und Senke simultan und unabhängig zu steuern. Diese Eigenschaft macht den MMC insbesondere für Anwendungen mit Netzen unterschiedlicher Natur attraktiv – etwa bei Kopplung an schwache Netze, wo schnelle Transienten auf der einen Seite potenziell die Stabilität auf der anderen gefährden könnten. Diese Fähigkeit wird durch die installierte Kapazität sowie die entwickelte Regelungsstruktur ermöglicht. Zur Kompensation der nichtlinearen inneren Zusammenhänge kam die Input-Output-Feedback-Linearisation zum Einsatz, um eine lineare und entkoppelte Regelung von DC-, AC- und Zirkulationsströmen zu ermöglichen. In einer kaskadierten Struktur beeinflussen diese Ströme die mittlere Energie in den Arm-Kondensatoren. Da diese Regelung sensitiv gegenüber Parametervariationen ist, wurde ein erweiterter Störbeobachter entwickelt. Darauf aufbauend wurde ein Zweipunkt-Regler (2-DOF) zur gezielten Steuerung der Armenergien entworfen, der zwischen Störungen und Referenzänderungen differenzieren kann. Die Leistungsfähigkeit des Reglers wurde anhand eines im Rahmen dieser Arbeit aufgebauten Laborprototyps validiert. Um zusätzlich Hardwarebeschränkungen zu berücksichtigen, wurde ein prädiktiver Regler mit langem Vorhersagehorizont als äußere Schleife untersucht. Dieser bietet gute Regelgüte unter gleichzeitiger Einhaltung von Randbedingungen hinsichtlich maximal übertragener Leistung und gespeicherter Energie. Der Regler wurde in einer Processor-in-the-Loop-Umgebung getestet, um seine Praxistauglichkeit unter verschiedenen Prädiktions- und Restriktionshorizonten zu evaluieren.

Darüber hinaus wird die Entwicklung eines mobilen Seitenumrichters (MSC) vorgestellt, der speziell für die Elektrifizierung schwerer landwirtschaftlicher Maschinen konzipiert wurde. In diesem anspruchsvollen Anwendungsbereich, in dem Elektrifizierung bisher nur schwer realisierbar ist, versorgt ein Mittelspannungs-Gleichstromnetz (MVDC) mehrere Maschinen gleichzeitig, was die Gesamteffizienz des Systems deutlich erhöht. Der MSC ist für die direkte Integration in jede Maschine vorgesehen und nutzt eine MMC-Architektur zur Transformation des MVDC auf die benötigten Niederspannungs-Gleichstrompegel (LVDC) der bordeigenen Subsysteme. Im Gegensatz zu herkömmlichen Ansätzen erreicht der Umrichter durch eine erhöhte Anzahl permanent eingeschalteter Submodule ein hohes Spannungsübersetzungsverhältnis – ohne Einsatz eines Transformators – und steigert dadurch die Leistungsdichte, wenngleich auf Kosten der verfügbaren Spannungsstufen. Trotz der stark nichtlinearen Struktur des resultierenden Schaltbildes wurden verschiedene Betriebsarten umfassend analysiert und anhand eines 300 kW-Demonstrators experimentell validiert. Zudem wurde ein reduziertes Modell entwickelt, das den Entwurf eines adaptiven Reglers unterstützt, der robuste und differenzierte Reaktionen auf Störungen und Referenzänderungen ermöglicht. Im Vergleich zu konventionellen Lösungen zeigte sich eine

signifikant verbesserte Dynamik und Anpassungsfähigkeit – ideal für die stark schwankenden Lastbedingungen in der Landwirtschaft.

Um das volle Potenzial der vorgestellten Ansätze auszuschöpfen, sollten in zukünftigen Arbeiten die in dieser Dissertation identifizierten Grenzen gezielt adressiert werden. Im Verlauf der Untersuchungen traten mehrere offene Fragestellungen auf, die klare Anhaltspunkte für weiterführende Forschung liefern. So wurde beispielsweise deutlich, dass das Erreichen einer vorgegebenen Transientenform zwar ein wünschenswertes Ziel darstellt, jedoch durch gemischtfrequente Anteile im Zirkulationsstrom erheblich erschwert wird – insbesondere während dynamischer Referenzverfolgung.

Das Konzept der Leistungsentkopplung könnte überdies auf weitere Funktionalitäten von Umrichtern zur Netzverknüpfung ausgedehnt werden, insbesondere unter Fehlerbedingungen oder bei Netzunsymmetrien. In solchen Szenarien treten zusätzliche gemischtfrequente Komponenten sowohl auf AC- als auch auf DC-Seite auf, was die Wirksamkeit der Feedback-Linearisation und die Robustheit des Störbeobachters beeinträchtigen kann. Fortschritte in diesem Bereich würden gleichzeitig die Leistungsfähigkeit der entwickelten MPC-Strategie verbessern. Trotz deren guter Gesamtleistung wurden in bestimmten Energiespeichern geringfügige Randbedingungsverletzungen beobachtet, vermutlich infolge von Modellabweichungen im geschlossenen Kreis des Zirkulationsstroms.

Auch die Erforschung alternativer Optimierungsmethoden zur praktischen Implementierung der langhorizontigen MPC ist ein vielversprechender Ansatz, um die Anwendbarkeit des Reglers unter realen Bedingungen weiter zu verbessern. Der Einsatz leistungsfähigerer eingebetteter Plattformen könnte zudem die Performance und Skalierbarkeit positiv beeinflussen.

Bezüglich des MSC stellt die hardwareseitige Umsetzung des vorgeschlagenen adaptiven Reglers einen zentralen nächsten Schritt dar – insbesondere vor dem Hintergrund der vielversprechenden Simulationsergebnisse. Darüber hinaus eröffnet die Integration von Leistungsentkopplungsprinzipien in den Betrieb des MSC ein spannendes Forschungsfeld. Dies erfordert allerdings zunächst die Entwicklung eines dedizierten Energieregler für die in dieser Arbeit vorgestellte Umrichterarchitektur.

Curriculum Vitae

Name Pedro Leal dos Santos
Born in Lisbon, Portugal

Education

2010 – 2014 B.Sc. in Electrical Engineering – Polytechnic of Lisbon
2013 Erasmus program – Eindhoven Fontys University
2014 – 2016 M.Sc. in Power Engineering – RWTH Aachen University

Experience

2017 – 2018 Research and Development Engineer – Digatron Power Electronics GmbH
2018 – 2024 Research Associate – University of Kaiserslautern-Landau
2025 – Research and Design Engineer – Maschinenfabrik Reinhausen GmbH